UNIVERSITY OF SOUTHAMPTON

School of Civil Engineering and the Environment

THE SHEAR BEHAVIOUR OF THE REINFORCED CONCRETE FOUR-PILE CAPS

by

Jing Cao

A thesis submitted for the Degree of Doctor of Philosophy in the School of Civil Engineering and the Environment of the University of Southampton

September 2009

UNIVERSITY OF Southampton
School of Civil Engineering and the Environment

To my parents and my grandmother for their self-giving encouragement and patience

‘…Moreover the works already known are due to chance and experiment rather than to science; for the sciences we now possess are merely systems for the nice ordering and setting forth of things already invented; not methods of invention or directions for new works…’

Sir Francis Bacon (1561AD - 1626AD)

‘Heaven rewards the diligent.’
天道酬勤。

Confucius (551BC - 479BC)

UNIVERSITY OF SOUTHAMPTON

ABSTRACT

SCHOOL OF CIVIL ENGINEERING AND THE ENVIRONMENT

Doctor of Philosophy

THE SHEAR BEHAVIOUR OF THE REINFORCED CONCRETE FOUR-PILE CAPS

by Jing Cao

There has been a consistent discrepancy between UK design standards BS5400 and BS8110 in the prediction of the shear capacity of 2-way spanning reinforced concrete pile caps from bending theory-based empirical design formulae. This causes designers difficulty to predict an accurate shear capacity of the pile cap. The inherently empirical character of the formulae is due to the fact that the formulae have been extrapolated from semi-empirical shear formulae for simply supported deep 1-way spanning beam structures, and been further empirically developed for 2-way spanning caps. Thus the essential cause of the discrepancy is that the formulae lack both physical explanation in terms of the cap's shear behaviour, and sufficient basis as empirical formulae due to the shortage of experimental data.

This research focuses on the revelation of the true shear capacity and failure mechanism of pile caps by consideration of a particular prototype form, namely a singly reinforced four-pile concrete cap under wall loading. It is aided by a series of laboratory experiments which are validated by an advanced non-linear numerical modelling for the reinforced concrete structure. The experience from the numerical modelling is taken further to carry out a parametric study expanding the sample size to a range covering more practical samples and covering different load patterns in order to enrich the limited data from the experiments.

The results give a verdict that both BS5400 and BS8110 are conservative with the former one most conservative. The level of conservatism of the standards, the actual shear capacity and failure mechanism of the cap vary with key pile cap dimensions such as longitudinal and transverse pile spacing, shear enhancement factor, and the width of the cap over which the shear enhancement factor is applied. The shear behaviour of pile caps is also influenced by the load patterns. In this research, the strut-and-tie method has been proved to be a more efficient and precise method than the empirical formulae because it presents a physical explanation of the shear mechanism. Suggestions to improve the design method are given.

A particular feature of this research is the application of a digital photogrammetry technique (PIV), normally applied in soil and fluid mechanics, to a solid mechanics situation. The tool has successfully detected the full-field displacement on the concrete surface and strains which are of high magnitude. The outputs have been compared with those from numerical modelling and they are in the same order of magnitude. The thesis describes the procedure of the application and an analysis of errors expected to occur in its application.

Table of Contents

List of Tables

List of Figures

List of Symbols

General

a_v: shear span (mm)

A: shear enhancement application factor

A_s: total area of the reinforcement in the cap longitudinal direction (mm^2)

$A_{s90\%}$: 90% the total area of the reinforcement in the cap longitudinal direction (mm^2)

b: width of pile cap (mm)

b': cap transverse width on which the shear enhancement factor is applied (mm)

d: effective depth of pile cap (mm)

$\frac{2d}{a_v}$: shear enhancement factor

d': pile depth (mm)

$D14'$: relative soffit deflection at position of potentiometer 14 (mm)

E_c: elastic modulus of concrete (N/mm^2 or MPa)

E_s: elastic modulus of steel (N/mm^2 or MPa)

f_{cu}: concrete cube compressive strength (N/mm^2 or MPa)

f_t: concrete tensile strength (N/mm^2 or MPa)

f_y: yield strength of reinforcement (N/mm^2 or MPa)

F: shear capacity of pile cap calculated from STM (kN)

G_f: fracture energy (J)

h: depth of pile cap (mm)

h_c: width of wall loading (mm)

h_{cr}: crack band width (mm)

h_o: overhang of pile cap in both longitudinal and transverse directions (mm)

h_p: pile diameter (mm)

kh_p: longitudinal pile spacing (mm)

kh_w: transverse pile spacing (mm)

l: length of pile cap (mm)

$m_{BS5400b}$: modification ratio of the actual failure load from experiments and FEA over the prediction from bending theory based shear formulae in BS5400

$m_{BS5400S}$: modification ratio of the actual failure load from experiments and FEA over the prediction from STM in BS5400

$m_{BS8110b}$: modification ratio of the actual failure load from experiments and FEA over the prediction from bending theory based shear formulae in BS8110

$m_{BS8110S}$: modification ratio of the actual failure load from experiments and FEA over the prediction from STM in BS8110

m_{nSTM}: modification ratio of the actual failure load from experiments and FEA over the prediction from new STM

M: internal bending moment calculated based on external load ($N \cdot m$)

n: transverse pile spacing divided by pile diameter ($= \frac{kh_w}{h_p}$)

R^2: coefficient of determination

v_c: nominal shear stress or nominal shear strength on a vertical beam or cap cross-section (N/mm^2 or MPa)

V: internal shear force calculated based on the external load (N)

V_c: shear failure load or shear capacity (kN)

p_1, p_2, p_3: first, second and third principal stress in concrete (N/mm^2 or MPa)

x, y, z: co-ordinate axis in FEA analysis defined by DIANA

α, γ: space angle in strut-and-tie system

β: shear retention factor; space angle in strut-and-tie system

γ_m: partial safety factor for design material strength

ε^{cr}: crack strain; when concrete tensile stress drops to zero is the ultimate crack strain

ε^{e}: ultimate elastic strain

ε_1: total crack strain or maximum principal strain

κ: internal state variable equivalent to plastic strain

ρ: reinforcement ratio (mm^2/mm^2)

σ_{sx}: stress in longitudinal reinforcement or in x co-ordinate (N/mm^2 or MPa);

σ_{sy}: stress in transverse reinforcement or in y co-ordinate (N/mm^2 or MPa);

σ_v: Von Mises stress (N/mm^2 or MPa)

PIV

d: resultant displacement in the object co-ordinates (mm)

I: summation of value of tricolor in one *IA*

IA: interrogation area

n: population of *IA* samples

NCC: nominal cross-correlation

r_u, r_v: ratio of real horizontal and vertical displacement in image co-ordinates over displacement from PIV in same unit

R: ratio of the length in mm in object co-ordinates over the length in *pixel* in image co-ordinates for a fixed distance; value of NCC

u, v: horizontal and vertical displacement relative to the wall loading on concrete surface in object co-ordinates (mm)

U, V: horizontal and vertical displacement relative to the wall loading bottom edge on the concrete surface in the image co-ordinates (*pixel*)

U', V': horizontal and vertical displacement relative to the ground on concrete surface in the image co-ordinates (*pixel*)

x, z: horizontal and vertical co-ordinates in PIV calculation

γ_{xz}, γ_{zx}: shear strain

$\Delta u, \Delta v$: relative horizontal and vertical displacement of u, v between two horizontal neighbouring *IAs* in object co-ordinates (mm)

$\Delta U', \Delta V'$: relative horizontal and vertical displacement of U', V' between two horizontal neighbouring *IAs* in image co-ordinates (*pixel*)

$\varepsilon_{xx}, \varepsilon_{zz}$: horizontal and vertical direct strain

Acknowledgement

I am deeply indebted to those whose helps and assistances have been so precious to me without which this thesis is never able to be completed.

I would like to thank

Dr. Alan G. Bloodworth, my supervisor, for his very kind and patient direction on my research work both in office and laboratory. The improvement of my written English is also attributed to him;

Dr. D.J. White from Cambridge University who shared the knowledge of PIV and software GeoPIV8 which has been applied throughout this research;

Mr. D.J. Lynock, Mr. M.S. Rose, Ken Yeates and other staffs in the Heavy Structural Laboratory of University of Southampton, for their devoted inductions and technical aids to my laboratory experiments;

Dr. Anthony Lock, who developed the camera control software for the application of PIV, for his academic guidance to the PIV technique;

Dr. Ming Xu, my colleague, for his contribution to the project on the numerical modelling and the laboratory experiments;

Prof. Stuart Moy, for his advice on calibrating potentiometers;

Prof. M.M.K. Lee, for giving me the precious opportunity to carry out the research in UK;

EPSRC, for the research funding which supported my work and living in UK;

The school administrative staffs and those ever being my friends, office colleagues, my flatmates and housemates including Chenyi Yao, Jing Zhang, Caihong Yu, with whom I have enjoyed a colourful life rather than only the everyday research work;

Bridge Division in Mott MacDonald Ltd. Croydon office where I worked, for accommodating a flexible time scheme for me to work through my thesis;

Finally, all of my family members in Shanghai, especially my father Mr. Zuyu Cao, my mother Mrs. Yuzhu Li and my grandmother, for their positive, supportive attitude and their understanding and patience. This work is also contributed to my grandfather passing away.

Chapter 1 Project introduction and methodology

1.1 A short introduction to the pile cap structure

Piled foundations are part of a structure used to carry and transfer load from the superstructure to the bearing strata underlying some depth below the ground surface. The main parts of the foundation are the pile and pile cap. They play different roles. The pile cap, a stocky reinforced concrete (RC) structure being sandwiched between supporting piles from underneath and an upper column or wall loading, distributes the concentrated load downwards to the piles by which the concentrated load is further transformed and dispersed into piles and soil.

Pile caps are utilized in both bridge and building construction. Depending on different geological conditions, the unique characters of superstructure and construction methods, the materials used and the formations of pile and pile cap, various subcategories are available.

A typical four-pile cap is supposed to be a 2-way spanning structure rather than a 1-way spanning structure. This means that the shear behaviour of the pile cap could be three-dimensional rather than the in-plane shear behaviour of a beam. The load applied from the superstructure is also complex for pile caps. Vertical load dominates, but horizontal loads also exist, such as wind load and traction-skidding force transmitted downwards through pier from a bridge support without a sliding bearing supporting system. These horizontal loads in general further result in a moment at the base of the column joining the top of the pile and the reaction from soil strata (Figure 1.1).

These together cause a complex shear resistant mechanism of the pile cap structure. Bearing in mind that the dimensions of the pile and upper loaded area is comparable with the depth and the width of the cap, one can conclude that they are likely to be significant parameters that affect the resisting behaviour of the cap body. In addition, the cap in practical service works with cracks, which changes the way the loading is transmitted. It is always difficult for engineers to design an RC pile cap to resist shear force.

To simplify and clarify the research objective, the aspect of the pile cap is simplified as shown in Figure 1.2: A cuboid cap is supported by four axisymmetric circular section piles assumed to bear both axial force and moment. This type of pile cap is the simplest and most designed in practical engineering and is frequently taken (by for example the British Standards) as the basis to explore other caps with more complex configurations. The type of load can either be a concentrated load, as shown in Figure 1.2 (a), or extend to a full-length

wall loading extending across the whole cap width, as shown in Figure 1.2 (b). The pile cap is assumed to be simply reinforced longitudinally and transversely and without shear reinforcement.

1.2 Current shear design methods and the outline of the problem for the pile cap designing

Current design methods for the pile cap shear capacity in the RC building standard, BS8110: Part 1 (1997) and the RC bridge standard, BS5400: Part 4 (1990) are semi-empirical formulae based on the bending theory. Strut-and-tie method (STM) is also allowed in both standards, but rules for defining the geometry of the strut-and-tie system and the design strength of the concrete strut are not specific.

A problem which arises when designing the pile cap is the discrepancy between the bending theory based formulae for the pile cap shear capacity prediction in BS5400 and BS8110. The implication is that one standard is unsafe or the other is conservative, or that both deviate from the accurate prediction.

The unjustifiable discrepancy arose during the historical development of the standards including the development of some of the key parameters in the design formulae such as the shear enhancement factor and the way it is to be applied on the cap width to enhance the shear capacity, which represents the 2-way feature of the pile cap. The development of this issue in each British Standard has been independent of the other and been based on empirical methods. As of today, although the shear enhancement factors in BS8110 and BS5400 are the same, the cap width on which the shear enhancement factor is applied is defined in different ways. When the cap width or the pile spacing in the cap width direction *i.e.* the transverse direction, is large enough, BS8110 specifies the shear enhancement factor can be applied on a cap width of maximum three times the pile diameter centred above each pile head. However, BS5400 specifies that even if the transverse pile spacing is large, the shear enhancement factor can only be applied on a cap width equal to one times the pile diameter above each pile head. Neither of these two standards supplies physical explanation for this.

Compared with the other parameters in the design formulae, such as the concrete compressive strength, reinforcement ratio and the depth of the pile cap, the shear enhancement factor and the cap width on which the shear enhancement factor is applied are the most significant for the discrepancy between the design formulae in BS8110 and BS5400.

1.3 Research aims

The overall aims of the project are to

1. investigate the shear capacity and shear mechanism of RC pile caps, typically of those in the laboratory experiments and in numerical modelling with specified dimensions;

2. investigate the validity of the bending theory based formulae of shear design for pile caps in BS5400 and BS8110;

3. suggest a new design method which predicts more accurately the shear capacity of pile caps.

1.4 Research methodology

In the first step of the research, a review of the shear theories behind the design formulae in the British Standards and other countries' standards was done. This helped to fully understand the background theory of the formulae and then to explain the discrepancies of the formulae described in Section 1.2.

A series of experiments on the shear capacity of the four-pile cap under a full-length wall loading (Figure 1.2 (b)) were carried out, to obtain direct results of the ultimate failure loads and the indication of the failure mechanism.

Finite element analysis (FEA) was applied in analysing the experimental samples so that the states of some mechanical variables, for instance the stress and strain in the cap body and in the reinforcement, and thus the failure mechanism, could be revealed. The FEA results were validated against the failure load, crack, displacement and strain distribution on the cap surfaces, soffit deflection and the strain in reinforcement from the experiments, to ensure the validity of the numerical modelling. Following this, a parametric study was carried out for a broader range of model dimensions than the tested samples but still under full-length wall loading. The models range from shallow caps to deep caps and from 1-way spanning to 2-way spanning caps. The commercial software, DIANA, was used.

The shear capacities of pile caps from the experiments and FEA were compared with the predictions from shear design formulae and STM in BS5400 and BS8110. Because the STM is ambiguously defined in both standards, and based on the fact that the method is so flexible that a structure could be idealized, theoretically speaking, by an infinite number of schemes of strut and tie assembly, only one simplified STM was examined in this project which is shown in Figure 1.3. The investigation of an optimized STM is beyond the scope of this thesis.

The influence of the load pattern (from concentrated loading to full-length wall loading) on the shear capacity and the shear mechanism of pile caps was investigated by studying a published pile cap experiment under concentrated load and a model under full-length wall loading from the parametric study in this research.

Particle image velocimetry (PIV), an example of a photogrammetry technique, was adopted throughout the experiments, by which the full-field displacement distribution on the cap surface was directly recorded. The full-field concrete strain distribution was then derived based on the displacement distribution. The application of PIV proved to be an alternative method to the traditional strain gauge to validate the results from FEA. The approximate strain distribution in the main reinforcement from PIV helped to reveal the shear mechanism of the pile cap. Because using the PIV technique to obtain the displacement and strain distribution of an RC structure is uncommon, an error analysis for the technique was specifically reported as an independent subject. The application of PIV was accomplished by a Matlab based software GeoPIV8.

The research aims and methodologies are shown in Figure 1.4.

1.5 Thesis organization

Chapter 2 introduces shear theories of 1-way spanning shallow and deep RC beams and their extension to the 2-way spanning RC four-pile caps. The current design methods in British Standards are introduced. The research problem arising from the discrepancy between the two British Standards is introduced;

Chapter 3 describes the experimental procedures, preceded by a literature review on previous pile cap experiments from which lessons for this research were learned. A brief introduction to the set up for PIV application for the experiments is presented. Basic observations of the crack distributions and failure loads are presented;

Chapter 4 presents a background to photogrammetry including the PIV technology and its application to the experiments. It also describes the practical issues associated with the PIV application using GeoPIV8 software on the concrete surface of pile caps to obtain the displacement, strain and stress distributions;

Chapter 5 describes the numerical modelling procedure. It also describes the validation work between the results from FEA and experiments including the PIV observations. A discussion of the validation work using the PIV technique is given. The failure loads and shear mechanisms from FEA of experimental samples and parametric models are reported;

Chapter 6 validates the expression of the nominal shear stress provided by the current design formulae. It also presents the quantitative comparisons between the failure loads from the experiments and numerical modelling and the prediction from current design methods in BS5400 and BS8110, in order to highlight the accuracy of the standards. The influence of the load pattern on the shear capacity and shear mechanism of the RC pile cap is investigated as an extension of the parametric study. A suggestion for the improvement of the current bending theory based design formulae is presented. In addition, a new STM, which is a modification of the current STM in British Standards, is introduced, giving a more reasonable prediction;

Chapter 7 is the major conclusions from this research and recommendations for future work;

Appendix I introduces the principles of PIV and the GeoPIV8 software and an error analysis of the technique described in Chapter 4;

Appendix II is a frame analysis for the pile cap samples in experiments;

Appendix III is a report of the crack distributions on surfaces of the experimental samples at the failure step;

Appendix IV is DIANA batch commands;

Appendix V is a list of published conference papers.

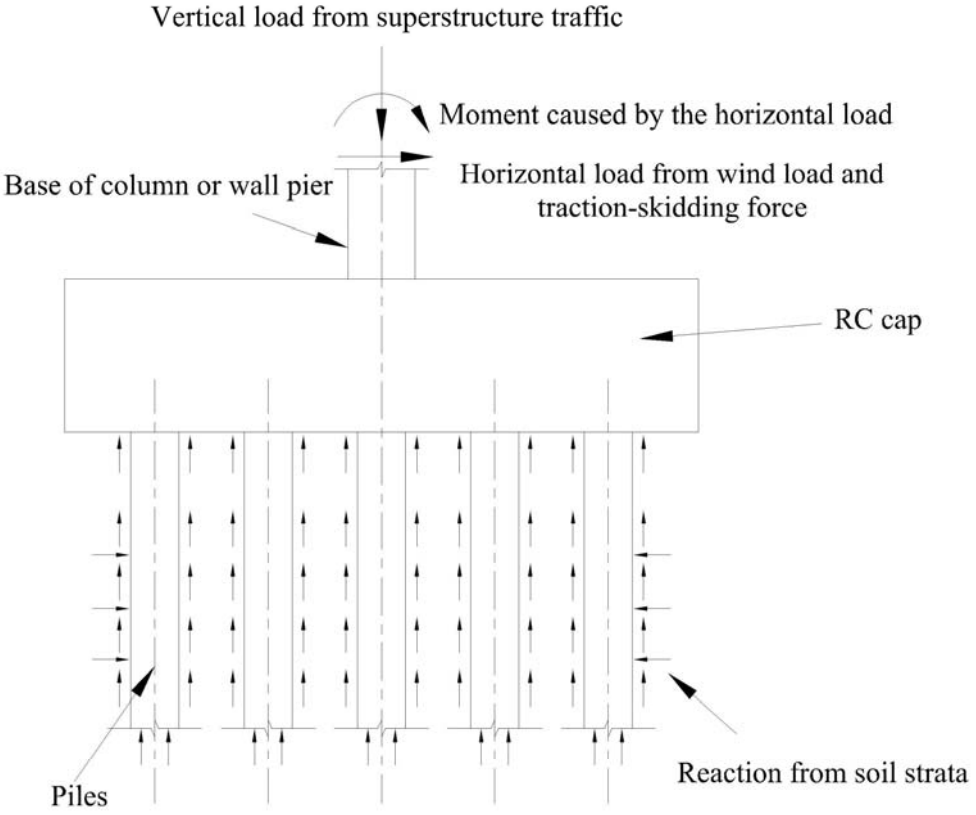

Figure 1.1 Schematic load conditions on the pile cap in practice

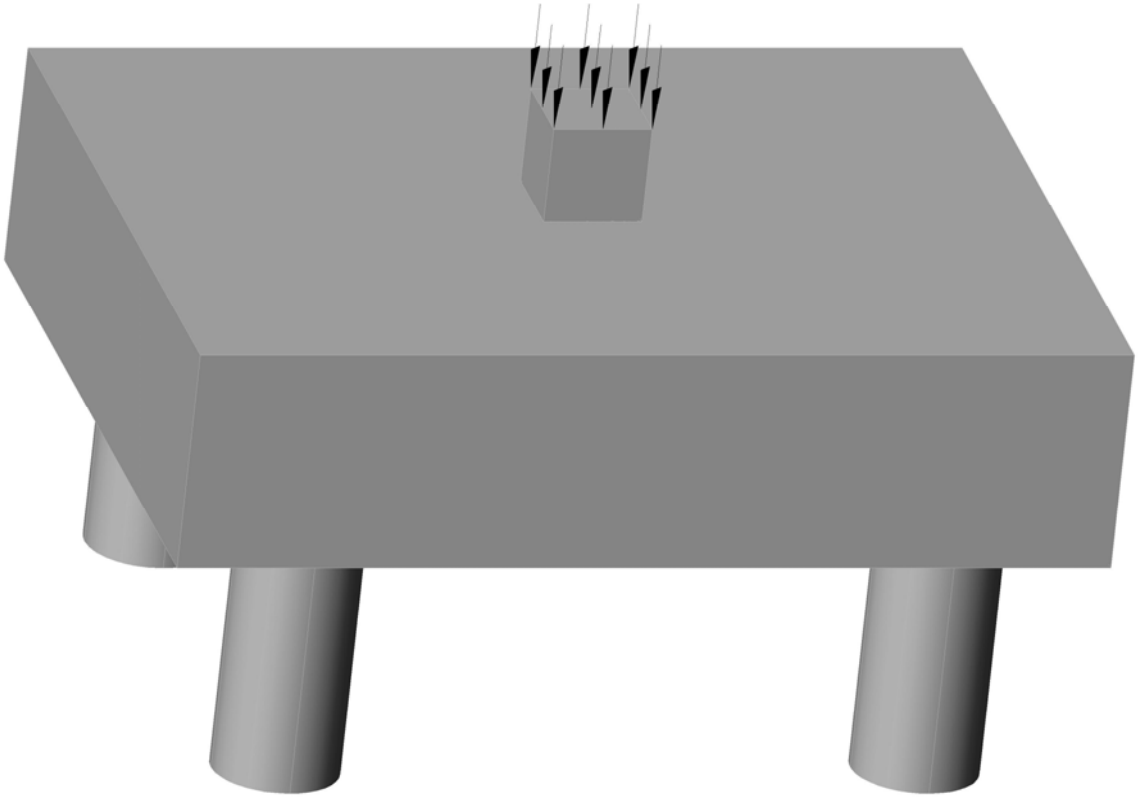

(a) Four-pile cap under a concentrated load

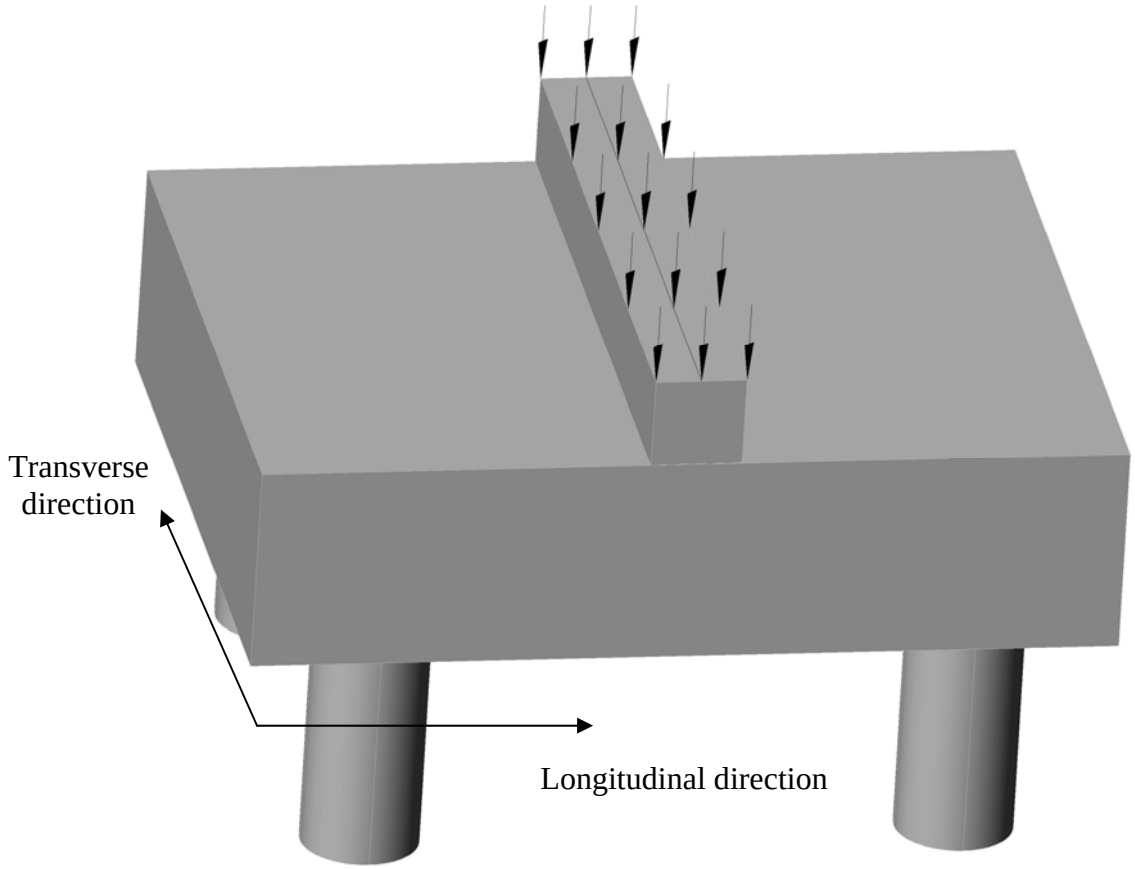

(b) Four-pile cap under a full-length wall loading used in the project

Figure 1.2 Load conditions in a simplified pile cap

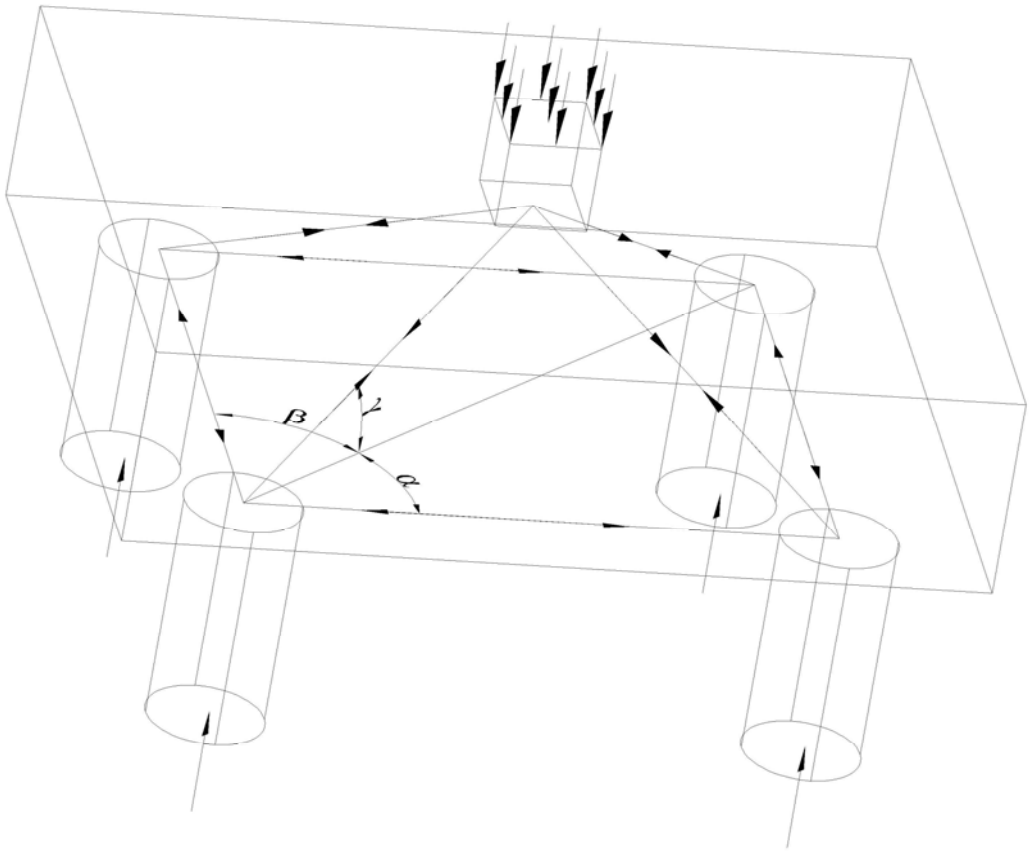

Figure 1.3 Strut-and-tie system assumed in a pile cap under a concentrated load or a wall loading

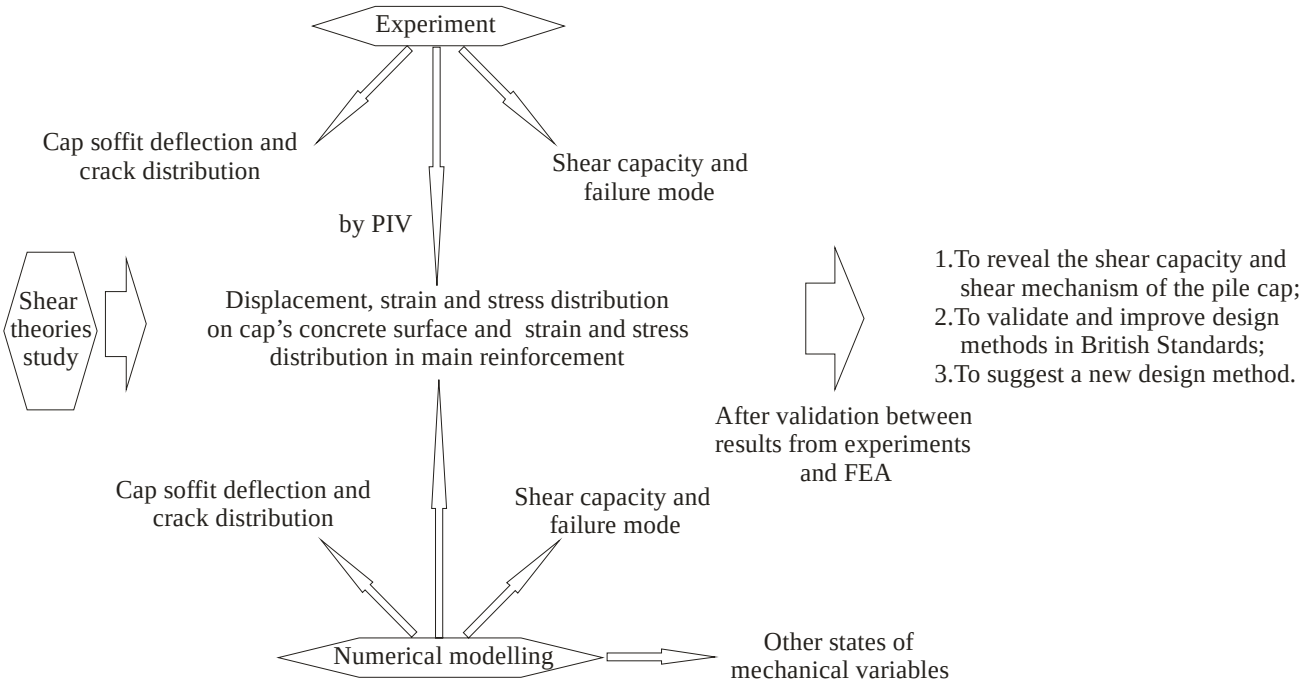

Figure 1.4 Research aims and methodologies

Chapter 2 Shear theories and shear design methods

2.1 Introduction

There has been research into the shear behaviour of RC beams for about a century (Regan, 1993). A number of methods to predict the shear capacity of RC beams have been established. The most straightforward method is to construct a shear mechanism based on an experimental observation of crack distributions. Another method is to construct an imaginary failure mode such as the truss and strut-and-tie system. Plastic methods are also available. There are also empirical methods based on statistical methods by analysing numerous experimental data.

This chapter starts with an introduction of the shear mechanisms, shear theories and design methods for 1-way spanning RC beams. Then it leads to how the design methods for 1-way spanning beams have been developed into the methods for 2-way spanning pile caps. It can be seen that the shear design formulae for pile caps in BS5400 and BS8110 are an extension of that for 1-way spanning beams. The possible reasons for the discrepancy between the shear design formulae in BS5400 and BS8110 are given.

The shear design methods in different nations are briefly discussed. A discussion of the current shear design formulae in BS8110 and BS5400 is given. The unjustifiable discrepancy between the two formulae is shown by systematically comparing key parts of the design formulae.

The beam type in this chapter, unless otherwise specified, is assumed to have a rectangular cross section and to be under a concentrated vertical load, without shear and compression reinforcement.

2.2 Shear mechanism in 1-way spanning RC beams

2.2.1 General shear cracking and failure modes in RC beams

Cracking in an RC beam is triggered by the stress not only from an internal bending moment but also from an internal vertical shear force. Shear failure is always associated with a failure mechanism corresponding to a status of shear cracking at the failure step.

Based on the observation from practice and experiments, shear failure of an RC beam can be classified into three modes: diagonal tensile failure (Kong, 1990), shear compression failure (Sato *et al*, 2004) and diagonal shear splitting failure (Kong, 1990). As shown in

Figure 2.1, in diagonal tensile failure, normally appearing in shallow beams where the shear span a_v (Figure 2.1) is larger than twice the beam effective depth d ($a_v > 2d$), the critical shear crack develops, connecting the support and the load and extends over the entire depth of the beam, causing the beam to split into two parts. In shear compression failure, normally appearing in medium depth beams ($d \le a_v \le 2d$), the diagonal shear crack extends deeply into the compression zone, such that the compressive region at the crack head fails due to crushing. When the concentrated load is closer to the support or in deep beams ($a_v < d$), the beam tends to fail by the diagonal shear splitting. The failure is marked by the splitting of an inclined concrete strut that is initiated at the mid depth of the beam.

2.2.2 Mathematical description of a cracked RC beam

Section 2.2.1 gives a macroscopic description of the shear failure modes in an RC beam at a qualitative level. This section gives a quantitative description of the shear mechanism.

Once a beam is subjected to an external load P (concentrated or uniformly distributed), it reacts, in order to resist the external load, by the reaction force R from supports or by the internal shear force V and internal bending moment M from inside the beam which varies with distance x along the beam (Figure 2.2).

Two basic questions need to be answered about how the shear mechanism of a beam works under the external load P. The first one is what the distribution of the shear mechanism along the beam would be like under P at failure step. The second one is how the shear mechanism along the beam varies with increasing P. The first question has been satisfactorily answered, whilst the second question is still unknown to researchers.

The first question is answered as following. It is assumed that a crack-bearing RC beam still behaves with small deflections and works in integration so that the beam action $V = \frac{dM}{dx}$ still applies. Under P at the failure step, M at a section intersected by a shear crack is thus defined as:

$$M(x) = T(x)z(x) \qquad (Eq.2.1)$$

where $T(x)$ is the tensile force in the main tensile reinforcement and $z(x)$ is the length of the lever arm between the resultant compressive force $C(x)$ in the compressive region and the main tensile reinforcement (Figure 2.2). Differentiating both sides of *Eq.*2.1 with respect to x gives (Russo *et al*, 2005):

$$V = \frac{\partial M(x)}{\partial x} = \frac{\partial T(x)}{\partial x} z(x) + \frac{\partial z(x)}{\partial x} T(x) \qquad (Eq.2.2)$$

$\frac{\partial T(x)}{\partial x} z(x)$ represents the beam action when $z(x)$ is constant (Figure 2.2) *i.e.* the variation of internal moment is caused by the reduced force T in the main tensile reinforcement through bond force between concrete and reinforcement. $\frac{\partial z(x)}{\partial x} T(x)$, describing the behaviour of the inclined shear crack, represents an arch action when $T(x)$ is constant (Figure 2.2) *i.e.* the variation of the internal moment is caused by the reduced lever arm length z from one end of the inclined shear crack towards the beam's support, while the force T in the reinforcement remains constant based on the assumption that the bond force is totally lost.

The second question to be answered is about the variation of the shear mechanism with the increasing load P. With the increasing P, a bending crack and shear crack appear concurrently and compete to grow. Finally, one overrides the other and the beam fails by either the bending crack or the shear crack. This procedure is quantitatively unknown unless the derivative below can be solved and explained in a similar way as *Eq.*2.2.

$$\frac{\partial M(x,P)}{\partial P} = \frac{\partial (T(x,P) z(x,P))}{\partial P}$$

where T and z are functions of both x and P.

This section introduces a mathematical solution to explain the shear mechanism of RC beams. *Eq.*2.2 is one of the fundamental equations in empirical methods (Section 2.7) to obtain the shear capacity of RC beams.

2.2.3 Elements contributing to the beam shear mechanism

As shown in Figure 2.3, the applicability of *Eq.*2.2 to the crack-bearing RC beam or in other words the assumption of the cracked beam in small deflection and integration that ensures the beam action is maintained by the vertical shear stress in the compression region above a shear crack, aggregate interlock across the shear crack, dowel action, and the tensile stress field that is mobilised in the concrete through the reinforcement-concrete bond (Martin-Perez & Pantazopoulou, 2001).

The integration of the shear stresses over the depth of the compression zone above the shear cracks gives a component of the vertical shear force, which is sometimes thought to be the explanation for the 'concrete contribution'.

The physical explanation of the aggregate interlock is that once a shear crack appears, there is a trend that the crack surfaces would slip relative to each other. The aggregate protruding from the crack surfaces resist this movement. The mechanism involves a relationship between four parameters: shear stress along crack interfaces, normal stress to the crack interfaces, crack width and crack slip (Gambarova, 1981; Walraven, 1981; Millard and Johnson, 1984; Nissen, 1987). This mechanism decays rapidly after cracking or after the opening of the crack width (Martin-Perez, 2001). The important role of the transfer of the shear stress along crack interfaces in the redistribution of diagonal compression fields in beams with or without shear reinforcements is well known in compression field theory (CFT) and modified compression field theory (MCFT) (Collins, 1978; Kupfer *et al*, 1973), important theories contributing to many design standards (Section 2.4.3);

In dowel action, the vertical tearing force transmitted from tensile reinforcement is resisted by the concrete surrounding the reinforcement. It is the primary resistance mechanism against shear failure after the breakdown of aggregate interlock (Martin-Perez & Pantazopoulou, 2001). Dowel action is not very significant in members without shear reinforcement. The maximum shear in a dowel is limited by the tensile strength and stiffness of the concrete cover supporting the dowel.

The bond force between the reinforcement and the surrounding concrete is essential to ensure the cracked RC beam continues to act in beam action. Without it, the concrete beam is mainly under diagonal compression and the thrust line is a straight diagonal line (Kani, 1964).

Section 2.2 introduces a general shear mechanism of RC beams. Most shear design methods are constructed on the basis of this section.

2.3 Design methods based on a proposed visible shear mechanism

This section presents the shear design methods for RC beams developed from shear theories constructed on shear mechanisms observed from experiments (*e.g.* Zararis, 2003).

2.3.1 Method based on Regan's Theory

Regan's theory is the one that relates most closely to the design methods of the modern British Standards, BS8110 and BS5400. It assumes that the shear crack rotates apart (Figure 2.4), in both shallow and deep beams, and that final shear failure is caused by the biaxial compression failure of the compressive region at the head of a critical shear crack.

For shallow beams, in the same way as when calculating a beam's bending moment capacity, the depth of the neutral axis x (Figure 2.4) when the beam is failed by a shear crack

is defined as the distance from the top of the beam to the tip of the critical shear crack propagating into the compressive zone.

By applying a failure criterion $\tau = 0.4 f_{cu}^{0.67}$ (Regan, 1971), the maximum shear force for the shallow RC beam contributed by the compressive zone is

$$V_{cu} = 0.27 f_{cu}^{0.67} bx$$

Further, by introducing an empirical depth of neutral axis x at the limit state for local damage in the form of

$$\frac{x}{d} \approx 1.3 \left[\frac{100 A_s}{bd} \cdot \frac{1}{f_{cu}} \right]^{0.33}$$

which is similar to that in the calculation for the bending capacity of the beam, where d is the effective depth of the beam (Figure 2.4), one can obtain the beam's nominal shear strength

$$v_c = \frac{V_{cu}}{\gamma_m bd} = \frac{1}{\gamma_m} 0.35 \left[\frac{100 A_s}{bd} \cdot f_{cu} \right]^{0.33} \qquad (Eq.2.3)$$

*Eq.*2.3 shows the nominal shear stress of the diagonal tensile failure (Figure 2.1) in shallow beam bearing a critical inclined shear crack.

For deep RC beams, a critical shear crack appears at the ultimate limit state connecting the support and a bi-directional high compression stress region under the concentrated load. This is the case especially when the shear span a_v, generally speaking the distance between the concentrated load and the support (Figure 2.4), is less than $2d$. The rule of plane sections remaining plane is totally invalid for cross sections crossed by the dominant shear crack. The equation of the neutral axis $\frac{x}{d}$ as that in shallow beam, obtained by the strain distribution along the cross section, must be replaced by the one expressed by integrated deformations shown as:

$$\frac{x}{d-x} = \frac{\Delta_{cc}}{\Delta_{st}}$$

Where x is the depth of the neutral axis at the head of the shear crack, Δ_{cc} (Figure 2.4) is the total shortening of the extreme compressed fibre along the length of the shear crack and Δ_{st} (Figure 2.4) is the corresponding lengthening of the tensile reinforcement in a horizontal projected length of the shear crack (Regan, 1993) c (Figure 2.4). After integration of strains

along the shear crack (Regan, 1971), the ratio of the neutral axis depth to the effective depth can be approximated as:

$$\frac{x}{d} = 0.5\frac{M}{Vd}\cdot\left(\frac{100A_s}{bd}\right)^{0.5}\cdot f_{cu}^{-0.33}$$

where M and V are the internal bending moment and shear force at the head of a critical shear crack caused by the external load.

If it is considered that the external load is a concentrated vertical load, then $M = V \times c$ or $M = V \times a_v$ (Figure 2.4), which gives the corresponding nominal shear strength expressed as:

$$v_c = \frac{1}{\gamma_m}0.375 \times \frac{2d}{a_v}\left(f_{cu}\frac{100A_s}{bd}\right)^{0.33} \qquad (Eq.2.4)$$

where the partial safety factor $\gamma_m = 1.5$ (Regan, 1973). *Eq*.2.4 shows the nominal shear stress of medium and deep RC beams under shear compression failure or diagonal shear splitting failure (Figure 2.1).

This can be compared with the shear design formulae in BS8110 for deep beams:

$$v_c = \frac{1}{\gamma_m}0.79\frac{2d}{a_v}\left(\frac{100A_s}{bd}\right)^{\frac{1}{3}}\left(\frac{400}{d}\right)^{\frac{1}{4}}\left(\frac{f_{cu}}{25}\right)^{\frac{1}{3}}$$

and in BS5400 for deep beam

$$v_c = \frac{1}{\gamma_m}0.27\frac{2d}{a_v}\left(\frac{100A_s}{bd}\right)^{\frac{1}{3}}\left(\frac{500}{d}\right)^{\frac{1}{4}}\left(f_{cu}\right)^{\frac{1}{3}}$$

in which γ_m is suggested as 1.25 in both standards.

It is concluded that the theory behind the shear design formulae in BS8110 and BS5400 is consistent with Regan's theory for shallow and deep beams except the addition of the depth factor $\left(\frac{400}{d}\right)^{\frac{1}{4}}$ and $\left(\frac{500}{d}\right)^{\frac{1}{4}}$. The formulae are thus bending theory based and semi-empirical.

The pile cap is normally longitudinally deep (Figure 1.2 (b)). The shear prediction for 2-way spanning pile caps from BS5400 and BS8110 is based on Regan's theory for 1-way spanning deep beams. The discrepancy between the two standards (Section 2.10) could be the result of the independent development of the empirical parameters in both standards such as the cap width on which the shear enhancement factor $\frac{2d}{a_v}$ (a factor to enhance the shear

capacity of the RC beam when the external load is close the support or when a cross section for shear designing is close to the support, see Section 2.10.1) is applied to v_c (Section 2.10).

The discrepancy between the shear prediction and the real shear capacity could be explained by the difference in shear mechanisms between a 2-way spanning pile cap and a 1-way spanning deep beam, *e.g.* v_c should be enhanced in a very complicated way across the cap width, and the shear mechanism in the direction of cap width should be considered. It can also be explained by the inaccuracy of Regan's theory for deep beams, *e.g.* the shear crack no longer rotates apart in deep beams but is rather being compressed axially as in a compressive concrete strut.

2.3.2 Method based on Kani's concrete teeth theory

Kani's contribution is the introduction of the concrete teeth (Figure 2.5 (a)) into the shear mechanism of RC beams. The failure of an RC beam without shear reinforcement could be divided into three modes depending on the beam dimensions: Bending failure at mid span in a shallow beam, bending failure of the concrete teeth between two Kani's teeth cracks in a medium beam, and arch failure in a deep beam (Figure 2.5). Kani's theory is to answer two questions: 1. what is the internal mechanism of the so-called shear failure of an RC beam? 2. what is the capacity of this mechanism?

In Kani's theory, the central bending failure can be overtaken by the failure of the concrete teeth. The comb-like teeth, when the concrete beam is being loaded centrally, act as a cantilever (Figure 2.5 (a)) being pulled at its tip by the bond force transmitted from the tensile reinforcement between two teeth cracks. Without considering the aggregate interlock force, the cantilever is purely bent by the bond force at one end and fails in bending at the root of the cantilever when the tensile strength of concrete is reached. This initiates the shear crack at the root of the concrete teeth (Figure 2.5 (a)).

The development of the concrete teeth between shear and central bending cracks could be superseded by the maturing of a remaining arch action in which the normal tensile stress on a typical cross section in the arch is maximum near the shear crack and gradually reduces towards the beam top edge as shown in Figure 2.5 (b). That is to say, the shear strength of RC beam could be the strength of the remaining arch once Kani's teeth break, losing strength to carry the internal shear force (Kani, 1964).

Cracking consistent with these three failure modes could develop concurrently after the beam begins to be loaded. Finally one of the three failure modes dominates, determined by the ratio of shear span over beam depth ($\frac{a_v}{d}$).

The relationship among resistant strengths of the three failure modes is suggested by Kani to be plotted as a 'valley' (Figure 2.6) for an RC beam with a typical concrete compressive strength and reinforcement ratio, expressed in terms of the corresponding bending moment at the central section when the particular failure happens. The continuous line describes the strength of an RC beam as a function of $\alpha = \frac{a_v}{d}$.

Based on Figure 2.6, the strength of an RC beam under concentrated load can be generalized as:

$$M_{CR} = Min(Max(M_{CRA}, M_{CRT}), M_{FL})$$

where M_{CR} is the central resisting moment when the beam fails, M_{CRA} is the central resisting moment if the arch fails, M_{CRT} is the central resisting moment if the concrete teeth fail and M_{FL} is the central resisting moment if the beam fails by central bending (Figure 2.6). It can be seen in this figure that the watersheds or transitional points of the continuous line are that (i) when $\frac{a_v}{d}$ is larger than 5.6, beam fails by the central bending; (ii) when $\frac{a_v}{d}$ is between 5.6 and 2.5, teeth cantilever failure occurs; (iii) when the beam becomes relative deep *i.e.* $\frac{a_v}{d}$ is lower than 2.5, arch action takes the place of Kani's teeth failure. Since the arch strength is still lower than the central bending resistance, the beam fails eventually by the failure of the compressive arch.

As Figure 2.6 shows, a series of test data (the shaded area) match the curve relative well when $\frac{a_v}{d}$ is larger than 2. But when $\frac{a_v}{d}$ is lower than 2 or when the beam becomes deep, the discrepancy between the real strength (the shaded area) and the theoretical strength (the continuous line) becomes large. Notice that for very deep beam ($\frac{a_v}{d}$<1), there is a shortage of test data. For these beams, the arch failure could be replaced by the failure of the compressive splitting crack the compressive stress along which is uniform (Figure 2.5 (c), *cf*. Figure 2.5 (b) for arch action). This behaviour is not considered in Kani's theory.

The above introduction of Kani's valley is a general description. With different concrete strengths and reinforcement ratios, a cluster of Kani's valleys are achieved. Kani's theory considered the experimental data such as the width of the concrete teeth (a key factor that determines the shear strength), and a perfect bond condition was assumed.

Kani's theory is instructive since it describes a full range of the beam resistance mechanisms including the shear mechanism and their transition points covering a wide range of beam dimensions. The transition between arch action and teeth action represents the shear behaviour in deep beams. Compared with Regan's theory in Section 2.3.1, Kani's theory explains the shear behaviour of RC beams based on a more reasonable and visualized crack distribution.

2.3.3 Method based on Kotsovos' compressive force path concept (CFP)

This design method is based on the CFP concept which considers that the load-carrying capacity of an RC beam is associated with the strength of concrete in the region of the paths along which the compressive force (C) is transmitted to the support. As shown in Figure 2.7, CFP (Figure 2.7 (b)) explains the general behaviour of the shear cracking described in Section 2.2.1 (Figure 2.7 (a)). The shear failure is considered to be related to the development of the tensile force (T) in the region of the path, caused by (i) changes in the path direction; (ii) varying intensity of the compressive field along the path; (iii) complex stress status at the tips of inclined cracks; (iv) bond failure along main reinforcement (Kotsovos, 1987).

As shown in Figure 2.7 (b), the shape of the compressive path varies with the variation of $\frac{a_v}{d}$. For shallow beams, the compressive path is bi-linear, changing direction somewhere in the shear span or the segment of mixed bending moment and shear force. The shear crack reaches near the turning point of the bi-linear path. Failure occurs when the capacity of this region to sustain the combined compression-tension stress field is exceeded. For medium beams, the beam fails in the compression zone above the tip of the shear crack, where the compressive force C caused by the bending moment, and the vertical tensile force T, meet, reducing the strength of the concrete in this area. For deep beams, a compressive force path connecting directly the load and support appears. The failure is caused by the compressive force C along the path.

2.4 Truss method

The three methods stated in Section 2.3 are lower bound theory based approaches in which the shear resistance is obtained based on a final failure mechanism. Another similar

method, as shown in this section, considers the shear cracks to distribute uniformly and in parallel and to be interactive with the shear reinforcement and main reinforcement. The beam in the truss method is imagined as a truss model in which the shear capacity is supplied by a typical in-plane 'material' making up the beam.

As shown in Figure 2.8, the 'material' includes tensile reinforcement and parallel compressive concrete struts separated by parallel concrete cracks. The beam fails when this 'material' fails. The shear strength of the material or the nominal shear strength of an RC beam, v, is taken as the maximum vertical shear stress on a unit of such material (Figure 2.8) which is loaded under principal stress (f_1, f_2) parallel and perpendicular to a crack. The strength of such 'material' under bi-axial stress status is obtained from experiments, as described in Sections 2.4.1 and 2.4.3).

2.4.1 Truss model

As can be seen in Figure 2.8, in a typical truss model the compression region and the tensile region of an RC beam carry the forces C and T respectively (Hoang & Nielsen, 1998). The shear force V_c is carried by the 'material' in the web composed of reinforcement and parallel compressive concrete struts.

In the truss method, the key issue is to obtain the relationship between the principal strain and principal stress of the 'material' ($f_1 - \varepsilon_1$) when under shear stress v, combined in the case of a deep beam with the transverse compressive stress (Section 2.4.2).

Ritter (1899) and Morsch (1902) developed a truss model that neglected the tensile stresses f_t in the cracked concrete and assumed that the angle of the diagonal compression stress would remain at $45°$ after concrete cracking. Then it was suggested that this angle may deviate from $45°$ (Lampert & Thurlimann, 1968). Another development of the truss model is the introduction of a compatibility equation by Collins (1973) to determine the angle of the concrete strut. It was named 'compression field theory' (CFT) since the angle of the concrete strut was assumed to coincide with the angle of the inclination of the principal compressive stress and strain. Several truss models with cracks with fixed-angle (the direction of the cracking is fixed) and rotating-angle (the direction of the cracking rotates to be parallel to the direction of the concrete principal stress) were established (*e.g.* Nielsen, 1967; Lampert & Thurlimann, 1968; Hsu, 1993). More developments of the truss model include the introduction of the softening behaviour of the concrete struts (*e.g.* Robinson & Demorieux, 1968; Vecchio & Collins, 1981).

The CFT was further improved to the modified compression field theory (MCFT) after realizing that tensile stress f_t perpendicular to cracks still exists in concrete between two inclined cracks (Figure 2.9 (a)). f_t reaches its maximum halfway between two neighbouring cracks and drops to zero at the crack surface (Figure 2.9 (a), (b), (c)). MCFT also assumes the shear stress v_{ci} is transferred along the crack surface by the aggregate interlock or friction (Figure 2.9 (c)) (ASCE-ACI Committee, 1998).

The constitutive curve of the 'material' ($f_1 - \varepsilon_1$) from MCFT contributes to many FEA commercial software. For example, in DIANA it is named as the total strain crack model, which is considered as the counterpart of the smeared cracking model (DIANA, 2002).

2.4.2 Transverse stress

Figure 2.8 shows a truss model for a shallow beam. The truss method is also available for a deep beam where both transverse stress and shear stress appear. In a deep beam under a concentrated load P, the load from the top and the reaction from the support create a large distribution of compressive stresses p (Figure 2.10 (a)) transverse to the horizontal axis of the longitudinal beam (Kong, 1990). Therefore the unit of the material in the truss model is not only loaded by the vertical shear stress v but also by the transverse compressive stress p (Figure 2.10 (b)).

The distribution of p, which varies horizontally in general and along the neutral axis of the beam in particular (Figure 2.10 (a)), is influenced by the variation of the ratio $\frac{a_v}{h}$ (Kong, 1990), where h is the total depth of the beam. The smaller the ratio is, the higher p is and thus the stronger the 'material' is since the opening of the crack perpendicular to the principal compressive stress is suppressed by the transverse p. Therefore, the unit of the material can bear more vertical shear stress v than in shallow beams and the shear capacity is therefore enhanced in deep beams.

2.4.3 A design method based on modified compression field theory (MCFT)

As shown in Section 2.4.1, a method based on MCFT is an application of the truss method considering the constitutive relationship of the 'material' bearing shear in the truss model. In the method, the nominal shear strength v is taken as the shear stress when the 'material' fails and the shear resistance force V_c of the truss model is equal to v multiplied by the area of the beam cross section (Figure 2.8).

Tests of in-plane reinforced concrete panels (Vecchio & Collins, 1986), based on which the MCFT theory was developed, demonstrated that tensile stresses f_t existing in the concrete significantly increases the ability of the reinforced concrete to resist the shear stress (Collins *et al*, 1996). In addition, the magnitude of the local shear stress v_{ci} along the cracks was found to be related to and limited by the crack width w and the aggregate size a (Figure 2.9 (d)). The average value of the tensile stress in the concrete f_t was limited by an average shear stress in the concrete between two neighbouring cracks. Therefore the constitutive relationship $f_1 - \varepsilon_1$ of the material was obtained. The relationship was related to the concrete compressive strength $f_c^{'}$. The shear resistance force V_c of the truss model was presented as :

$$V_c = \beta\sqrt{f_c^{'}}bd$$

where β was related to the angle of the concrete crack. As can be seen in Table 2.2 and Section 2.9, this design method based on MCFT is widely used in American and Canadian Standards.

The truss method is based on an imaginary crack distribution *i.e.* parallel cracks with fixed or varied angle intersected by horizontal and vertical reinforcement such that it can apply in RC beams both with and without shear reinforcement (when the ratio of the vertical reinforcement equals zero). It is suitable for both shallow and deep beams. But the truss method is not suitable for very deep beams, where the stress distribution is extremely distorted. The following section presents a method for very deep beams.

2.5 Strut-and-tie method (STM)

In this method, as the name 'strut-and-tie method' suggests, a solid structure is simplified into a truss structure where the stress distribution is assumed to be integrated and transmitted in the form of forces through the strut (C) and tie (T) system. Figure 2.11 shows a typical strut-and-tie system. The shear capacity of the structure is the capacity of the strut-and-tie system to resist load P. STM is based on the lower bound theory.

STM is particularly suitable for the analysis of local regions where the stresses and strains are so disturbed and irregular, widely known as the D-region, that they are not amenable to mathematical solutions, resulting in the angle of the concrete struts being irregular (Hsu, 1998). STM considers the complete flow of forces within the structure rather than just the forces at one particular section (Adebar, Kuchma & Collins, 1990). Unlike

design methods based on Regan's, Kani's theory or truss model, STM does not account for the development of the cracking and its influence on the shear mechanism.

A softened strut-and-tie system satisfying equilibrium, compatibility, and constitutive laws of cracked reinforced concrete, has been successfully proposed to determine the shear strengths of beam-column joints (Hwang & Lee, 2000), deep beams (Hwang *et al*, 2000a), corbels (Hwang *et al*, 2000*b*) and squat walls (Hwang *et al*, 2000). Previous experiments also showed that the STM was found to describe more accurately the behaviour of 2-way spanning deep pile caps than other methods (Clarke, 1973; Adebar & Zhou, 1996).

Several issues need to be mentioned when applying STM in structures such as pile caps. Firstly, STM assumes there is enough strength at the nodes in the strut-and-tie system (Figure 2.11), and this needs to be reflected in practice by the detailing in the joint areas. For example, the tensile reinforcement is required to pass through the joint area with sufficient anchorage length. Secondly, concrete is weak in tension, so the concrete always acts as compressive struts and the reinforcement as tensile ties. Thirdly, the compressive strength of the concrete strut varies with the varying strut shape. For example a prismatic concrete strut must have different compressive strength from a bottle-shaped or fan-shaped concrete strut. Finally, the strut-and-tie system fails by the failing of either the yielding of reinforcement ties or the crushing of concrete struts.

STM is suitable for shallow and deep beams with and without shear reinforcement (Tan *et al*, 2003). The STM can also be used for both pre- and post-tensioned deep beams (Tan, Tong & Tang, 2001).

2.6 Kinematics method

The kinematics method is based on upper bound plastic theory. In a lower bound theory, it suffices to find a load path to transfer the load to the supports, satisfying the yield criteria throughout the structure, and then equilibrium equations are applied to calculate the capacity. In upper-bound theory, a kinematical failure mechanism is required and then the energy principle is used to provide the upper-bound load (Ashour, 2000). The lower-bound theory based methods, such as the truss method and STM, can only be applied in simple loading cases. However, it is easier to develop an upper bound solution for even the most complicated loading cases (Ashour, 2000), from concentrated loading to distributed loading.

An example of the application of the kinematics method is schematically described in Figure 2.12 for an RC beam. A curved yield line representing a critical shear crack is introduced to represent a failure zone separating two rigid blocks along which discontinuities

of the in-plane displacement occur. It has been proven (Jensen, 1982; Ashour & Morley, 1994, 1996) that the optimum shape of the yield line is a hyperbola under any loading condition based on the assumption that concrete is a perfectly rigid plastic material obeying the modified Coulomb failure criteria with zero tension cut-off (Chen, 1982; Nielsen, 1984). The instantaneous centre of the relative movement of the rigid block I and II separated by the yield line is $O'(x, y)$ (Figure 2.12).

Equilibrium is then established between the total energy W_{i1} dissipated in the concrete along the yield line plus in the shear reinforcement crossing the yield line (W_{i2}) and the external work done by the external force P ($W_e(P)$) *i.e.* $W_e(P) = W_{i1} + W_{i2}$. The minimum value of the shear capacity $P_{\min}$ is then obtained by differentiating the above energy equilibrium with respect to the co-ordinates x, y. If the minimum value is found to be equal to the maximum shear capacity from lower bound theory, the value is treated as the real shear capacity of the RC beam.

The kinematical method is constructed on an imaginary shear failure mechanism. It can be applied to both shallow and deep RC beams with and without shear reinforcement under any form of loading. But it is difficult to construct an accurate yield line along which the energy absorbed in the beam is dissipated.

2.7 Empirical method

A study (Rebeiz, 1999) associated with the statistical method was presented to establish an alternative method to predict the shear strength for an RC beam without shear reinforcement. This was done by fitting a predicted design formula with more than 350 data obtained from existing sources of shear experiments. The first step was to determine a basic format of the shear strength using dimensional analysis. Three important variables: the shear-span-to-depth ratio ($\frac{a_v}{d}$), the concrete compressive strength ($f_c^{'}$), and the tensile reinforcement ratio (ρ) were considered. Then the equation was predicted as:

$$v_c = \frac{V_c}{bd} = k_1 \left(f_c^{'}\right)^{b1} (\rho)^{b2} \left(\frac{d}{a_v}\right)^{b3} + k_2$$

In the second step, the exponents $b1$, $b2$, $b3$ and the coefficients $k1$, $k2$ were determined from a nonlinear multiple regression analysis. The aim was to find a shear design formula

which gave the shear prediction of the highest coefficient of determination and the lowest standard deviation against the accurate shear capacity.

A similar analysis was done by Russo *et al* (2005). The difference is that a semi-empirical design formula was developed from *Eq*.2.2 which can be explained physically. The unknown parameters in the formula were then determined from more than 900 test data.

The other important and newly developed empirical method is the neural network in which the shear capacity of RC beams is predicted by an algorithm to simulate the cognitive function of the brain (Sanad & Saka, 2001; Jenkins, 1999; Kim *et al*, 2004; Cladera & Mari, 2004).

Statistical methods can apply to all types of RC beams ranging from shallow to deep beams with and without shear reinforcement, as long as the number of experimental data is abundant.

2.8 Methods to predict the punching shear capacity

In Sections 2.3~2.7, discussions are concentrated on the normal shear failure in 1-way spanning RC beams. These shear theories and methods, except the truss method, can also be applied in a 2-way shear failure such as punching shear failure of an RC plate or a pile cap under a concentrated load. The punching shear design methods are not much different from that for the normal shear failure but are implemented for a 2-way failure mode. For example, the punching shear capacity can be calculated by obtaining the compressive area surrounding the concentrated load which bears the vertical shear force (Gomes & Regan, 1999).

Table 2.1 concludes the applicability of the shear methods mentioned in this chapter to shallow and deep beams with and without reinforcement. It can be seen that, apart from the applicability of the mechanism method to shallow and deep beams with shear reinforcement being unknown because of lack of relevant literature, other methods can be applied in all types of RC beams. The mechanism method, STM, kinematics method and empirical method are also applicable to 2-way spanning pile caps. Since the constitutive relationship of the concrete material in the truss model is based on the behaviour of in-plane reinforced concrete, the truss method cannot be applied in pile caps.

2.9 Shear design methods in different national standards

This section briefly introduces the main shear design methods for 1-way spanning RC beams and their development to the shear design for 2-way spanning pile caps in different national standards, which is summarised in Table 2.2.

For shallow beams, design methods in BS8110 and BS5400, developed from CP110 (1972), are based on Regan's theory (Section 2.3.1), a method based on a visual shear mechanism. But the standards in America, Canada, other European countries, Japan and China generally adopt a softened truss method based on a truss model with variable or fixed angle or MCFT. For deep beams, in BS8110 and BS5400, the shear enhancement factor $\frac{2d}{a_v}$ is applied to the shear design formula of shallow beams. In other standards, STM or introducing an enhancement multiplier or a coefficient is a popular method.

For pile caps, all the design standards have been developed from shear design methods for beams in a very empirical way because of the shortage of experimental data. Therefore, more variables need to be introduced in the design formulae. In BS8110 and BS5400, the design formulae for pile caps are developed from the bending theory based shear formulae for deep beams by adding a shear enhancement application factor A (Section 2.10.1). A similar method appears in Japanese Standard by adding a coefficient c (Table 2.2).

Meanwhile, BS8110 and BS5400 adopt the suggestion by Clarke (1973) that the shear enhancement factor $\frac{2d}{a_v}$ only be applied on the width of a critical plane that lies above pile heads (Figure 2.13 (a)). If considering a critical shear surface of tapered shape cutting all four piles, $\frac{2d}{a_v}$ is to be applied on the curve segments lying above pile heads (Figure 2.13 (b)). The definition of the shear span of pile caps is also changed from that of beams. As Clarke (1973) suggested, the critical shear plane is at the face of the load and then the shear span a_v is the distance between the edge of the load and the cap cross section 20% inside the pile inner surface (Figure 2.13 (a), (b)).

In some national standards, an alternative design method for pile caps is to apply STM (Table 2.2). Because there are more than one possible configuration of the strut-and-tie system for a pile cap, STM is based on experience. Two 2-way strut-and-tie systems for pile caps (Yan, 1954; Blevot & Fremy, 1967) projected to the front surface of the pile cap are shown in Figure 2.14. These two systems assume the horizontal force T is transmitted through reinforcement linking the pile heads. The positions of the intersection of the concrete

compressive struts above the centre of the cap top surface are different between the two systems, which reflect the influence of the pile diameter and load dimension.

2.10 Discussion on current shear design methods for pile caps

In this section, two design methods in both BS5400 and BS8110 are presented *i.e.* the methods based on bending theory, and STM. The bending theory based formulae give a discrepancy between the two standards, which is to be solved in this research (Section 1.2).

2.10.1 The discrepancy between two bending theory based design formulae

BS8110 and BS5400 suggest similar shear design formulae for pile caps based on bending theory developed from Regan's theory (Section 2.3.1). The key dimensions of the four-pile cap adopted in the formulae are depicted in Figure 2.15.

For BS8110:

$$v_c = \underbrace{\frac{0.79}{\gamma_m} MAX\left(\left(\frac{f_{cu}}{25}\right)^{1/3}, 1\right)}_{PartI} \underbrace{\left(\frac{100A_s}{bd}\right)^{1/3}}_{PartII} \underbrace{MAX\left(\left(\frac{400}{d}\right)^{1/4}, 0.67\right)}_{PartIII} \underbrace{\left(\left(\frac{2d}{a_v}\right)A + (1-A)\right)}_{PartIV} \quad (Eq.2.5)$$

For BS5400:

$$v_c = \underbrace{\frac{0.27}{\gamma_m}(f_{cu})^{1/3}}_{PartI} \underbrace{\left(\frac{100A_s}{bd}\right)^{1/3}}_{PartII} \underbrace{MAX\left(\left(\frac{500}{d}\right)^{1/4}, 0.70\right)}_{PartIII} \underbrace{\left(\left(\frac{2d}{a_v}\right)A + (1-A)\right)}_{PartIV} \quad (Eq.2.6)$$

where v_c is the nominal design shear stress uniformly distributed on a vertical cross section of a cap width b and effective height d under design shear capacity V_c (*i.e.* $v_c = \frac{V_c}{2bd}$). BS8110 states that v_c must in no circumstances exceed $0.8\sqrt{f_{cu}}$ or $5\ N/mm^2$ even if the caps are reinforced to resist shear. BS5400 has a similar limit $0.75\sqrt{f_{cu}}$ or $4.75\ N/mm^2$. The upper limits include the partial safety factor γ_m.

In *Part I*, γ_m is the partial safety factor on material strength taken as 1.25 in both standards for concrete and f_{cu} is the design cube strength of concrete at 28 days, not to be greater than $40\ N/mm^2$. BS8110 states that v_c should be multiplied with a factor $\left(\frac{f_{cu}}{25}\right)^{1/3}$ if f_{cu} is larger than $25\ N/mm^2$;

In *Part II*, A_s is the total area of longitudinal reinforcement, the effect of which on shear capacity is illustrated by the power order of $\frac{1}{3}$. This is less than its influence on bending capacity illustrated by the power order of 1. $\frac{100A_s}{bd}\%$ is also called the reinforcement ratio;

Part III is the depth factor representing the size effect (Section 2.10.2). BS8110 states that the depth factor $\xi_s = \left(\frac{400}{d}\right)^{1/4}$ is not to be less than 0.67 for beams without shear reinforcement, while in BS5400, the depth factor $\left(\frac{500}{d}\right)^{1/4}$ is not to be less than 0.70 and not to be more than 1.5 when the cap effective depth $d \le 100mm$;

Part IV is implicit in British Standards *i.e.* it is not specifically present in the current formulae. In *Part IV*, the shear enhancement factor $\frac{2d}{a_v}$ serves to increase the shear strength when the shear span a_v is less than $2d$. a_v is the shear span defined as the distance between the edge of the loading or the cross section considered in the shear design and 20% of the pile diameter inside the pile inner edge (Figure 2.15). The key discrepancy between the two standards lies where the width of the cap on which the shear enhancement factor applies is defined. This concept is expressed by a shear enhancement application factor *A* defined as the width b' on which shear enhancement factor applies (Figure 2.15) divided by the overall cap width b (*i.e.* $A = \frac{b'}{b}$). b' has different definitions in the two standards. BS8110 suggests b' to be the sum of the widths of strips of maximum three times the pile diameter centred on each pile head depending on the relative dimension of the transverse overhang h_o and pile transverse spacing kh_w, whereas BS5400 suggests the width b' to be the sum of the widths of strips of one pile diameter centred on each pile head (Figure 2.15).

In *Eq.*2.5 and *Eq.*2.6, one can notice that *Part I, Part III* and *Part IV* are the potential sources of the discrepancy between the two standards. Comparison of these three parts between the two standards is given in Figure 2.16 (a), (b) and (c). The figures show the variation of the discrepancy of *Part I, Part III* and *Part IV* with the concrete strength f_{cu}, pile cap effective depth d and the pile transverse spacing kh_w respectively. The reinforcement ratio *i.e. Part II* is not a source of the discrepancy.

Figure 2.16 (a) shows that the ratio of *Part I* between the two standards is lower than 1.19. When the concrete strength is above $25\,N/mm^2$, the ratio is around 1.0. Figure 2.16 (b)) indicates that for a pile cap with usual cap depth *e.g.* above $150\,mm$, the ratio of *Part III* between two standards is around 0.946 implying a small discrepancy. Figure 2.16 (c) shows the ratio of *Part IV* between two standards for a pile cap with typical dimensions with the pile diameter $h_p = 130mm$, the transverse overhang $h_o = 100mm$ and the cap effective depth $d = 199mm$. It can be seen that the ratio depends on the values of both $\frac{2d}{a_v}$ and A, being as high as 1.87 ($\frac{2d}{a_v} = 6$) when kh_w is $390\,mm$, after which A for BS8110 begins to fall. In this case, $390\,mm$ is three times the pile diameter h_p *i.e.* the ratio of the transverse pile spacing over the pile diameter $n = \frac{kh_w}{h_p} = 3$. This implies that for most four-pile caps, the major source of the discrepancy between the two standards is *Part IV* determined by $\frac{2d}{a_v}$ and A, especially when the transverse pile spacing is at three times the pile diameter at which the discrepancy is a maximum.

There is no definition of the load pattern dimensions in the two design formulae. Though the punching shear design method for pile caps under a concentrate load is presented, the variation of the normal shear capacity of a pile cap under different load patterns is not considered in *Eq.*2.5 and *Eq.*2.6.

2.10.2 Discussion of the key parameters in shear design formulae

- **Shear enhancement factor**

As discussed in Section 2.3.1, the integration of the deformation along the inclined shear crack to calculate the depth of the neutral axis of a deep beam causes directly the appearance of the additional term $\frac{2d}{a_v}$ in v_c (*Eq.*2.4) for deep beams (*cf.* *Eq.*2.3 for shallow beams). This term is normally denoted as the shear enhancement factor, which implies the fact that the average shear strength on a cross section of an RC beam at the failure step becomes larger once the shear span becomes short.

Another explanation of $\frac{2d}{a_v}$ is shown in Section 2.4.2 and Figure 2.10. The formation of a compression strut in a deep beam introduces a transverse stress p on a horizontal section through the beam. The introduction of the shear enhancement factor is then caused by p or the formation of the compressive strut which reduces the tensile stress normal to the principal compressive stress. This enables the additional shear force to be added (Kong, 1990).

- **Shear enhancement application factor**

This is the factor that differentiates a 2-way spanning pile cap from a 1-way spanning beam because if $A<1$, it implies that the shear enhancement factor is not applied across the whole cap width. Though the value of A in British Standards is empirical, the concept behind it is associated with the application of $\frac{2d}{a_v}$ on a cap width which depends on whether the compressive concrete strut forms or not along the cap width. So a reasonable A should reflect an accurate physical behaviour of the pile cap.

From *Eq.*2.5 and *Eq.*2.6 it can be seen that if other parameters keep unchanged, the shear capacity v_c is in the linear relationship with $\frac{2d}{a_v}$ or A. A further study on this relationship is to be carried out in this research.

- **Longitudinal reinforcement and concrete strength**

The ratio of the longitudinal reinforcement determines the depth of the neutral axis of an RC beam the concrete above which the shear force is resisted. The shear failure criteria associated with the concrete depth is relevant to the concrete compressive strength $\left(f_{cu}\right)^{1/3}$. The influence of the longitudinal reinforcement on shear capacity of pile caps is to be studied in this research while the influence of concrete strength is not to be studied.

A shortcoming of *Eq.*2.5 and *Eq.*2.6 is that only the contribution of the longitudinal reinforcement is considered, neglecting the influence of the reinforcement in the cap transverse direction. A study on this is to be carried out.

- **Size effect**

The size effect in the shear design formulae is expressed in the form of a depth factor, ξ_s (Section 2.10.1), causing the shear strength to reduce with increasing cap depth.

One explanation of the size effect is that with increasing beam size, the width of the shear crack increases accordingly. But the size of the aggregate does not increase proportionately and most likely stays unchanged. This means that the aggregate can no longer fully block the relative movement of the two faces of the shear crack, reducing the shear capacity of the beam. Another explanation is that for an RC beam with an increased size, out-of-plane actions caused by the unintended eccentricities of the applied in-plane load are more likely to lead to a premature loss of load-carrying capacity such as in a buckling of an inclined concrete strut (Kotsovos & Pavlovic, 1997).

2.10.3 STM in British Standards

As an alternative shear design method, STM is also allowed in BS8110 and BS5400. BS8110 suggests the longitudinal reinforcement tie is limited to a strip not wider than three times the pile diameter, centring on each pile, *i.e.* the same as the shear enhancement factor application width b' (Figure 2.15). The longitudinal reinforcement is to be placed uniformly along the transverse direction. This agrees with the argument in Section 2.10.2 that the cap width on which $\frac{2d}{a_v}$ is applied is related to the compressive concrete strut which forms the strut-and-tie system. In BS5400, all longitudinal reinforcement can be taken into account as a tie, provided 80% of it is placed in strips anchored directly over the pile heads.

The two standards do not specify the compressive strength of the concrete strut and how the reinforcement in the cap transverse direction is to be considered in the strut-and-tie system. The latter issue is also to be studied in this research.

2.11 Summary

The mainstream shear design methods and the corresponding shear theories for 1-way spanning RC beams and 2-way spanning pile caps have been introduced in this chapter. The design methods for beams are derived based on a visible mechanism, the truss method, STM, kinematics method or empirical method. However the theoretical research is lacking for the shear capacity of 2-way spanning RC pile caps. So the applicability of these methods to pile caps is relatively restricted. The current shear design method for pile caps is thus very empirical in a way mainly to extend the 1-way design formulae into two-way by adding a coefficient lacking physical explanations.

This research arises from a discrepancy of the shear prediction from the bending theory based shear design formulae for pile caps between BS8110 and BS5400. Because the two formulae have been developed independently in history, the discrepancy is mainly relevant to

the different definitions of the shear enhancement application factor A and depends on the value of the shear enhancement factor $\frac{2d}{a_v}$.

It is suspected that A and $\frac{2d}{a_v}$ are the key parameters that influence the accuracy of the current shear design formulae for pile caps that are normally longitudinally deep. The current formulae can neither physically explain the shear behaviour of very deep RC beams by using the formation of $\frac{2d}{a_v}$, nor explain the 2-way shear behaviour of pile caps by using the formation of A. In addition, the behaviour of the transverse reinforcement is not considered in the current shear design formulae and STM for pile caps. The influence of the load pattern dimensions on the shear capacity of the pile cap is not present in the current design method. These issues are to be investigated in this research.

Table 2.1 The applicability of the shear design methods

	Shallow beam with shear reinforcement	Shallow beam without shear reinforcement	Deep beam with shear reinforcement	Deep beam without shear reinforcement	Pile cap without shear reinforcement
Mechanism method	Not known	Yes	Not known	Yes	Yes
Truss method	Yes	Yes	Yes	Yes	No
STM	Yes	Yes	Yes	Yes	Yes
Kinematics method	Yes	Yes	Yes	Yes	Yes
Empirical method	Yes	Yes	Yes	Yes	Yes

Table 2.2 Summary of the shear design methods for RC beams and pile caps in different national standards

	Nation or region	Shallow beam (with or without shear reinforcement)	Deep beam (with or without shear reinforcement)	Pile cap (without shear reinforcement)
CSA A23.3-94 (Canadian Standards for the Design of Concrete Structures, 1994)	Canada	MCFT	STM	Not known
JTG D62-2004 (Chinese Code for Design of Highway Reinforced Concrete and Prestressed Concrete Bridges and Culverts, 2004)	China	Truss method	Introduce an enhancement multiplier	STM
European CEB/FIP Model Code (Fédération Internationale du Béton /Fédération Internationale de la Précontrainte,1990)	Europe	Truss method based on a truss model with variable angle	STM	Not known
Japanese Code (Japan Road Association Design specifications of highway bridges, 2002)	Japan	Arch action plus a truss method based on a truss model with variable angle	Introduce modifying coefficient β_a	Introduce modify coefficient c (Masahiro *et al.*, 2003) or STM
BS5400 (1990)	UK	Methods based on a visual shear mechanism	Introduce an enhancement factor $\frac{2d}{a_v}$	Introduce A or STM
BS8110 (1997)	UK	Methods based on a visual shear mechanism	Introduce an enhancement factor $\frac{2d}{a_v}$	Introduce A or STM
ACI Code 318-95 (American Concrete Institute Building Code, 1995)	USA	Truss method based on a truss model with fixed angle 45°	Introduce an enhancement multiplier	STM
AASHTO's LRFD Bridge Design Specification (1994)	USA	MCFT	STM	STM

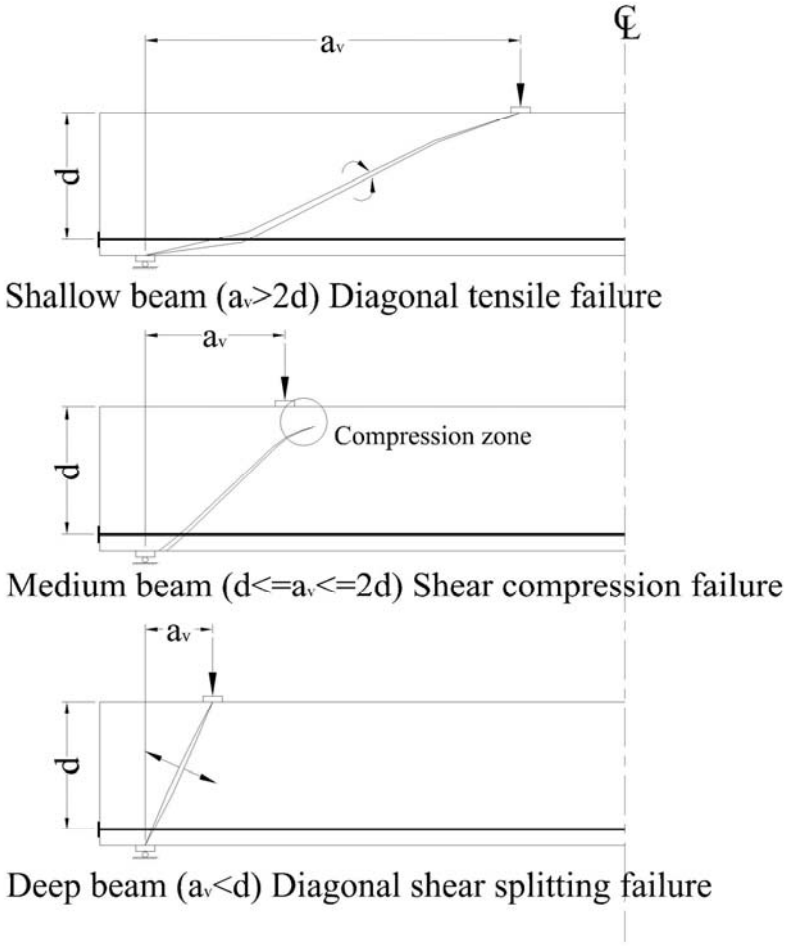

Figure 2.1 General distribution of shear cracking at failure step and shear failure modes

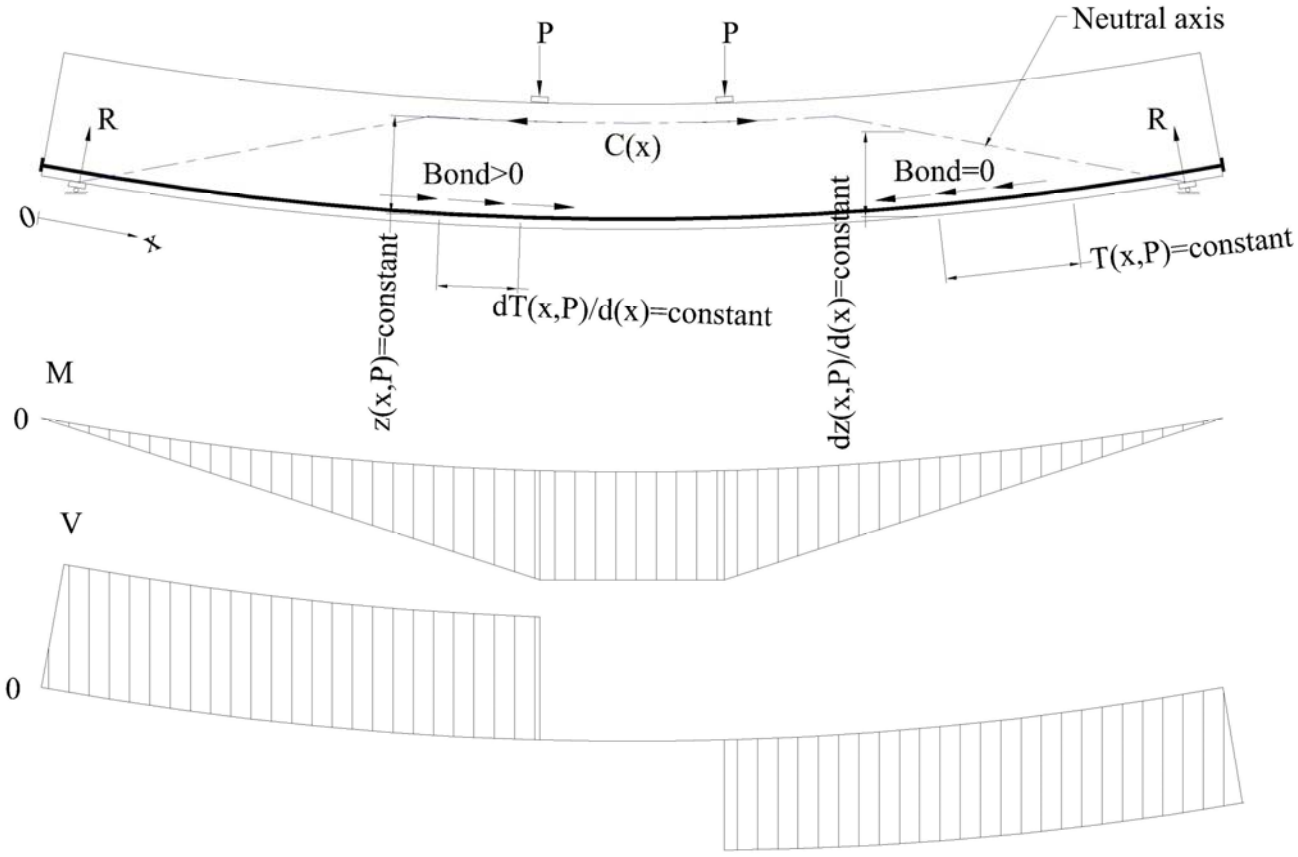

Figure 2.2 Mathematical description of the shear mechanism explaining *Eq*.2.1 and *Eq*.2.2

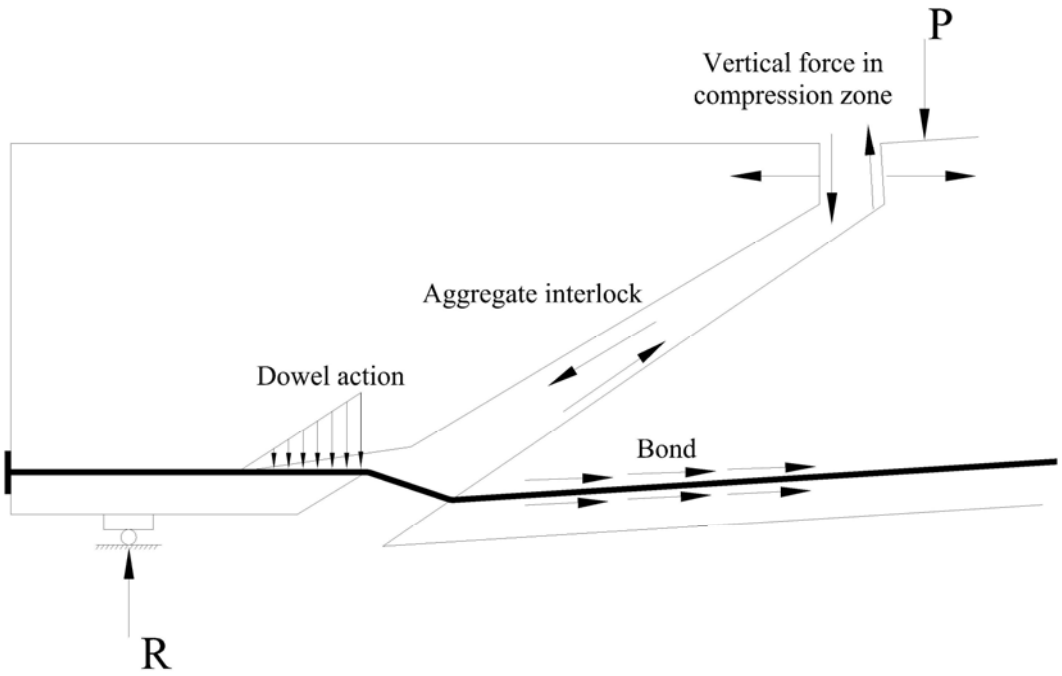

Figure 2.3 Detail shear mechanism supporting the beam small deflection and integration assumption in *Eq*.2.1 and *Eq*.2.2

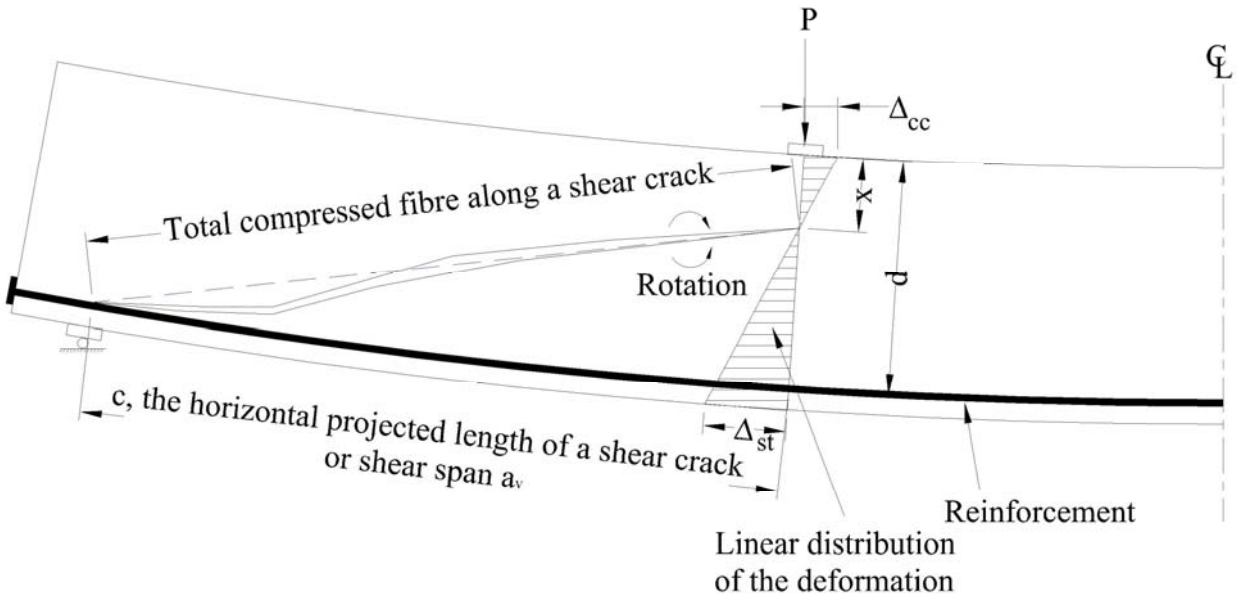

Figure 2.4 Assumption of the shear mechanism of RC beams in Regan's theory

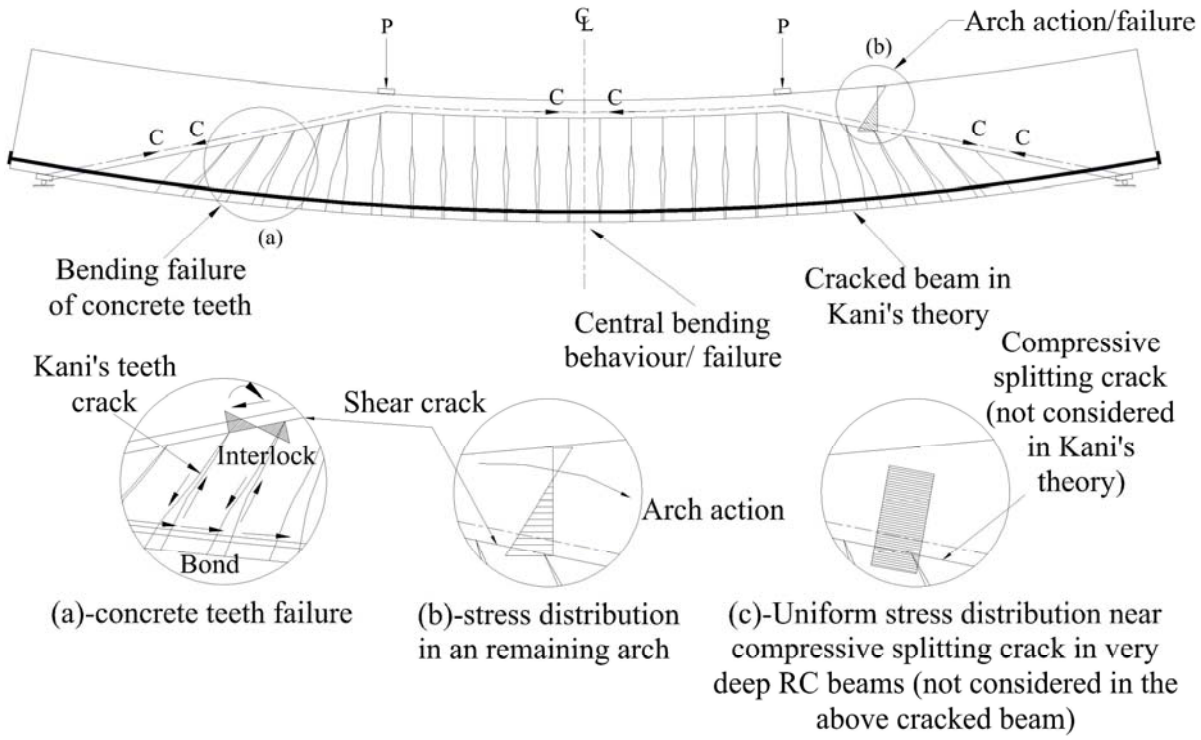

Figure 2.5 Assumption of the shear mechanism in Kani's concrete teeth theory

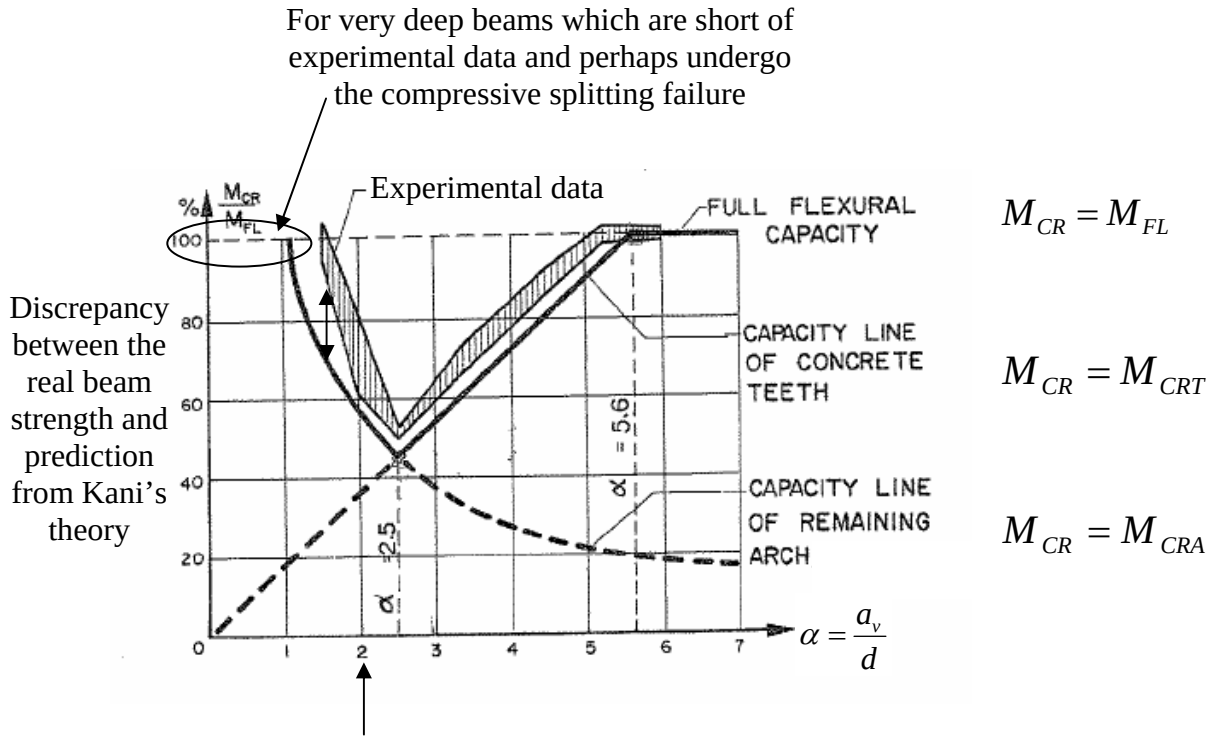

Figure 2.6 Kani's valley for an RC beam without shear reinforcement with typical concrete compressive strength and reinforcement ratio (Kani, 1964)

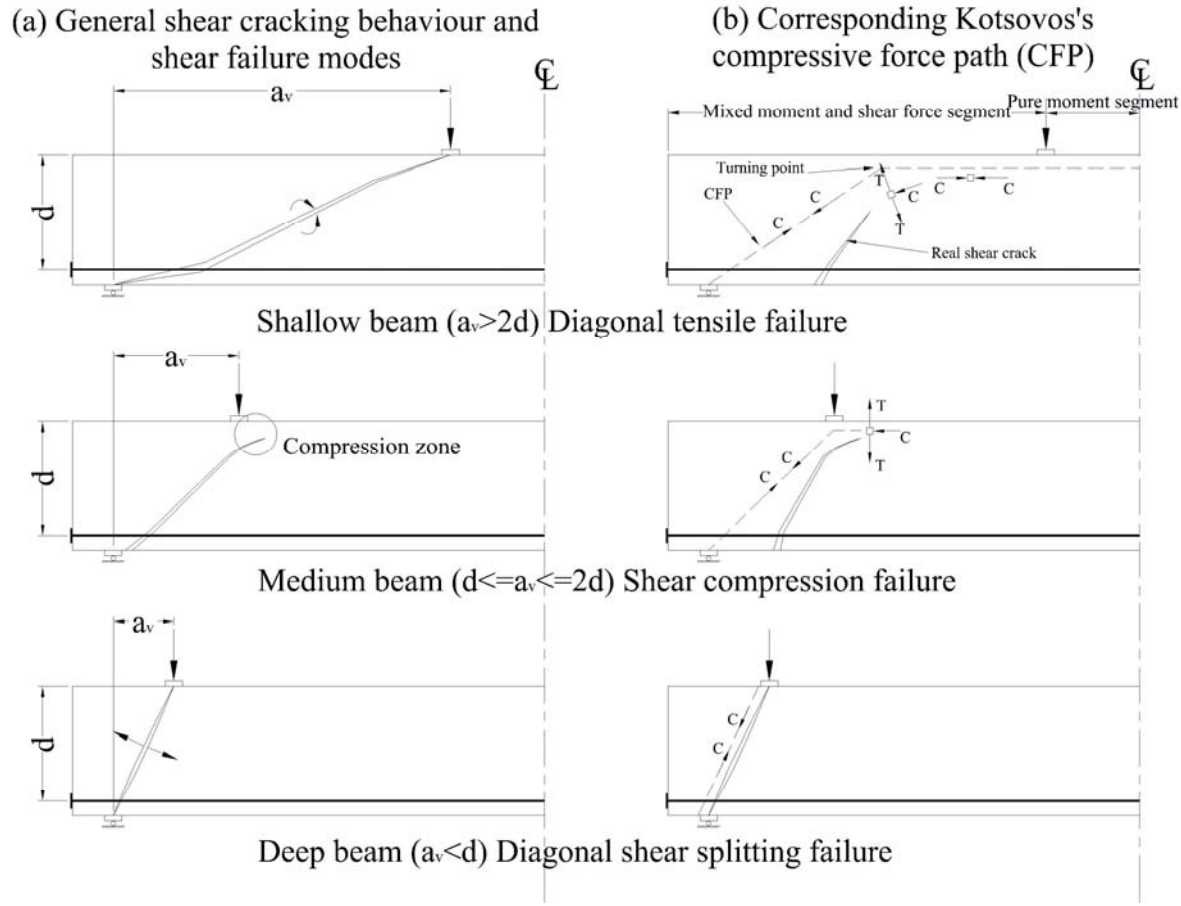

Figure 2.7 Comparison between the behaviour of the general shear cracking and the corresponding Kotsovos' compressive force path concept (CFP)

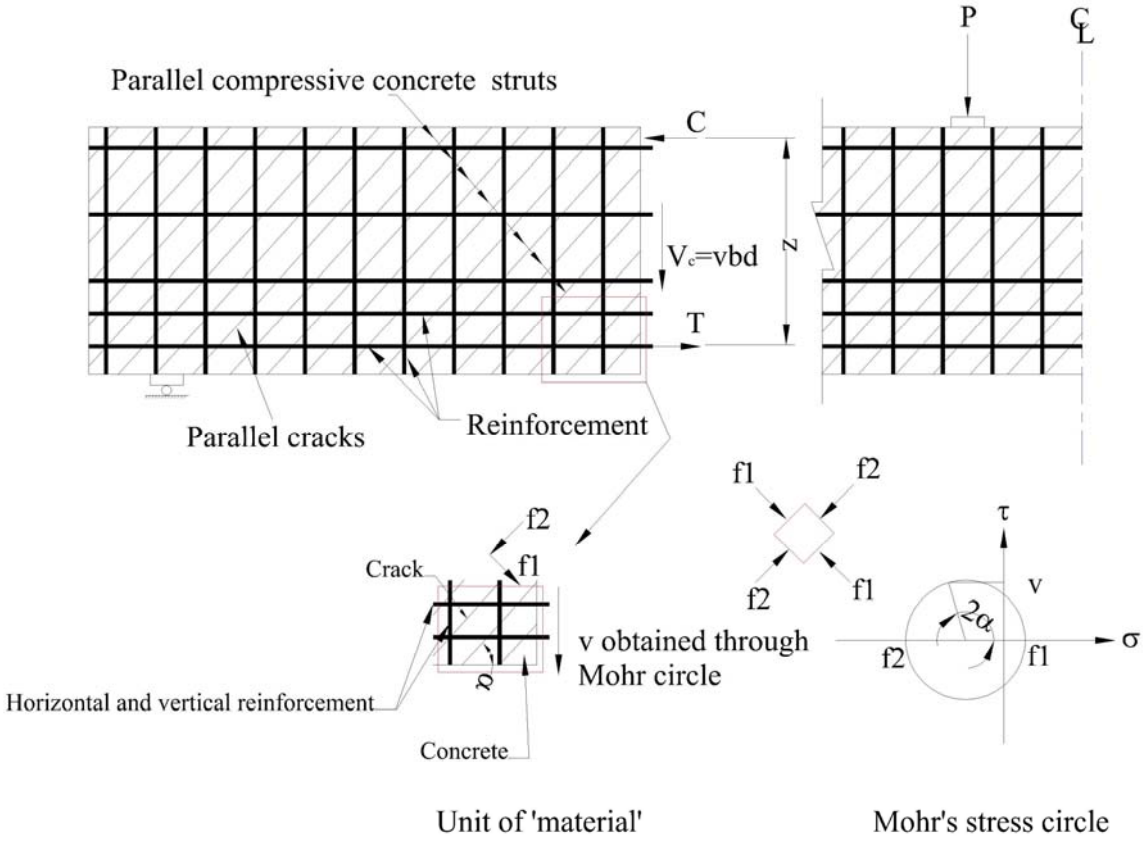

Figure 2.8 General truss model in the truss method

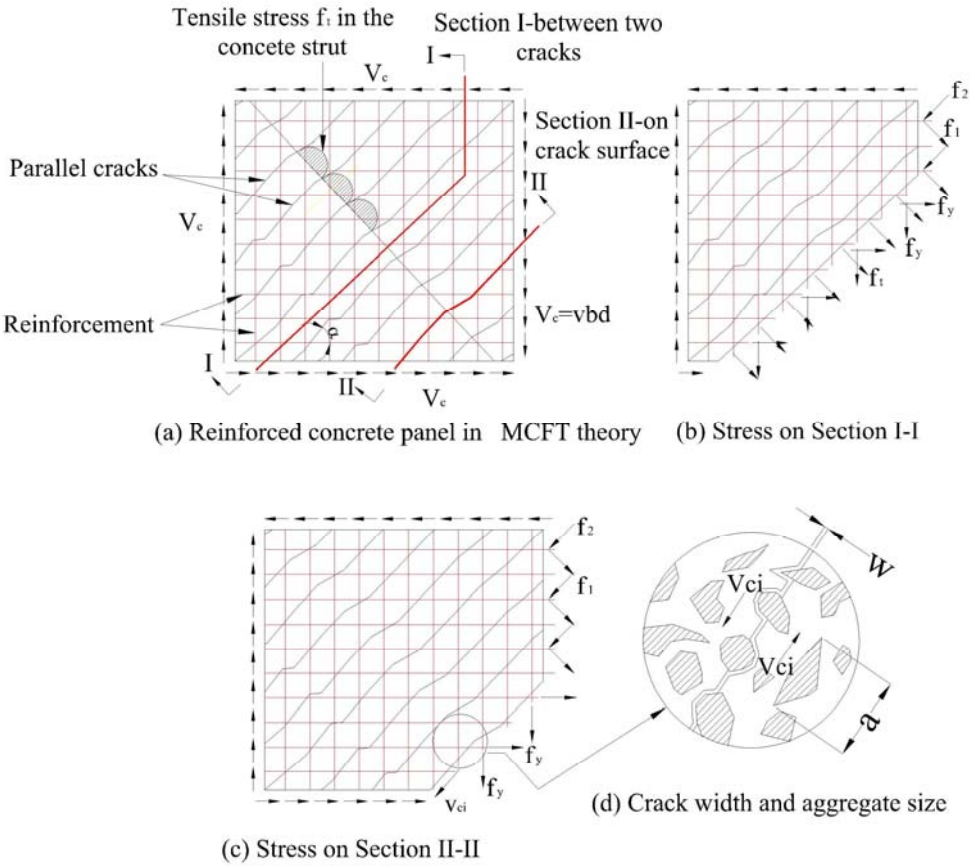

Figure 2.9 Panel model of the cracked concrete in MCFT

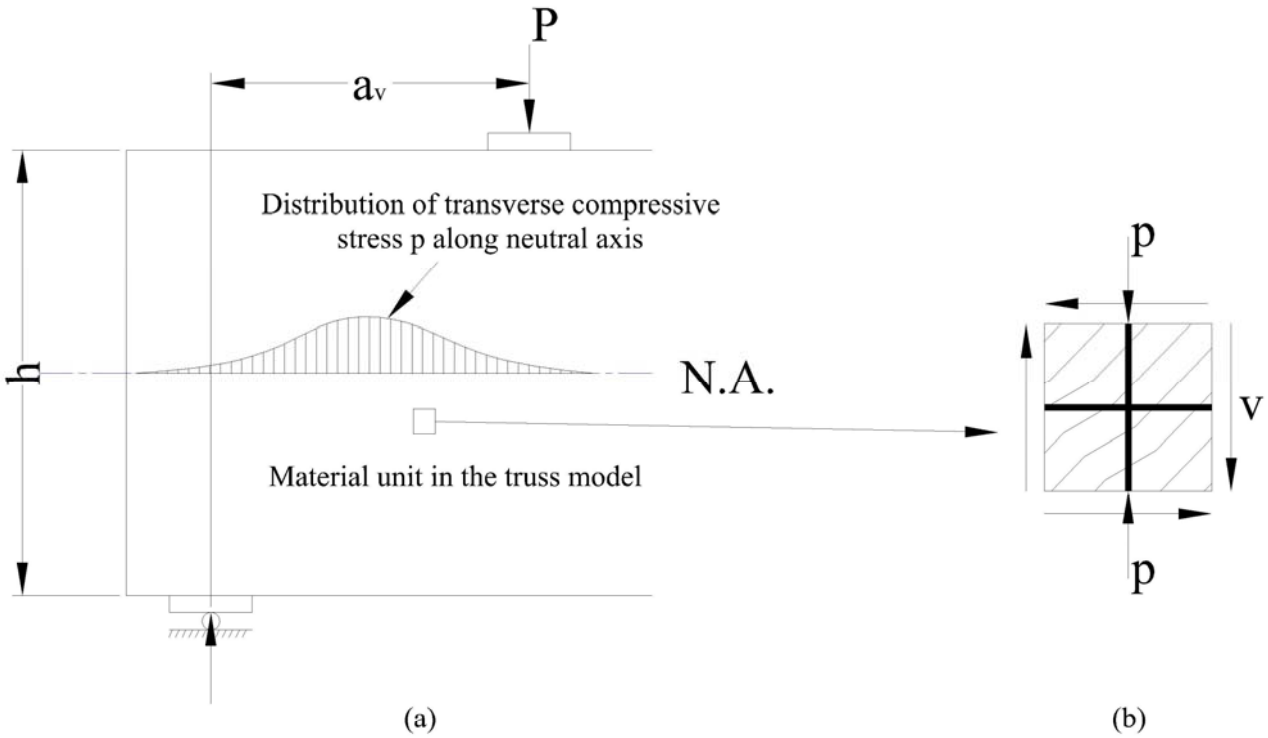

Figure 2.10 Illustration of the appearance of the transverse compressive stress *p* in a deep beam (Kong, 1990)

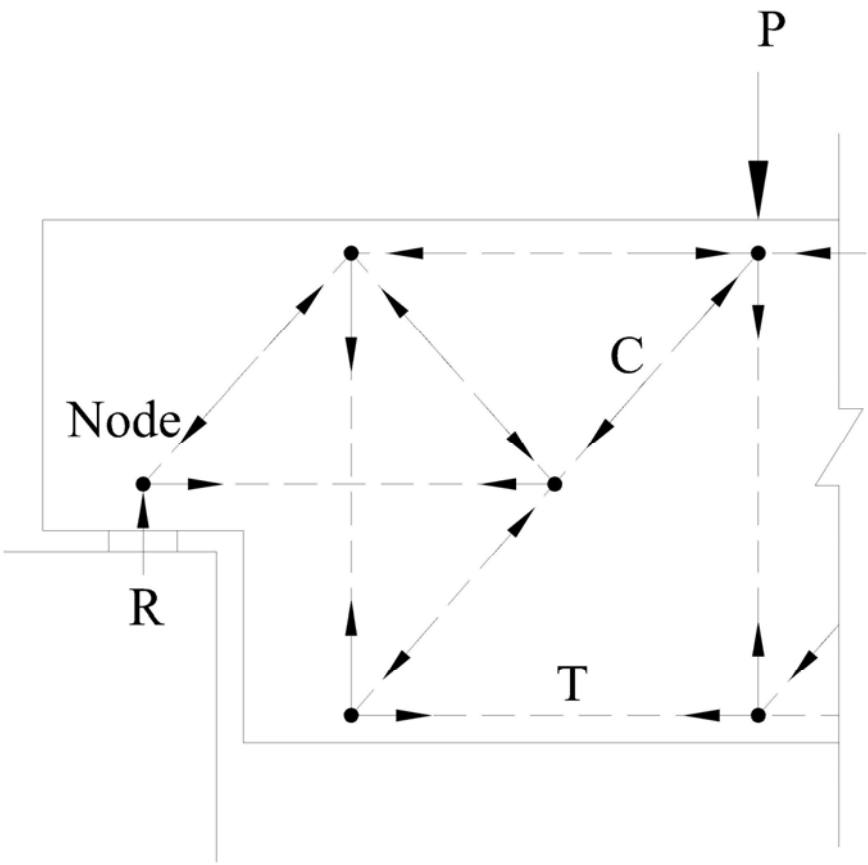

Figure 2.11 A possible strut-and-tie system in a D-region

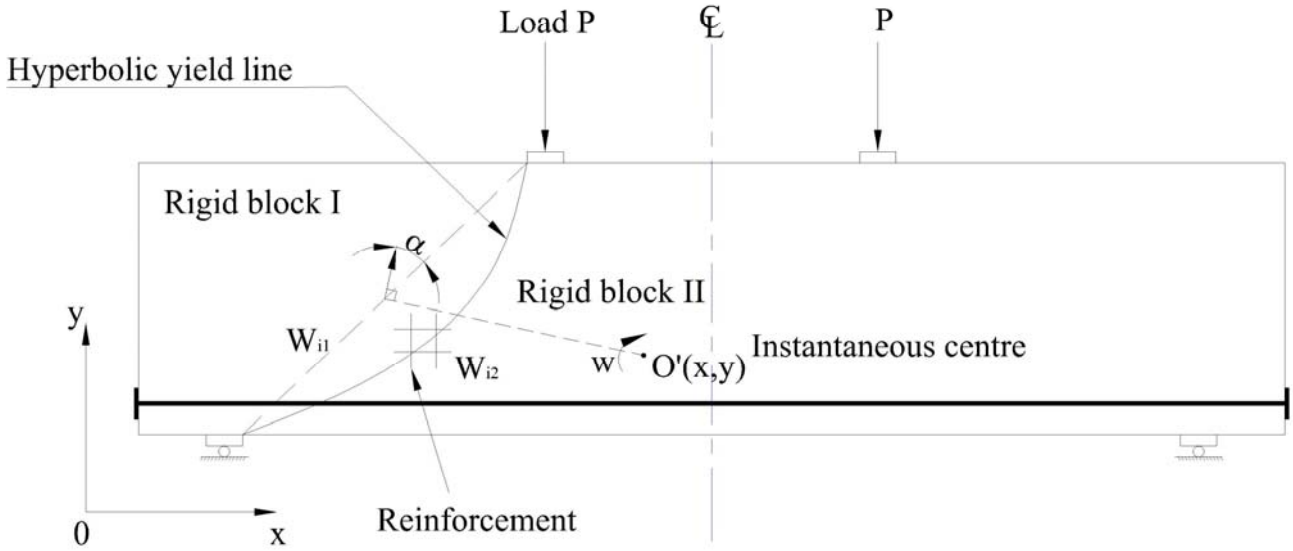

Figure 2.12 Assumption of the shear mechanism in a kinematics method

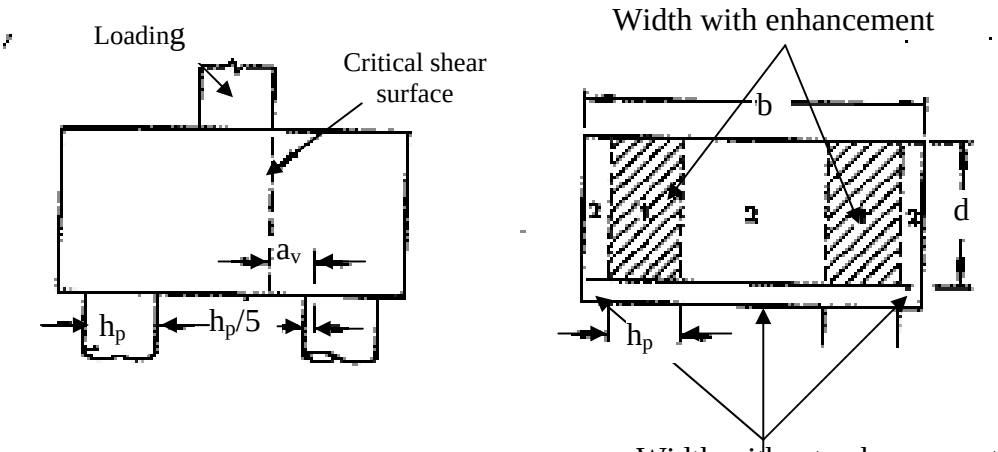

Front surface (longitudinal direction)

Cross-section above pile centre (transverse direction)

(a) Definition of the shear enhancement factor and its application width in proposed method 1 (Clarke, 1973)

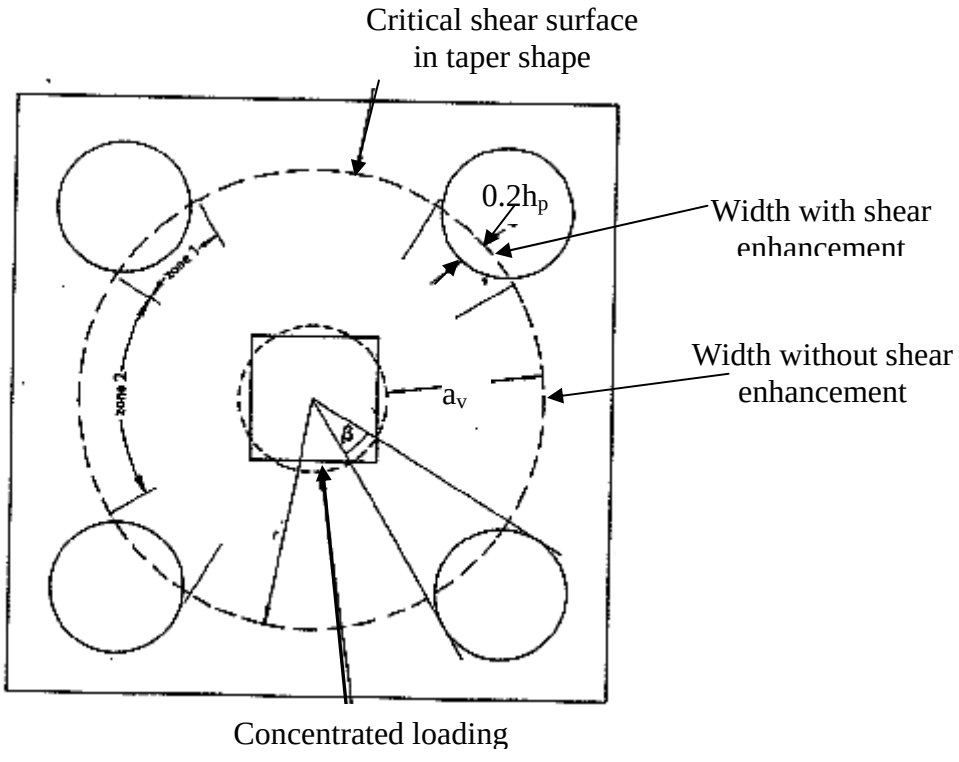

(b) Definition of the shear enhancement factor and its application width in proposed method 2 (Clarke, 1973)

Figure 2.13 Clarke's shear model in the pile cap

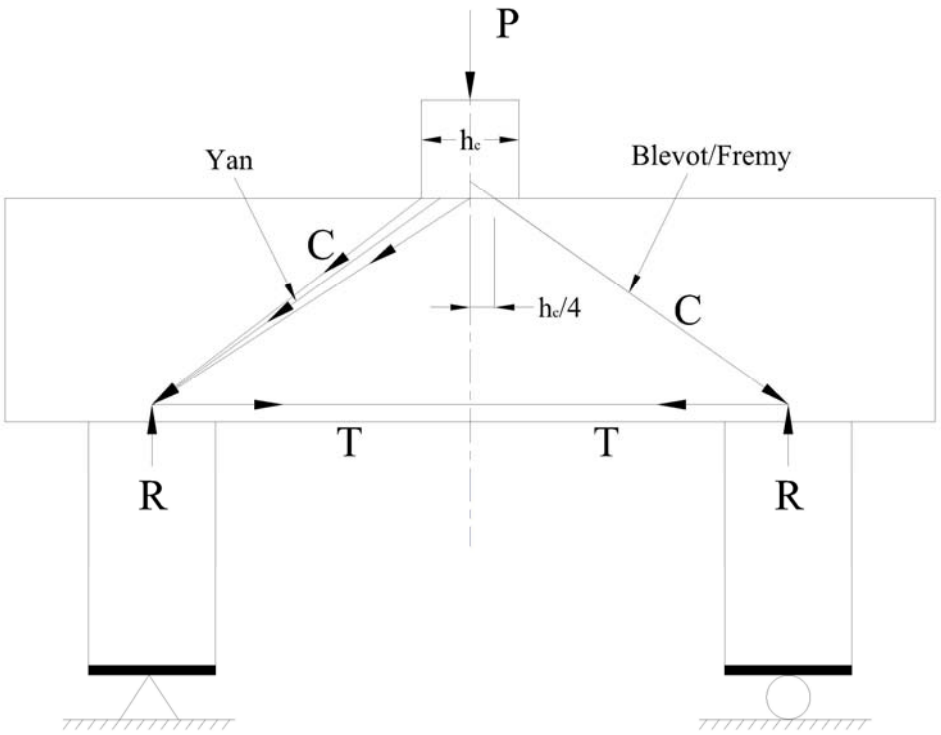

Figure 2.14 Two strut-and-tie systems for a pile cap projected to the cap front surface

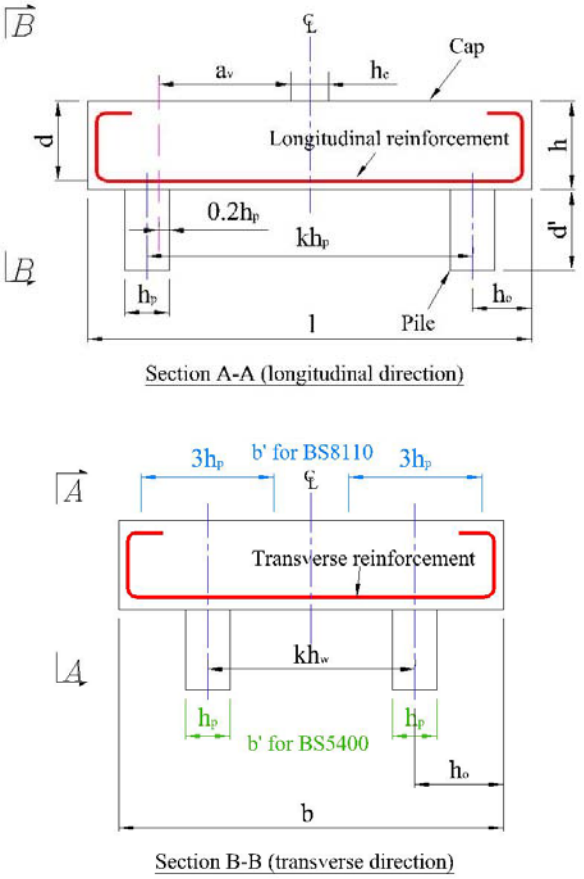

a_v: shear span;
b: pile cap width;
b': width on which shear enhancement factor is applied;
d: pile cap effective depth;
d': pile depth;
h: pile cap depth;
h_c: width of wall loading;
h_o: longitudinal and transverse overhang;
h_p: pile diameter;
kh_p: longitudinal pile spacing;
kh_w: transverse pile spacing;
l: pile cap longitudinal length.

Figure 2.15 Key dimensions of the pile cap and the width on which the shear enhancement factor is applied b'

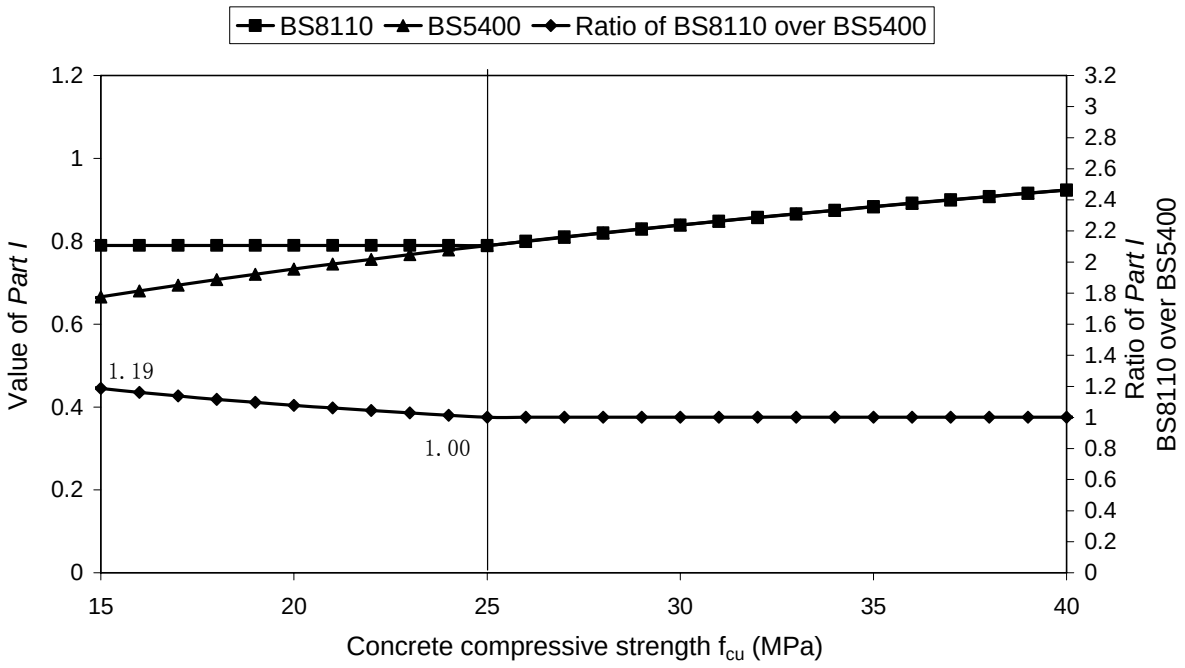

(a) Comparison of *Part I* between BS5400 and BS8110

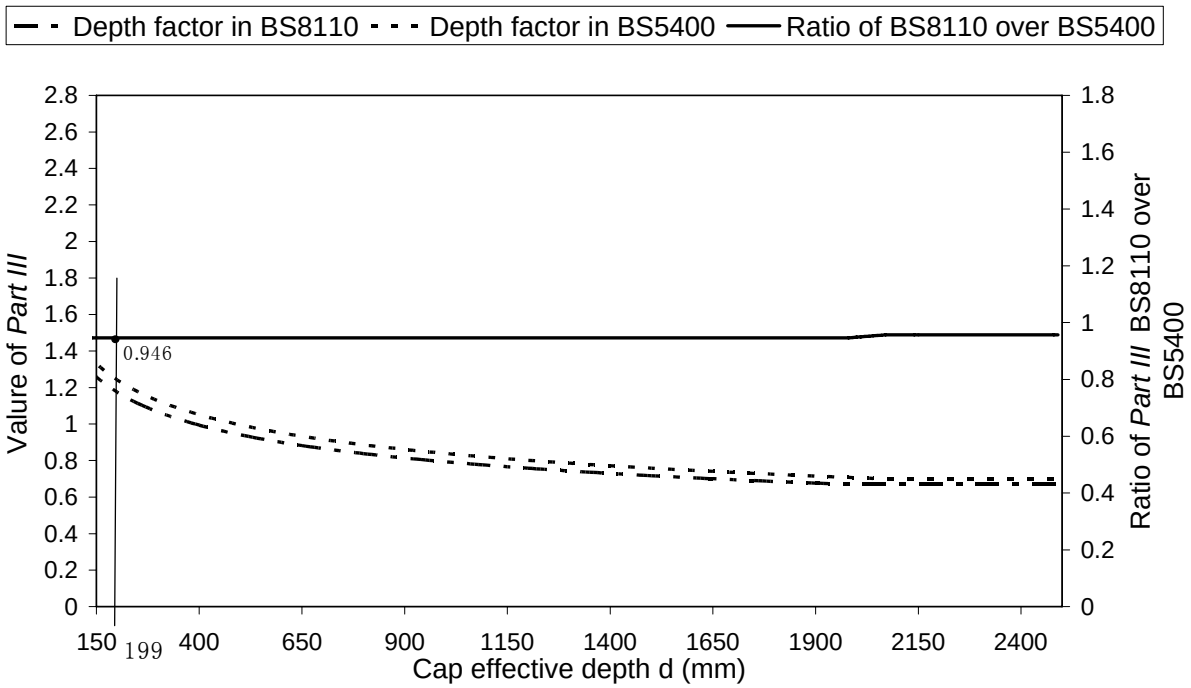

(b) Comparison of *Part III* between BS5400 and BS8110

Figure 2.16 An example of the discrepancy of the shear design formulae between BS5400 and BS8110

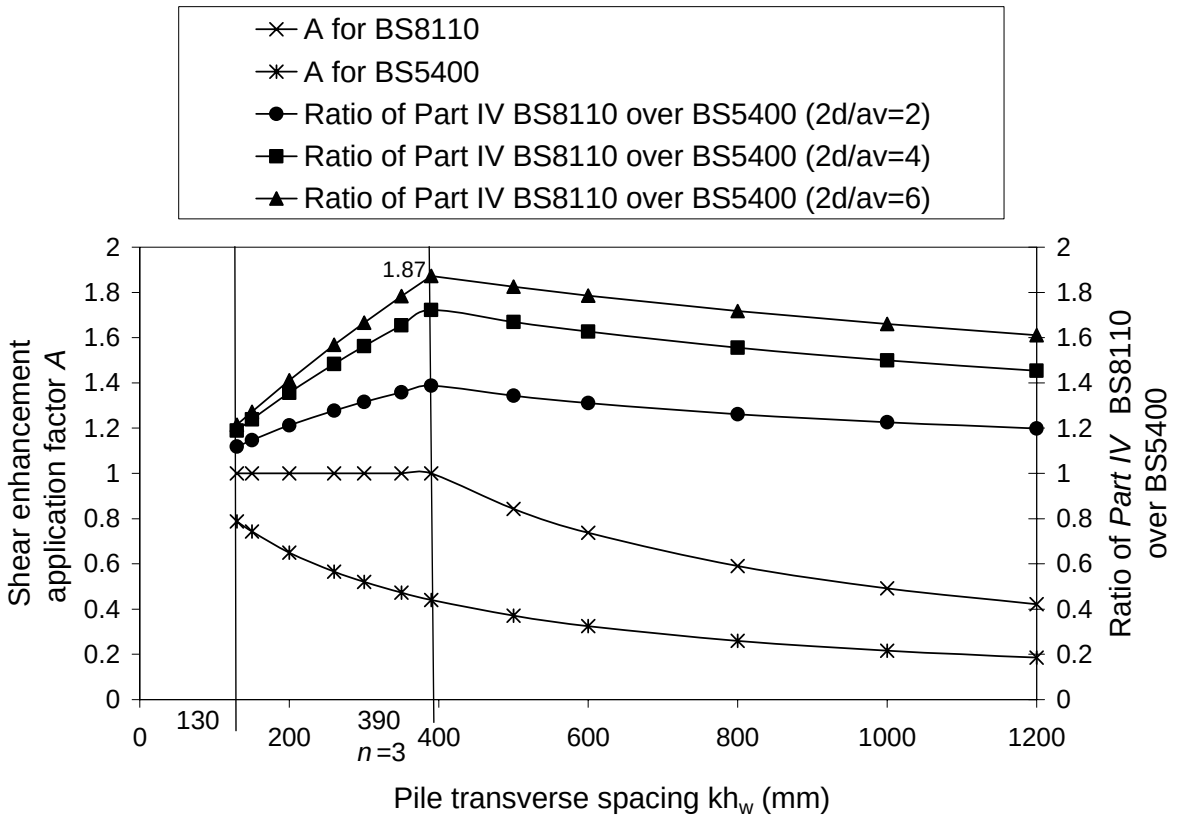

(c) Comparison of *Part IV* between BS5400 and BS8110

Figure 2.16 An example of the discrepancy of the shear design formulae between BS5400 and BS8110

Chapter 3 Design and execution of the laboratory experiments

3.1 Introduction

A literature review on the pile cap experiments carried out by other researchers is given in this chapter. Valuable lessons were learned from these experiments which benefited the design and execution of the laboratory experiments in this research.

A series of ½ scale to ¼ scale four-pile cap samples were tested in the laboratory to investigate the shear capacity. The preparation work and the procedure of the experiments are described. The variables of the experimental samples were the shear enhancement factor, the shear enhancement application factor and the reinforcement ratio. The setup of the PIV technique to measure the displacement and strain distribution on the cap concrete surface is briefly given. More details are provided in Chapter 4.

A selection of the experimental results is presented including the crack distributions and propagations, the failure loads and the failure types and the influence of reinforcement ratio on the pile cap shear capacity.

3.2 Previous researches and lessons learned for this research

Compared with the shear experiments for 1-way spanning RC beams, experiments on 2-way spanning pile caps are small in number. Tests by Clarke (1973), Hobbs and Stein (1957), Sabins and Gogate (1984) and Adebar, Kuchma and Collins (1990) have been reviewed, including looking at the sample scale, the cap shape, the type and number of piles, the support condition, reinforcement configuration in the pile cap, the load pattern, failure type, failure load and the research objective (Bloodworth, Jackson & Lee, 2001).

In order to investigate the then used CP110 (1972), Clarke (1973) tested fifteen ½ scale reinforced concrete pile caps, each with four piles, varying in the pile spacing, the reinforcement layout and the anchorage type. Four different reinforcement anchorage types (non anchorage, nominal anchorage, full anchorage and full-plus-bob anchorage) and three different reinforcement layouts (grid, bunched square and bunched diagonal) were investigated. The load was supplied to the four piles by four jacks, the load in each of which was recorded. All these samples were subjected to a concentrated load from above the cap.

Hobbs and Stein (1957) tested about seventy 1/3 scale centrally loaded two-pile caps to verify a permissible stress design method based on an elastic analysis. In these experiments,

the existence of the pile was realized by a rectangular steel plate in contact with the underside of the cap which was supported by rollers underneath, rather than by true piles as in Clarke's experiments. It was difficult to extrapolate the shear capacity of the two-pile caps to that of four-pile caps by just doubling the failure load because these two types of pile caps may fail in different mechanisms.

In Sabins and Gogate's experiments (1984), aiming at verifying the ACI code (1977) and CRSI Handbook code (1978), 1/5 scale four-pile caps were tested. A concentrated load in circular shape was applied.

In order to test the appropriateness of the STM contained in the ACI Building Code and the Canadian concrete code, Adebar, Kuchma and Collins (1990) tested six full scale pile caps by varying the cap's effective depth d but kept the amount of longitudinal reinforcement A_s unchanged. The samples were all cast into non-regular geometry with the piles arranged in a diamond shape rather than a square shape.

Chan and Poh (2000) tested three pile caps of $1000\,mm$ square in plan and $400\,mm$ in depth to investigate the behaviour of a newly invented pre-cast pile cap, the capacity of which was compared with the BS8110 prediction. A concentrated load was applied and the piles were supported on rollers.

Other experiments include the tests to investigate the size effect on the punching shear capacity of pile caps (Regan, 1998).

The common attributes of the set up of the above experiments are:

(i) the freedom of rotation was assigned to the pile base except in Clarke's experiments;

(ii) concentrated load was applied.

Regarding the instrumentation, Demec readings were taken to determine the strain profile on concrete surfaces through the depth of the cap in Clarke's experiments (Clarke, 1973). Strains in two of the main reinforcement, one of which passed over the top of two piles while the other ran along the centre-line of the cap, were measured by strain gauges. Due to the problem of the bond failure, no satisfactory strain readings were obtained (Clarke, 1973).

Learning from the above experiments, some basic ideas of the experiment design for this research were obtained. A certain depth of the pile was to be included in the cap rather than just using a steel plate as the support condition. This was to make the sample closer to reality. Restricted by the experimental conditions, vertical support was to be given to the whole pile base *i.e.* restrained the rotation of the pile base while the horizontal movement was allowed (Section 3.6). Compared with the freedom of rotation assigned to the pile base, this support condition was closer to the reality. Full-length wall loading (Figure 1.2 (b)) was to be applied to ensure the low liability of the caps to fail in punching.

Considering the inconvenience and the malfunction of Demec readings and strain gauges in the experiments of RC structures, a non-contact PIV technique was to be applied to investigate the distribution of the stress and strain on the cap concrete surface and in the main longitudinal reinforcement.

3.3 Development of the sample design

In total, four batches of samples were tested (Table 3.1). In order to clarify the identity of all pile caps, samples in different batches were numbered in an efficient way, generalized as: 'BbNn'. The first 'B' represented 'Batch' followed by 'b' representing batch number (from 1 to 4). The third 'N' was the cap series being either A or B. The final 'n' was the sample number within each cap series. For example, B4A3 meant the 3rd sample in Batch 4 Series A.

The design strategy for sample dimensions is sketched in Figure 3.1. As mentioned in Section 2.10.1, the key parameters influencing the discrepancy between BS5400 and BS8110 are the shear enhancement factor $\frac{2d}{a_v}$ and shear enhancement application factor A. The dimensions of the pile cap samples were designed to obtain a range of values of $\frac{2d}{a_v}$ and A.

In order to investigate the influence of $\frac{2d}{a_v}$, Series A (A1-A5) were designed to vary $\frac{2d}{a_v}$ but keeping A constant by varying the longitudinal pile spacing and keeping the transverse pile spacing constant. For example, as shown in Table 3.3 (b), for samples in Batch 4 Series A, $\frac{2d}{a_v}$ ranged from 1.28 (B4A1) to 3.59 (B4A5).

In order to investigate the influence of A, Series B were designed to vary A while keeping a constant shear enhancement factor $\frac{2d}{a_v}$ by varying the transverse pile spacing, while keeping the longitudinal spacing constant. This also resulted in the varying ratio n of the transverse pile spacing over one pile diameter. For example, as shown in Table 3.3 (b), for samples in Batch 4 Series B, A based on BS8110 ranges from 0.67 (B4B4) to 1 (B4B1) and n ranged from 2.31 (B4B1) to 5.38 (B4B4).

The Series B (B1-B4) had less reinforcement ratio than Series A (Table 3.3 (b)). Pile cap A2, with the same value of $\frac{2d}{a_v}$ as in the samples in Series B but with larger reinforcement

ratio, was designed to study the influence of the reinforcement ratio on the shear capacity of pile caps.

The reinforcement ratio was initially calculated in accordance with BS8110 with the intention that the bending failure be suppressed by the shear failure. The samples were also designed to avoid punching shear failure. Reinforcement was given a full anchorage length beyond the centre-line of the piles and had full bob-ups from the cap bottom to its top surface. However most of the best experimental results were obtained only from Batch 4. In Batch 1, 2, and 3, experiments were not totally successful because of the following reasons:

(i) Cap's shear capacity was actually higher than the capacity of the testing machine;

(ii) Bending failure happened rather than the shear failure;

(iii) Pile without reinforcement was crushed before the cap failed.

Point (iii) happened more often when the pile was separate to the cap body so that a load concentration occurred at the interface between the pile top surface and the cap soffit. Sometimes it happened where pile base sat directly on the steel platten of the testing machine.

In order to control the samples to fail in shear, lessons were learned from Batches 1, 2 and 3. These problems were not completely solved until Batch 4. In Batch 4 samples, shear cracks played a major part in the failure and the failure load was normally lower than the capacity of the testing machine and the cap's bending capacity. There was no extensive pile crushing in Batch 4 but one individual case of such failure. A brief summary of the sample development and the major changes made is listed in Table 3.1.

The variation of the predicted capacity and the actual capacity for cap A1 in the four batches with the variation of key efficient parameters to improve the shear behaviour of the pile cap is shown in Table 3.2. The most efficient methods, which must be implemented simultaneously, to reduce both the shear and bending capacity of the pile cap and at the same time to reduce the shear capacity more quickly than the bending capacity were:

(i) to reduce the concrete design strength;

(ii) to reduce the shear enhancement factor;

(iii) to reduce the effective depth and the width of the cap;

(iv) to cast the piles into the cap body.

It can also be seen in Table 3.2 that the reinforcement ratio was increased from B1A1 to B4A1. This may cause the ratio of the bending capacity (power order of $\frac{A_s}{bd}$ is 1 in design formula) over shear capacity (power order of $\frac{A_s}{bd}$ is $\frac{1}{3}$ in design formula) to increase and thus the shear failure may appear before the bending failure.

3.4 Sample dimensions and reinforcement arrangement

3.4.1 Sample dimensions

Key pile cap dimensions for all samples, following the design strategy and development described in Section 3.3, are summarised in Table 3.3 (a) and Table 3.3 (b).

As shown in Table 3.3 (a), the longitudinal pile spacing kh_p varied in Series A. For example, in Batch 4 Series A, kh_p was from $400\,mm$ to $800\,mm$. The transverse pile spacing kh_w varied in Series B. For example, in Batch 4 Series B, kh_w was from $300\,mm$ to $700\,mm$.

Other dimensions such as the effective cap depth d, cap width b, pile diameter h_p and the width of the wall loading h_c *etc*. also varied in different series. For example, d was $369\,mm$ in Batch 1 and was kept as $269\,mm$ in Batch 2 and 3. It reduced further to $199\,mm$ in Batch 4 Series A. For Series A, b of $800\,mm$, $600\,mm$ and $500\,mm$ were used from Batch 1 to 4. Following the change of b, the pile diameter h_p reduced from $230\,mm$ to $130\,mm$. The width of the wall loading h_c was 200 mm and 100 mm in Batch 1, 2 and Batch 3, 4 respectively. The pile depth d' was taken as $260\,mm$ in all samples.

As shown in Figure 2.16 (b), for a cap with depth larger than $199\,mm$, the ratio of the size effect between BS8110 and BS5400 is between 0.946 and 1. So the discrepancy between the two standards influenced by the size effect cannot be investigated in this research. The size effect was not designed as a variable to investigate its influence on the accuracy of the design formulae.

Because of the limitations shown in Section 3.3, the transverse overhang h_o (Figure 2.15) in these samples was not larger than 1.5 times the pile diameter. For instance, for samples in Batch 4, transverse overhang h_o =100 mm (Figure 3.3) which was shorter than $1.5\times h_p = 195mm$. The maximum width of longitudinal yielding tie in STM and the relevant maximum cap width on which the shear enhancement factor is applied centred over each pile as specified in BS8110 are three times the pile diameter (Section 2.10.3). In this research, however, it was assumed that the cap width of $3\times h_p$ was deemed to be reached once the longitudinal tie lies on a width of (transverse $h_o + 1.5\times h_p$) over each pile, actually shorter than $3\times h_p$. Considering the full-length wall loading that makes the longitudinal reinforcement behave in some sense close to 1-way, this assumption is reasonable since $3\times h_p$

could be achievable if h_o is further increased in case current tie width of (transverse $h_o + 1.5 \times h_p$) is actually reached.

3.4.2 Reinforcement cage in the cap and piles

In the cap's bottom, reinforcement was distributed in the longitudinal and transverse directions at uniform bar centres of $50\,mm$ in all samples, passing sufficient distance over pile heads and fully bent up. Main reinforcement diameters of $12\,mm$ and $10\,mm$ were used in Series A and B (Table 3.4) with concrete cover $25\,mm$. With the variation of the cap effective depth, this resulted in various reinforcement ratios (mm^2/mm^2 or %) as shown in Table 3.3 (b). B4B1 had the same dimensions as B4A2 but with less reinforcement ratio. The detailing of the reinforcement complied with BS8666 (2000). Welded mesh A393 was provided on the cap top surface to control the cracking rendered by the concrete shrinkage. A photograph of a typical cage is shown in Figure 3.2. The four piles were reinforced by vertical bars and horizontal stirrups only in Batch 3 and Batch 4.

Reinforcement details for Batch 4 Series B are shown in Figure 3.3 as a reference.

3.5 Material properties

Concrete and reinforcement properties for all the pile caps are listed in Table 3.4.

3.5.1 Concrete strength f_{cu}

The 28 day characteristic concrete strength was initially specified as $30\,N/mm^2$ in Batch 1 and 2. In Batch 1, the composition of the concrete and the constituent materials were specified by a concrete ready-mix supplier to obtain the required strength. The caps were cast in the courtyard of the laboratory. Six $100\,mm$ concrete cubes were produced at the same time.

The concrete mix design for Batch 2 and later batches was carried out manually following a standard concrete mix design form (Taylor, 2000). Pile caps and cubes were cast by an outside precast manufacturer. For Batch 2, the plant offered two concrete cubes for each sample. The cubes were tested in the laboratory just after each experiment ended. The real f_{cu} was unexpectedly high, reaching above $50\,N/mm^2$.

To effectively reduce the real f_{cu} in Batch 3 and 4, the characteristic concrete strength was reduced to $20\,N/mm^2$ (Table 3.2). The standard deviation for the concrete design strength was reduced from $5\,N/mm^2$ in Batches 1 and 2 to $2\,N/mm^2$. In Batch 3, concrete cubes at 28 days were tested by a professional material testing company. In Batch 4, three

concrete cubes for each sample were produced. Cubes were tested in the school's laboratory just after each experiment ended.

It is clear from Figure 2.16 (a) that f_{cu} slightly influences the discrepancy between BS8110 and BS5400 when $f_{cu} < 25MPa$. But from Table 3.4, it can be seen f_{cu} was almost constant in each batch. Therefore, the influence of f_{cu} on the discrepancy between two standards cannot be investigated in this research. The concrete strength was not designed as a variable to investigate its influence on the accuracy of the design formulae.

3.5.2 Strength of reinforcement f_y

The specified characteristic strength of the reinforcement in all the batches was $460\,N/mm^2$ and the real strength was estimated as $600\,N/mm^2$ when initially predicting the cap shear capacity for design purposes.

In Batch 4, the yield strength of reinforcement of diameter 12mm (T12) was tested in the School's laboratory. The mean yield strength of $547\,N/mm^2$ from a total of 16 bars was obtained, which was taken as the yield strength of reinforcement f_y. The mean peak value was $646\,N/mm^2$. T10 reinforcement was assumed to have the same yield strength and peak value. The reinforcement in Batches 1~ 3 was assumed for the purposes of back-calculation to have the same yield and peak strength as in Batch 4.

3.6 Basic experimental setup

The experimental setup and the pile boundary conditions are shown in Figure 3.4.

The 150 tonne Instron column-testing machine in the Heavy Structural Laboratory of Southampton University served as the load application system. A hydraulic actuator jack beneath a lower steel platten lifted up the platten whereupon the pile cap was placed.

In Batch 3 and 4, bedding material (self-levelling screed) was placed under the pile base (Figure 3.4). The bedding material was held by a cardboard tray (Figure 3.5 (a)). This measure was taken to avoid piles from being crushed by the local load concentration. In Batch 3, the tray was placed directly on the lower steel platten, while in Batch 4 the tray stood on two plastic sheets between which there was a layer of oil (Figure 3.5 (b)) to release the horizontal restraint on the pile base.

In all batches, soft boards (Figure 3.4) were introduced between the concrete spreader beam top surface and the load cell platten, and between the concrete spreader beam bottom

surface and the cap top surface. With the soft boards, load can be spread uniformly on to the cap top surface avoiding any unexpected crushing of the concrete spreader beam or the cap beneath it.

In Batch 1 and 2, piles were cast separately from the cap (Table 3.2), only giving the cap a vertical support. In Batch 3 and 4, piles were cast into the cap, providing independent vertical force and moment reactions to the cap, which is closer to the practical situation. The reaction at the pile base was supplied by an eccentric upward force (Figure 3.4). The setup in Batches 3 and 4 was thus close to a rigid frame.

As a rigid frame, a hogging moment above pile head was expected. Since the shear behaviour is relevant to the distribution of the bending moment (Section 2.3.1), a frame analysis was done to study the influence of the hogging moment M_h above the pile head. It was calculated (Appendix AII) that the ratio between M_h and the sagging bending moment at central span M_s was given by:

$$\left|\frac{M_h}{M_s}\right| = \frac{1}{1+2\left(\frac{l_2}{l_1}\right)\left(\frac{I_1}{I_2}\right)} \qquad (Eq.AII.1)$$

where I_1, I_2 were the second moment of the equivalent transformed concrete cross sections of cap and pile respectively; l_1, l_2 were the length of the bar elements representing the cap and piles respectively (Section AII.1).

It is clear from $Eq.AII.1$ that the ratio $\left|\frac{M_h}{M_s}\right|$ increases with the decreasing $\frac{I_1}{I_2}$ and $\frac{l_2}{l_1}$. For all the samples in Batch 4, I_2 and l_2 were the same. B4A1 had the largest l_1 and smallest I_1 since I_1 was the same in Batch 4 Series A and increased in Batch 4 Series B (the slight reduction of the reinforcement ratio in Series B was deemed not to reduce I_1). So B4A1 had the largest ratio $\left|\frac{M_h}{M_s}\right| (= \frac{1}{26.4})$ among all the samples in Batch 4 (Section AII.2), implying M_h was relatively small compared to M_s. Its influence on the pile cap shear behaviour can be neglected.

High shear force and shear deformation in the pile caps were expected in the experiments. However the frame analysis showed that based on the support condition of the pile cap in this research, the shear force and deformation do not influence $\left|\frac{M_h}{M_s}\right|$ (Section AII.3).

3.7 Instrumentation

Figure 3.6 shows the setup of the instrumentation in the experiments.

Since the 150 tonne machine capacity had a built-in safety margin, the maximum load it can give is about 144 tonne. Load was sensed by a load cell which was connected with an upper adjustable steel platten being mounted on a spherical bearing to allow rotation. Load data from the load cell was transmitted through the control panel of the testing machine and then into a data logger to be recorded by SmartStrain™ software in the computer.

A 2-way configuration of 15 potentiometers (maximum range $-15\,mm \sim 15\,mm$) was designed in order to collect two-dimensional information of the cap soffit deflection (Figure 3.7). Deflection values from potentiometers were also recorded by the data logger at a frequency of 1 Hz. The 15 potentiometers were calibrated before the experiments. A simple method was used in which the ratio between the output voltage to a known displacement was calculated. As shown in Figure 3.8, the known displacement was obtained from two steel plates with different known thicknesses.

The distribution of displacement and strain on the cap front surface, crack distribution which was manually highlighted during the experiment and the crack propagation were surveyed by the non-contact PIV technique (Chapter 4). The cap front surface was photographed by an Olympus digital camera with 2288×1712 *pixels* resolution controlled remotely by a computer. Crack propagation on the back surface was also recorded by a manually controlled digital camera. The crack distribution on the six surfaces of the caps at failure step was also recorded, using the terminologies of the cap surfaces shown in Figure 3.9.

3.8 Testing procedure

The experiments began with giving the cap two vertical displacements without loading for a PIV error analysis (Chapter 4 & Appendix I). Then an initial load lower than $30\,kN$ was applied to the fully prepared pile cap sample in order to cause the consolidation of voids possibly existing at the interface of different elements (*e.g.* between the concrete spreader beam and upper steel platten) and in the bedding material, which otherwise cause noise in the final load-displacement curve. The load was then reduced back to near zero for the main test.

Both the load control method and the displacement control method were applied. Load and displacement steps or increments were applied respectively at speed of $50\,kN/\min$ and $1\,mm/\min$. The load or displacement was held constant at the end of each increment, leaving an interval (Figure 3.10) during which the experimenter investigated and highlighted the crack

distribution on both front and back surfaces of the cap. A photograph was taken during each interval for the PIV analysis. If growing cracks were highlighted during an interval, two consecutive photographs were taken before and after the cracks were highlighted.

In the load control method, during the initial loading steps when the structure deformation was linear, the load increments ranged from $25\,kN$ to $100\,kN$ in different tests. After judging that the shear or bending cracks on the concrete surface were beginning to mature fast and that the structure was becoming dangerous and unstable indicating the onset of the yield stage (Figure 3.10), control was changed to displacement control with displacement increments ranging from $0.25\,mm$ to $1.5\,mm$. Displacement control is safer than load control when close to structural failure. The load control method for B4A1 is shown in Figure 3.10.

Due to the fact that considerable creep accumulated during the load interval when the structure was under the load control method (Figure 3.10), which was not modelled in FEA being validated (through PIV) in further study, some samples in Batch 4 were deliberately loaded by displacement control method, *e.g.* B4A4 (Figure 3.10) and B4A5. In the displacement control method, the displacement increments, ranging from $0.25\,mm$ to $1.5\,mm$, were subscribed to the pile cap throughout the experiment. The total distance between the load cell steel platten (Figure 3.4) and the bottom steel platten was kept constant between displacement increments so that creep causing the extra deflection of the cap soffit was relatively low. The displacement increment was reduced once cracking on the cap surface began to mature fast.

In FEA (Chapter 5), for the experimental load-displacement curve of samples using the load control method, the extra deflection caused by the creep accumulated during the load interval was subtracted from the total deflection, *e.g.* B4A1 as shown in Figure 3.10.

The data transmitting system in the experiment is shown in Figure 3.11. The experimental procedure with the two loading methods is shown in Figure 3.12.

3.9 Results and discussions

3.9.1 Crack description and cap deflection

In addition to the samples shown in the section, the whole report of crack distributions at the failure step for all the samples in Batch 3 and 4 and the crack characteristics and types discussed below are shown and annotated in Appendix AIII. The terminologies of the six surfaces of the cap are shown in Figure 3.9.

- **Crack distributions at failure step**

The first characteristic of the crack distributions discussed in the following paragraphs was that under full-length wall loading, for caps with small transverse pile spacing kh_w, the crack distributions on front and back surfaces at failure were similar to those expected for 1-way shear failure, and the cap behaved close to 1-way shear behaviour.

Take B4A4 front surface as an example (Figure 3.13). The front surface shows a standard crack distribution in a shear failure similar to a 1-way spanning deep beam, *i.e.* the bending crack propagated a long way into the region under the wall loading, and the critical compressive splitting crack developed linking the loaded area and the area above the pile head. The concrete near the tip of the shear crack was crushed. The inclined compressive stress was expected to dominate in the inclined strut confined by the surrounding concrete.

A compressive splitting crack also appeared and was fully developed on the back surface left side in B4A2 (Figure 3.14) and on the front surface right side in B4A3 and B4B3. These cracks initiated near the middle of the inclined crack. It was only on B4A4 front (Figure 3.13) and back surfaces and on B4A5 front surface right side (Figure 3.15 (a)) that the widely opened compressive splitting crack initiated from the huge crushing of the concrete under the wall loading where the concrete severely spalled off. In most samples, the central bending crack linked the front and back surfaces of the cap on the cap soffit (Figure 3.17).

In caps with medium $\frac{2d}{a_v}$, Kani's tooth crack appeared, but without failure and of rather short length and in the period between the initial propagation of a central bending crack and the appearance of the critical shear crack. This indicated that these samples were in the transition from shallow beam (cap) to deep beam (cap). A good example is shown on the back surface of B4A2 ($\frac{2d}{a_v}$=1.69) (Figure 3.14). This is in line with the Kani's valley in Figure 2.6, that when $\frac{a_v}{d}$ is small (for B4A2, $\frac{a_v}{d}=1.18$), though the Kani's teeth crack develops, the failure does not end with the failure of the teeth but with the failure of the remaining concrete arch (Figure 2.5 (b)) or with the compressive splitting of inclined shear crack.

In almost all the samples, the existence of the hogging moment indicated in Section 3.6 was proved by the cracks above pile heads, which extended to the top surface cutting inward by a limited distance normally just to the area above the pile. This was exemplified on B4A5 front and top surfaces (Figure 3.15 (a), (b)). This indicates that under the wall loading, 1-way

shear behaviour does not occur across the whole transverse cap width or otherwise the hogging cracks should link the front and back surfaces on the top surface.

As shown in Figure 3.16, the theoretical or the real shear span a_v in a single beam span under concentrated load and any support condition (simply or continuous) is the distance from the cross section at the contra-flexure point (*i.e.* zero bending moment) to that at the maximum moment. Therefore, the presence of the hogging moment indicates that the real shear span a_v should be shortened from the distance between the pile centre and the central span. The British Standards achieve this by shortening a_v to be between the edge of the wall loading and the cross section 20% the pile diameter inside the inner edge of the pile (Section 2.10.1). However, in Section 3.6, it was proved that the hogging moment is relatively small such that a_v in the current standards may be shorter than the real a_v (see Section 6.4.1).

The second characteristic of the crack distributions was that with the increasing pile transverse spacing kh_w, the cracking on the cap soffit became more 2-way, indicated mainly by the cracks occurring perpendicular to the main bending cracks on the soffit such as in B4B2, B4B3 (Figure 3.17) and B4B4. This implied that the larger kh_w, the more possible that the reinforcement in the transverse direction took part in the shear resistance, and the bigger role the 2-way behaviour of the cap and the behaviour of an individual corner pile played relative to the normal shear behaviour in a 1-way spanning beam.

As shown in Figure 3.18, for B4B4, Crack (a) was definitely a bending crack induced by the bending moment in the transverse direction. This was ensured by its shape on the right surface (Figure 3.9) which was vertically upwards rather than inclined. Crack (b) indicated the behaviour around an individual corner pile. Its shape on the right and left surfaces was inclined and short. It might be a potential punching shear crack caused by the individual pile. A similar crack also appeared in B4B3 (Figure 3.17) and B4A5. However, no pile cap finally failed by the punching shear failure of the corner pile. The type of Crack (c) is between a bending crack and punching shear crack.

The third characteristic of the crack distribution was the crushing crack at the edges of the wall loading. It was caused by crushing of the concrete immediately under the wall loading such as on the top surface of B4A3 (Figure 3.19). However, in experiments no sample actually failed by the crushing of the concrete under the wall loading.

The last characteristic of the crack distribution, as can be seen in B4A5 (Figure 3.15 (a), Figure 3.20)), was that the critical inclined shear crack flattened at the lower end near the pile

head, where the tail of the crack swept across the pile head, whilst on the cap soffit, the corresponding shear crack stopped at the pile head rather than linking the whole transverse width. This indicated that the critical shear crack as seen on the front and back surface was not uniformly distributed across the whole cap width.

A diagonal tensile crack (Figure 2.1) was only observed in a few samples because of the fact that most samples had large $\frac{2d}{a_v}$. In B4A1, where the wall loading, which was unfortunately asymmetrical, was biased to the back half of the cap (Section 3.9.2), a diagonal tensile crack appeared on the back surface left side (Figure 3.21), draping and bending downwards and widely opening. Except B4A1, other samples in Batch 4 Series A had a tendency to fail by the compressive splitting shear failure as in a 1-way spanning deep beam. The shear failure was the most apparent in B4A5 (Figure 3.20), where based on the cracks on the soffit, the bending crack linking the front and back surfaces was much less opened than the cracks near the piles linking the compressive splitting shear cracks on the front and back surfaces.

- **Crack propagations**

In all samples, cracks initiated with the bending cracks from the cap mid-span. The occurrence of the Kani's teeth cracks in the experiments is a debatable point. In shallow beams, Kani's teeth cracks are normally readily discernable, and are regarded as a transitional crack type linking bending cracks and shear cracks. In relatively deep caps as in the experiments, Kani's teeth cracks were less apparent and less densely distributed, but still did occur, in a form shorter and steeper than in a shallow beam. The cracks started at the cap soffit near the first bending crack and then extending upwards at an angle towards the edge of the wall loading *e.g.* on B4A2 back surface (Figure 3.14). This propagation normally occurred for a while and then stopped, being superseded by the propagation of the compressive splitting shear crack. This was because the short span constrained them from fully maturing, and the formation of the concrete compressive strut preceded the appearance of arch action which is deemed as a result of maturing of the Kani's teeth cracks (Section 2.3.2).

Compressive splitting shear cracks along the concrete strut usually initiated at the mid-height of the cap and then propagated in both directions towards the pile head and the wall loading *e.g.* on the front surface of B4A3, B4B3 and back surface of B4A2 (Figure 3.14). A compressive splitting crack can also initiate because of crushing of the concrete immediately

under the wall loading, such as on the front and back surfaces of B4A4 (Figure 3.13) and front surface of B4A5.

Sometimes, the bending crack and the critical shear crack matured rapidly one after the other with both opening widely, but one finally overwhelming the other. Apart from B4A4 (shear failure without any significant bending crack on front surface (Figure 3.13)) and B3A1 (bending failure without any significant shear crack on back surface (Figure 3.22)), bending failure and shear failure were always very close at the failure step. For example, as can be seen on the back surface of B4A1 and B4A4, and the front surface of B4A3 (Figure 3.23), caps failed in shear but with significant central bending cracks propagating widely and upwards deeply. On the other hand, the back surface of B4A3 (Figure 3.24) showed a bending failure with significant critical shear cracks.

- **Summary of the crack distribution and propagation**

The crack distributions and propagations in the Batch 4 samples indicated that most of them failed in shear or were very close to shear failure, and so are valuable to be compared with the predictions from the shear formulae in the British Standards.

Though there were similarities of the crack distributions to 1-way spanning RC beams, the hogging cracks only cutting a limited distance into the cap, the transverse bending crack perpendicular to the central bending crack, the punching shear cracks around individual piles and the tail of the shear crack stopping at the pile head on the cap soffit were indications of 2-way shear behaviour of the pile caps under the full-length wall loading. The appearance of transverse bending cracks suggests that any method developed semi-empirically or physically should consider the role of the transverse reinforcement. For example, the STM should consider the transverse reinforcement tie. The semi-empirical formulae *Eq*.2.5 and *Eq*.2.6 do not consider the behaviour of the transverse reinforcement which is not reasonable.

- **Cap deflection**

As shown in Figure 3.10, the early bending and shear cracks appearing in the cap in the elastic stage did not change the initial stiffness of the cap. The deflection of the centre of the cap soffit increased linearly and remained in a small range, not more than $5\,mm$. The deflection suddenly increased after the onset of the yield stage, the point that was normally marked by the beginning of the maturing of the critical shear crack or the central bending crack on the front or back surfaces.

The deflection could be very large in the yield stage before the structure finally failed, implying the failure was rather ductile. This could either be because of the yield behaviour of

the longitudinal reinforcement in bending failure or a gradual softening of the compressive concrete strut in the shear failure. This proved that in structures of short shear span, even in the absence of shear reinforcement, shear cracking does not necessarily result in immediate failure (Regan, 1999). The ductile behaviour in pile caps with large transverse pile spacing may also be because of the cap's transverse behaviour *i.e.* the ductile behaviour of the transverse reinforcement which caused the cap to remain ductile even when the shear crack on the cap front and back surfaces appeared.

3.9.2 Failure type and failure load

The failure loads V_c and types for the pile caps in Batch 3 and 4 are listed in Table 3.5. The failure types were judged from the final crack distribution on the front and back surfaces.

The table shows that B3A1, B3A2, B4B1 and B4B2 failed by bending. B3A3, B4A1, B4A2, B4A3, B4B3 and B4B4 partially failed in shear because of asymmetric loading against front and back surfaces of pile caps (Table 3.5). This asymmetric loading was caused by the unavoidable unequal stiffness of the piles and the unequal stiffness of the front half and back half of the cap (Figure 3.9). B4A1 was the only case in which the cap failed by a diagonal tensile shear crack appearing on the back surface, since its longitudinal pile spacing was relatively large. Other caps partially failing in shear experienced compressive splitting shear failure. In B3A3, B4A3 and B4B4, mixed bending failure and shear failure was recorded.

In B4B4, the shear cracks on both front and back surfaces that caused a mixture of bending failure and shear failure matured very quickly at the end part of the experiment. The compressive splitting shear crack developed during the final loading steps (Figure 3.25) was deemed to be caused by the cyclic loading (unloading and reloading) during the end part of the experiment using the displacement control method (Figure 3.26). It sheds light on cap behaviour in bridge structures under the real traffic service, the load of which is cyclic, though it was not absolutely comparable to that.

B4A4 was the most ideally failed in shear in that the shear cracks were symmetrically distributed on both front and back surfaces, right and left sides. In B4A5, though the cap failed prematurely by Pile 3 (Figure 3.9) being crushed (Figure 3.15 (a)), based on the observation of the distribution and the large width of the compressive splitting shear crack, the obtained final failure load was deemed to be close to the cap's real shear capacity.

Judging from the width and distribution of shear cracks at failure step, it is concluded that the failure load and type of B3A3, B4A4, B4A5 and B4B4 were deemed to be well represented by the experiment. Other pile caps should have a higher shear capacity than the observed failure loads.

From Table 3.5, it is seen that for samples in Batch 3 Series A and Batch 4 Series A, the failure load or the shear capacity of pile caps increased with decreasing pile longitudinal spacing or with increasing shear enhancement factor. For samples in Batch 4 Series B, the failure load or the shear capacity increased with increasing transverse pile spacing.

As discussed in Section 3.9.1, transverse cracks along the two edges of the wall loading indicated potential localised crushing failure of concrete under the loading. The transverse bending crack and punching shear crack on the cap soffit indicated potential bending failure in the transverse direction and punching shear failure of the pile. These failure types, however, were not actually observed in any sample.

3.9.3 Influence of reduced reinforcement ratio on a cap's shear behaviour

One purpose of the reduced reinforcement ratio of the caps in Series B (Section 3.3, Section 3.4.2) was to investigate how the amount of longitudinal reinforcement influences the cap shear behaviour.

B4A2 and B4B1 had the same dimensions, and the difference in the concrete cube strength is small (Table 3.4). It is concluded that the failure types differed between the two caps (Table 3.5) only because of the reduction of the diameter of the longitudinal reinforcement from $12\,mm$ in B4A2 to $10\,mm$ in B4B1 (reduction of the reinforcement ratio from 1.137% to 0.786%) (Table 3.3(b)). The potential failure type for B4A2 was compressive splitting shear failure on both front and back surfaces while B4B1 failed by bending. This indicated that the influence of the longitudinal reinforcement ratio on the bending capacity of pile caps was bigger than on the shear capacity. This is consistent with the bending and shear design formulae in British Standards, in which A_s in bending design has a power order of 1, while in the shear design it has only a power order of 1/3. The influence of the reduction of the transverse reinforcement was not considered.

3.10 Summary

A series of experiments were designed to investigate the influence of the shear enhancement factor $\frac{2d}{a_v}$, the shear enhancement application factor A and the reinforcement ratio on the pile cap shear behaviour and capacity. The former two are the key parameters causing the discrepancy between BS8110 and BS5400.

17 four-pile caps in reduced scale were tested in the laboratory. The design of the sample dimensions, the load pattern, the pile type, the support condition and the experimental

procedure was constrained by the practical conditions in the laboratory. PIV was involved into the experimental procedure by means of a set up with a digital camera. More details of this technique are given in Chapter 4.

The nine samples in Batch 4 were deemed as effective in that most of them failed in shear, though the previous eight in Batches 1, 2 and 3 contributed valuable lessons to make Batch 4 successful. Samples in Batch 4 showed a variety of shear failure types from diagonal tensile shear failure to compressive splitting shear failure judged from the crack distribution and propagation on the cap front and back surfaces.

The crack distribution and propagation on the cap front and back surfaces suggested that the pile cap under full-length wall loading seemed to behave in shear as a 1-way spanning deep beam. However, based on the cracks on the cap top, right and left surfaces and the cap soffit and the punching shear cracks appearing around the individual piles, there were evidences that it actually behaved as 2-way. This is especially true in Batch 4 Series B samples, those with wider transverse pile spacing in which reinforcement in transverse direction took part in the shear resistance.

The failure loads of samples in Batch 3 and 4 gave a certain conclusion that the shear capacity of the pile cap was a function of the pile longitudinal and transverse pile spacing. The failure load increased with the decreasing longitudinal pile spacing and the increasing transverse pile spacing. The influence of the reinforcement ratio on the pile cap shear capacity was smaller than on the pile cap bending capacity. A more detailed analysis of the shear capacity of the experimental pile caps is given in Chapter 6.

Table 3.1 Development and major changes in all batches of samples tested

Pile cap No.	Pile constitution	Pile cast into or separated to the cap	Why not successful?	Improvements made for the following batches
Batch 1	Unreinforced concrete; Being surrounded by plastic sleeve.	Separated	Bending and shear capacity was higher than the capacity of the testing machine	Reduced cap depth to reduce the cap's failure load.
Batch 2	Unreinforced concrete; Not being surrounded by plastic sleeve.	Separated	Bending and shear capacity were still higher than the capacity of the testing machine; Pile crushed in some samples during the experiments.	Further reduced cap dimensions; Pile was to be reinforced and designed to be cast into the cap body; Bedding material was to be applied between the pile base and the steel platten; Reduced concrete design strength.
Batch 3	Reinforced concrete.	Cast into cap	Bending failure happened before the shear failure; Pile base was restrained against moving freely by friction with steel platten.	Further reduced cap dimensions to increase the possibility that shear failure happens ahead of the bending failure; Oil was to be pasted between the pile base and the steel platten.
Batch 4	Reinforced concrete.	Cast into cap	N/A	N/A

Table 3.2 Methods to reduce the shear capacity more quickly than the bending capacity of the pile cap

Pile cap No.	Concrete design strength f_{cu} (MPa)	$\frac{2d}{a_v}$	d (mm)	b (mm)	Pile cast or separated to the cap	Reinforcement ratio ρ (%)	BS8110 shear prediction (kN)	BS5400 shear prediction (kN)	External force when predicted bending failure happens (kN)	Actual failure load (kN)	Failure type
B1A1	30	1.89	400	800	Separated	0.613	650.4	524.7	946	>1440	No failure
B2A1	30	1.33	300	600	Separated	0.841	300.2	277.7	649	>1440	No failure
B3A1	20	1.33	300	600	Cast into cap	0.841	262.3	242.6	462	960	Bending failure
B4A1	20	1.28	230	500	Cast into cap	1.137	185.7	175.4	309	592	Partial shear failure

Table 3.3 Sample dimensions and reinforcement arrangement (a)

Pile cap No.	Pile cap depth h (mm)	Effective cap depth d (mm)	Pile cap length l (mm)	Pile cap width b (mm)	Pile diameter h_p (mm)	Longitudinal pile spacing kh_p (mm)	Transverse pile spacing kh_w (mm)	Wall loading width h_c (mm)
B1A1	400	369	1500	800	200	1100	400	200
B2A1	300	269	1500	600	150	1100	300	200
B2A2	300	269	1250	600	150	850	300	200
B2A3	300	269	1150	600	150	750	300	200
B2A4	300	269	1050	600	150	650	300	200
B3A1	300	269	1500	600	150	1100	300	200
B3A2	300	269	1250	600	150	850	300	200
B3A3	300	269	1150	600	150	750	300	200
B4A1	230	199	1100	500	130	800	300	100
B4A2	230	199	950	500	130	650	300	100
B4A3	230	199	850	500	130	550	300	100
B4A4	230	199	800	500	130	500	300	100
B4A5	230	199	700	500	130	400	300	100
B4B1	230	200	950	500	130	650	300	100
B4B2	230	200	950	650	130	650	450	100
B4B3	230	200	950	750	130	650	550	100
B4B4	230	200	950	900	130	650	700	100

Table 3.3 Sample dimensions and reinforcement arrangement (b)

Pile cap No.	Reinforcement ratio ρ (%)	Ratio of the transverse pile spacing over pile diameter $n\left(=\frac{kh_w}{h_p}\right)$	Shear enhancement factor $\frac{2d}{a_v}$	Shear enhancement application factor A	
				BS8110	BS5400
B1A1	0.613	2.00	1.89	1	0.5
B2A1	0.841	2.00	1.33	1	0.5
B2A2	0.841	2.00	1.92	1	0.5
B2A3	0.841	2.00	2.34	1	0.5
B2A4	0.841	2.00	2.99	1	0.5
B3A1	0.841	2.00	1.33	1	0.5
B3A2	0.841	2.00	1.92	1	0.5
B3A3	0.841	2.00	2.34	1	0.5
B4A1	1.137	2.31	1.28	1	0.52
B4A2	1.137	2.31	1.69	1	0.52
B4A3	1.137	2.31	2.14	1	0.52
B4A4	1.137	2.31	2.47	1	0.52
B4A5	1.137	2.31	3.59	1	0.52
B4B1	0.786	2.31	1.69	1	0.52
B4B2	0.786	3.46	1.69	0.908	0.40
B4B3	0.786	4.23	1.69	0.787	0.347
B4B4	0.786	5.38	1.69	0.67	0.29

Table 3.4 Concrete and reinforcement properties

Pile cap No.	28 days concrete characteristic cube strength (N/mm^2)	Real concrete cube compressive strength at 28 days or on the day of test f_{cu} (N/mm^2)	Reinforcement diameter (mm)	Reinforcement mean yield strength f_y /peak strength (N/mm^2)
B1A1	30	38.7	12(T12)	547/646
B2A1	30	50.2	12(T12)	547/646
B2A2	30	49.5	12(T12)	547/646
B2A3	30	48.8	12(T12)	547/646
B2A4	30	45.1	12(T12)	547/646
B3A1	20	32.0	12(T12)	547/646
B3A2	20	32.0	12(T12)	547/646
B3A3	20	32.0	12(T12)	547/646
B4A1	20	20.3	12(T12)	547/646
B4A2	20	21.8	12(T12)	547/646
B4A3	20	24.3	12(T12)	547/646
B4A4	20	24.4	12(T12)	547/646
B4A5	20	23.0	12(T12)	547/646
B4B1	20	19.5	10(T10)	547/646
B4B2	20	25.6	10(T10)	547/646
B4B3	20	24.7	10(T10)	547/646
B4B4	20	21.0	10(T10)	547/646

Table 3.5 Failure load and failure type for experimental samples in Batch 3 and 4

Pile cap No.	Failure load $V_c\,(kN)$	Failure type from front and back surfaces	Symmetric or asymmetric loading against front and back surfaces of pile caps	Failure type of models in FEA for experimental samples
B3A1	965	Bending failure on front and back surfaces	Symmetric	N/A
B3A2	1226	Bending failure on front and back surfaces	Symmetric	N/A
B3A3	1395	Mixture of bending failure on both front and back surfaces and compressive splitting shear failure on front surface right side and back surface right side	Asymmetric	N/A
B4A1	592	Diagonal tensile shear failure on back surface left side	Asymmetric	Shear failure with wide bending crack
B4A2	548	Compressive splitting shear failure on back surface left side	Asymmetric	Bending failure with wide compressive splitting shear crack
B4A3	919	Mixture of compressive splitting shear failure on front surface right side and bending failure on back surface	Asymmetric	Bending failure with wide compressive splitting shear crack
B4A4	1052	Compressive splitting shear failure on left side on front surface and right side on back surface	Symmetric	Compressive splitting shear failure with wide bending crack
B4A5	1244	Compressive splitting shear failure on front surface right side/pile crushing	Symmetric	Compressive splitting shear failure/pile crushing
B4B1	622	Bending failure with widely opened shear crack on both front and back surfaces	Symmetric	Compressive splitting shear failure with wide bending crack
B4B2	713	Bending failure on both surfaces	Symmetric	Bending failure with wide compressive splitting shear crack
B4B3	769	Compressive splitting shear failure on front surface	Asymmetric	Bending failure with wide compressive splitting shear crack
B4B4	1048	Mixture of bending failure and compressive splitting shear failure on front surface left side and back surface both sides	Asymmetric	Bending failure with wide compressive splitting shear crack

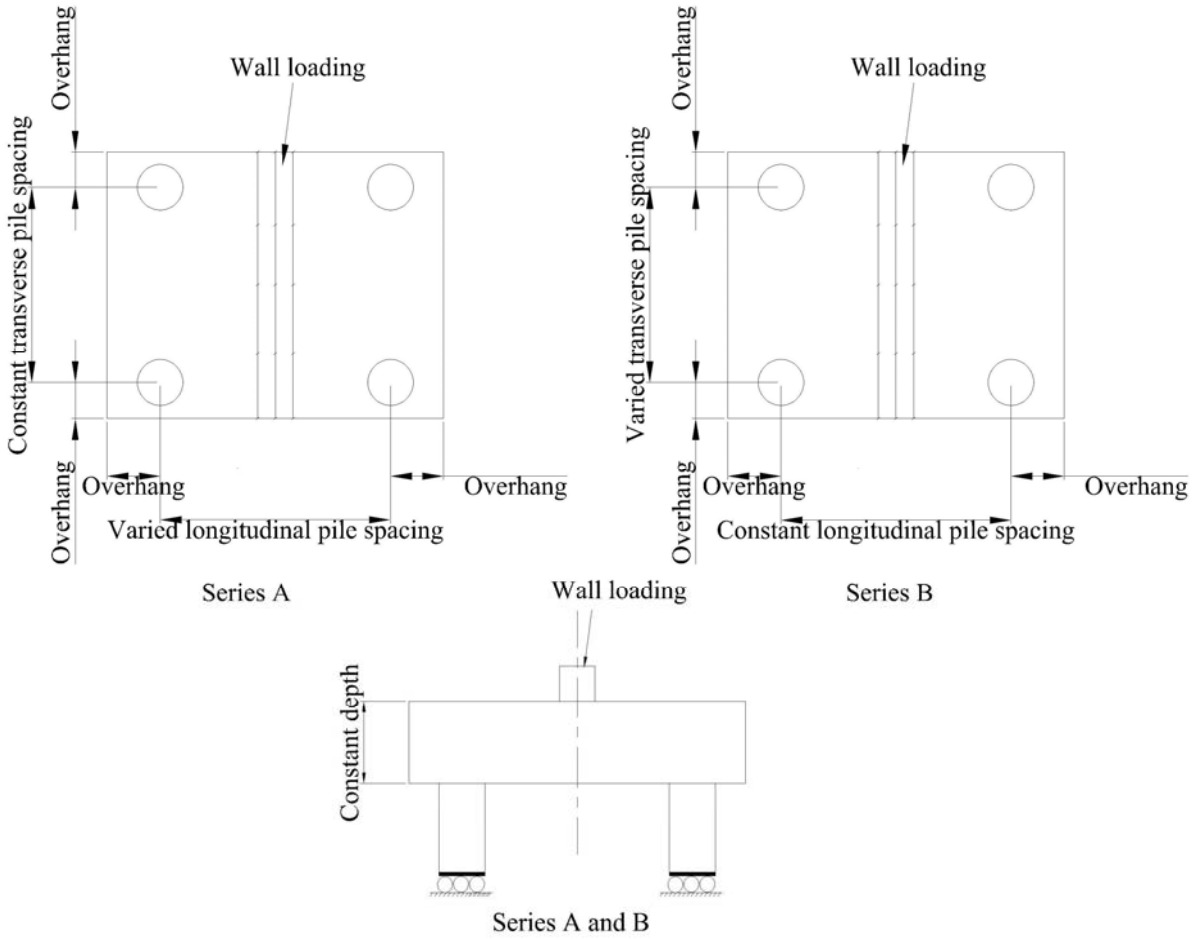

Figure 3.1 Design strategy for sample dimensions

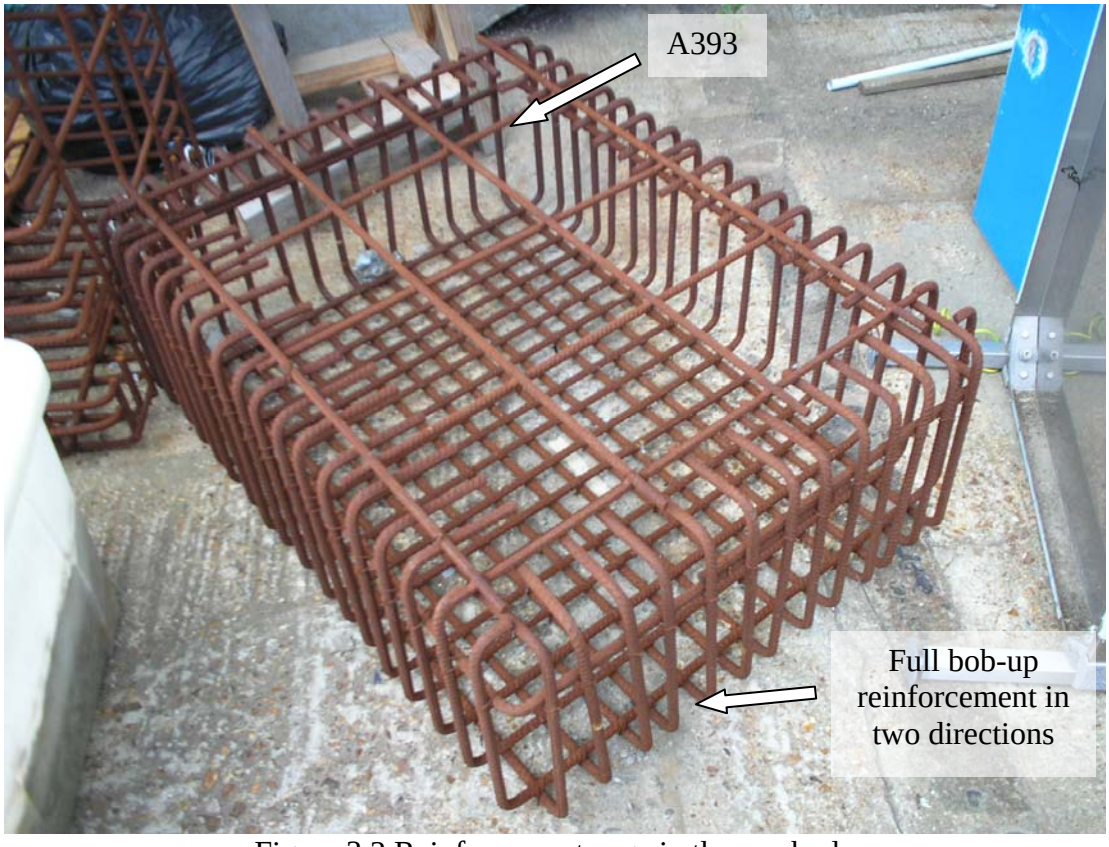

Figure 3.2 Reinforcement cage in the cap body

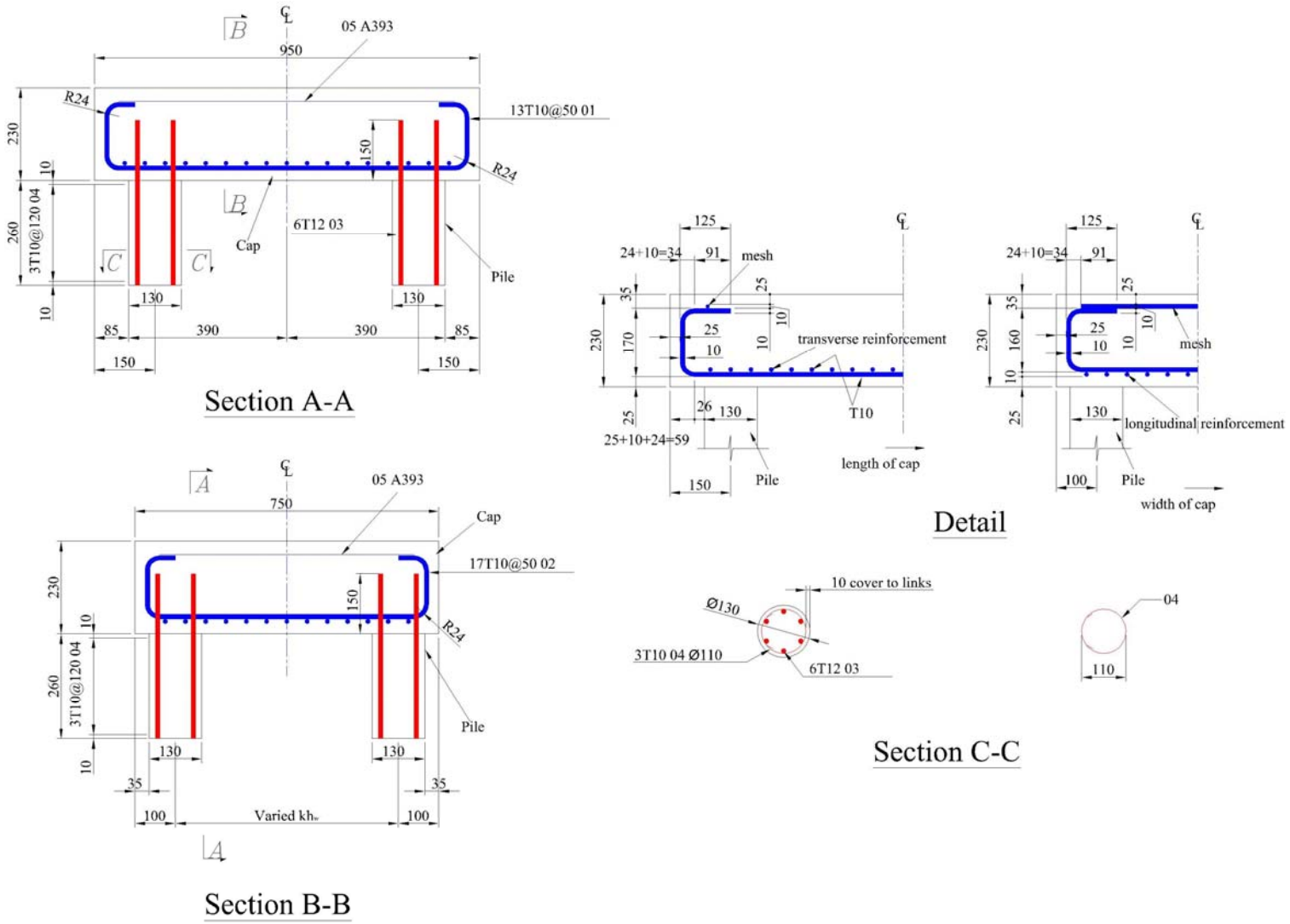

Figure 3.3 A reference of reinforcement details (Batch 4 Series B, all in *mm*)

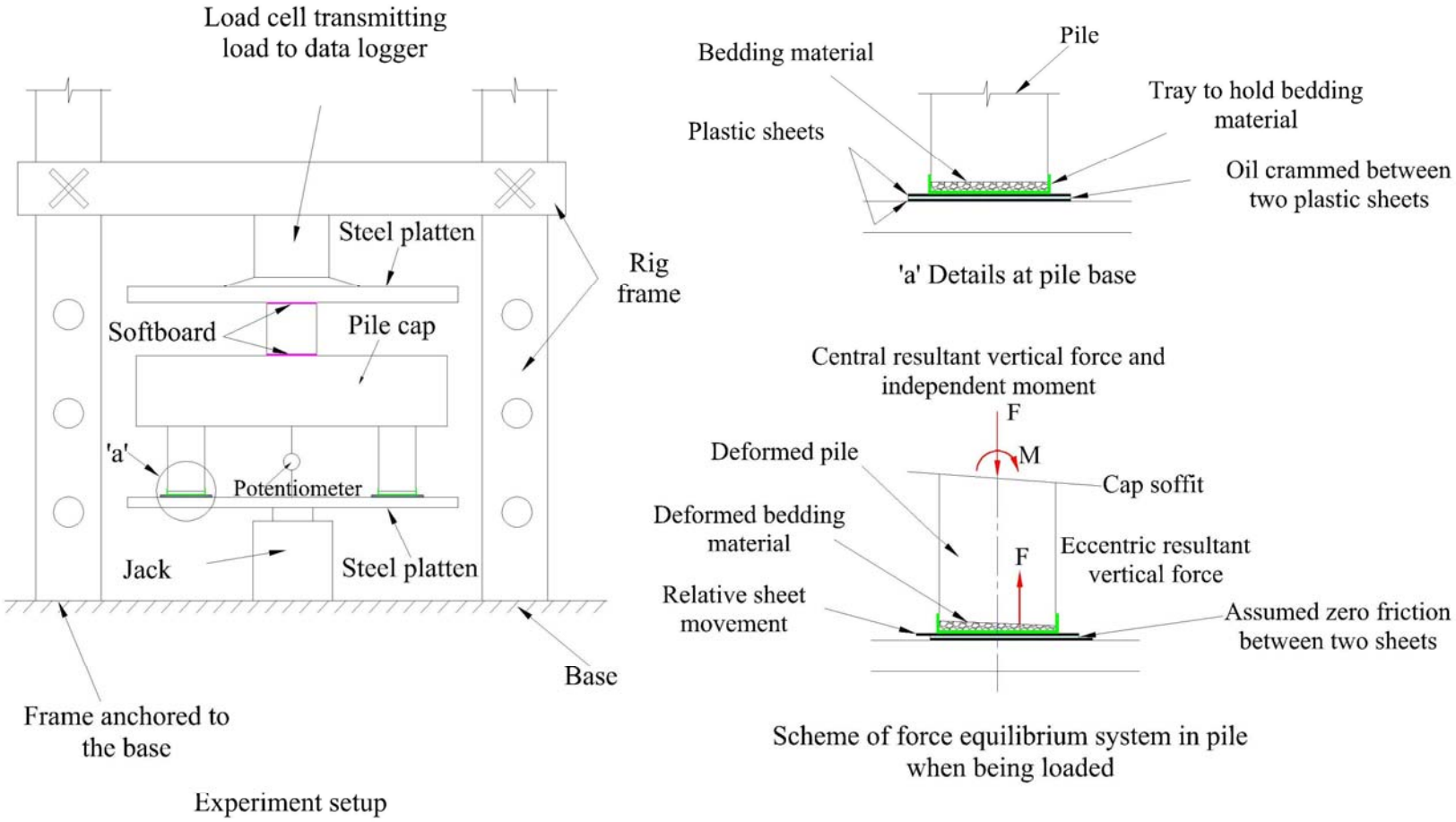

Figure 3.4 Experiment setup and Batch 4 pile boundary condition

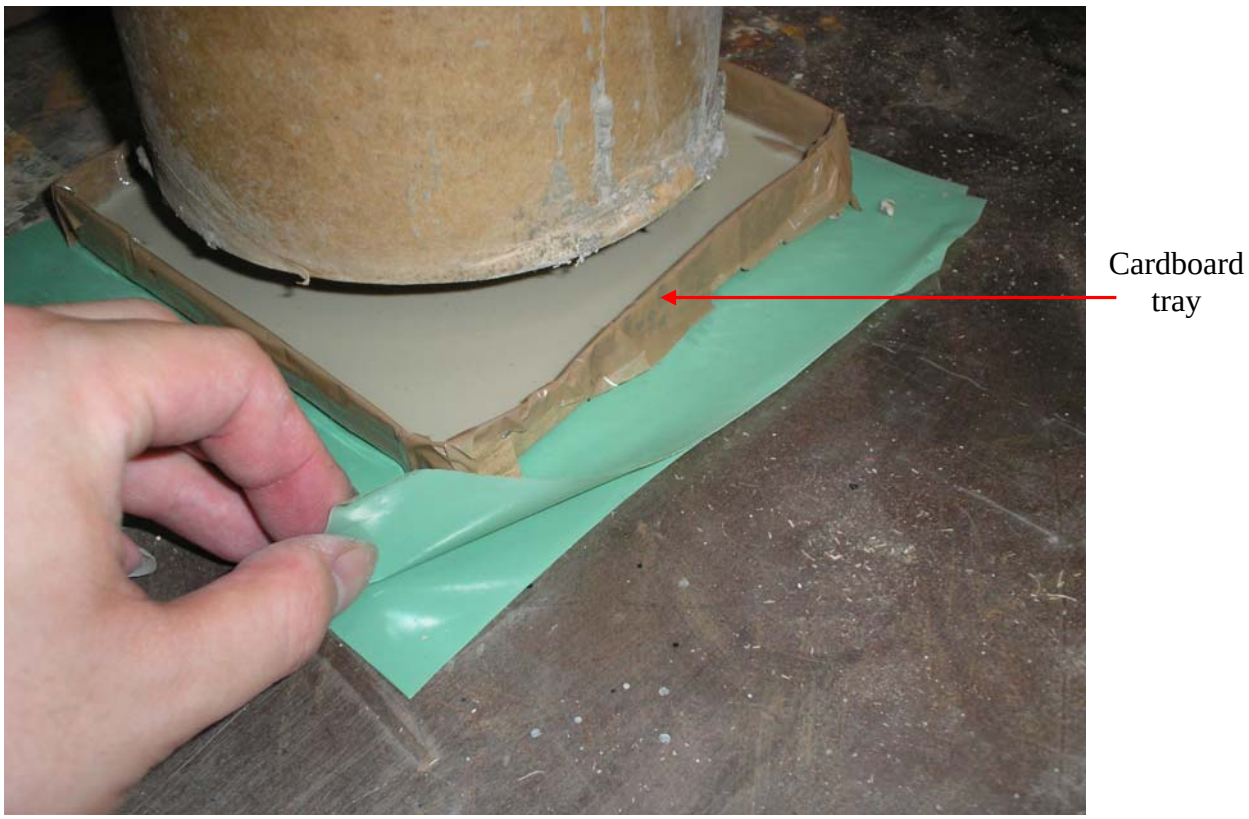

(a) Cardboard tray holding the bedding material

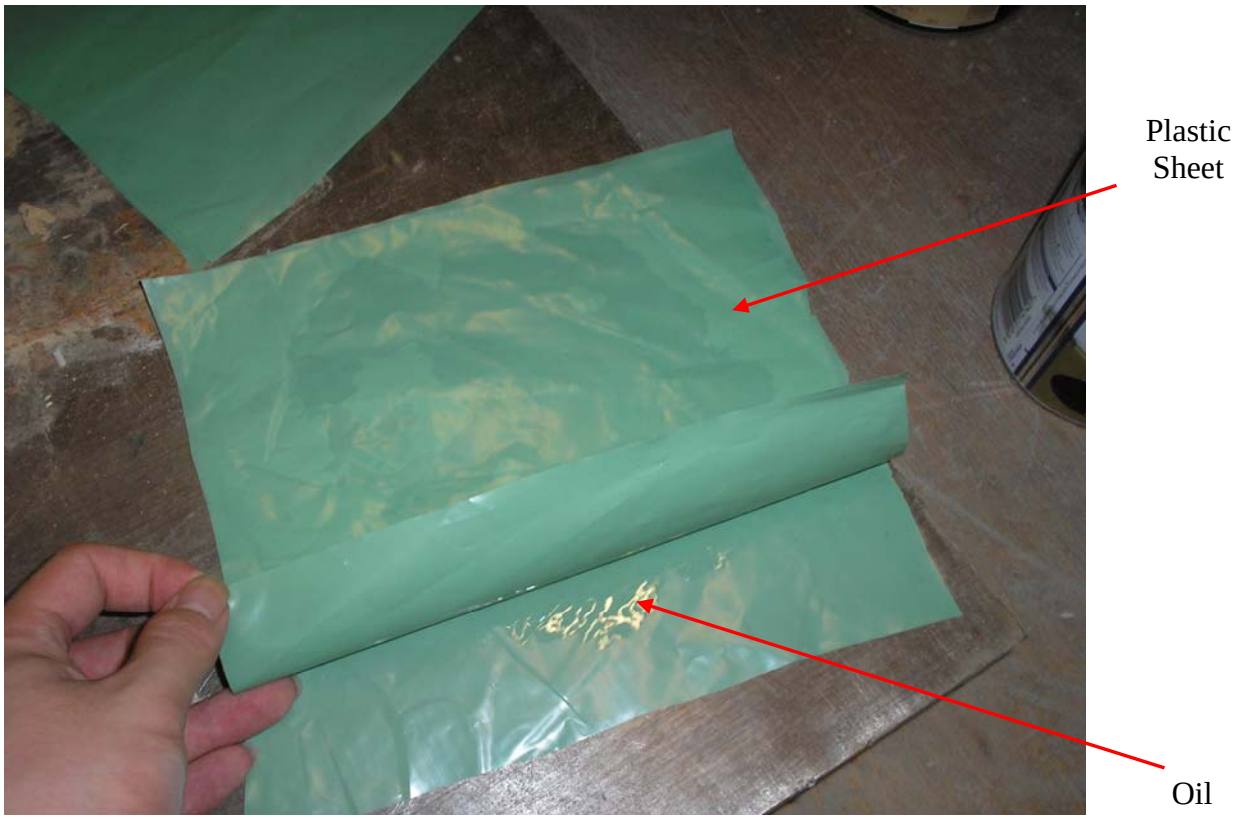

(b) Plastic sheet crammed with oil

Figure 3.5 Treatment for the pile support condition in Batch 4

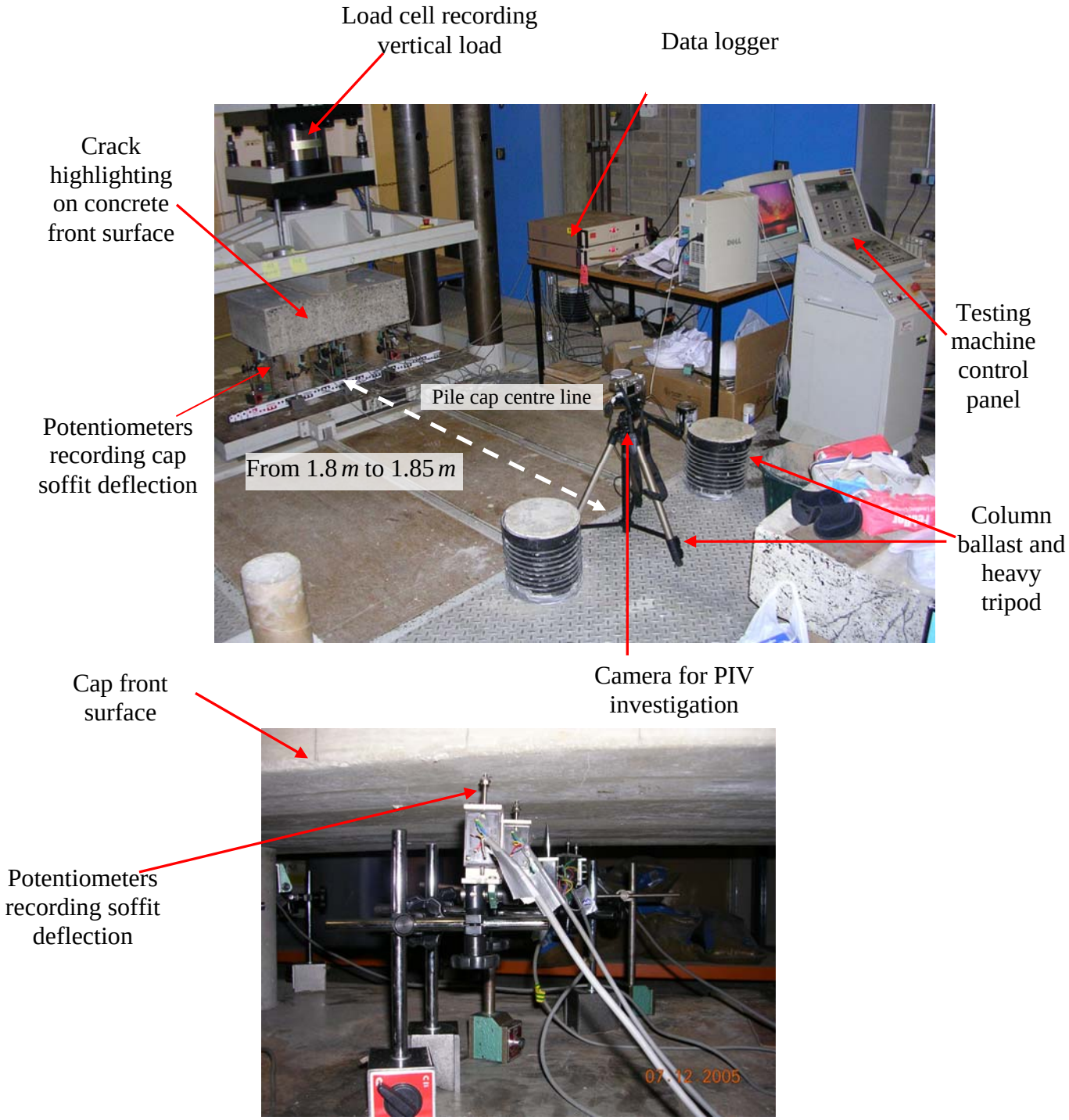

Figure 3.6 Panorama of the instrumentation setup

Cap back surface

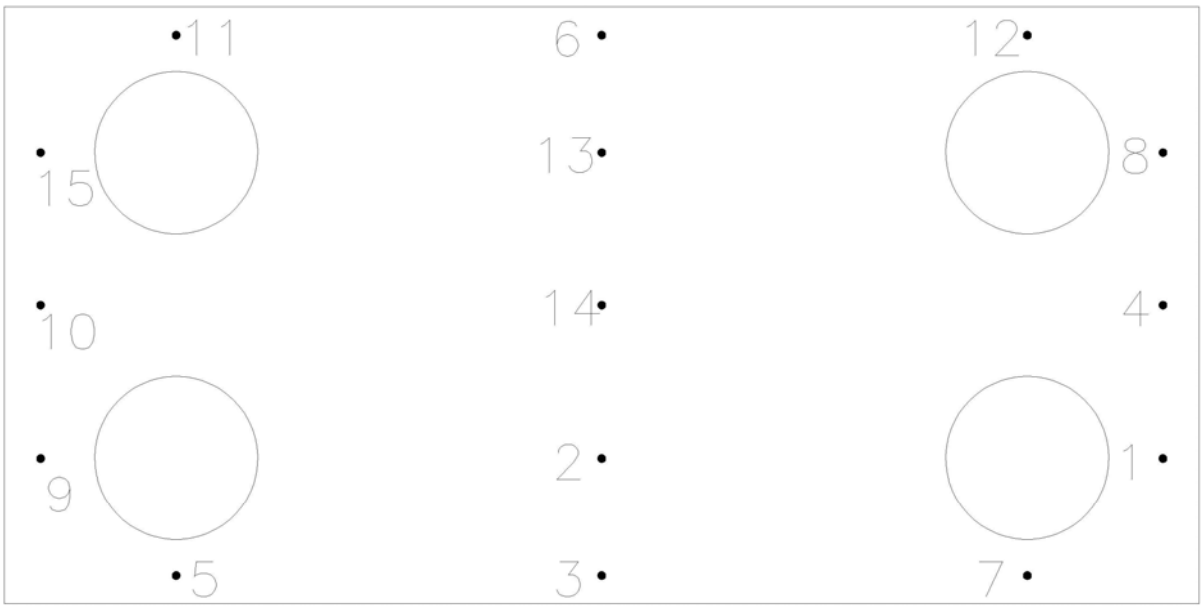

Cap front surface

Figure 3.7 Configuration of the potentiometers on cap soffit (plan view)

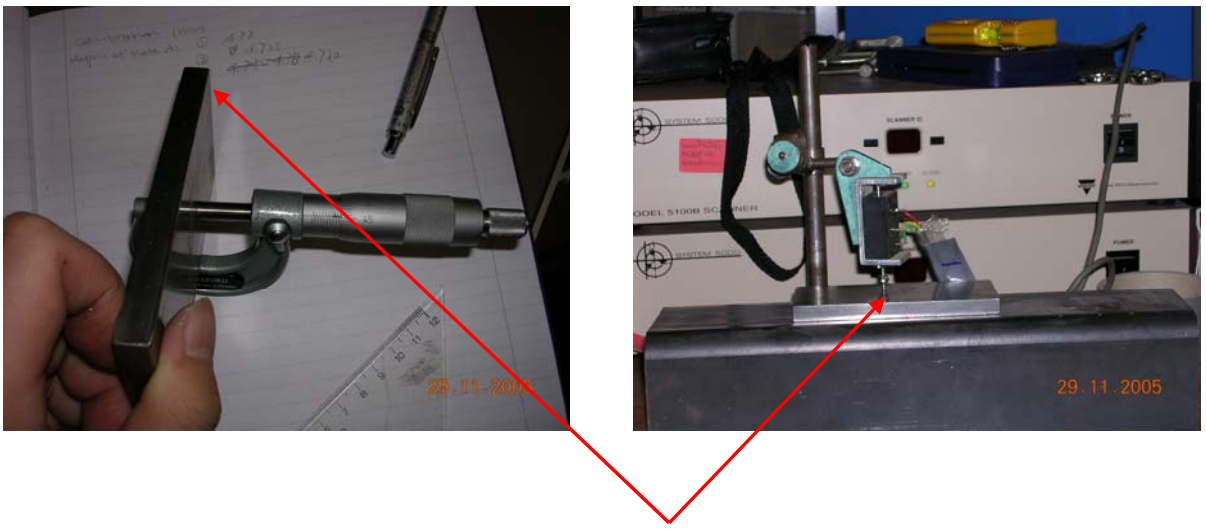

Steel plate with known thickness

Figure 3.8 Potentiometer calibration

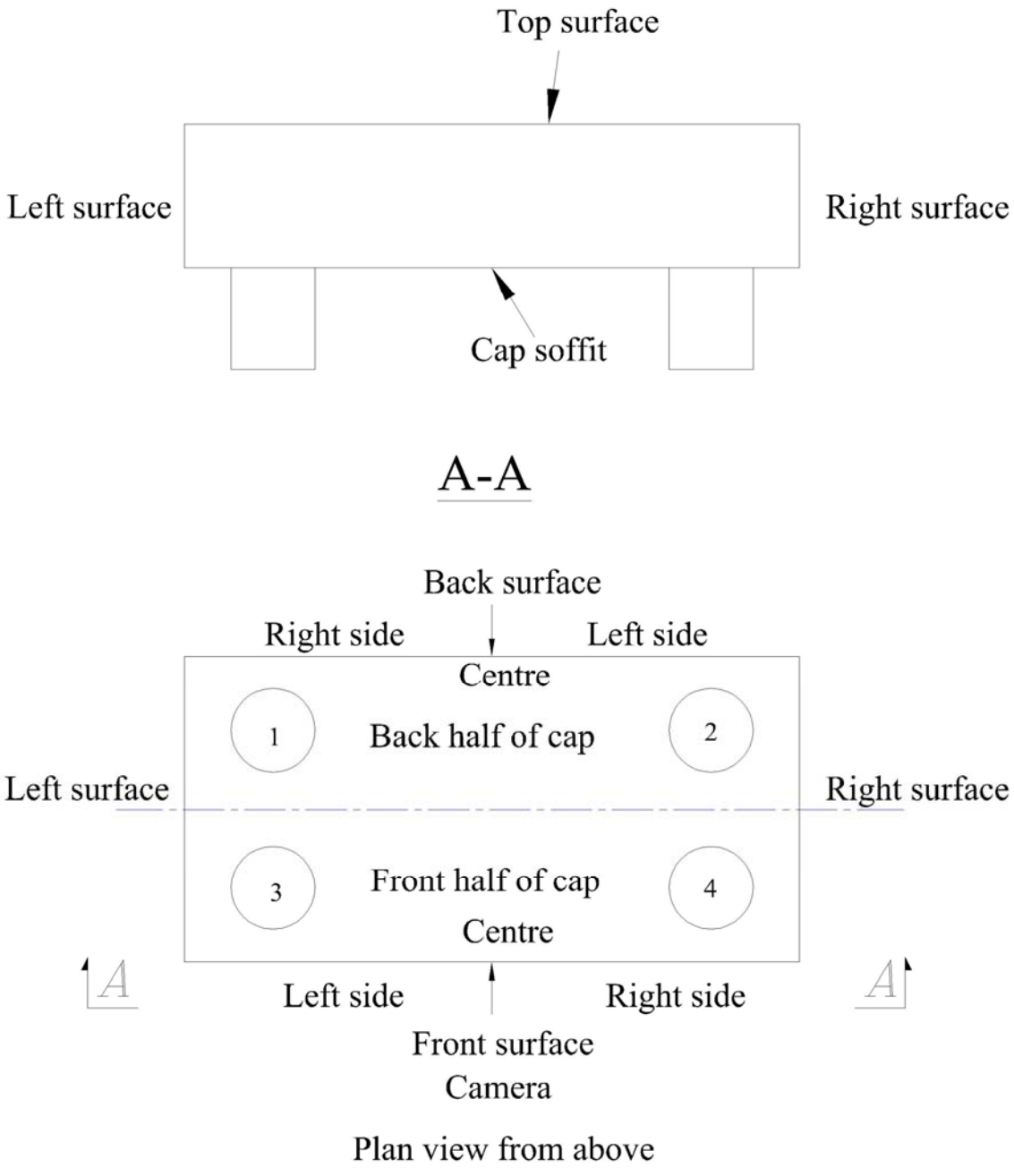

Figure 3.9 Terminologies for describing the crack distribution and propagation

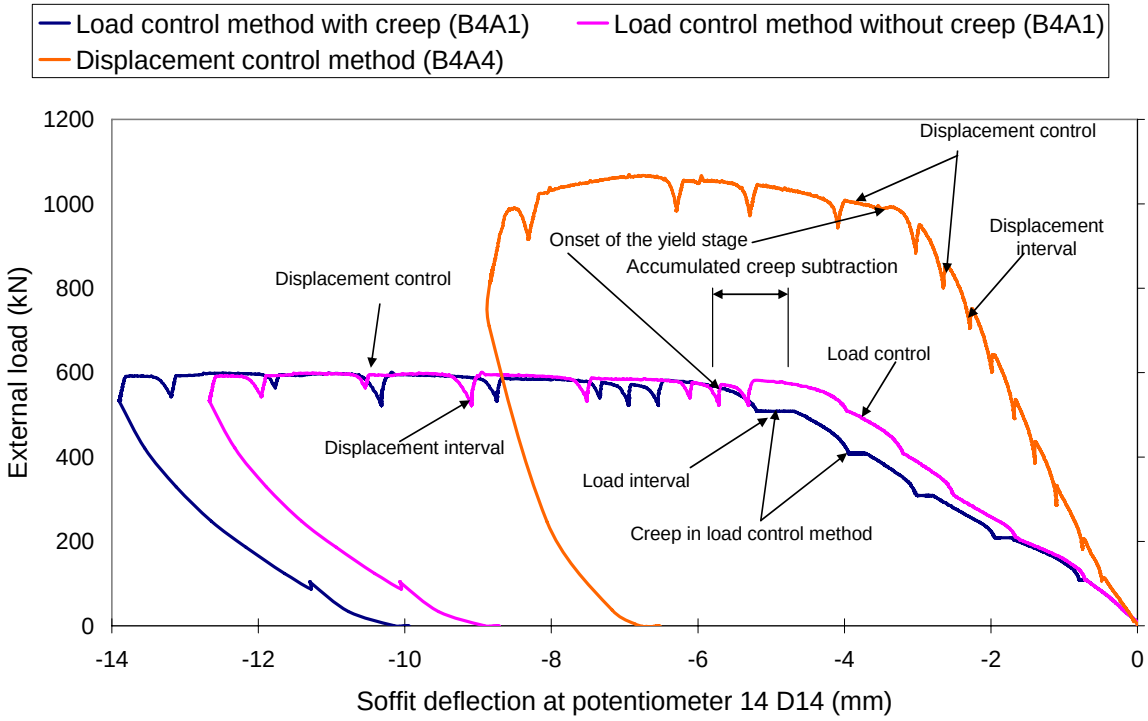

Figure 3.10 Load-displacement curve before and after creep subtraction from two loading methods

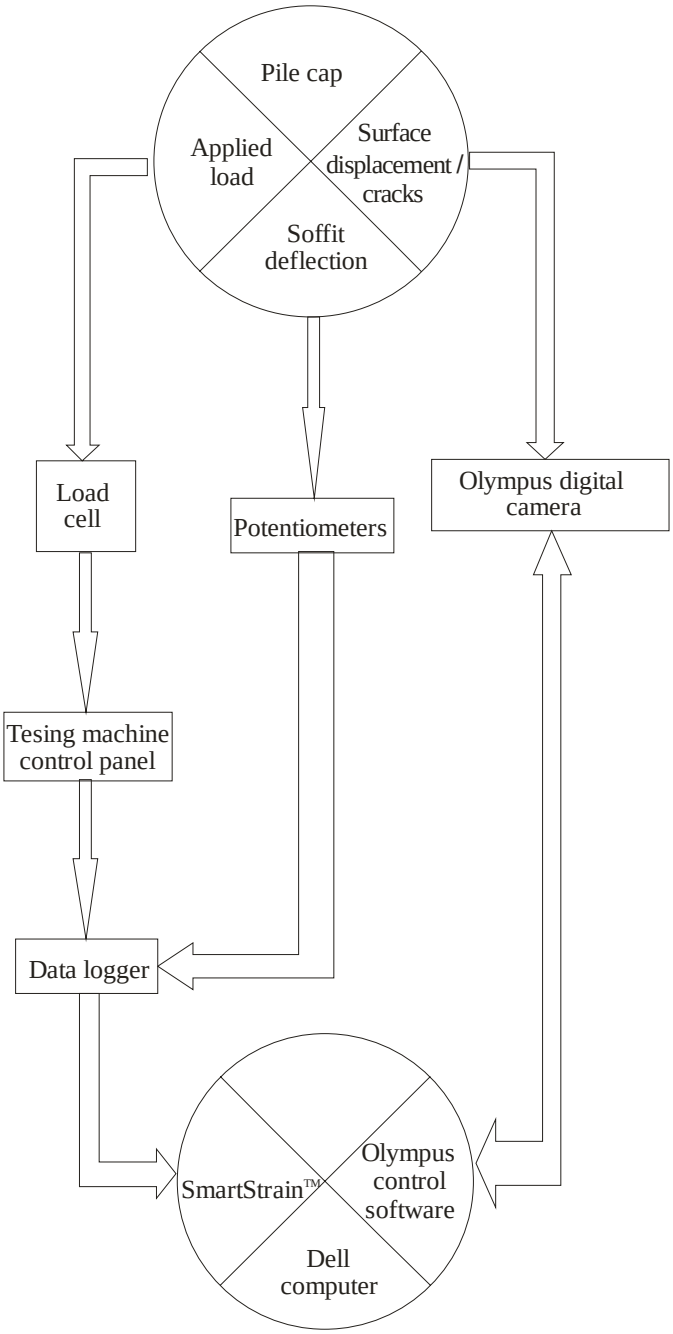

Figure 3.11 Data transmitting system

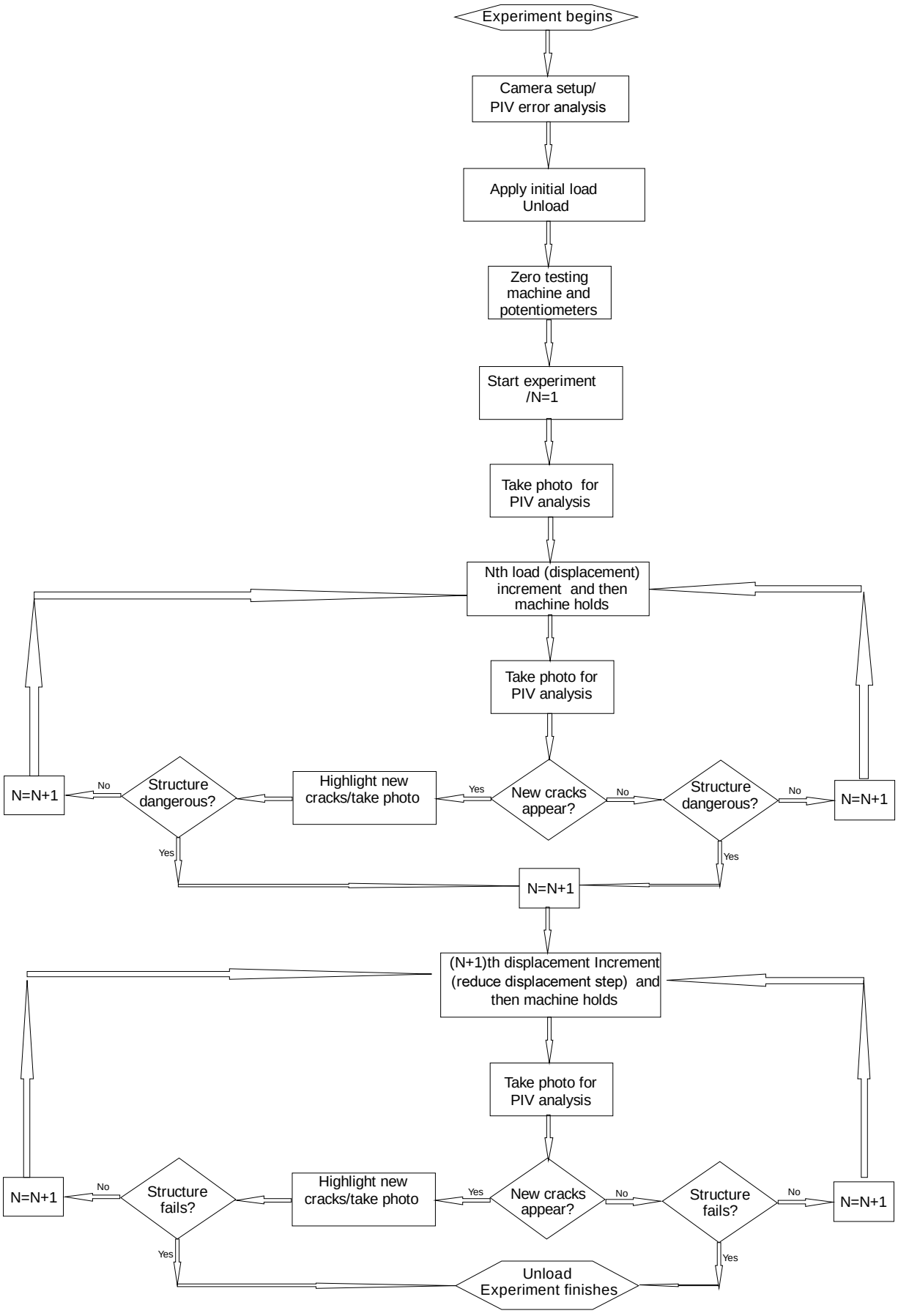

Figure 3.12 Experiment procedure of the load control method (displacement control method)

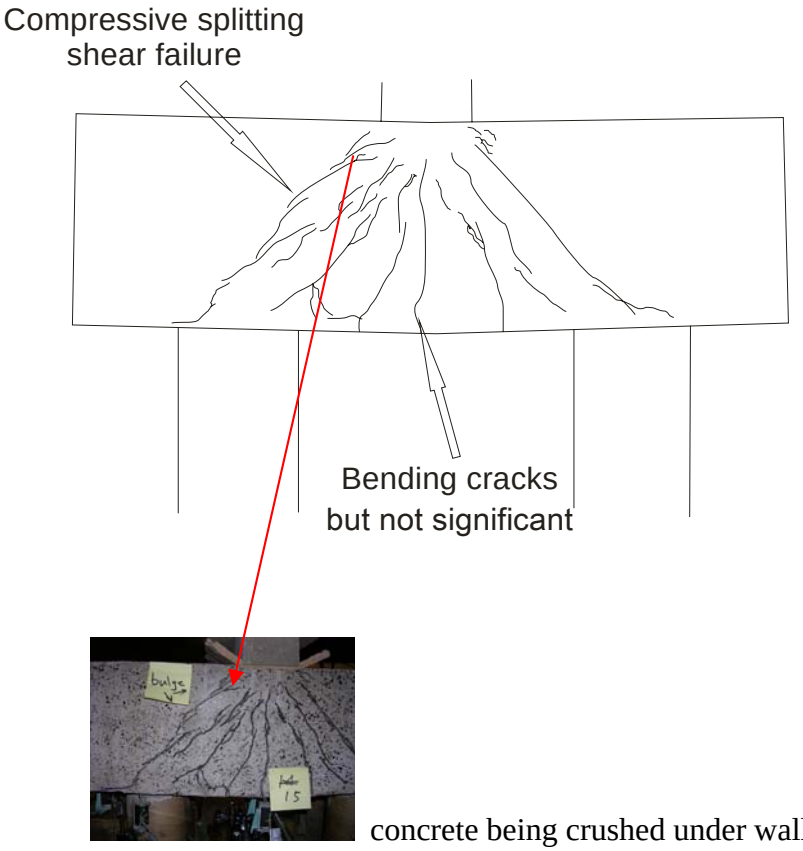

Figure 3.13 Crack distribution on B4A4 front surface at failure step

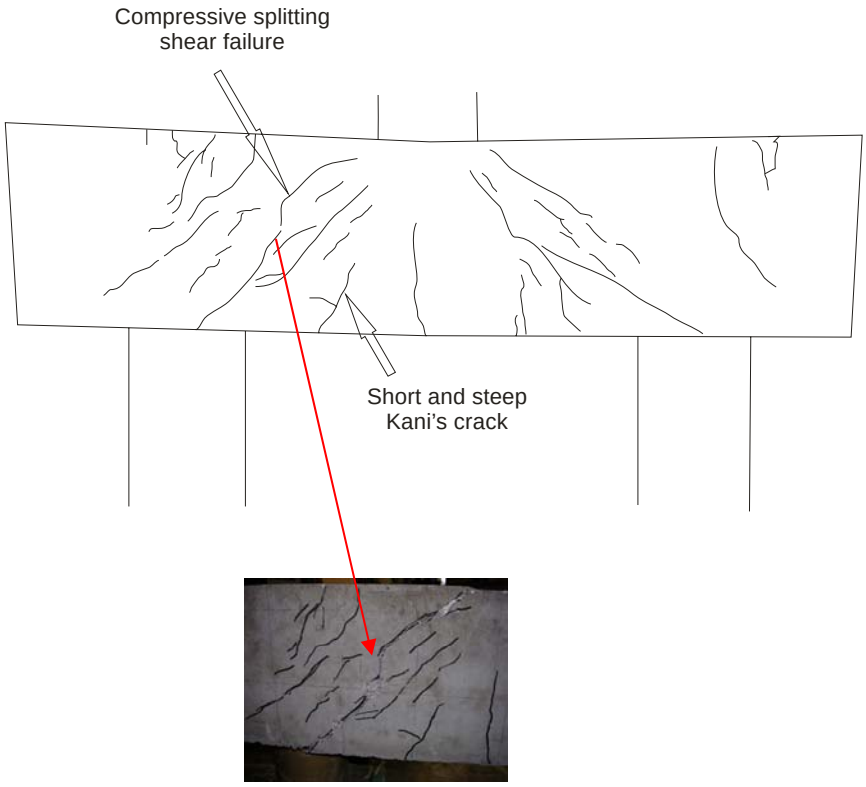

Figure 3.14 Crack distribution on B4A2 back surface at failure step

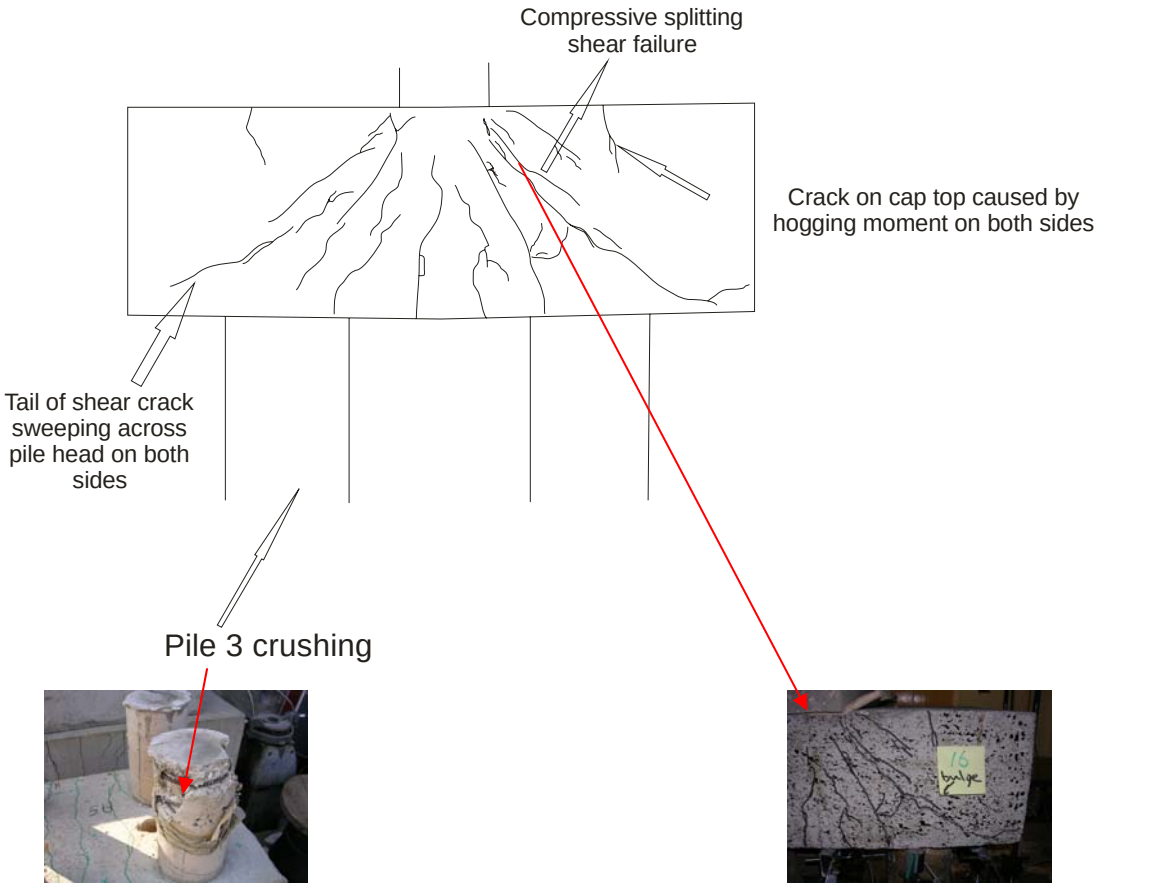

(a) Front surface

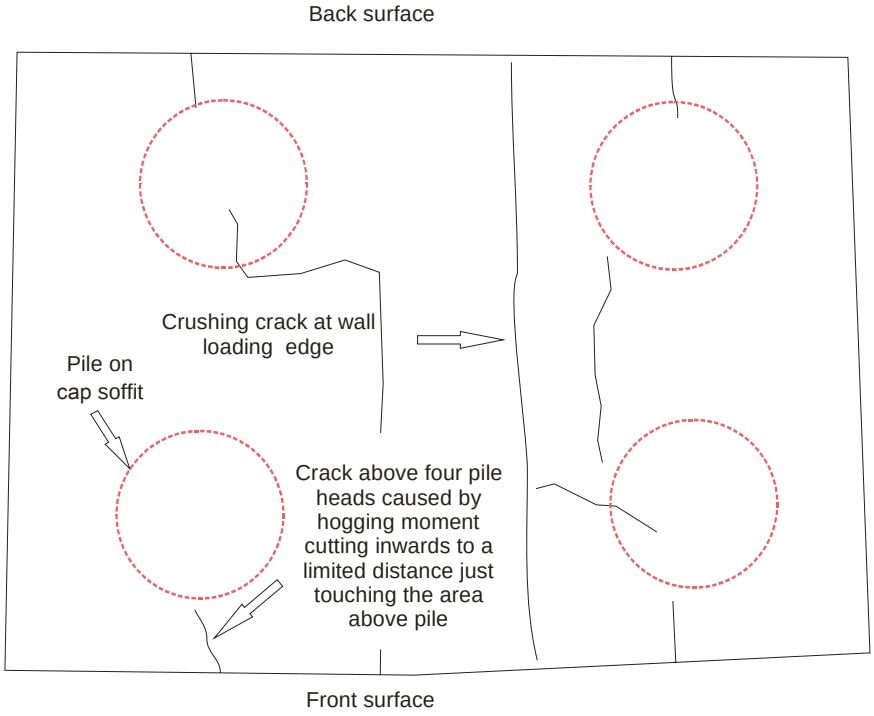

(b) Top surface

Figure 3.15 Crack distribution on B4A5 at failure step

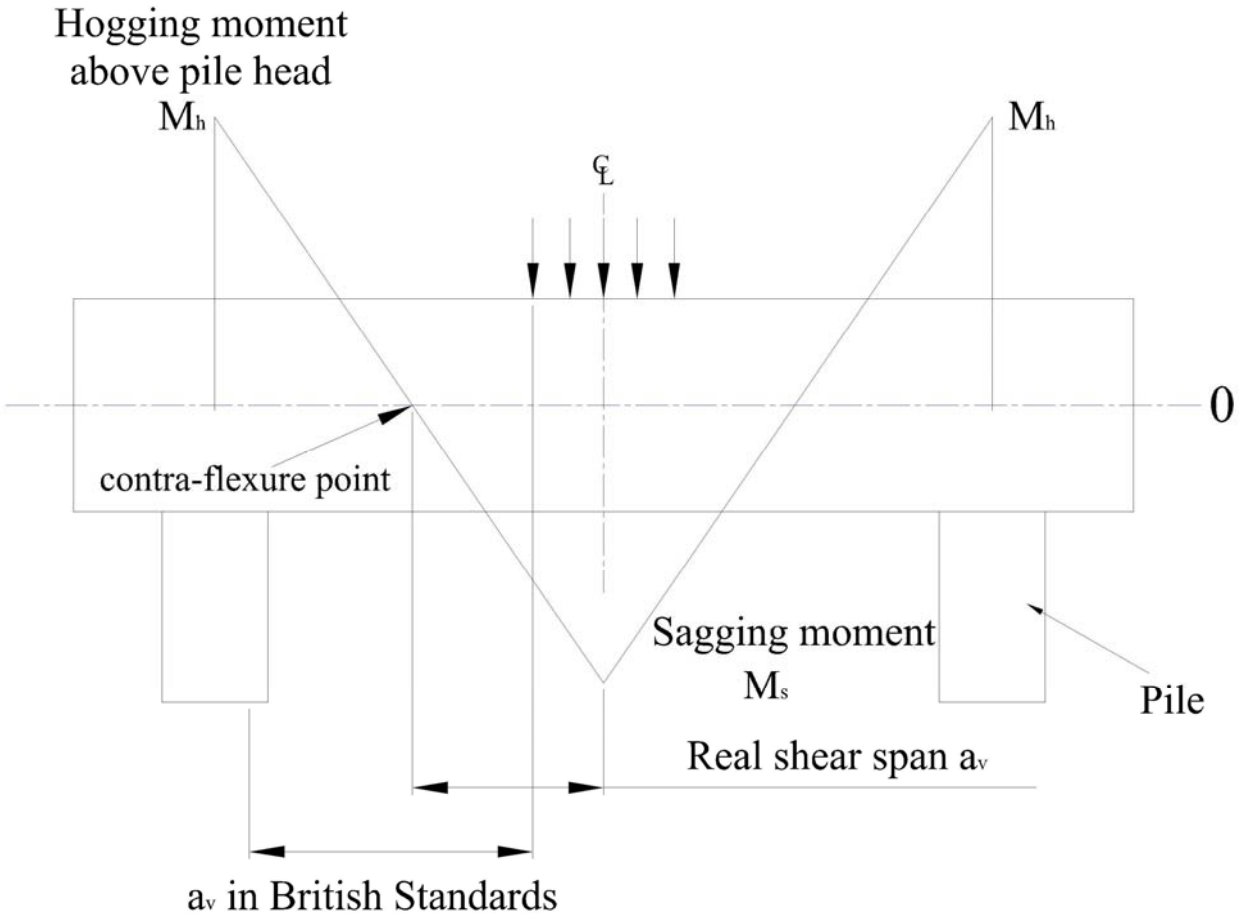

Figure 3.16 Shear span in the cap with hogging moment above pile head

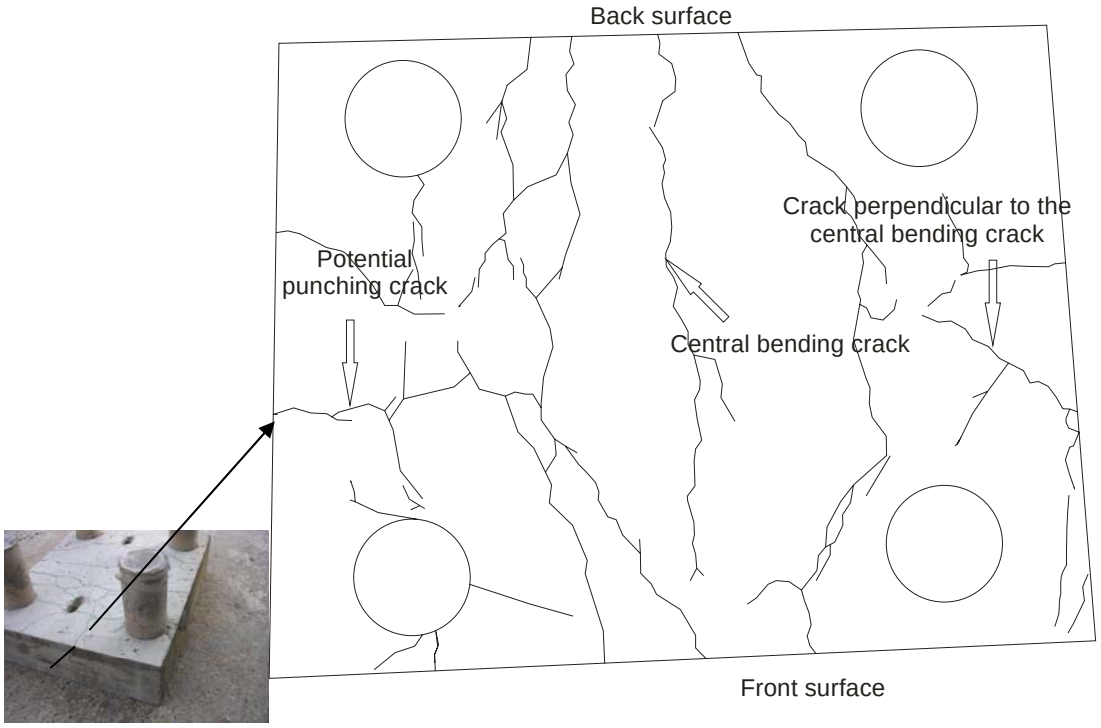

Inclined punching crack on right surface

Figure 3.17 Crack distribution on B4B3 cap soffit at failure step

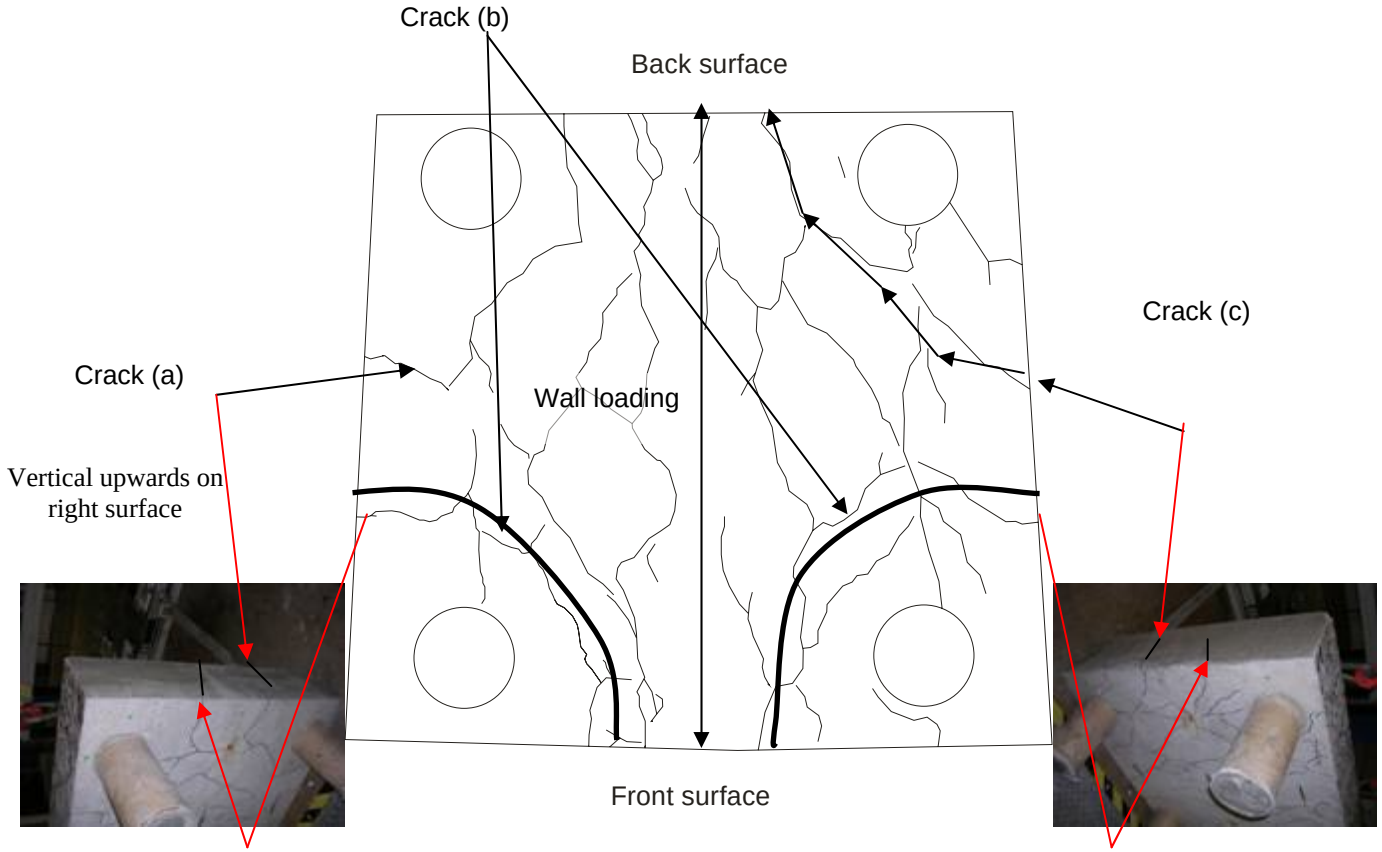

Inclined punching crack on right surface

Inclined punching crack on left surface

Figure 3.18 Crack distribution on B4B4 cap soffit at failure step

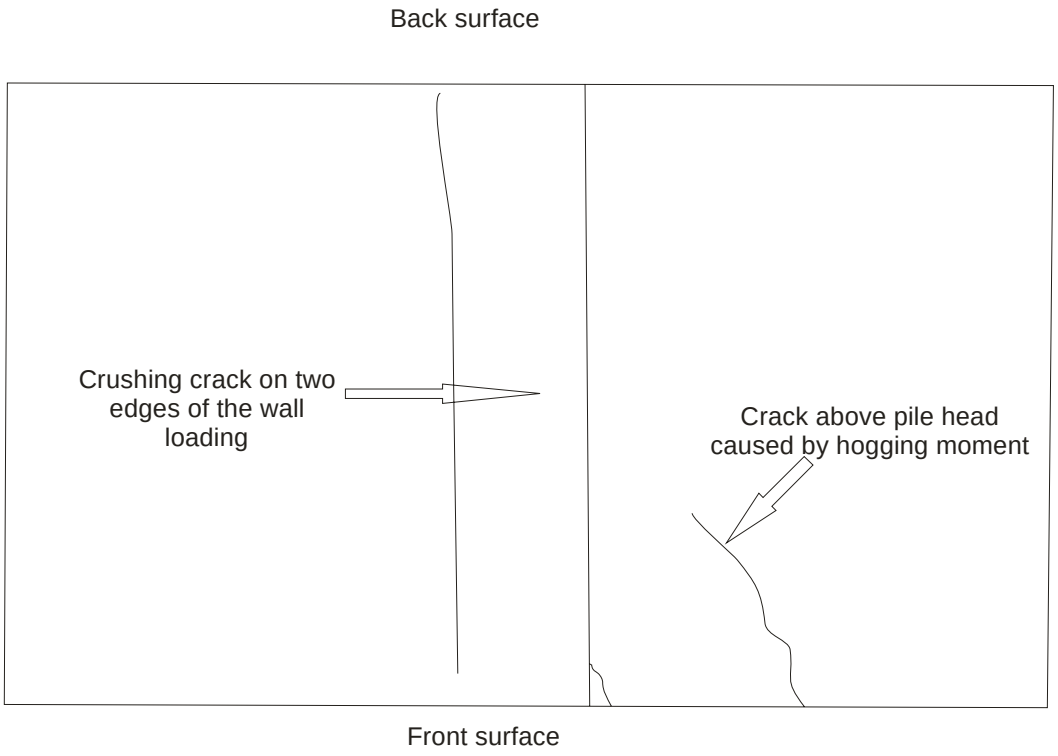

Figure 3.19 Crack distribution on B4A3 top surface at failure step

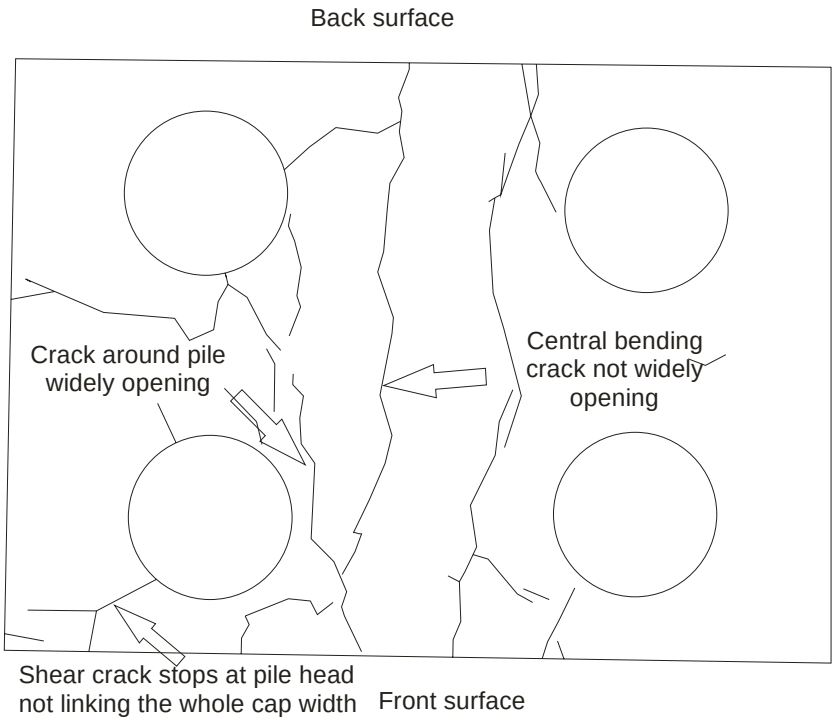

Figure 3.20 Crack distribution on B4A5 cap soffit at failure step

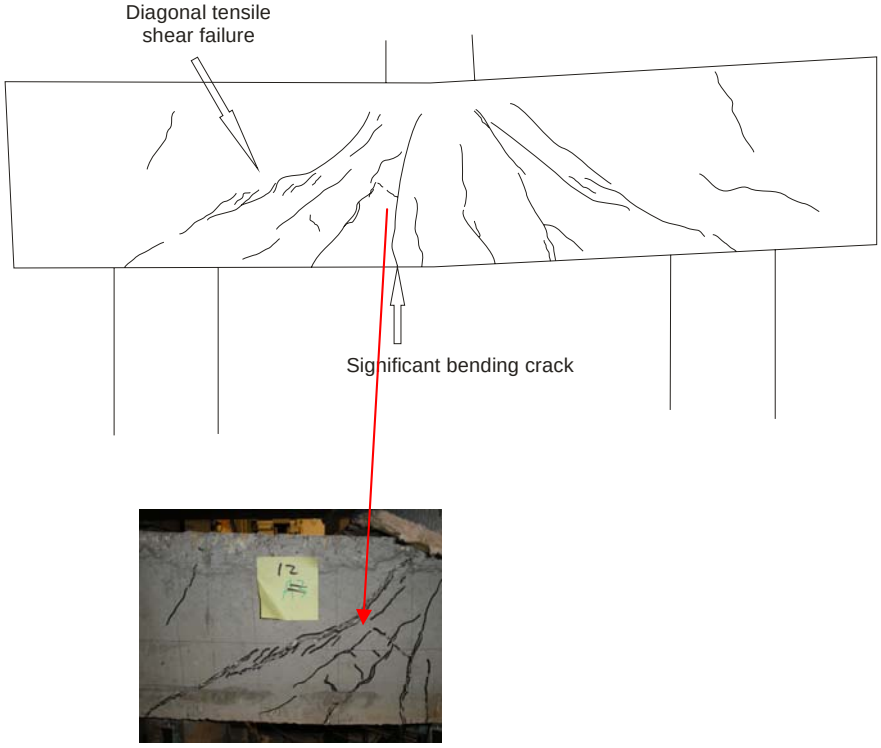

Figure 3.21 Crack distribution on B4A1 back surface at failure step

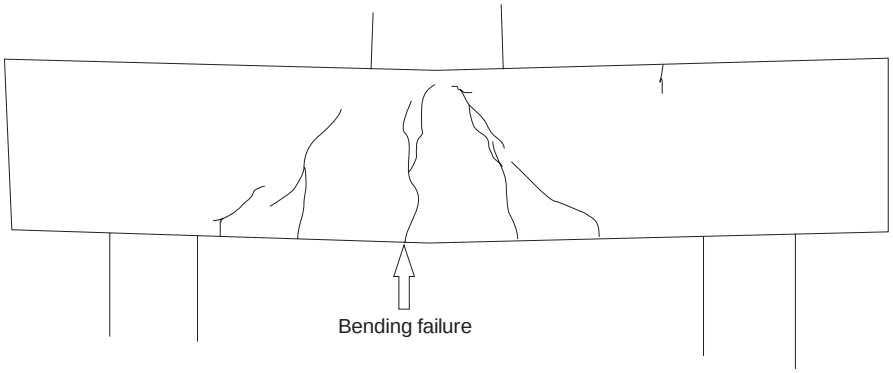

Figure 3.22 Crack distribution on B3A1 back surface at failure step

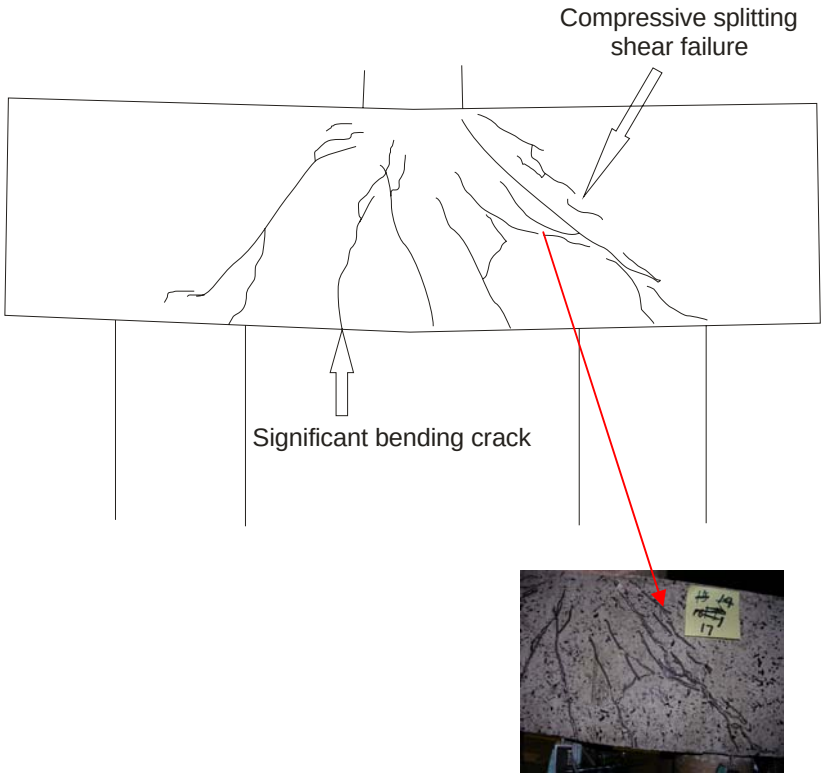

Figure 3.23 Crack distribution on B4A3 front surface at failure step

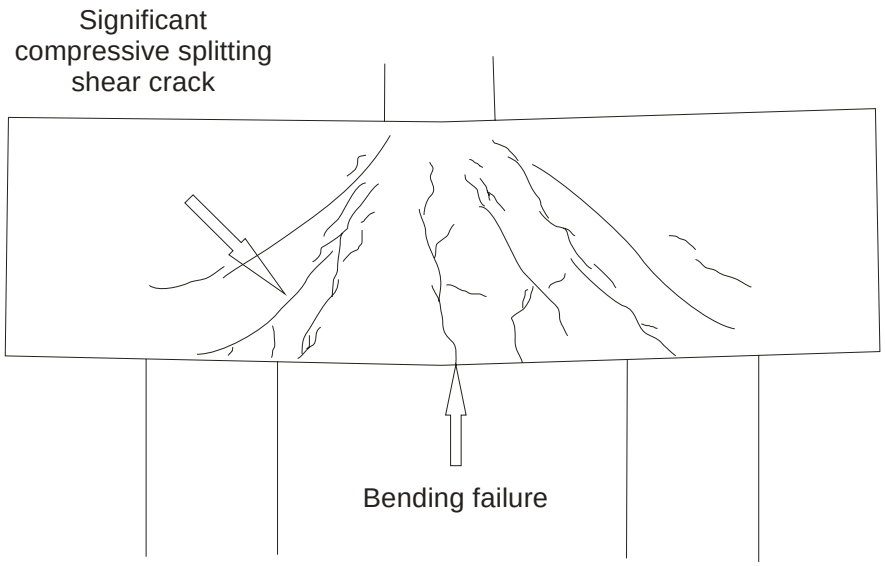

Figure 3.24 Crack distribution on B4A3 back surface at failure step

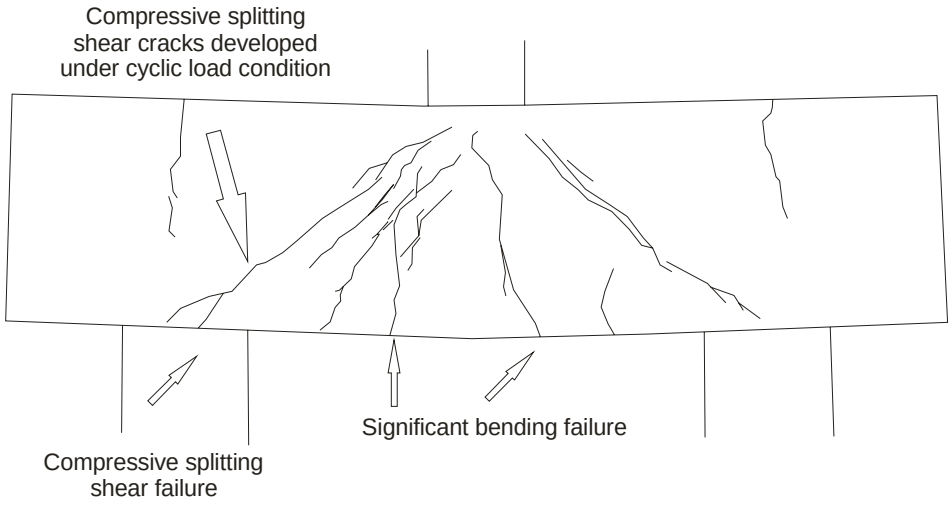

Figure 3.25 Crack distribution on B4B4 front surface at failure step

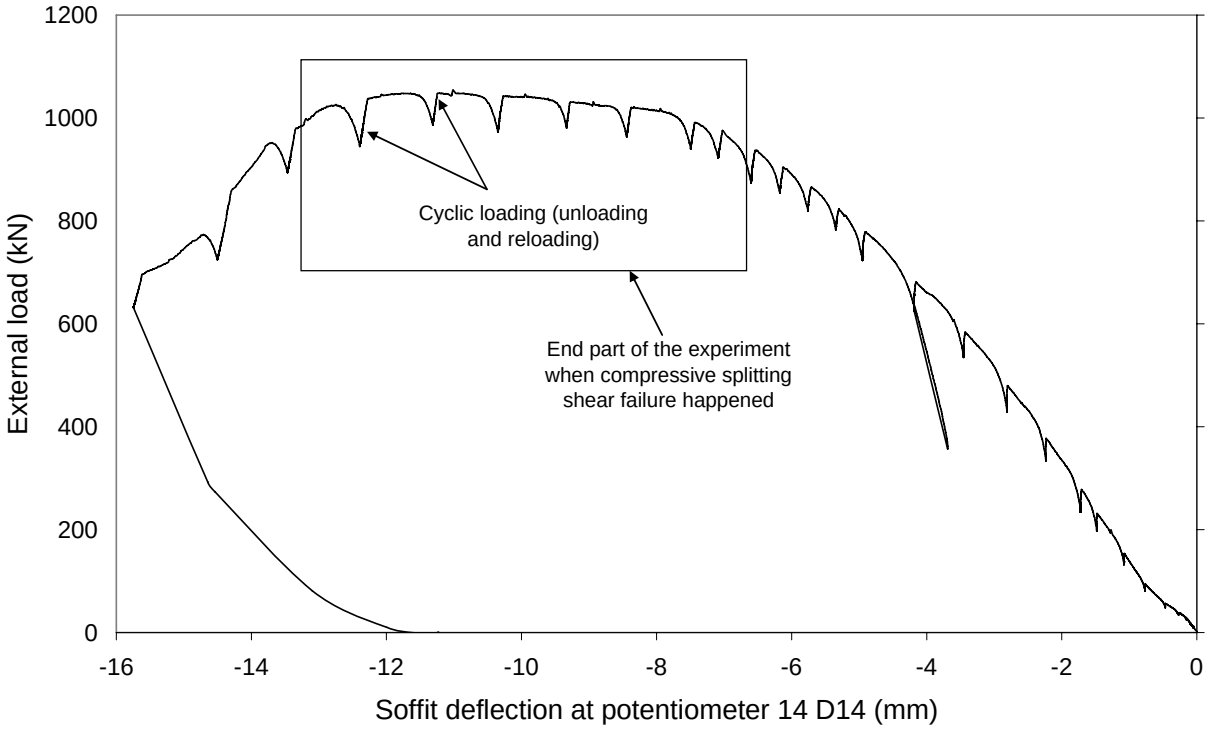

Figure 3.26 Cyclic load condition in the displacement control method in B4B4

Chapter 4 Application of particle image velocimetry (PIV)

4.1 Introduction

In this chapter, an introduction to photogrammetry is presented leading to the choice of particle image velocimetry (PIV) for this research, implemented by a purpose-built software GeoPIV8 to obtain the full field displacement on the cap front surface. The concrete strains were then calculated based on the displacement directly read from GeoPIV8. One objective of PIV application was to validate the FEA results (Chapter 5) such as the displacements and the strains on the cap concrete surface and the strain in reinforcement, replacing the traditional validation method by using strain gauges.

The whole procedure of the application is described. PIV was only applied to samples in Batch 3 and 4, all of which experienced a final failure (Section 3.3). Some results from PIV are presented in this chapter. A discussion on the limitation of the results is given.

The PIV technique and the issue of errors built in the technique are briefly introduced. The details of the PIV principle, the software GeoPIV8 and an attempt to analyze the errors are shown in Appendix I.

4.2 Introduction to photogrammetry

Photogrammetry applies the algorithm of image recognition between two images before and after the movement of a target area (Section AI.2.1) occurs. Merits of photogrammetry over the traditional measuring methods such as strain gauges are its non-contact full-field measurement of displacements and strains on the target area and that it is economic in labour and time cost.

4.2.1 Photographic surveys to measure the movement of targets

Several beams subjected to shear failure were investigated through digital photogrammetry (Qu *et al,* 2006). Displacements were obtained by tracing a set of target square tags attached on the concrete surface. The square tags were painted in black and white (Figure 4.1 (a)). A recognition system (Zernike, 1934) was applied to trace the position of the centre of the tag after finding the cross point of black and white parts (the pixel gravity centre

of a tag) such that the movement of a typical tag was measured. Results showed that the maximum principal tensile strain from the system matched well with the shear crack distribution (Figure 4.1 (b)).

Jeppsson (2000) investigated the possibility of a contact-free monitoring of an RC beam under concentrated load using digital images in which an array or a grid of white round shape dots were sprayed on the beam being loaded for a shear experiment. A Canon Powershot 600 digital camera, giving a resolution of 830×622 *pixels*, was used. The movement of the white dots was then traced by calculating the movement of the centre of the dots between two loading steps. The relative displacement of the two surfaces of a critical shear crack both normal and parallel to the crack were calculated in order to assess the role played by the aggregate interlock in the shear mechanism of RC beams.

Another popular photographic survey is PIV, a close range photogrammetry. It has been applied for a long history. As shown in Figure 4.2, traditional PIV was originally used in fluid mechanics to measure flow velocity through correlating the chemical components of the imaging of seeds (mica particles), sprayed deliberately into the flow, on two consecutive exposures on one light sheet or a traditional film. An image intensity field (Raffel, 1998) was constructed by introducing a transfer function that converted light energy of the image of an individual particle inside an interrogation volume into an electronic signal or an optical transmissivity such that a correlation can be used to trace and record the maximum movement of the interrogation volume.

With modern digital technology and software, traditional PIV has been developed into digital PIV with higher efficiency and reliability (Appendix I). Digital PIV analyses two consecutive digital photos by correlating the tricolour of the pixels in a certain interrogation area (IA) rather than tracing the centre of a discrete target. This is achieved by a certain amount of mathematical manipulation (Section AI.2).

Digital image correlation (DIC) is a similar method to digital PIV but applies an iterative matching method in the correlation by which the pixels that ‘escape’ out of, or ‘engage’ into the original interrogation area caused by the direct strains and shear strains are step-by-step ‘pulled’ back, or ‘pushed’ away (Srinivasan *et al*, 2005; Chu, Ranson, Sutton & Peters, 1985; Sutton, Wolters, Ranson & McNeil, 1983). It improves the accuracy of the results compared

with digital PIV results since the whole tricolour information in an interrogation area (IA) is retained.

4.2.2 A digital PIV application to a large strain measurement

Combined with a single digital camera, the work by White (2002) is probably the most representative of an attempt to combine digital photography with PIV. A Kodak DC280 digital camera of the maximum resolution $1760 \times 1168 pixels$ was used to measure large strain sand deformation when a pile was driven in it. Encased in a protective aluminium frame, the camera was fixed on a metal frame to keep it still during the experiment.

A Matlab based software GeoPIV8 (White, 2002) was used to achieve the digital PIV technique (Section AI.3) from which the direct output was the resultant displacement between two consecutive digital photos. GeoPIV8 allows a flexible method of execution. For instance, the size of the interrogation area and the distance between the interrogation areas can be easily adapted for different situations. The complex correlation and sub-pixel interpolation (Section AI.3) can be swiftly carried out by the software. GeoPIV8 also provides a friendly interface for the user to present the displacement vectors.

4.2.3 Errors in the digital PIV with GeoPIV8

Errors are a common issue in photogrammetry in general, and have particular features in the application of the digital PIV with GeoPIV8.

The performance of a measuring system can be assessed by considering the errors associated with accuracy and precision. Accuracy is defined as the systematic difference or the system error (Section AI.4.2) between a measured quantity and the true value. Precision is defined as the random difference or the random error (Section AI.4.2) between multiple measurements of the same object (White, 2002). The standard deviation is used to represent the level of the precision.

The system error stems from non-coplanarity between the lens plane and the plane of the target area, image distortion due to the lens distortion and CCD (charge-coupled device) distortion and pixel non-squareness (*i.e.* the physical partition on the CCD is not strictly square). Most of these cause errors during the transmission of the object from the object

co-ordinates into the image co-ordinates where GeoPIV8 works. Random error is a result of the camera resolution and precision of the methodology of digital PIV with GeoPIV8 associated with the feature size (Section 4.3.4) on the target area and the influence of the non-uniform distribution of features.

System error can be balanced off through a camera calibration. A matrix transforming the co-ordinates in the object space to the image space was carried out to correct the system error (White, 2002). Random error can be effectively reduced either by multiple measurements such that the mean value of the displacement of each IA (Section AI.2.1) reaches the correct value, or by improvement in the camera resolution.

The setup of a single camera (Section 4.2.2) also introduces errors in the out-of-plane displacement. It is evident that the displacement of the surface of a 2-way spanning cap is different from the in-plane displacement of a 1-way spanning beam. Even with full-length wall loading applied on the cap, which makes the cap closer to 1-way, one cannot avoid the possibility of out-of-plane displacement, which would only be discernable by a set of two digital cameras placed symmetrically with an angle ϕ to the concrete surface (Figure 4.3). The set up in Figure 4.3 requires a high accuracy in camera placement, an extension of the calibration work and the high expenditure. So if a single camera is applied to the pile cap experiments, in-plane displacement must be always assumed (Section 4.3.1).

4.2.4 Photogrammetry method chosen for this pile cap project

In light of the detailed information on the PIV technique presented by many papers, the availability of the free software GeoPIV8 which utilizes the digital PIV and the easy setup for the experiment, it was decided to apply digital PIV with GeoPIV8 by a single digital camera to this pile cap project.

An important issue in this research was to decide whether large strain or small strain was to be measured. Large strain is analyzed by defining an undeformed reference co-ordinate system and a deformed reference co-ordinate system enabling the deformation to be decomposed by a deformation gradient matrix into strain and rigid rotation (White & Bolton, 2004). On the contrary, in the small strain analysis, direct strain and shear strain are assumed

unchanged along a certain base length. The small strain assumption does not involve the deformed reference co-ordinate system, which normally rotates. Therefore rigid rotation is unobtainable in small strain analysis. However, the influence of the rotation on the results can be assessed by manually rotating a sample by a known angle. Results showed that the angle among 1˚ to 7˚ will not affect the displacement value obtained based on small strain assumption such that the influence could be neglected (Hung & Voloshin, 2003).

Large strains in soil were measured by PIV (Section 4.2.2). In the pile cap project, however, small strains or Cauchy strain tensors were assumed because the compressive strain when concrete was crushed was of the order of magnitude 0.001, significantly less than the threshold value of 0.05 between small strain and large strain. This was consistent with the further validation between the PIV and FEA results where the small strain assumption was also made (Chapter 5). Rigid rotation of the cap concrete surface during the experiment was assumed to be small, so its influence on the small strain assumption can be neglected.

Other issues such as the need to provide features on the concrete surfaces and the appearance of the concrete cracking were dealt with as described in Section 4.3.

The principle of digital PIV, how it is implemented in GeoPIV8 and the details of an error analysis are shown in Appendix I.

4.3 Implementation of the digital PIV with GeoPIV8

4.3.1 Treatment for single camera

An Olympus digital camera with 2288×1712 *pixels* resolution was chosen. It was assumed that out-of-plane displacement of the cap front surface was not considered such that only a single commercial camera was required. This required the camera's lens plane be parallel to the investigated concrete surface. To achieve this as far as possible, the camera was installed on a base tripod placed on the centre line of the pile cap (Figure 3.6) such that the camera mounted on the tripod was almost on the centre line of the pile cap. The tripod platform was adjusted so that its bubble indicated it was horizontal. A bubble-bearing gradienter was used to position the camera (lens) vertical (Figure 4.4); The camera was then

slightly adjusted so that the whole image was almost symmetrically projected on its LCD screen against the vertical centre line of the cap (Figure 4.5).

The camera was also required to be stable to avoid in-plane and out-of-plane movement caused by the vibration of the tripod and camera. In-plane translational and rotational movement of the camera does not influence the strain but the displacement. To solve the problem, two heavy weight stocky concrete columns (Figure 3.6) were placed either side of the tripod, acting as ballasts.

In order to subtract any in-plane displacement of the camera that did occur during the experiment, a reference area with similar surface features to the cap was fixed on the still background behind the cap (Figure 4.5), the displacement of which obtained from PIV was deemed as the in-plane displacement of the camera.

4.3.2 Camera control software

To capture consecutive digital photos with the same optical parameters such as focus, aperture and zoom, Olympus camera control software was used (Figure 3.11). Controlling the camera remotely by a computer also helped to keep the camera stable. As the distance between the camera and cap surface was almost same in each experiment (from 1.8 m to 1.85 m, Figure 3.6), these optical parameters were adjusted to give the clearest photo and kept identical for each sample. Once parameters were set in the control software, the camera shutter was then also controlled by the software. Photos were then transmitted directly from the camera to the computer.

4.3.3 Transformation between object and image co-ordinates system

A survey levelling staff was placed horizontally under the cap front surface in the same plane (Figure 4.6). The levelling staff was used to obtain a ratio R mapping the distance in $pixel$ units in the image co-ordinates system from GeoPIV8 into the real distance in mm in the object co-ordinates system.

In this research, $50\,mm$ (an ‘E’ shape on survey levelling staff, Figure 4.7) was taken as the base length in order to calculate the ratio R. The longer the base length is, the lower the

system error will be in R. It was thought $50\,mm$ would not produce high errors influencing the validation with FEA. In the digital photo, there was a transitional area between the light and dark area (Figure 4.7) in which the boundary line of the base length needed to be determined. The boundary line between these two areas was assumed to coincide with one of the columns of pixels in this transitional area. To trace the boundary position, it was assumed that the first column in the transitional area was the boundary line (Figure 4.7). Thus, the number of pixels in the horizontal direction covering the $50\,mm$ scale could be counted, and the ratio R was equal to $50\,mm$ divided by the number of pixels it covered.

Because of the lens non-squareness (Section 4.2.3), the value of R could be different in the horizontal and vertical directions. In this research, it was assumed R was equal in both directions. Though R is also influenced by the position of the levelling staff in the photo because of the potential lens distortion, this factor was neglected. Therefore, R was constant foe each IA position. Values of R for samples in Batch 3 and 4 are given in Table 4.1.

4.3.4 Features on concrete surface

In fluid mechanics, the target area is visualized by distributing a suspension of mica particles on the surface of the water (Figure 4.2). In solid mechanics, as in this research, the target area should be either kept unchanged if the feature of its natural surface can offer sufficient contrast, or manually painted with spots, each a unique feature.

The natural texture of soil in high tricolour contrast (Figure 4.8 (a)) was utilized in the driven pile project (Section 4.2.2), while in this research artificial particles were painted on the concrete surface because of the low tricolour contrast of the concrete natural texture between dark and light features (Figure 4.8 (b)). This was done with a natural sponge dipped with black non-flash paint and dabbed on the concrete surface (Figure 4.9). The softness and deformability of the natural sponge was believed to give unique surface features and high contrast between dark and light features on the concrete surface. One surface example is shown in Figure 4.6.

4.3.5 Determination of IA size, IA spacing and size of search area

Section 4.2.1 introduces the concept of the interrogation area IA. The definitions of the IA size, IA spacing in the first photo and the size of search area are given in Section AI.2.1 and are shown in Figure AI.1 (a). In this research, these basic dimensions were determined by the following factors:

- The IA array, defined by the IA spacing, in the first photo determined the positions where displacement vectors were obtained, which further influenced the representation of the strain distribution. The array should be arranged such that it can supply sufficient detail of information describing the cracked concrete surface;
- The magnitude of the random error depended on the ratio between the size of the surface features (Section 4.3.4) in the photo and the size of one pixel and the ratio between the size of the surface features and the size of an IA. The more pixels a unique feature shape covered, the more information (tricolour value) was recorded and the more accurate the result was. The more unique features an IA covers, the more accurate the result was. As shown in Figure 4.10, a rule of thumb was that the size of the surface feature should be at least $3\times3 pixels$ and at least three features at the maximum size should be enclosed by one IA;
- To apply PIV to a cracked concrete surface, at least one IA was required to be on each side of a crack but not intersected by the crack in order to avoid excessive noise (Section 4.3.7 and Figure 4.11). IA size was therefore required not to be too large, reducing the chance to struggle with cracks. The IA spacing must be carefully chosen by judging the crack distribution;
- One principle for choosing the size of search area was that the value should be larger than the maximum possible translation of an IA in any direction that occurred between the first (in this research the first loading step) and the second photos (in this research the final failure step or the onset of the yield stage);
- Choosing these dimensions was always a trade-off, balancing between the analysis time and the random errors. With the increasing IA size, random errors were reduced (Section AI.4.4) but the analysis time increased exponentially.

Considering all the factors above, the dimensions chosen for samples in Batch 3 and 4 are listed in Table 4.2 after trial and error tests. A basic image of a target area and its IA array is shown in Figure 4.5.

4.3.6 Pre-test for GeoPIV8 error analysis

For each sample in Batch 4, a pre-test for an error analysis (Appendix I) was done before the main experiments, to investigate the system and random errors in the technique (Section 3.8). In the pre-test, the cap was given two separate vertical displacements by the testing machine without loading (Figure 4.6). A dial gauge was set on the cap top surface to measure the real displacement of the cap. The analysis was done by comparing the displacement recorded by the testing machine and the dial gauge with PIV results. Because the displacement given to the cap during the pre-test was comparable to the displacement of the pile cap surface at failure, the analysis can provide valuable error information for the displacements from PIV for any loading step during the main experiment.

4.3.7 Post-processing

This section presents the processing of the original data read from GeoPIV8 to obtain the interested displacement and strain distribution on the concrete surface. In this research, only the displacement and strain increment between the photos taken at the first loading step and the failure step or between the first loading step and the onset step of the yield stage were analyzed.

The basic co-ordinates system used in the analysis is shown in Figure 4.5. The horizontal rows of IA are referred to as 'IA series in z direction'. The vertical columns of IA are referred to as the 'IA position in x direction'.

- **Noise displacement elimination**

Readings from GeoPIV8, the horizontal and vertical displacement vectors in pixel units in the image co-ordinates system, $(U^{'},V^{'})$, relative to the ground or to the camera can be obtained.

When a crack newly opened or widened and was highlighted in the second photo, $(U^{'},V^{'})$ might be miscalculated from an incorrect correlation since there were new features or new pixels with sudden tricolour change (*e.g.* the dark shade of the opening of a crack or of the highlighting) moving into an IA in the second photo, at the same time as more original pixels in the first photo moved out of the IA than caused by the surface distortion. This produced noise displacement (Figure 4.12 (a)). Only an IA which covers at least one crack (Figure 4.12 (b)) is affected by noise displacement. As can be seen in Figure 4.13 (a), noise values appearing in $(U^{'},V^{'})$ deviated up and down from their correct values. One dimensional interpolation was applied to eliminate the noise value, replacing it by the mean value from its horizontal neighbouring two IAs (Figure 4.13 (b)). In some situations, two or three neighbouring IAs intersected several cracks which often happened in high density cracked areas (Figure 4.11). Therefore the interpolation was carried out in this region across more than one IA. The final interpolated value cannot accurately represent the displacement of the covered area, but the error was low.

- **Displacement relative to the wall loading**

An important aim of the PIV application was to validate the FEA results. In FEA, the pile base was fixed while a prescribed displacement was applied at the wall loading position (Chapter 5). So the direct displacement vector read from FEA was relative to the pile base, equivalent to the bottom steel platten in the experiment (Figure 3.4). $(U^{'},V^{'})$ from PIV, however, were relative to the ground rather than the bottom steel platten. In order to compare the result from FEA with PIV results, displacement was required to be defined in a same co-ordinates system. This was done by calculating the cap's horizontal and vertical displacement relative to the bottom edge of the wall loading.

In FEA, this can be done easily by commanding the program to give the displacement relative to the centre point of the wall loading. In PIV, the relative horizontal and vertical displacement in pixel units (U,V) in image co-ordinates system were calculated by subtracting the displacement relative to the ground $(U^{'},V^{'})$ from GeoPIV8 by the mean value

of the displacement vectors in pixel units relative to the ground of a group IAs immediately under the wall loading (Figure 4.14).

The displacement vectors read directly $(U^{'},V^{'})$ and displacement vectors relative to the wall loading (U,V) from GeoPIV8 are shown in Figure 4.15 (before noise value elimination). One can see that this processing also eliminated the influence of the relative horizontal slippage between the concrete spreader beam and cap and of the crushing of the soft board and concrete spreader beam such that (U,V) can be compared with FEA results.

Because the displacement of the reference area (Section 4.3.1) was found to be very small, the in-plane camera movement was neglected so that no subtraction from $(U^{'},V^{'})$ for it was needed. Thus the expected real relative surface displacement u and v in mm units in the object co-ordinates system were given by:

$$u = U \times R \times r_u \quad \text{and} \quad v = V \times R \times r_v$$

where r_u, r_v were the deviation ratios considering the system error *i.e.* the ratio between the real displacement and PIV results in the image co-ordinates. The ratios were obtained from the pre-test (Section 4.3.6) and described in detail in Section AI.4.5. R has been explained in Section 4.3.3. Finally the absolute value of the resultant displacement $d = \sqrt{u^2 + v^2}$ in mm was validated with FEA results (Chapter 5).

- **The horizontal strain and the total crack strain (first principal strain)**

When calculating strains, the small strain assumption was made (Section 4.2.4). The formulae for the horizontal and vertical direct strains and shear strains are as follows:

$$\varepsilon_{xx} = \frac{\Delta u}{\Delta x}$$

$$\varepsilon_{zz} = \frac{\Delta v}{\Delta z} \qquad (Eq.4.1)$$

$$\gamma_{xz} = \gamma_{zx} = \frac{\Delta u}{\Delta z} + \frac{\Delta v}{\Delta x}$$

where Δu and Δv were obtained by calculating the horizontal and vertical relative displacement (u,v) of two IAs with corresponding horizontal and vertical spacing $\Delta x, \Delta z$, the base length on which the strain was calculated.

The direct horizontal strain ε_{xx} at reinforcement level thus reflected the total horizontal strain in the reinforcement closest to the cap front surface, if perfect bond was assumed. However, the assumption that a perfect bond exists between the reinforcement and the concrete was no longer true in close proximity to a crack on the concrete surface, and so the high concrete strain near the crack cannot be taken on its own as evidence that the steel had yielded. However, if the measured concrete strain was averaged over a base length comparable to the spacing between cracks, a reasonable estimate of the average reinforcement strain can be obtained (Cao & Bloodworth, 2007). The base lengths $\Delta x, \Delta z$ were so chosen that they were reasonable lengths to represent a mean strain in the reinforcement at cracks, in this research, taken as 64 *pixels* *i.e.* double the IA spacing (Table 4.2).

The maximum in-plane direct and shear strains can be easily calculated as follows:

$$\varepsilon_{1,2} = \frac{\varepsilon_{xx} + \varepsilon_{zz}}{2} \pm \sqrt{\left(\frac{\varepsilon_{xx} - \varepsilon_{zz}}{2}\right)^2 + \left(\frac{\gamma_{xz}}{2}\right)^2}$$

$$\frac{1}{2}\gamma_{\max} = \sqrt{\left(\frac{\varepsilon_{xx} - \varepsilon_{zz}}{2}\right)^2 + \left(\frac{\gamma_{xz}}{2}\right)^2}$$

Because for concrete the strain when its tensile strength is exceeded, ε^e, was far less than the value of crack strain ε^{cr}, the total crack strain or the maximum principal strain $\varepsilon_1 (= \varepsilon^e + \varepsilon^{cr})$ can well represent the crack strain ε^{cr} on the concrete surface.

4.3.8 Discussion on the limitation of the strain results

The minimum precision *i.e.* the minimum standard deviation of the displacement (Section 4.2.3) the GeoPIV8 can reach is ± 0.01 *pixels* (White, 2002). Since the strain is a function of the difference of two displacements (*Eq.*4.1), the minimum standard deviation

delivered to the strain obtainable is $\varepsilon = \pm\frac{0.01+0.01}{64} = \pm 0.000312$. Therefore, if not considering the system error, the precision GeoPIV8 produces may influence the strain results when the real strain is at low level, especially within the range near ± 0.0003.

Considering the case of concrete, if the cube compressive strength is taken as $20\,MPa$, tensile strength as $2\,MPa$ and Young's modulus E=$28000\,MPa$, the strain in concrete at which cracks appear is $\frac{2}{28000} = 0.000071$, the strain at the concrete compressive yielding point is $-\frac{20}{28000} = -0.000714$ and the strain at concrete crushing is widely acknowledged as -0.0035. It was clear that the precision of GeoPIV8 or the random errors influenced the strain results in the concrete tensile and compressive stress field before the tensile cracks and concrete compressive yielding appeared. For the tensile stress field, it was considered that the random errors can be neglected only after the tensile strength was reached such that the tensile strain suddenly increased exceeding far above $+0.0003$. For the compressive stress field, the random errors can be reasonably neglected when the compressive strain was below *e.g.* -0.0003 *i.e.* from sometime before the concrete was yielded and crushed.

4.3.9 Example results from digital PIV with GeoPIV8

Before the results are given, it is necessary to note that though the base length was taken as 64 *pixels*, strains were calculated at 32 *pixels* intervals *i.e.* at the *IA* spacing (Section 4.3.5). Figure 4.16 shows a relationship between the *IA* array and the *IA*s at which ε_{xx} and ε_{zz} can be obtained. It can be seen that one cannot report the displacement and strain over the whole target area. This figure also suggests a possible effective region (shaded area) that the strain at the centre of an *IA* (*IA*1) could be applied to.

Figure 4.17 gives an example of good results of a full-field maximum principal strain ε_1 from PIV compared with the crack distribution from the experiment for B4A5 at the onset of the yield stage (Figure 3.10). As can be seen in Figure 4.17 (a), the area *abcd* in Figure 4.17 (c) where strains are calculated is smaller than the target area. From Figure 4.17 (c), the high

maximum principal strain ε_1 from PIV locates exactly where the inclined compressive splitting crack appears from the experiment as shown in Figure 4.17 (b). Therefore, PIV results give an acceptable matching with the experimental observation.

It is also clear from Figure 4.17 (c) that in the areas of low tension and compression *i.e.* the right and left upper corners and mid span at the bottom edge of the cap (in B4A5, the central bending crack was much less opened, Figure 3.20), the PIV results from GeoPIV8 are severely influenced by the random error (Section 4.3.8) *i.e.* high principal compressive strain appears reaching as high as -0.005.

4.4 Summary

A basic background of photogrammetry and its application are introduced. Digital PIV, as one popular photogrammetry method, was used throughout this research. The results were used to validate FEA results, to determine the strain in longitudinal reinforcement in the cap and to reveal the shear behaviour on cap front surface. This application has been rarely used in RC structures by previous researchers.

This chapter attempts to demonstrate the workability of the digital PIV achieved by the software GeoPIV8 to obtain the full-field distribution of displacements and strains on an RC surface. Though the random error built in the technology influenced the PIV results in concrete area in low tension and compression, the maximum principal strain were considered to match well with the shear crack distribution from experimental observation. Compared with the random error, the influence of the system error in displacement and strain on this research is low.

The most difficult issue in applying digital PIV to a concrete surface was the appearance of cracks, which produced noise values and reduced the reliability of the technology. With an optimal disposition of IA array *i.e.* a reasonable choice of IA size, IA spacing, size of the search area and the base length on which strain was calculated, the disturbance from cracks was reduced to a minimum.

Table 4.1 Ratio R for samples in Batch 3 and 4

Pile cap No.	Base length on survey levelling staff (*mm*)	Equivalent pixel	R (*mm* / *pixel*)
B3A1	50	68.31	0.732
B3A2	50	69.17	0.723
B3A3	50	68.88	0.726
B3A4	50	71.15	0.703
B4A1	50	68.03	0.735
B4A2	50	66.90	0.747
B4A3	50	68.88	0.726
B4A4	50	68.03	0.735
B4A5	50	65.76	0.760
B4B1	50	68.03	0.735
B4B2	50	72.00	0.694
B4B3	50	71.15	0.703
B4B4	50	79.09	0.632

Table 4.2 Dimensions of IA array for samples in Batch 3 and 4

	IA size	IA spacing	Size of search area
Batch 3	20×20 *pixels*	32 *pixels*	60×60 *pixels*
Batch 4	20×20 *pixels*	32 *pixels*	40×40 *pixels*

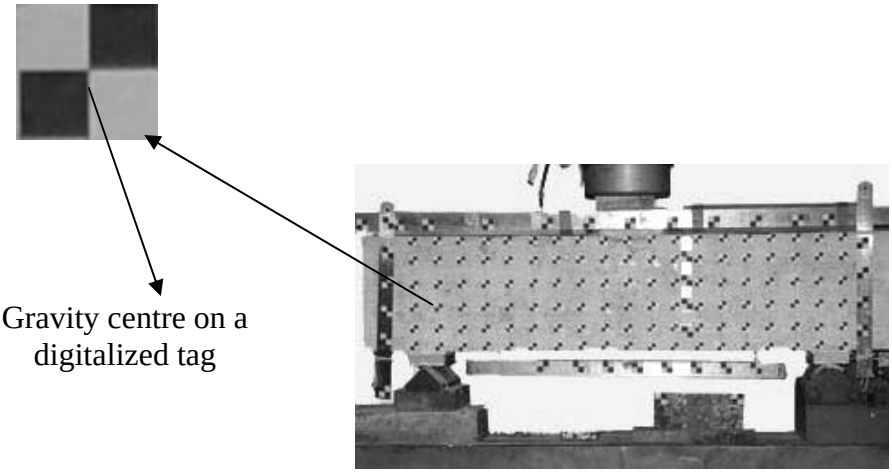

(a) Black and white tags on an RC beam surface

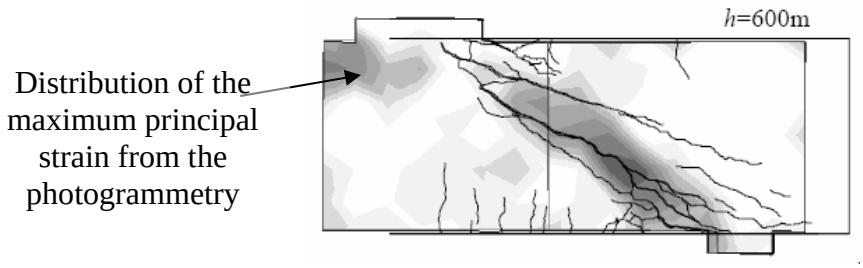

(b) Comparison between the maximum principal strain from the photogrammetry and the crack distributions from the experiment observation

Figure 4.1 A digital photogrammetry application to an RC beam in shear failure (Qu *et al*, 2006)

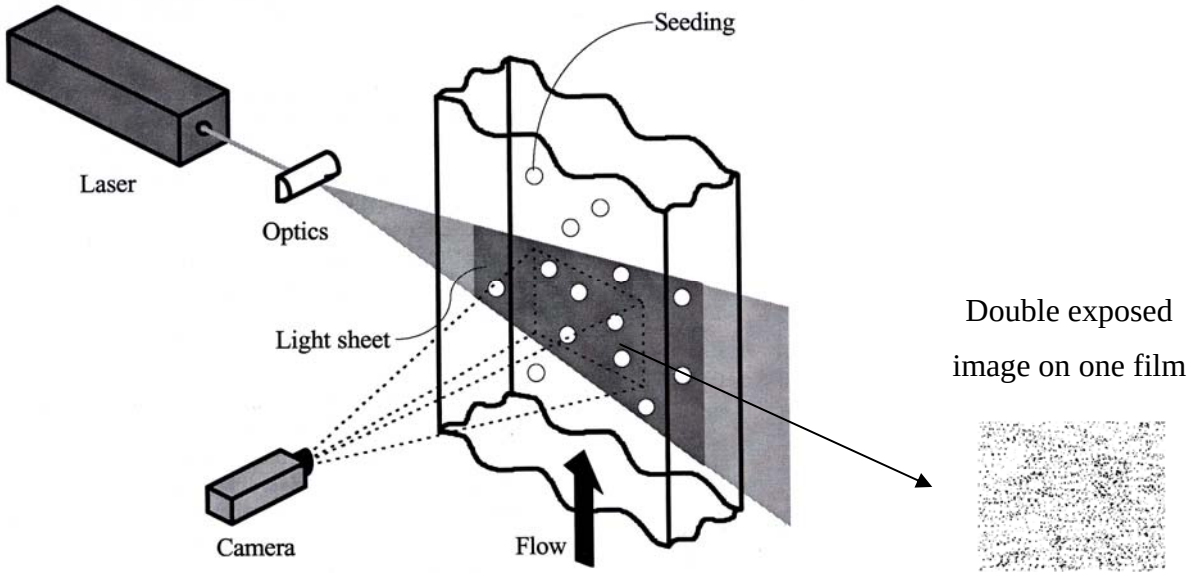

Figure 4.2 Application of a traditional PIV in fluid mechanics (DANTEC DYNAMICS, 2006)

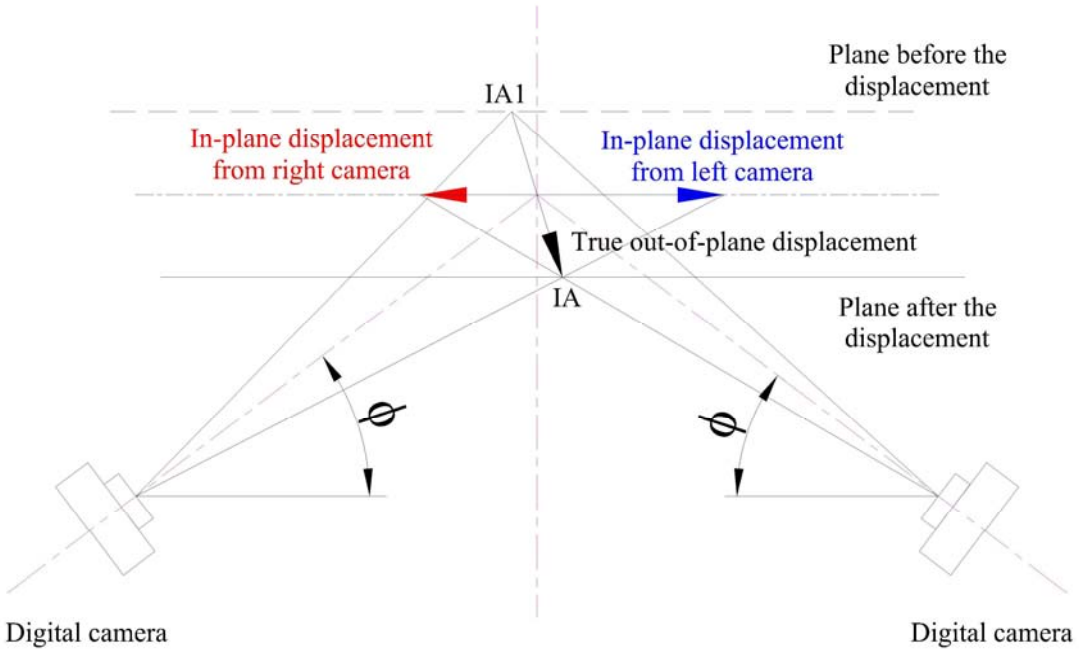

Figure 4.3 PIV set up to obtain an out-of-plane displacement by two cameras

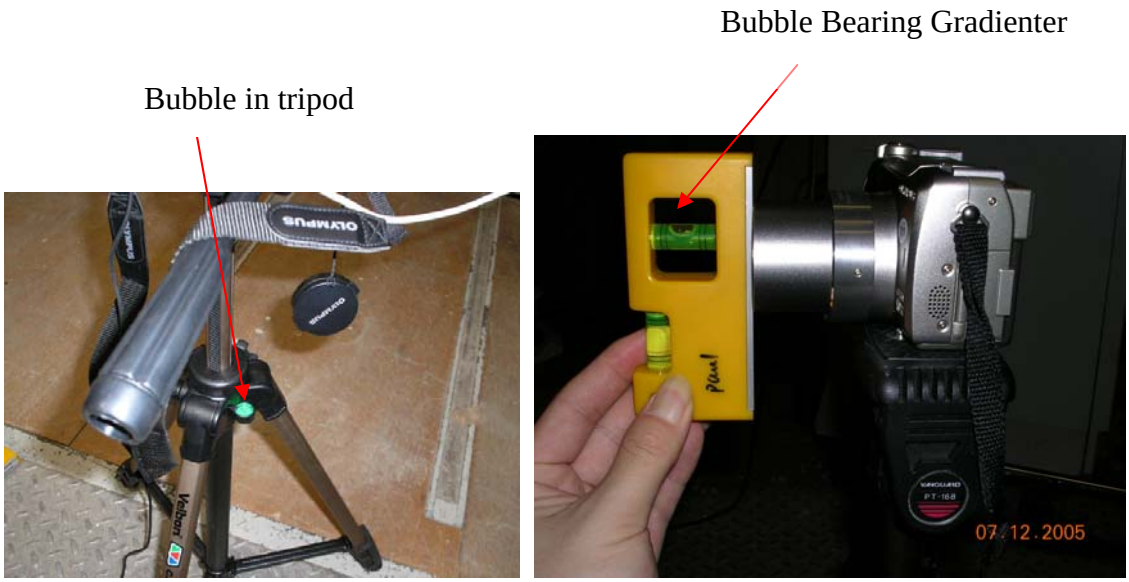

Figure 4.4 Tripod kept horizontal and camera (lens) kept vertical

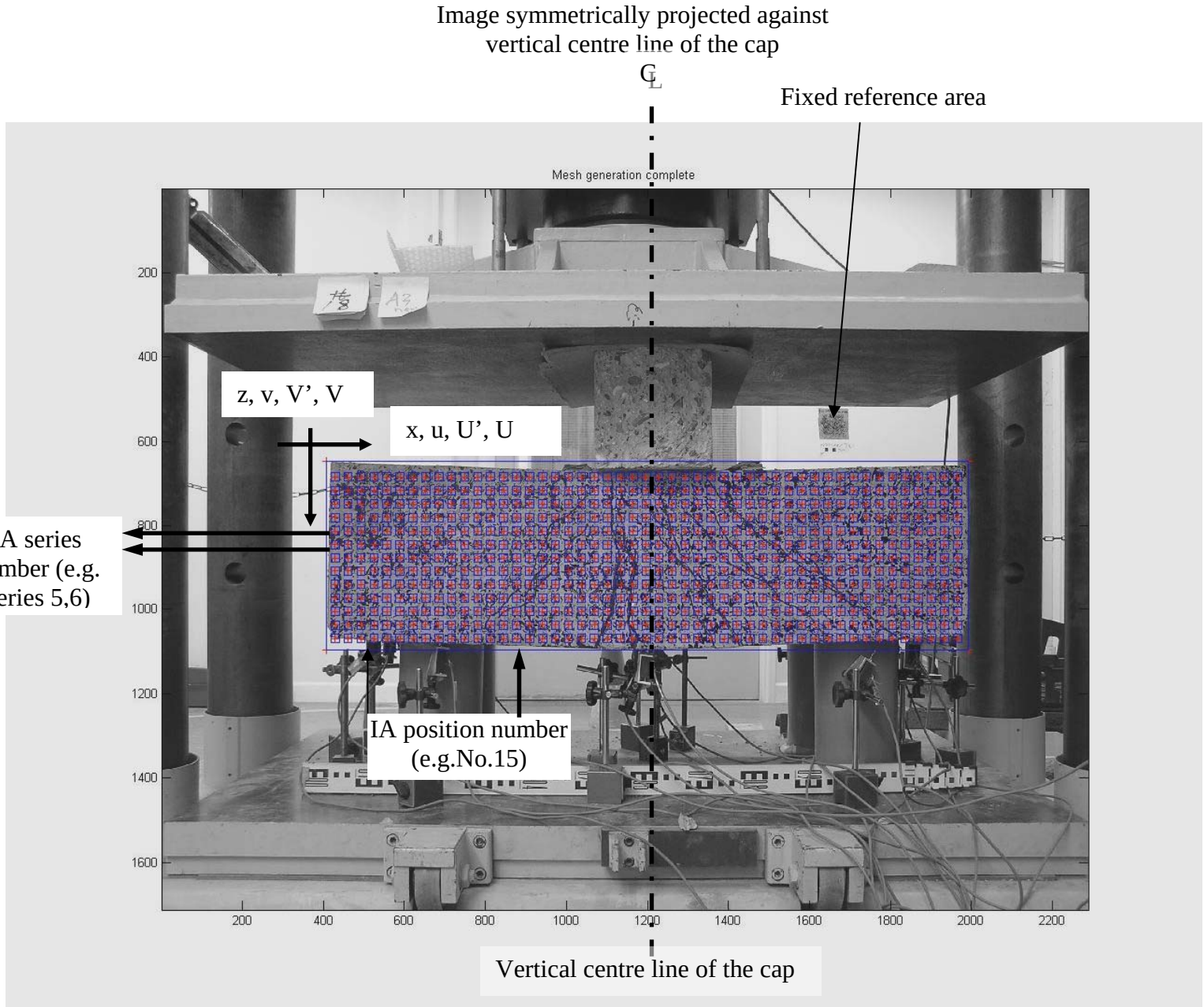

Figure 4.5 Co-ordinates system of *IA* array and the reference area used in the digital PIV

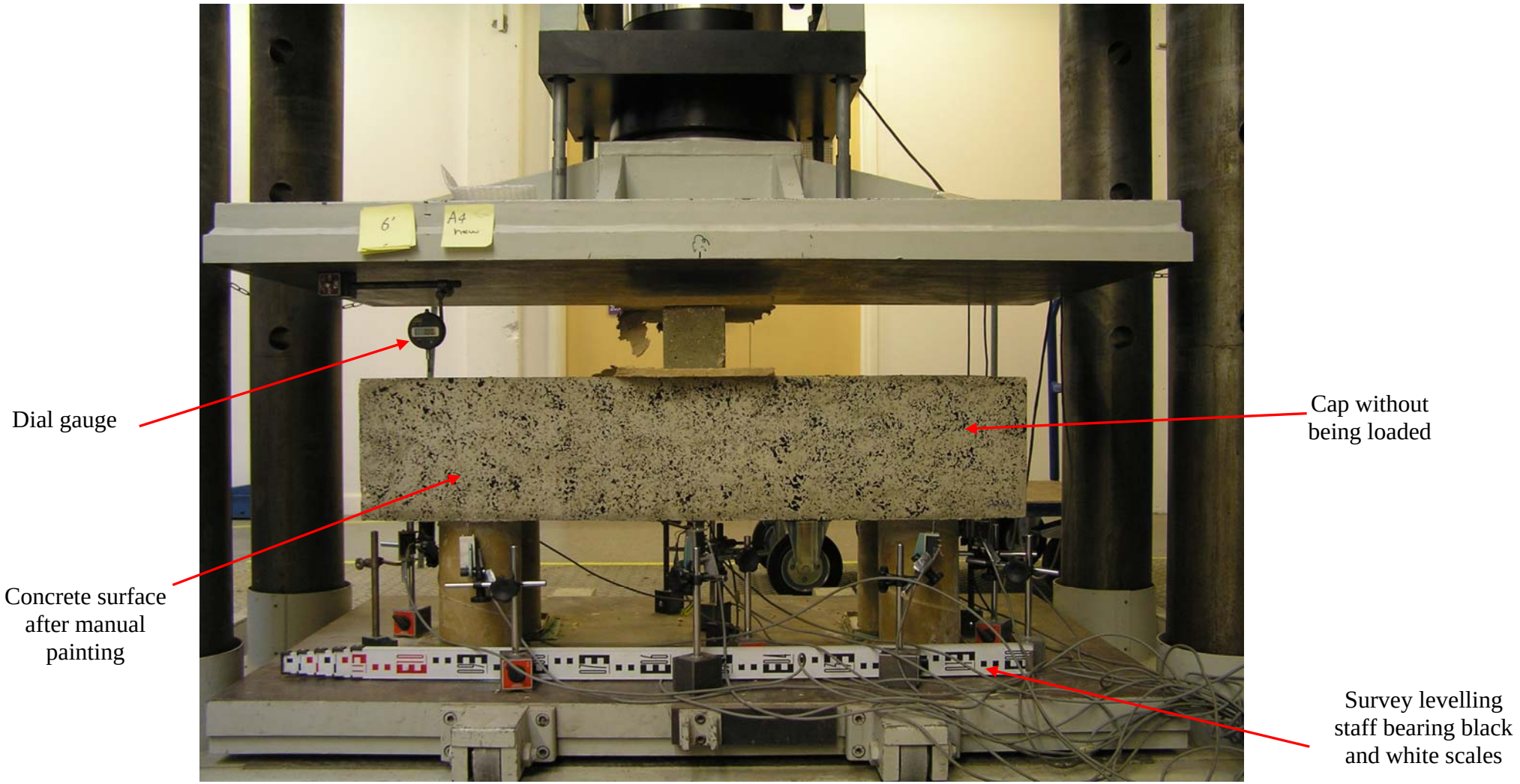

Figure 4.6 PIV pre-test for an error analysis

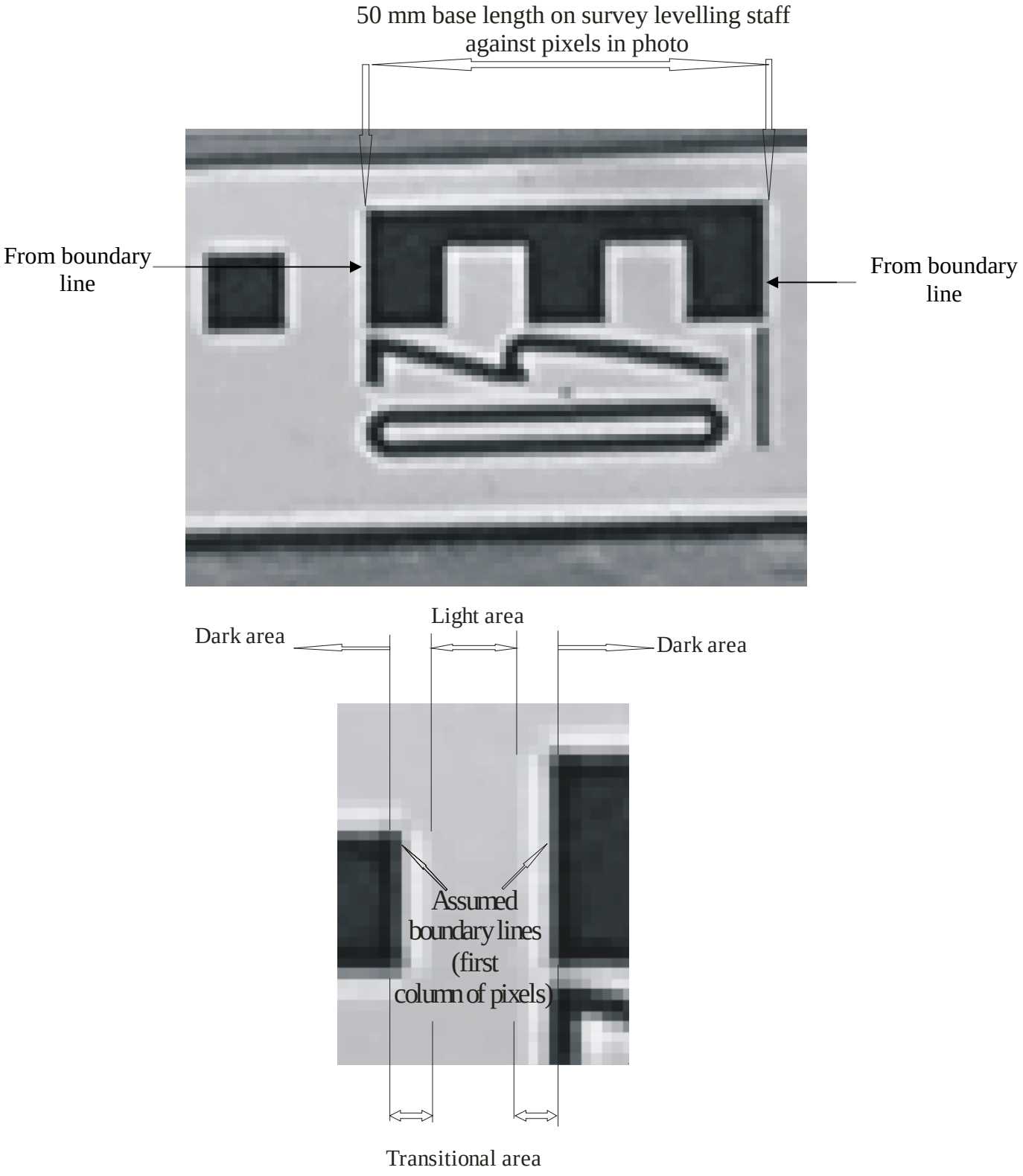

Figure 4.7 Base length and transitional area

(a) Natural texture of soil surface in high contrast $50 \times 50\,pixels$ (White, 2002)

(b) Natural texture of concrete surface in a pile cap in low contrast $90 \times 90\,pixels$

Figure 4.8 Contrast of surface texture of soil and concrete

Figure 4.9 Natural sponge dipped with black paint

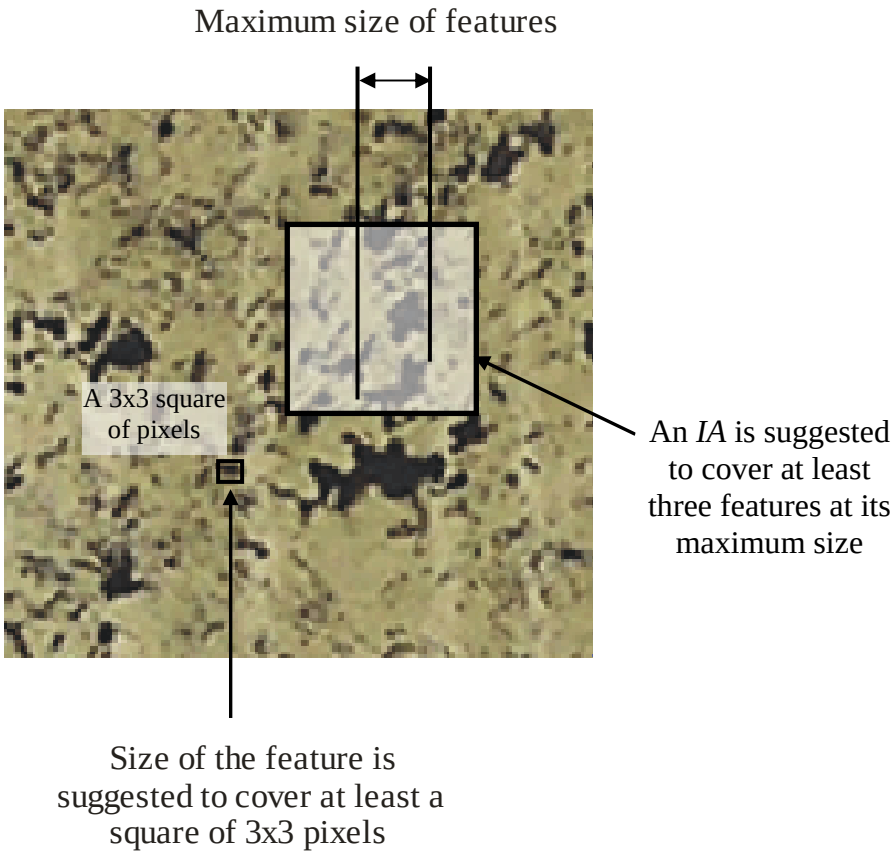

Figure 4.10 Rule of thumb for the size of a concrete surface feature

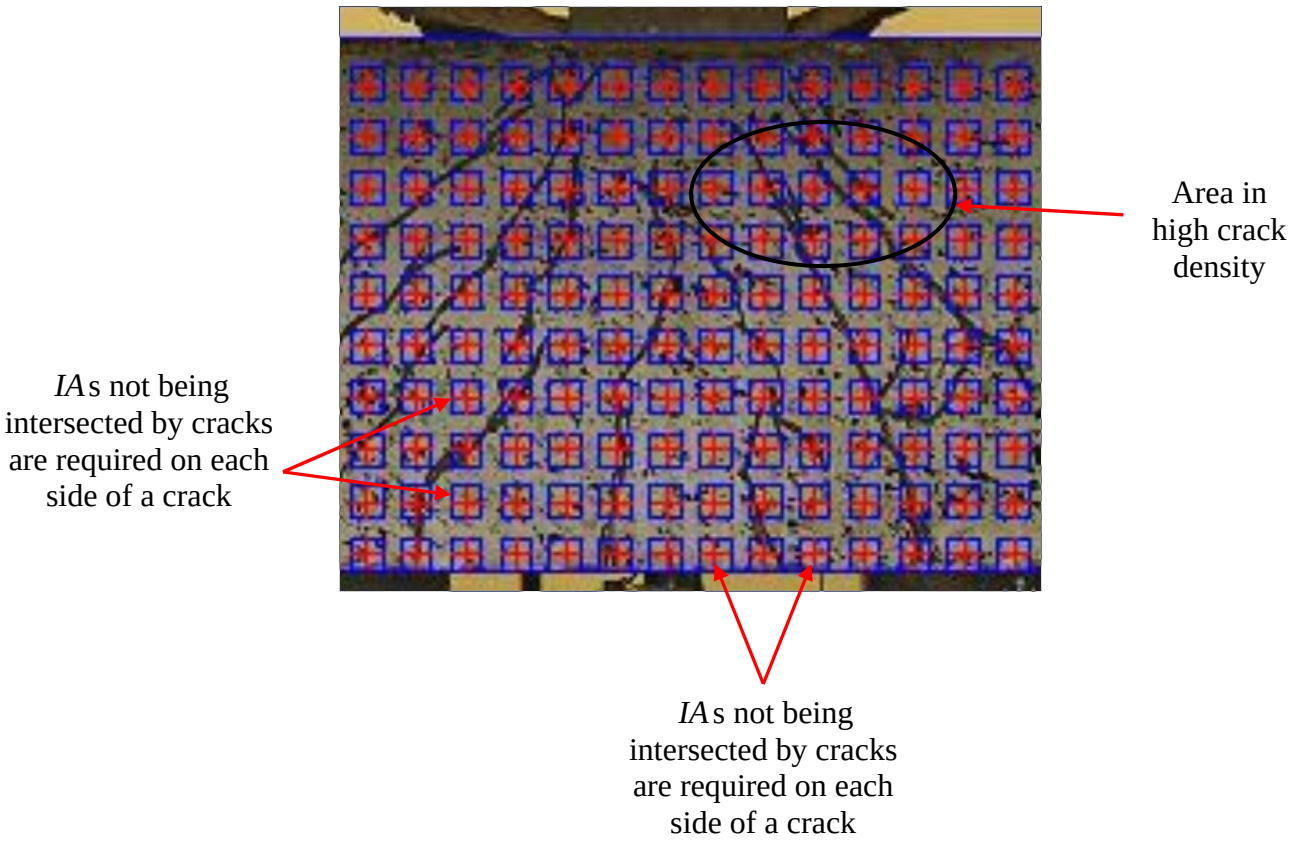

Figure 4.11 The choice of *IA* size and *IA* centre spacing to deal with cracks appearing on concrete surface

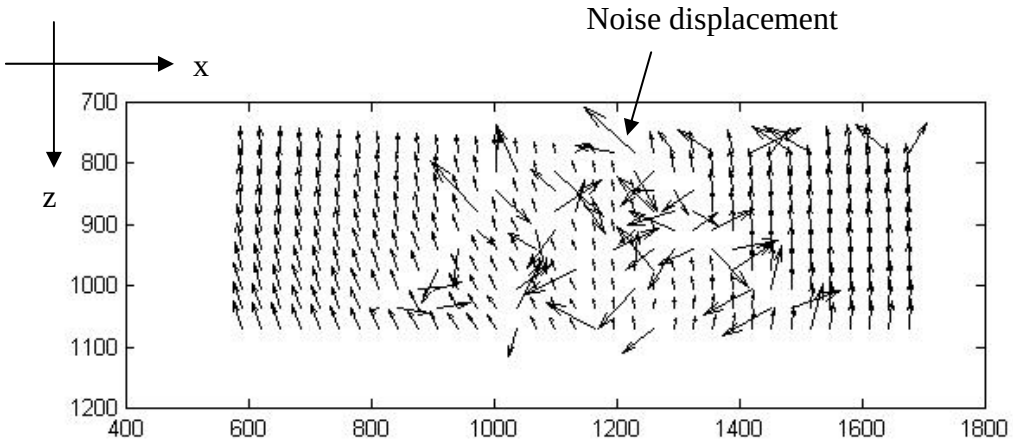

(a) Noise displacement from GeoPIV8

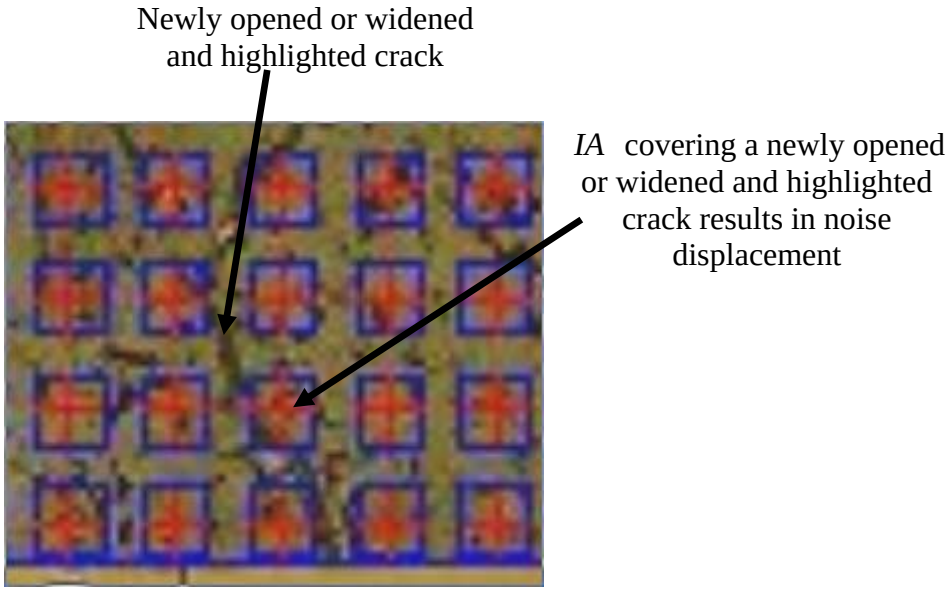

(b) *IA* producing noise displacement

Figure 4.12 Noise displacement from GeoPIV8

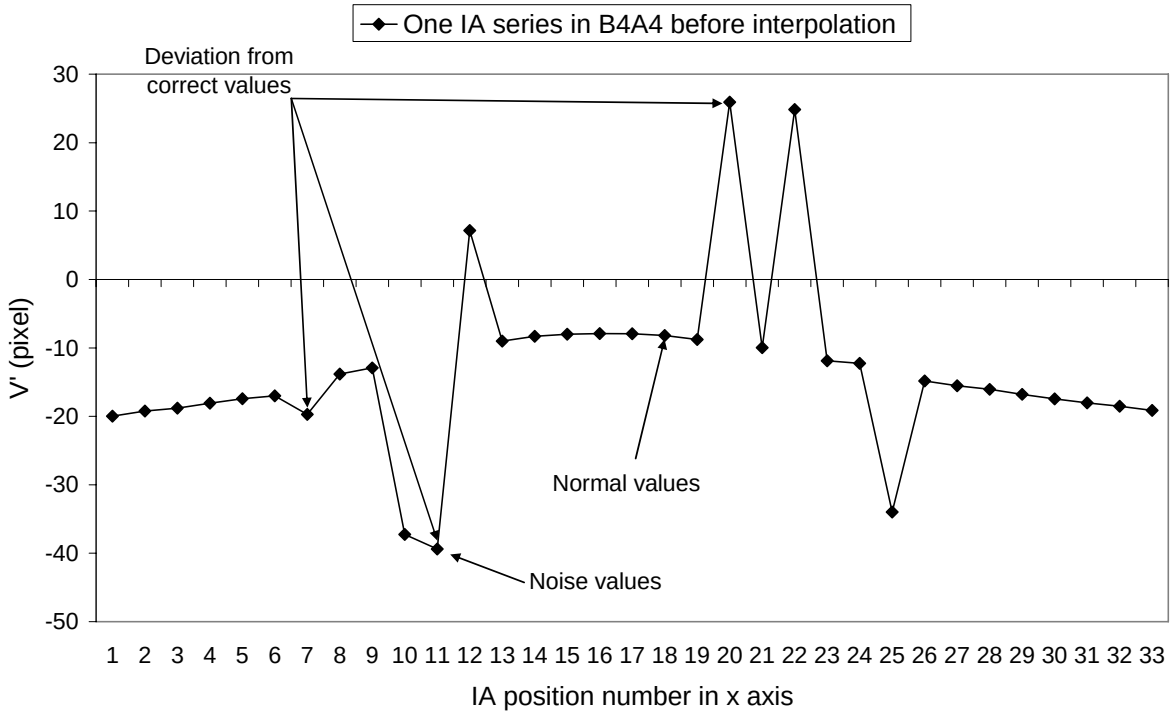

(a) Noise value before interpolation

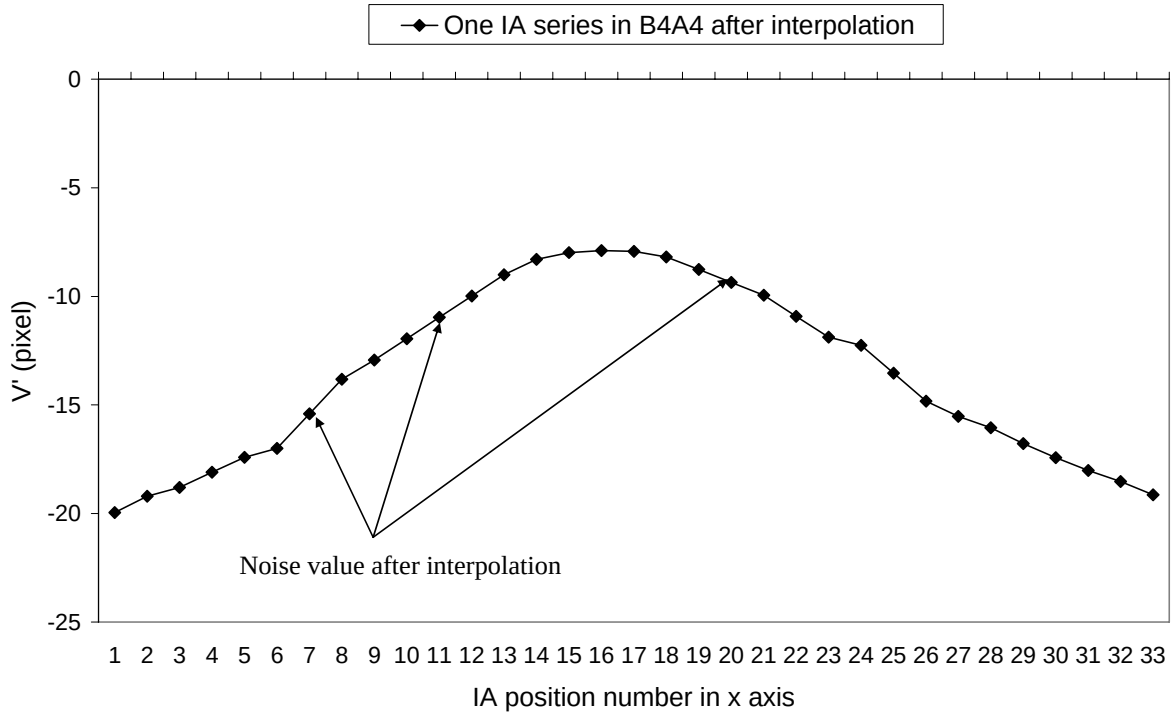

(b) Noise value after interpolation

Figure 4.13 Noise displacement elimination between failure step and first load step (B4A4)

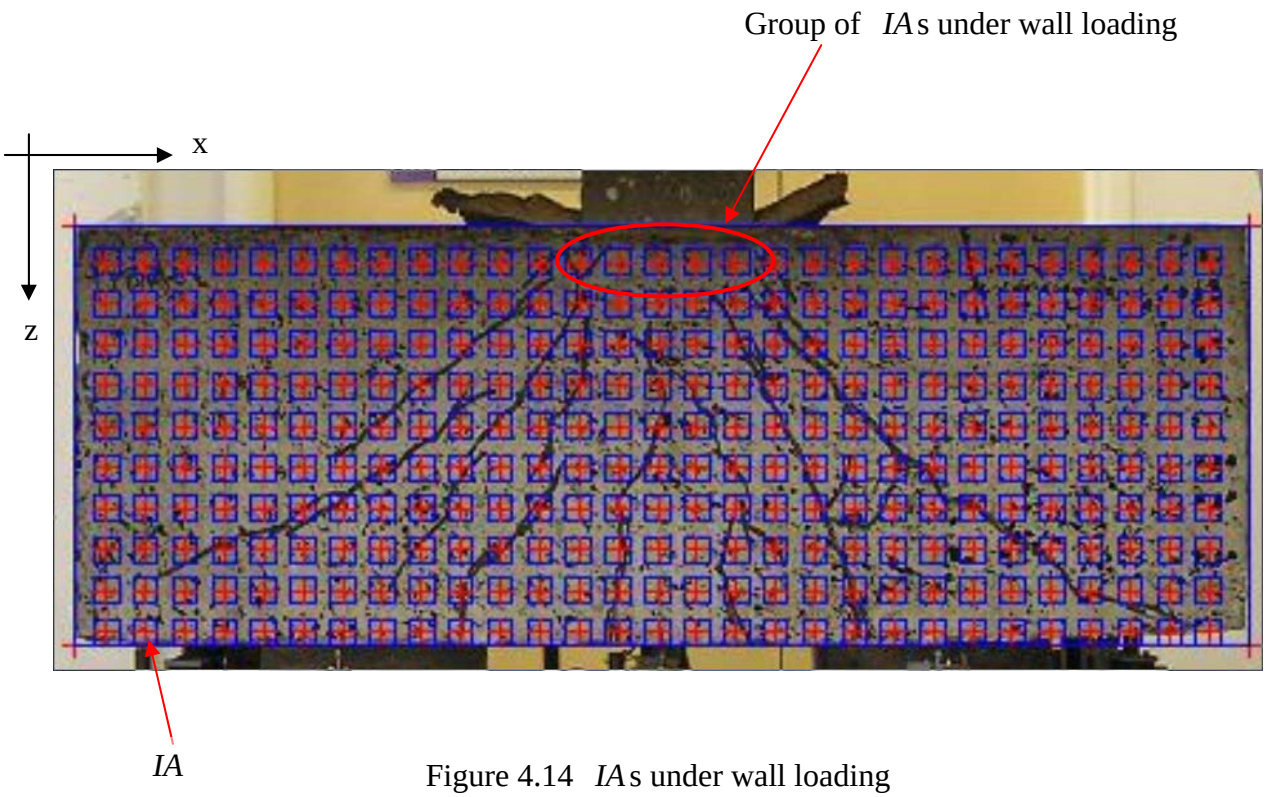

Figure 4.14 *IA*s under wall loading

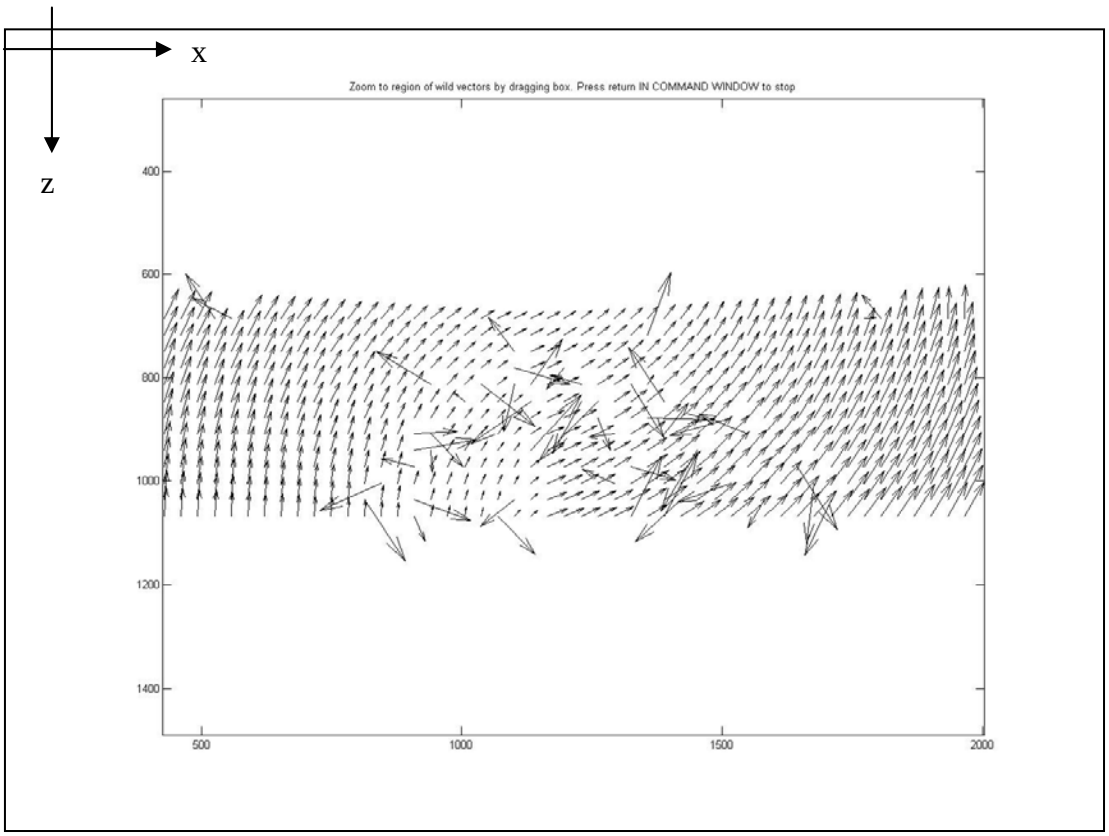

(a) Displacement relative to the ground or the camera

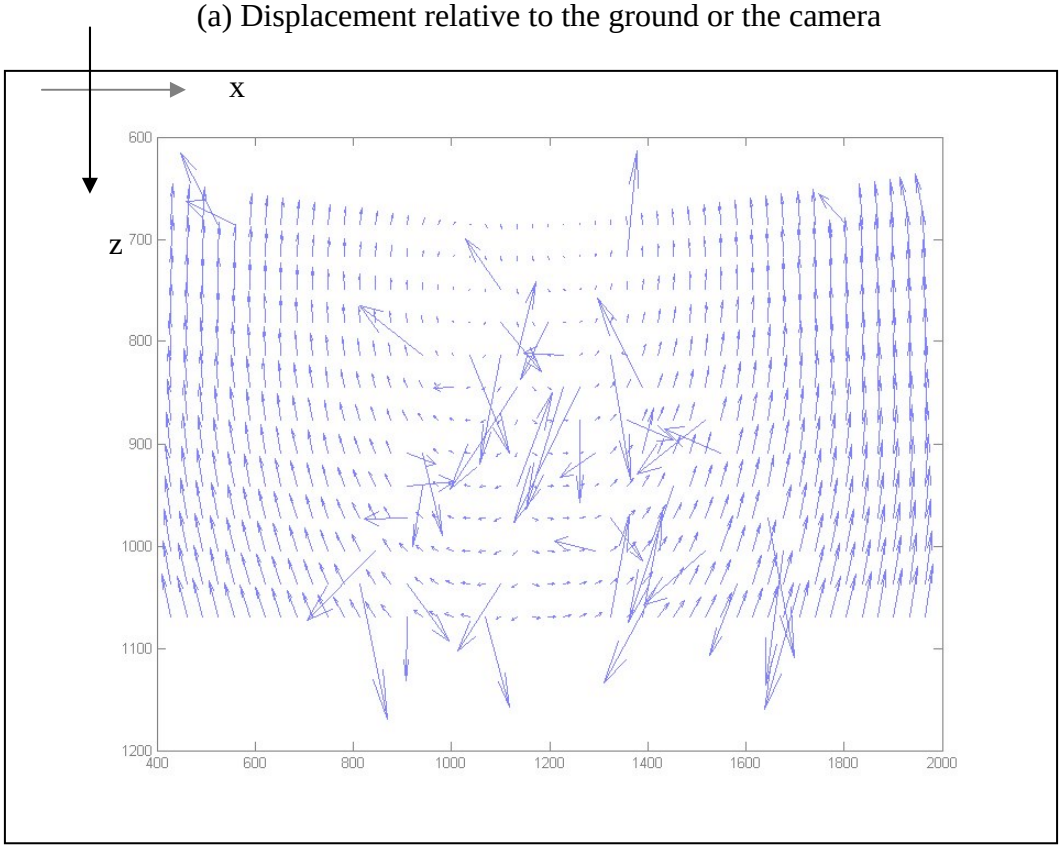

(b) Displacement relative to the bottom edge of the wall loading

Figure 4.15 Displacement relative to the ground and to the bottom edge of the wall loading between failure step and first load step from GeoPIV8 (B3A1), all in pixel units

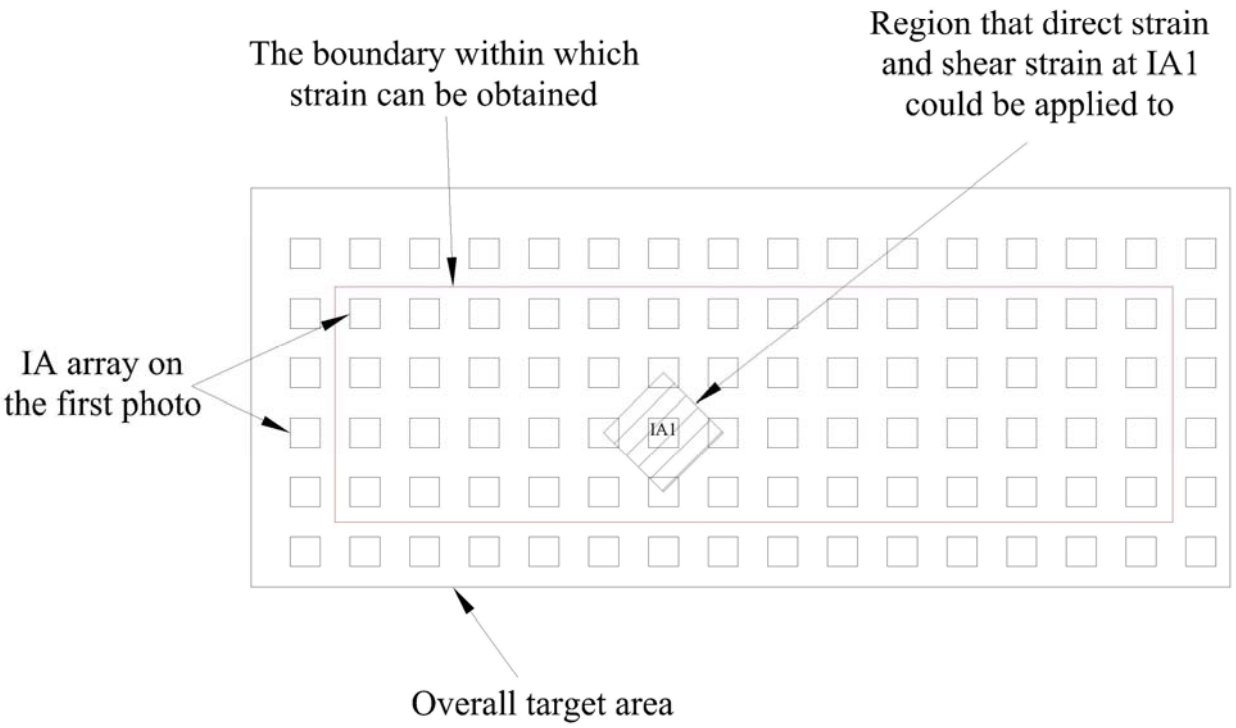

Figure 4.16 The relationship between IA array and the IAs at which ε_{xx} and ε_{zz} can be obtained

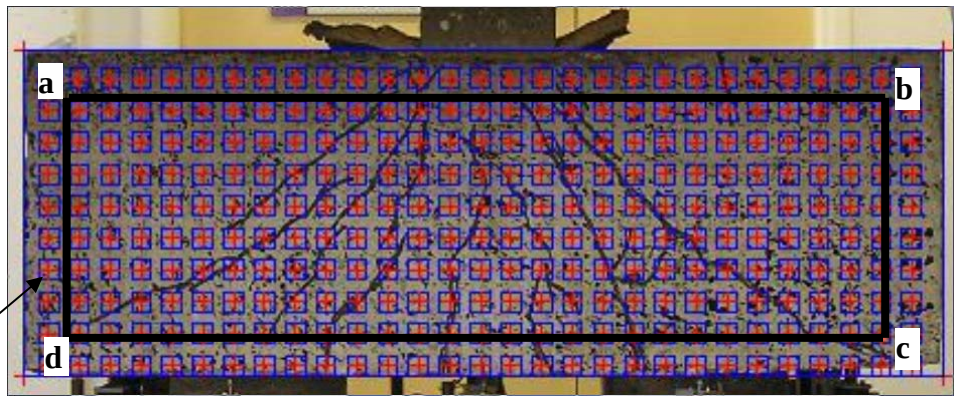

(a) *IA* division on concrete surface

Target area

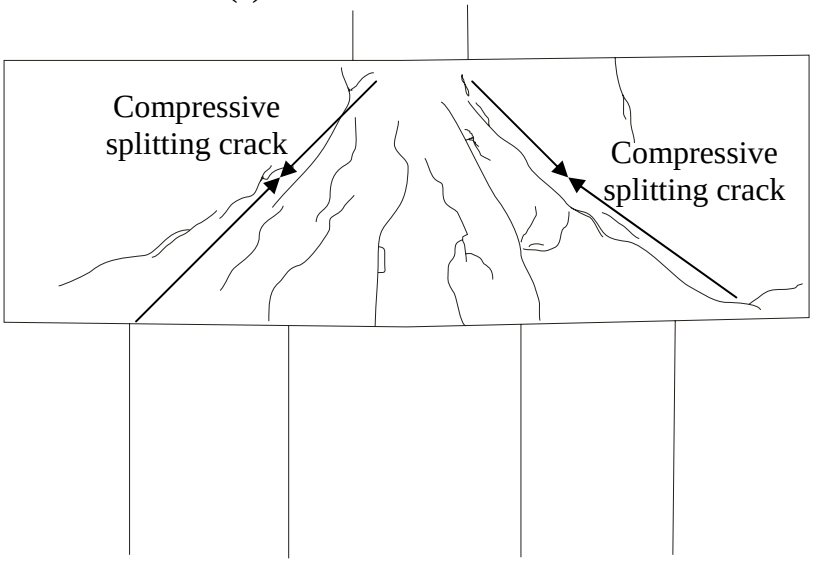

(b) Crack distribution from experiment at the onset of the yield stage

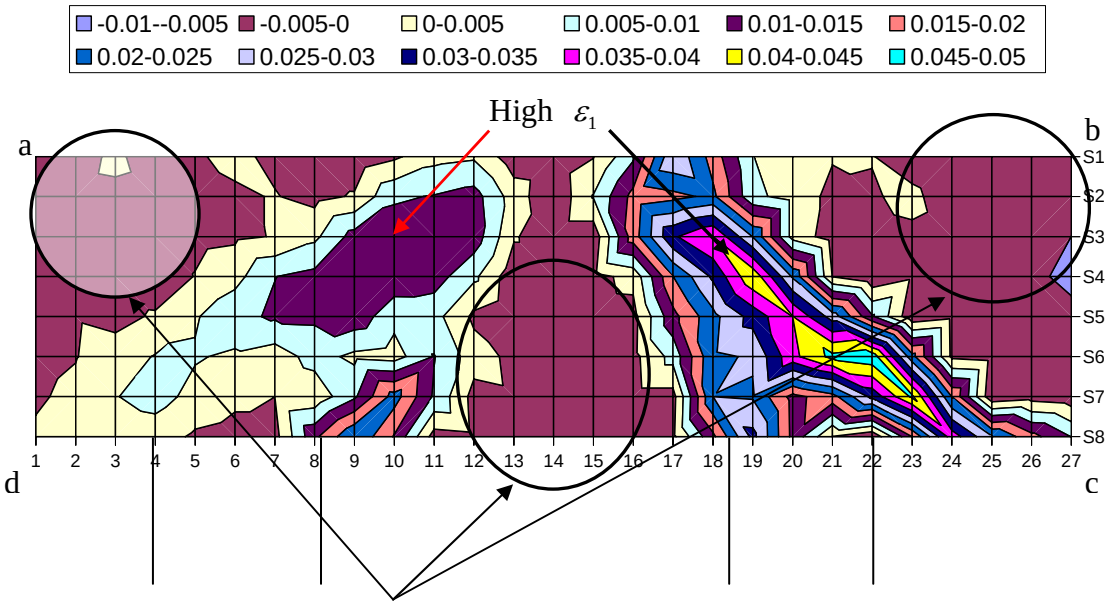

Area where random error influences the results

(c) Maximum principal strain ε_1 from PIV at the onset of the yield stage

Figure 4.17 Comparison between maximum principal strain ε_1 from PIV and crack distribution from experiment of B4A5 at the onset of the yield stage

Chapter 5 Finite element analysis of reinforced concrete pile caps

5.1 Introduction

The commercial software DIANA was used in this research. DIANA, under development at TNO since 1972, is a general purpose finite element code with the most appealing capabilities in the fields of concrete and soil (DIANA, 2002). The shear behaviour of a series of continuous RC beams without shear reinforcement was systematically investigated both by experiments and FEA using DIANA which gave satisfactory results (Keown, 2000).

FEA for the experimental samples in Batch 4, where shear failure appeared, was carried out to investigate the shear behaviour of the pile caps with a series of validation work. This validation work (Section 5.5) concentrated on the parameters of material properties and the discretisation of the mesh through the thickness of the cap. Whilst one parameter was being validated, the other parameters were fixed to a set of basic values as indicated in Sections 5.2~5.4. The optimum parameters were then used in a parametric study covering a wider range of pile cap dimensions than tested in the laboratory. The application of digital PIV to validate FEA is discussed.

The failure loads, failure mechanisms and their variation with pile cap key dimensions for models of experimental samples and models in the parametric study are presented.

5.2 Modelling procedures

5.2.1 Geometry, boundary condition and load condition

Considering the symmetry of the pile cap about its two centre lines in the longitudinal and transverse directions, only one quarter of the cap was modelled (Figure 5.1), with the assumed boundary condition as constraints only perpendicular to the boundary surfaces (Figure 5.2). The nodes on the pile base were vertically supported while the other two horizontal node freedoms were released in order to simulate the real boundary condition discussed in Section 3.6. A prescribed displacement over half the width of the full-length wall loading was applied downwards on a strip on the cap top surface (Figure 5.2).

5.2.2 Element type and mesh division

3-D 20-node isoparametric elements have been proven to be the best choice for 3-D structures (Bond, 1979). As shown in Figure 5.1, a 20-node isoparametric solid brick element

with a quadratic interpolation function and $3\times3\times3$ gauss integration scheme (CHX60, DIANA, 2002) was applied. The mesh density in the region under the wall loading was higher than in other parts of the cap. The mesh density in the piles was less than in the cap. 10 mesh layers were used in the cap body (Figure 5.1).

5.2.3 Reinforcement arrangement

The position of an individual reinforcing bar in the experimental pile caps was unlikely to influence the overall cap behaviour because of the relatively small reinforcement centre spacing (Section 3.4.2). Therefore, the reinforcement was modelled as a thin sheet located at the same level as the reinforcement in practice (Figure 5.1). The average reinforcement area per unit width of the sheet is $2.26\,mm^2/mm$ and $1.57\,mm^2/mm$ for Series A and B pile caps respectively.

In Batch 4 samples, reinforcement was placed in the piles (Section 3.4.2). A calculation showed that the contribution of the pile reinforcement only contributed 1/10 and 1/5 the total pile bending and compression stiffness respectively. Therefore piles in unreinforced concrete were modelled.

5.2.4 Bond-slip behaviour

The bond-slip behaviour between reinforcement and concrete can be modelled by introducing supplementary interface elements connecting a discrete reinforcement and its surrounding concrete (*e.g.* Hartl *et al*, 2000). Perfect bond can also be modelled by assuming the nodes in reinforcement elements and the connected nodes in concrete elements share a same displacement value. The higher the stiffness of the bond-slip behaviour, the higher the stiffness of the structure. The perfect bond assumption results in the stiffest structure with smallest deflections (Fafitis, 1994). However, the influence of the bond-slip behaviour on the load capacity is negligible (Johansson, 2000).

Considering the advantage of the simplicity of the perfect bond in FEA and that the concerns of research were the overall pile cap behaviour rather than the local behaviour (*e.g.* the interactive behaviour between the reinforcement and the surrounding concrete), the perfect bond assumption was applied.

5.3 Material properties

This section introduces the basic material properties used in FEA which differentiate the material properties used in the validation work in Section 5.5.

5.3.1 Concrete material

- **Linear stage**

Young's modulus was taken as 28000 MPa;

Poisson's ratio was taken as 0.2;

Concrete compressive strength f_{cu} was taken as the mean value from several 100 mm cube tests for each experimental sample (Section 3.5.1), and tensile strength f_t was assumed as 1/10 of f_{cu};

- **Non-linear stage**

Crack behaviour in tension region:

Constant tension cut-off for the smeared cracking model with fixed angle (Section 2.4.1) was used in the failure criterion as shown in Figure 5.3 (a);

Constitutive curve of the crack behaviour after tensile strength is reached was assumed as linear tension softening as shown in Figure 5.4;

Ultimate crack strain ε^{cr} was taken as 0.000311 (DIANA, 2005) as shown in Figure 5.4;

Behaviour in compression region:

Von Mises failure criterion was used as shown in Figure 5.3 (a).

Hardening and softening after yielding in compression region:

Ideal plasticity without hardening and softening was applied. The yield stress was taken as f_{cu}. Infinite maximum compressive strain was used. The widely acknowledged concrete maximum compressive strain 0.0035 was not used, as it was considered that the maximum compressive strain might be greater in pile caps because in most circumstances the compressive concrete strut causing failures is confined by the surrounding concrete.

Shear retention factor β was taken as constant 0.2;

5.3.2 Reinforcement

- **Linear stage**

Young's modulus was taken as 210000 MPa;

- **Non-linear stage**

Behaviour in both tension and compression regions:

The Von Mises failure criterion was used as shown in Figure 5.3 (b);

Hardening and softening after yielding in both tension and compression regions:

Ideal plasticity was taken with yield stress of $547\,MPa$. Infinite maximum strain was used as shown in Figure 5.5.

5.4 Iterative solver

5.4.1 Iterative solution method

A successful iterative solution method is necessary to solve the mathematical problem caused by non-linear material behaviour. There is little doubt that the Newton-Raphson process should be used when convergence is difficult to achieve (Zienkiewicz, 2000). Because of the difficulty in controlling the convergence of RC models, the default Newton-Raphson loading method was chosen as shown in Figure 5.6.

5.4.2 Convergence criterion

The convergence criterion adopted was to control the threshold of the energy norm ratio between two consecutive iterative steps. The energy norm was composed of the internal force vector $[F]$ and the node displacement vector $[\Delta]$. So it gave attention to both the convergence of the norm of the internal force vector and the node displacement vector which forms a trapezoidal shaded area (e.g. e_1 in Figure 5.6) under the constitutive curve (DIANA, 2002*)*.

A pilot study showed that unreasonable threshold of the criterion could cause unacceptable divergences. In co-operation with the methods in Section 5.4.3 and Section 5.4.4, an energy norm ratio ranging from 0.01 to 0.02 was found to be reasonable and was used.

5.4.3 Load step estimation

The load step was in form of a series of displacement steps which were transformed into load steps. The wall loading in the experiment was simulated by applying prescribed uniform downward displacements over the loaded area. Using this method avoids instability when the load-displacement curve turns down into a softening stage (DIANA, 2002*)*.

A linear analysis using the basic parameters (Section 5.1) was done in order to estimate the required size of the load step. Since the number of load steps in the linear stage was controlled to be not more than 20, the size of the load step was estimated as $0.05\,mm$ to $0.4\,mm$.

5.4.4 Strategy to avoid unexpected divergence

Experience from FEA of an RC beam failing in shear shows that the results may be very sensitive to the adopted iterative solver on account of the lack of convergence, or early divergence due to propagation of spurious mechanisms (Vidosa & Kotsovos, 1991).

An acceptable divergence in the FEA would occur at the same point as when the stiffness of the pile cap drops sharply in the experiment. In the real experiment, this divergence is caused by sudden stiffness drops in some parts of the structure, *e.g.* the inclined concrete strut being crushed in a compressive splitting failure, the reinforcement elongation after yield and the concrete being crushed in the compression region above a central bending crack in a bending failure and a brittle diagonal tensile failure (Section 2.2.1) in the structure failing in the linear stage. These sources of divergence should be accurately represented in a FEA.

Any other unexpected divergence not relating to any physical explanation in practice, and therefore assumed to be caused by an unreasonable iterative procedure was required to be prevented. In situations where experiment results are available, unexpected divergence in the FEA could be judged and avoided by comparing with failure load and failure type from experiments.

In this research, in order to avoid unexpected divergence, an initial estimation of the convergence criterion and the size of the load step was done (Section 5.4.2 and 5.4.3). Then, it was found to be necessary to gradually reduce the size of the load step and at the same time reduce the convergence criterion (energy norm ratio) but at a lower rate until the FEA results such as the failure load and the crack distribution at the failure step were consistent with experimental observations.

Sometimes it was difficult to judge the occurrence of unexpected divergence in the FEA because of shortage of experiment results for comparison. This required an alternative strategy, which is discussed with respect to the parametric study in Section 5.7.3.

5.5 Validation work

The FEA should be validated with experimental results before being used for further research. The target values were thus a set of experimental results that were to be validated against FEA. Target values included the load-displacement curve, crack distribution and by PIV, the distribution of displacement and strain on the cap front surface and the strain in the reinforcement. Since small strain was assumed in FEA, the strain can be compared with the PIV results where the same assumption was made (Section 4.2.4).

The experimental load-displacement curve from potentiometer 14 (Figure 3.7) was taken as the most important target value. Considering that in practice the crushing of the bedding

material at the pile base and imperfection in and the uneven elastic shortening of the piles may cause a lower stiffness of the pile cap than the ideal situation in the FEA after introducing extra rigid transition and rotation of the cap (Figure 5.7), the deflection at potentiometer 14 (centre of the soffit) relative to that at potentiometers 10 and 4 (Figure 3.7) was used *i.e.*:

$$D14' = D14 - \frac{D10 + D4}{2}$$

where $D14'$ was the relative soffit deflection at potentiometer 14 and $D4$, $D10$ and $D14$ were the absolute deflections relative to the steel platten directly read from potentiometers 4, 10 and 14 (Figure 5.7). In the FEA, $D14'$ was also taken as the displacement at the soffit centre relative to that at the position at potentiometers 10 and 4.

To be consistent with the co-ordinates system in FEA, the downward deflection read from the potentiometers was always taken as negative. The experimental load-displacement curves shown in this chapter were derived after subtracting the displacement due to creep (Figure 3.10).

5.5.1 Validation of mesh layers in the cap

Figure 5.8 is the comparison of the load-displacement curve among models with different numbers of mesh layers in B4A4 *i.e.* 10, 7 and 5. The results show that the models with 10, 7 and 5 mesh layers have similar load-displacement curves.

The basic model with 10 mesh layers (Section 5.2.2) required an average 10 hours runtime. With a reduced number of mesh layers, this time reduced sharply. The 7 mesh layers model only took about 2 to 3 hours. It was decided that 10 and 7 mesh layers be used in the models of experimental samples and models in the parametric study respectively (Section 5.7.2).

5.5.2 Validation of failure criteria for concrete in compression region

Three failure criteria available in DIANA were studied in the validation work: the total strain crack model, Drucker-Prager criterion and Von Mises criterion.

The total strain crack model, developed from MCFT (Section 2.4.1), describes the concrete constitutive behaviour under uniaxial tension and compression. The concrete properties such as the compressive strength were taken from Section 5.3.1. Concrete with fixed angle cracks and unlimited maximum compressive strain was used in the model.

In the Drucker-Prager criterion, the cohesion c was taken as $\frac{f_{cu}(1-\sin\phi)}{2\cos\phi}$, where ϕ is the friction angle, normally taken as 30° (DIANA, 2002). c and ϕ are the parameters associated with the failure envelope between the shear stress τ and normal stress σ from the maximum shear stress theory. Concrete with fixed angle cracks and linear tension softening cracking behaviour and with ideal plasticity in the compression region was used.

The Von Mises criterion was introduced in Section 5.3.1.

Figure 5.9 (a) and (b) shows the comparison of the load-displacement curves obtained from using the three failure criteria for caps B4A1 and B4A4. It can be seen that the initial stiffness of the curves from all failure criteria match well the experimental values. For B4A1, though the failure load from the total strain crack model is close to the experimental failure load, this model is not correct since B4A1 was asymmetrically failed (Table 3.5) and the real failure load should be higher than the failure load in the experiment. The failure loads from other two criteria are higher than the experimental failure load. For B4A4, the Von Mises and Drucker–Prager failure criteria can predict the failure load very well, with Drucker-Prager failure criterion prediction slightly lower than the experimental. The failure load from the total strain crack model does not match the experiment.

Figure 5.10 shows the comparison of the crack pattern on surfaces of caps from FEA using the Von Mises failure criterion with the experiment at the failure step. Figure 5.10 (a) shows that the crack pattern on B4A1 front surface matches well with FEA, both with huge inclined shear cracks, the hogging cracks above the pile head and considerable central bending cracks. Figure 5.10 (b) and (c) show the crack pattern on B4B4 top surface and soffit, in which the basic features of the crack pattern from experiment and FEA are close. For instance, as shown in Figure 5.10 (c), there are curved cracks surrounding the corner pile which are discernable both from experiment and FEA. The upward cracks on the side surface of cap B4B3 are shown in Figure 5.10 (d). The upward cracks observed in experiment also appeared in the FEA.

It is clear from the above discussion that the Von Mises failure criterion for concrete in the compression region, combined with other basic values of parameters (Sections 5.2~5.4), is a reasonable choice and therefore was used throughout the research.

5.5.3 Validation of ultimate crack strains

The ultimate crack strain ε^{cr} was taken as 0.000311 (DIANA, 2005) as a basic parameter (Section 5.3.1). ε^{cr} can also be obtained from the energy absorbed during the

maturing of a crack. As shown in Figure 5.4, for reinforced concrete, the ultimate $\varepsilon^{cr} = \frac{f_y}{E_s}$, where f_y and E_s are the yield strength and Young's modulus of reinforcement respectively. For concrete without reinforcement, the ultimate $\varepsilon^{cr} = \frac{2G_f}{f_t h_{cr}}$, where G_f is the fracture energy consumed in the formation and opening of all micro-cracks per unit area of plane (Bazant & Oh, 1983). f_t is the concrete tensile strength and h_{cr} is the estimated numerical crack bandwidth. The optimum value of h_{cr} could either be equal to three times the maximum aggregate size (Bazant & Oh, 1983) or $\sqrt[3]{V}$ where V is the volume of a solid mesh element (DIANA, 2002).

For pile caps with reinforcement along the bottom face of the caps, the elements in the cap body can be divided into two different types: the elements along the cap bottom face where the main reinforcement is located, and the elements in the remainder of the pile cap which are without reinforcement. For convenience, in this research, the elements were assumed to be either all concrete with reinforcement or all without reinforcement. It can be seen that the energy based ultimate ε^{cr} could vary with the variation of the model dimensions and mesh divisions.

Cap B4A4 (Table 3.4) was taken as an example for the validation.

If all the elements were assumed as reinforced concrete:

$$\varepsilon^{cr} = \frac{f_y}{E_s} = 547/210000 = 2.6\times10^{-3}$$

If all the elements were assumed as unreinforced concrete:

G_f may be taken from CEB-FIP (DIANA, 2002):

$$G_f = 119.24 J/m^2 (Nm/m^2)$$

If h_{cr} was taken as three times the maximum aggregate size which was approximated as $16\,mm$ based on the aggregate samples delivered to the laboratory:

$$h_{cr} = 3\times16mm = 48mm$$

Then,

$$\varepsilon^{cr} = \frac{2G_f}{f_t h_{cr}} = \frac{2\times119.24}{2.44\times48\times1000} = 2.04\times10^{-3}$$

If h_{cr} was from the volume of the elements in the FEA,

$$\varepsilon^{cr} = \frac{2G_f}{f_t\sqrt[3]{V}} = 3.24\times10^{-3}$$

where V was approximated as the mean volume of the minimum-sized mesh elements(those under the wall loading) and the maximum-sized mesh elements (those in the pile) (Figure 5.1). This shows that the energy based ultimate ε^{cr} for the samples in Batch 4 was around 0.003 for both reinforced and unreinforced concrete.

Figure 5.11 shows the comparison of load-displacement curves obtained using ultimate ε^{cr} of 0.003 and 0.000311 for B4A4. The curve with $\varepsilon^{cr} = 0.000311$ is just slightly lower than the curve with the energy based $\varepsilon^{cr} = 0.003$. Figure 5.12 shows a comparison of load-displacement curves for different ultimate ε^{cr} ranging from 0.000311 to 0.006 for B4A1 (Figure 5.4). It can be seen that the larger ε^{cr}, the stiffer the curve. The deflection at the onset of the yield stage increases with decreasing ε^{cr}. However, the failure load does not change with different ε^{cr}.

Finally, ultimate crack strain $\varepsilon^{cr} = 0.000311$ was used in all models of experimental samples and $\varepsilon^{cr} = 0.001$ was used for all the models in the parametric study because of its advantage in controlling the divergence (Section 5.7.2).

5.5.4 Validation of the hardening of reinforcement

The hardening behaviour is represented by the relationship between uniaxial stress σ and the internal state variable κ equivalent to the plastic strain in a $\sigma - \kappa$ curve (DIANA, 2002). The $\sigma - \kappa$ curve from reinforcement test showed that hardening appeared and reached a peak value at $646\,MPa$ (Section 3.5.2). In this research, it was assumed that hardening appeared after the onset of the yield stage and the hardening strain was taken as 0.006 (DIANA, 2002) as shown in Figure 5.5. Since in experiments, the hardening stage and the peak value could not be reached, the hardening model was compared with the ideal plasticity model with yield strength $547\,MPa$ (Figure 5.5).

As shown in Figure 5.13, the comparison shows that the reinforcement model with ideal plasticity gives a more accurate failure load than the hardening model, in which the failure load has a tendency to be higher than the experimental observation. The experimental load-displacement curve does not show apparent hardening behaviour (*i.e.* the curve turns immediately and keeps flat after elastic stage finishes). This may indicate that in the experiment, the hardening stage did not appear because of the potential large yield strain of the reinforcement. The peak value may appear if the experiment continued, but since large deflection of the pile cap is unacceptable in practice, it is suggested that the design stress of the reinforcement should be chosen as its yield strength rather than its peak strength.

So reinforcement with ideal plasticity with yield strength $547\,MPa$ was used in the FEA.

Table 5.1 shows the failure loads predicted by FEA, using the basic parameters, for samples in Batch 4 being compared with the failure loads V_c in the experiments. The ratio of failure loads in experiments to those from FEA is close to 1.0 for B4A4, B4A5 and B4B4. Since some of the remaining caps should have a higher shear failure load, *e.g.* B4A2 (Section 3.9.2), the ratio for them being below 1 is likely.

It is concluded from the above validation work that the basic parameters outlined in Sections 5.2~5.4 can give the closest results to the experiments. These basic parameters were then used for experimental samples to investigate the shear mechanism of pile caps. In the parametric study, these parameters were kept except for the number of mesh layers being seven, the crack strain $\varepsilon^{cr} = 0.001$ and the iterative solver being slightly changed (Section 5.7.3).

5.5.5 Discussion on the application of digital PIV to the FEA validation

The results from digital PIV were used to investigate the applicability of the technique to validate FEA using the basic parameters obtained above. B4A5 was chosen for the validation. Since B4A5 was loaded by displacement control method (Section 3.8), it was considered that the creep accumulated during the experiment was relatively low, reducing its influence on the validation work with FEA in which creep is not considered.

Ahead of the validation, extra work to verify the displacements from PIV obtained in the main experiment was carried out, in addition to the pre-test for error analysis which had already proved the accuracy of the technique (Section AI.4.2). Figure 5.15 shows the comparison of the deflection read from Potentiometers 5, 3 and 7 along the cap soffit front edge (Figure 3.7) of B4A5 in selected loading steps including the final loading step, with the relative vertical displacement v from the lowest series IAs (Section 4.3.5) at position of potentiometer 5-3-7 along $B-B$ (Figure 5.14) at the failure loading step (the positive v represents moving upward). From PIV, v of IA at potentiometer 3 relative to IAs at potentiometers 5 and 7 is $1.47\,mm$ at failure loading step. The deflection of potentiometer 3 relative to potentiometers 5 and 7 at the failure loading step is $1.28\,mm$. The two values are fairly close. It was then considered that the displacement obtained from the digital PIV was verified correct.

Figure 5.16 shows the comparison between the maximum principal strain ε_1 from PIV and crack strain ε^{cr} from FEA for B4A5 at the onset of the yield stage. It shows that the distribution of the crack strain ε^{cr} from FEA is compatible with the maximum principal strain

ε_1 from PIV, and with the crack pattern in the experiment where the central bending crack less opened and the inclined shear cracks fully matured (Figure 5.16 (a)).

Figure 5.16 (d) shows the comparison between the crack strain ε^{cr} from FEA and the maximum principal strain ε_1 from PIV along $A-A$. $A-A$ in the FEA (Figure 5.16 (c)) is not at the exactly same level as $A-A$ in the PIV (Figure 5.14), since the arrangement of the mesh in the FEA and the IA array in PIV are not the same although they are rather close. It is clearly shown that in the compressive strut area or the high strain area *e.g.* the range of the x co-ordinates between $175\,mm$ and $325\,mm$ in Figure 5.16 (d) (also see Figure 5.16 (b), (c)), the strains from FEA and PIV are higher than other areas, producing a similar hump shape.

The discrepancy between FEA and PIV in Figure 5.16 (d) is probably caused by the asymmetrical wall loading, with the wall loading tilted towards the cap front surface (see below) because of the unevenness of the stiffness of the cap and piles underneath (Section 3.9.2). This caused the strain on the front cap surface to be larger than the strain on the back surface.

Figure 5.17 shows the cap soffit deflection along the centre cap width *i.e.* the deflections read along potentiometers 6-13-14-2-3 (Figure 3.7) at different loading steps. The symmetrical deflection from FEA is also shown in the figure. The discrepancy between the FEA and potentiometers was caused by crushing of the bedding materials and shortening of the piles. The figure shows the deflection at potentiometer 3 near the cap front surface is always larger than at potentiometer 6 near the cap back surface, indicating that the cap tilted towards the cap front surface almost for all the loading steps. Figure 5.18 shows the soffit deflection along the right side of the cap *i.e.* deflections read along potentiometers 8-4-1 (Figure 3.7) which lifted up rather than deflected down since they are outside the pile centres. It can also be seen that the cap titled towards the front surface in all the loading steps.

In Figure 5.16 (d), the huge discrepancy of the strain at point ‘a’ between FEA and PIV, much higher than at point ‘b’, is supposed to be caused by the fact that in the experiment, the pile cap failed asymmetrically against centre line of cap front surface. The maximum principal strain ε_1 and the shear failure developed more quickly on the right side of the front surface than the left side (Figure 5.16 (a), Table 3.5).

Figure 5.19 shows the comparison between PIV and FEA of the resultant displacement d relative to the wall loading bottom edge (Section 4.3.7) on the B4A5 cap front surface at the onset of the yield stage. It can be seen that d from PIV has a similar distribution to d from the FEA. Figure 5.19 (c) shows the comparison of d from FEA and PIV along $A-A$ (Figure 5.19 (b)), indicating that in both cases in most positions along the cap length, d

ranges between $0\,mm$ and $5\,mm$ which are in the same order of magnitude. In both cases, d is larger far from the centre line of the cap than close to it. d from PIV is larger than from the FEA for the same reason as in the comparison for crack strain *i.e.* the wall loading tilted towards the front cap surface. The discrepancy between the FEA and PIV at point 'd' is larger than at 'c'. This is also because shear failure matured more quickly on the right side than the left side of the cap front surface.

It is concluded from the above discussion that the FEA model with basic parameters gives comparable strain and displacement results with the experimental results observed by PIV. Digital PIV can produce a full-field strain distribution which is much better than from traditional strain gauges with saving in labour and cost and enabling full-field validation of FEA output. The technique also supplies the possibility for full-field displacement validation with FEA which is impossible if using strain gauges. If the wall loading in the experiments can be controlled to be as symmetrical as possible, the discrepancy between PIV and FEA is expected to reduce to a minimum. The influence of creep was neglected in B4A5. However, the appearance of creep cannot be avoided even if the displacement control method is used as in B4A5. Considering the proportion of the deformation caused by creep at the beginning of the loading to the total creep deformation is dominant, if creep is considered in FEA, the validation work using PIV is to be more ideal.

5.6 Results from FEA for experimental samples

This section provides supporting evidence of the failure types and failure mechanisms for experimental samples from FEA output assisted by PIV. The evidences include the strain in the reinforcement, crack patterns and the distribution of Von Mises stress on the cap front surface and inside the cap body. A conclusion is further made as to how the shear mechanism of the pile cap in experimental samples can be best explained physically. Table 3.5 lists the failure types of samples in Batch 4 from the FEA, based on the crack patterns on the cap front and back surfaces. In DIANA, the positive x-direction points to the cap right surface, positive y-direction points to the cap front surface and the positive z direction is vertically upward, pointing to the cap top surface (Figure 5.1).

5.6.1 Reinforcement stress

The strain in the longitudinal reinforcement close to the cap front surface was assumed equal to the horizontal strain ε_{xx} on the cap front surface at reinforcement level, which in the experiments was read by PIV (Section 4.3.7). Samples in Batch 4 were taken for the

investigation by comparing photos at the initial and failure loading steps. As stated in Section 4.3.7, once the horizontal relative displacement of *IA*s was obtained, the average strain was calculated on a base length of 64 pixels. The distribution of ε_{xx} then can give an idea of the width of a critical crack and average strain over cracks, either at the lower end of a central bending crack or of a critical inclined shear crack.

The ε_{xx} distribution on the front surface of B4B2 is shown in Figure 5.20. The base length is approximatly $45\,mm$. It can be seen that ε_{xx} suddenly becomes high when at the lower end of major cracks. Values of ε_{xx} at the lower ends of three major cracks, either bending or shear cracks (Appendix III), in each sample are listed in Table 5.2. In each sample, concrete strain ε_{xx} and thus the strain in reinforcement closest to the cap front surface at these crack locations was above the reinforcement yield strain of 0.0026 (Section 5.5.3). Since the ends of these cracks normally locate along the longitudinal span, it is reasonable to consider that the reinforcement yielded along the whole longitudinal pile span at failure step (Figure 5.20).

This observation is proved by FEA in most samples. Figure 5.21 shows that the stress in longitudinal reinforcement σ_{sx} in B4B2 reaches yield ($547\,MPa$) on almost the whole longitudinal pile span over the cap width between the front surface and the pile head. σ_{sx} in the range of transverse pile spacing reaches $547\,MPa$ but slightly bends towards the pile head (Figure 5.21).

Two types of behaviour of the longitudinal reinforcement at the failure step in Batch 4 samples have been observed: acting as a yielding tie and not acting as a tie (either elastic or yielding *e.g.* in cap longitudinal bending behaviour). B4A1, failing in diagonal tensile shear (Table 3.5), is the only sample where the longitudinal reinforcement does not act as a tie. As shown in Figure 5.22, in B4A1, there appears a σ_{sx} gradient reducing from above $547\,MPa$ at the centre of the longitudinal span to around $300\,MPa$ above the pile head. However the rate of the reduction is lower than in a normal shallow beam.

In all the other samples in Batch 4, the longitudinal reinforcement acts as a yielding tie on the whole cap width, for example, Figure 5.21 for B2B2.

The stress in the transverse reinforcement σ_{sy} at the failure step increases with increasing transverse pile spacing. In all Batch 4 samples, tie behaviour in transverse direction, either elastic or yielding, has a tendency to form. The transverse tie action is concentrated above the pile head. In Batch 4 Series A samples, which have the smallest transverse pile

spacing, σ_{sy} is relatively low, ranging from $50\,MPa$ (B4A1) to $80\,MPa$ (B4A5). In Batch 4 Series B samples, σ_{sy} is significantly greater, ranging from 50 MPa (B4B1) to $300\,MPa$ (B4B4) and thus forming a transverse tie at high elastic stress.

Figure 5.23 (a) shows that in B4B3 ($n = 4.23, \frac{2d}{a_v} = 1.69$), a transverse tie at high elastic stress has a tendency to form at the failure step with σ_{sy} reaching between $149\,MPa$ and $239\,MPa$. This high σ_{sy} is consistent with the second character of the crack distributions (Section 3.9.1) *i.e.* as pile transverse spacing kh_w increases, the cracks on soffit becomes more 2-way, indicated by cracks occurring perpendicular to the main bending crack on the soffit. These together imply a potential bending failure or shear failure in the transverse direction of the pile cap.

5.6.2 Crack propagation and distribution

Section 3.9.1 has stated that for most samples in Batch 4, bending failure and shear failure were always very close at the failure step. This is also true in the FEA. Though many samples in Batch 4 failed by bending in the FEA, for example B4A2 (Table 3.5), wide shear cracks are also observed in FEA showing that bending failure and shear failure are very close.

For all Batch 4 samples in FEA, the compressive splitting shear crack linking the wall loading to the pile head matured at the failure step *e.g.* as shown in Figure 5.10 (a) for B4A1. For those caps observed to fail in bending in FEA, for example B4B3, the bending crack supersedes the compressive splitting shear crack only at the failure steps. Figure 5.24 shows the distribution of the crack strain ε^{cr} at the onset of the yield stage for B4B3 where such a compressive splitting crack dominates. This remains until at the failure step when ε^{cr} at the central span suddenly increases (Figure 5.10 (d)), and B4B3 fails in bending.

If considering the practical serviceability of pile caps, all the models in the FEA can be treated as having experienced shear failures *i.e.* the shear cracks caused failure before bending failure occurred.

5.6.3 Discussions of the failure mechanism in experiment samples

Based on the investigation of the stress in reinforcement from PIV and FEA (Section 5.6.1) and the crack propagation and distribution on the front and back cap surfaces (Section 5.6.2), for samples from B4A2 to B4B4, the failure mechanism points to strut-and-tie behaviour, in which the tie of longitudinal reinforcement reached yield and the tie of transverse reinforcement stays in the elastic stage.

A description of the failure mechanism by the strut-and-tie behaviour is that when the yield stage begins (the stage when the experimental load-displacement curve turns to flat as shown in Figure 3.10), the stress in the longitudinal reinforcement reaches a maximum and the longitudinal yielding tie begins to form, after which the peak value and the distribution of σ_{sx} is stable at around $547\,MPa$. The principal compressive stress p_3 and Von Mises stress σ_v of an inclined concrete strut linking the wall loading and the pile head also remain stable after the onset of yield. p_3 in the concrete strut is above the concrete strength f_{cu} because of the confinement of the concrete surrounding the strut, along which the largest crack strain ε^{cr} concentrates. The stress in the reinforcement and its stable status after yield is a result of the stable stress in the compressive strut. This forms a strut-and-tie system which last from the beginning of the yield stage to the failure step.

Figure 5.25 shows a typical example of such strut-and-tie behaviour at the onset of yield in B4A4. As can be seen in Figure 5.25 (a), the distribution of the Von Mises stress σ_v, which measures the level of the total strain energy absorbed in materials, indicates a 2-way curved concrete compressive strut bent towards the pile head. Figure 5.25 (b) shows p_3 dominating in the inclined concrete strut, exceeding f_{cu} ($24.4\,N/mm^2$, Table 3.4) in the upper part of the strut. The remaining lower part of the strut with $p_3 > f_{cu}$ bends inwards into the cap and towards the pile head which cannot be seen on the front surface (refer Figure 5.25 (a)). The distribution of crack strain highlighting the critical compressive splitting shear crack at the onset of yield, which finally develops to shear failure (Figure 3.13), is shown in Figure 5.25 (c). The shear crack along the concrete strut is caused by the inclined concentration of σ_v and p_3. The equivalent compressive concrete strut thus links the pile head and somewhere between the centre of the cap top and top front edge, as shown by a dash arrow in Figure 5.25 (a). In Figure 5.25 (d), the high σ_{sx} indicates a longitudinal yielding tie beginning to form at the onset of the yield stage, which lies on the whole cap width at failure step. σ_{sy} in B4A4 is around $60\,MPa$ at failure.

Figure 5.22 shows that the longitudinal reinforcement in B4A1 does not act fully as a tie. However, considering the rate of the reduction of σ_{sx} is less than in a normal shallow beam (Section 5.6.1) and σ_{sx} keeps above $400\,MPa$ along the longitudinal span, the failure load and failure mechanism in B4A1 can also be represented by the strut-and-tie behaviour.

Figure 5.23 (b) shows how the reinforcement stress σ_{sx} in B4B3 ($n = 4.23$) differs from what is specified in STM in current British Standards. The transverse pile spacing for B4B3 is

more than three times the pile diameter**.** It can be seen that on the whole cap width, σ_{sx} reaches yield such that the width of the yielding tie over each pile is larger than triple the pile diameter specified in BS8110 and BS5400 (Section 2.10.3).

5.7 Parametric study

The information from the models of the experimental samples is rather limited. It is necessary to expand the model range in a parametric study to obtain a more general view of the failure mechanisms of pile caps. In this parametric study, the only variables were the longitudinal and transverse pile spacing (Section 5.7.1), while other dimensions and material properties *etc*. were kept unchanged from previously (Section 5.7.1 and 5.7.2). As there were no experimental results available for validation, it is important to emphasize that all the results are only as accurate as the basic assumptions made in the FEA (Rombach, 2004).

5.7.1 Model dimensions

88 models under full-length wall loading were analysed. The range of dimensions is shown in Table 5.3. The longitudinal and transverse pile spacings kh_p and kh_w varied from $300\,mm$ to $1200\,mm$ and from $150\,mm$ and $1200\,mm$ respectively. Other pile cap dimensions were consistent with samples in Batch 4 *i.e.* the cap depth h =$230\,mm$, pile diameter h_p =$130\,mm$, pile depth d' =$260\,mm$, longitudinal overhang h_o =$150\,mm$ and transverse overhang h_o =$100\,mm$ (Table 3.3 (a)). The naming convention for the models, *e.g.* E1ij, is explained in Table 5.3.

Therefore, a wide range of shear enhancement factors $\frac{2d}{a_v}$ and ratio of the transverse pile spacing over the pile diameter n $\left(=\frac{kh_w}{h_p}\right)$ occurred in the parametric study (Table 5.3). Since in BS8110 if $n>3$, the cap width on which the shear enhancement factor applies (Section 2.10.1) and the width of the longitudinal tie for STM (Section 2.10.3) are limited to three times the pile diameters centred on each pile, n for E1*f model series was defined as 3 to investigate the validity of the current standards. The range of $\frac{2d}{a_v}$ and n for the experimental samples in all batches are shown in Table 5.3, enclosed by bold dash lines, showing that they lie within the bounds of the parametric study.

5.7.2 Mesh division and material properties

Mesh division was kept as same as in the models of the experimental samples, but with seven mesh layers through the cap thickness instead of 10.

Reinforcement was diameter $12\,mm$ bars at $50\,mm$ spacing in both longitudinal and transverse directions with bar centre at depth $31\,mm$ above the soffit. The average reinforcement area per unit width was thus taken as $2.26\,mm^2/mm$. Reinforcement yield strength was taken as $547\,MPa$. Concrete strength f_{cu} and f_t were taken as $25\,MPa$ and $2.5\,MPa$ respectively. In order to avoid piles being crushed before the cap fails, f_{cu} for the concrete piles was taken as $100\,MPa$. The ultimate crack strain ε^{cr} was taken as 0.001 to avoid unacceptable divergence.

All other parameters were taken as those for the models of the experimental samples (Sections 5.2~5.4). Based on Figure 2.16 (a) and (b), the discrepancy ratio of whole *Part I~III* of *Eq*.2.5 over *Eq*.2.6 (Section 2.10.1) for the 88 models was kept constant being $0.946\times1.00=0.946$. The 88 models eventually covered a wide range of the discrepancy ratio between *Eq*.2.5 and *Eq*.2.6 from 0.94 to 1.79.

5.7.3 Judgement of failure modes in FEA

Section 5.4.4 described the strategy to avoid unexpected divergence. But this strategy would not be effective in the parametric study since there are no experimental results available to judge whether a divergence is acceptable or not expected. The iterative solver to deal with this issue in the parametric study is described below.

The default Newton-Raphson loading method with a convergence criterion using energy norm ratio was taken. The range of load step size was from $0.2\,mm$ to $2\,mm$. The convergence criterion ranged from 0.005 to 0.05, more widely than the 0.01 to 0.02 used for experimental samples (Section 5.4.2) since there was expected to be a wider range of failure modes in the parametric study. At start, a series of prescribed load steps were applied with a certain convergence criterion within the range. If divergence happened, when structure either in the yield stage or while still in elastic, the failure load was judged in the context of that for other models, to check whether it followed a logical trend or not. If not, the analysis was repeated by gradually reducing convergence criterion and load step size. Especially if divergence happened in elastic stage, a reduced load step size was adopted and at the same time the convergence criterion was reduced but in a lower rate. This repetition continued until the curve went into the plastic stage or the failure load followed a logical trend of failure loads or

until the lower end of the load step range $0.2\,mm$ and lower end of the convergence criterion 0.005 were reached.

Once all the failure loads followed a logical trend, they were assumed to be the correct failure loads. Correct failure load involving divergence in the elastic stage was assumed to mean that the cap failed in a brittle way or failed in shear failure.

5.8 Results from parametric study

This section describes the failure loads and failure mechanisms for models in the parametric study. Figure 5.26 is a 2D surface plotting failure load V_c against the longitudinal and transverse pile spacing kh_w and kh_p. V_c increases with increasing kh_w, n or decreasing A. V_c also increases with decreasing kh_p or increasing $\frac{2d}{a_v}$. Most models fail in a ductile way.

Whether the failure is by bending and shear failure is judged based on the crack distribution on the front surface of caps, though in 2-way spanning pile caps the bending and shear failures as seen in 1-way spanning RC beams are impossible. Transverse bending or shear failures did not appear in all the parametric models.

Table 5.4 (a) shows the distribution of bending and shear failures and the occurrence of the longitudinal yielding reinforcement ties in the 88 parametric models. Caps with large kh_p fail by bending with huge central bending cracks (*e.g.* Figure 5.27), with σ_{sx} in the reinforcement having a similar distribution to Figure 5.22 and the longitudinal yielding tie does not begin to form. Compressive splitting shear cracks on the cap front surface become more apparent when $\frac{2d}{a_v}$ increases *e.g.* as shown in Figure 5.28. The longitudinal yielding tie occurs similar to Figure 5.21.

Table 5.4 (b) shows the distribution of the occurrence of yielding longitudinal reinforcement on the whole cap width at mid span either in shear or bending failures. In caps with large kh_w and relatively small kh_p, this yielding has a tendency to occur just on a strip over each pile head rather than over the whole cap width (*e.g.* Figure 5.29).

The strip width of σ_{sx} in yielding could be larger than three times the pile diameter for those pile caps with $n > 3$. For instance, as shown in Figure 5.30, in cap E1ei ($n = 4.62$) the longitudinal reinforcement yields across the whole cap width. This goes against the assumption of the current STM in BS8110 which specifies the width of the yielding tie to be three times the pile diameter for $n > 3$ (Section 2.10.3). The definition of the maximum cap

width of triple the pile diameter that $\frac{2d}{a_v}$ is applied, which is considered related to the strut-and-tie behaviour (Section 2.10.3), and the shear enhancement application factor A in BS8110 therefore lack a physical explanation (Section 2.10.2).

Table 5.4 (c) shows the distribution of the occurrence of high elastic stress or yielding in the transverse reinforcement ties. With increasing kh_w, the influence of the transverse reinforcement increases, which cannot be neglected in the shear resistance. Figure 5.31 shows the σ_{sy} distribution in E1ej. It can be seen that a transverse tie with σ_{sy} exceeding $547\,MPa$ appears. Normally the transverse tie concentrates on the pile head.

Compared with the description in Section 5.6, it is clear that failure types in experimental samples conforms that in the models in parametric study being enclosed by the bold dash lines in Table 5.4 (a) (b) (c).

5.9 Summary

This chapter explains the choices of the parameters in non-linear FEA of RC pile caps. Some of the parameters, especially those related to the material properties were validated with experimental observation. Instead of traditional strain gauges, the experimental observations from digital PIV such as the displacement and strain distribution on the cap front surface were used for the validation work. The optimal parameters from validation work were applied in 88 models in a parametric study expanded from the models of the experimental samples.

The results from the FEA of the experimental samples and models in the parametric study have been used to explain the shear mechanism of the pile caps under full-length wall loading. Strut-and-tie behaviour has been observed in most Batch 4 samples both from experiments and FEA. The behaviour involves a compressive concrete strut, a yielding tie in the longitudinal direction and an elastic tie in the transverse direction. For models in the parametric study, it is found that the failure loads and failure types represented by the stress distribution in reinforcement in both directions and the crack distribution on the cap front surface vary with the key size dimensions of $\frac{2d}{a_v}$, A or n.

The width of the longitudinal yielding tie over each pile in some models in experimental samples and parametric study is larger than three times the pile diameter, which defies the specifications for definition of shear enhancement application factor A in bending theory based design formula and the longitudinal tie width in STM in BS8110. The transverse reinforcement plays an important role in the shear resistance, as a tie either in high elastic

stress or yielding, when kh_w increases. This is not considered in either the bending theory based design formulae or STM in current British Standards. In designing shear capacity of pile caps, yielding stress rather than peak stress of reinforcement is suggested to be used. The hardening behaviour of longitudinal reinforcement may not appear before shear failure happens.

Through the validation work, the applicability of digital PIV to the analysis for RC structures has been proved, showing the advantage over the traditional strain gauges. The quality of the validation using PIV in this research could be further improved after ensuring symmetrical loading and involving the time effect of creep in the FEA.

Two samples of the batch commands read by iDIANA (DIANA, 2002) to simulate the models of experiment samples and in the parametric study are included in Appendix IV.

Table 5.1 Comparison of the failure loads between experiments and FEA using basic parameters

Pile cap No.	Failure load in experiments $V_c\,(kN)$	Prediction by FEA (kN)	Ratio of failure load in experiments over FEA
B4A1	592	632	0.94
B4A2	548	820	0.67
B4A3	919	1008	0.91
B4A4	1052	1064	0.99
B4A5	1244	1244	1.00*
B4B1	622	605	1.03
B4B2	713	812	0.88
B4B3	769	924	0.83
B4B4	1048	1040	1.00

*B4A5 failed mainly by the crushing of piles (Table 3.5). This is also the failure type in FEA. However, the real shear failure load was close to the observed failure load $1244\,kN$ (Section 3.9.2).

Table 5.2 Horizontal strain ε_{xx} on cap front surface at the lower end of bending cracks and shear cracks at longitudinal reinforcement level in the failure step measured by PIV

Pile cap No.	ε_{xx}		
B4A1	0.0659	N/A*	N/A
B4A2	0.0117	N/A	N/A
B4A3	0.0588	0.0477	0.0506
B4A4	0.0413	0.0548	0.0388
B4A5	0.0263	0.0389	N/A
B4B1	0.0675	0.0254	0.3172
B4B2	0.0210	0.0259	0.0238
B4B3	0.0297	0.0538	N/A
B4B4	0.0040	0.1236	0.0103
Three major cracks either bending or shear cracks	Crack 1	Crack 2	Crack 3

*No critical shear or bending cracks appeared

Table 5.3 Model dimensions in parametric study
All dimensions in *mm*

Range of the experimental samples

$kh_p(\frac{2d}{a_v})$ \ $kh_w(n)$		a 150 (1.15)	b 200 (1.54)	c 260 (2.00)	d 300 (2.31)	e 350 (2.69)	f 390 (3.00)	g 500 (3.84)	i 600 (4.62)	j 800 (6.15)	k 1000 (7.69)	l 1200 (9.23)
E1d	300(6.52)											
E1e	350(4.63)											
E1f	390(3.75)											
E1g	500(2.47)											
E1i	600(1.89)									E1ij		
E1j	800(1.28)											
E1k	1000(0.97)											
E1l	1200(0.78)											

Table 5.4 Distribution of failure types for models in parametric study
All dimensions in *mm*

Range of the experimental samples

(a) Distribution of shear failure or bending failure on cap front surface and the occurrence of longitudinal yielding reinforcement ties

$kh_p(\frac{2d}{a_v})$ \ $kh_w(n)$		a 150 (1.15)	b 200 (1.54)	c 260 (2.00)	d 300 (2.31)	e 350 (2.69)	f 390 (3.00)	g 500 (3.84)	i 600 (4.62)	j 800 (6.15)	k 1000 (7.69)	l 1200 (9.23)
E1d	300(6.52)											
E1e	350(4.63)											
E1f	390(3.75)											
E1g	500(2.47)											
E1i	600(1.89)											
E1j	800(1.28)											
E1k	1000(0.97)											
E1l	1200(0.78)											

	Shear failure (Longitudinal reinforcement yielding tie occurs)
	Bending failure (Longitudinal reinforcement yielding tie does not occur)

Table 5.5 Distribution of failure types for models in parametric study
All dimensions in *mm*

– – – – Range of the experimental samples

(b) Distribution of occurrence of yielding longitudinal reinforcement on the whole cap width or not at mid span

$kh_p(\frac{2d}{a_v})$ \ $kh_w(n)$		a 150 (1.15)	b 200 (1.54)	c 260 (2.00)	d 300 (2.31)	e 350 (2.69)	f 390 (3.00)	g 500 (3.84)	i 600 (4.62)	j 800 (6.15)	k 1000 (7.69)	l 1200 (9.23)
E1d	300(6.52)											
E1e	350(4.63)											
E1f	390(3.75)											
E1g	500(2.47)											
E1i	600(1.89)											
E1j	800(1.28)											
E1k	1000(0.97)											
E1l	1200(0.78)											

	Longitudinal reinforcement yield not on the whole cap width
	Longitudinal reinforcement yield on the whole cap width

(c) Distribution of occurrence of high elastic stress or yielding in the transverse reinforcement ties or not

$kh_p(\frac{2d}{a_v})$ \ $kh_w(n)$		a 150 (1.15)	b 200 (1.54)	c 260 (2.00)	d 300 (2.31)	e 350 (2.69)	f 390 (3.00)	g 500 (3.84)	i 600 (4.62)	j 800 (6.15)	k 1000 (7.69)	l 1200 (9.23)
E1d	300(6.52)											
E1e	350(4.63)											
E1f	390(3.75)											
E1g	500(2.47)											
E1i	600(1.89)											
E1j	800(1.28)											
E1k	1000(0.97)											
E1l	1200(0.78)											

	Transverse reinforcement tie in high elastic stress or yielding occurs
	Transverse reinforcement tie in high stress or yielding does not occur

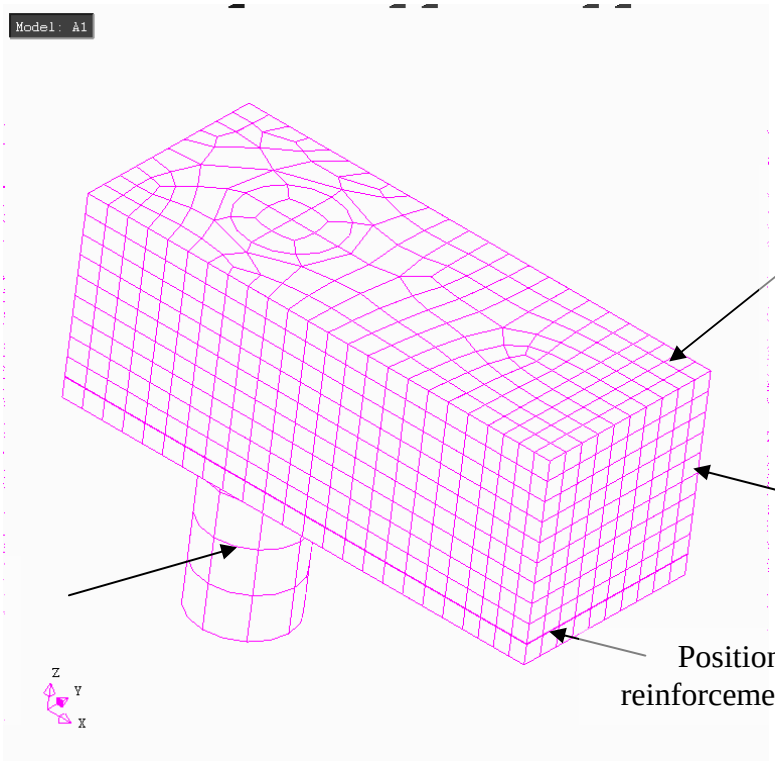

Figure 5.1 A basic geometry and mesh division of model of ¼ of an experimental pile cap

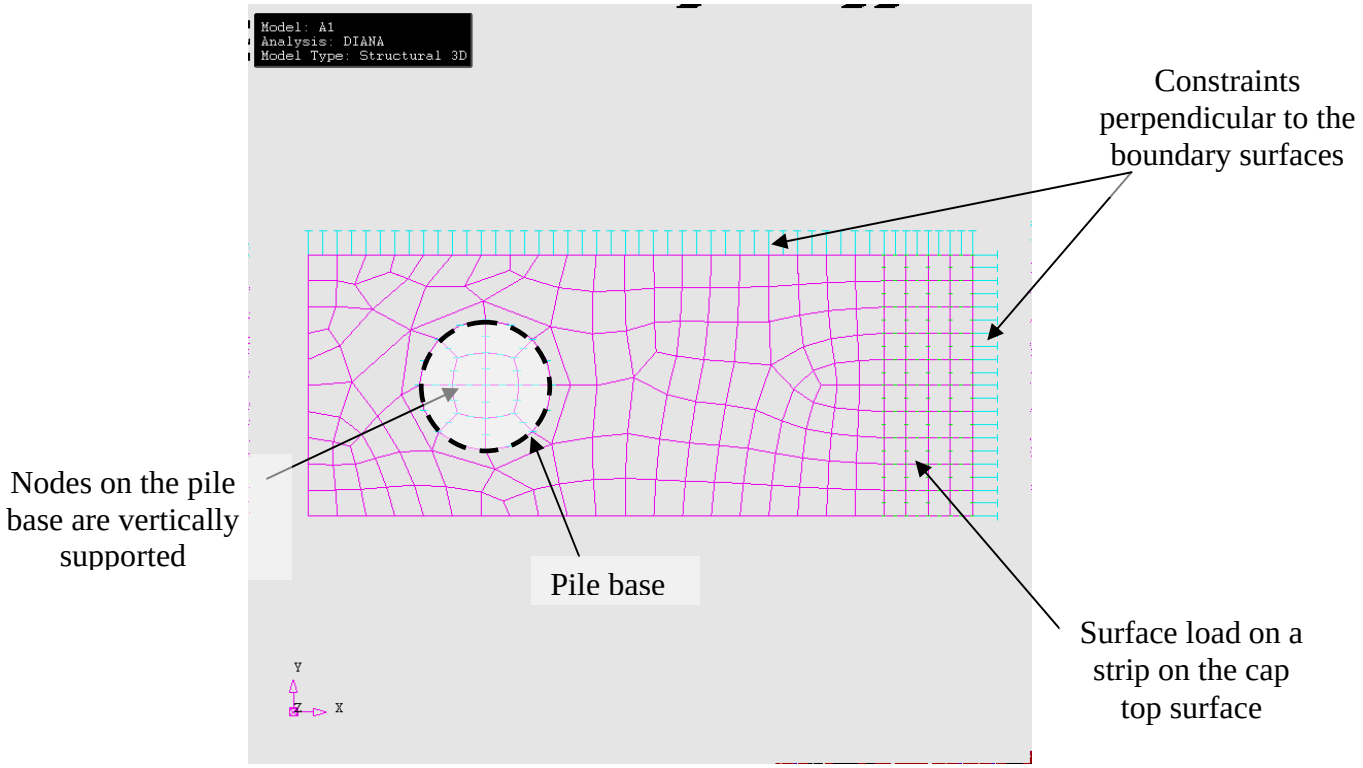

(a) Plan view

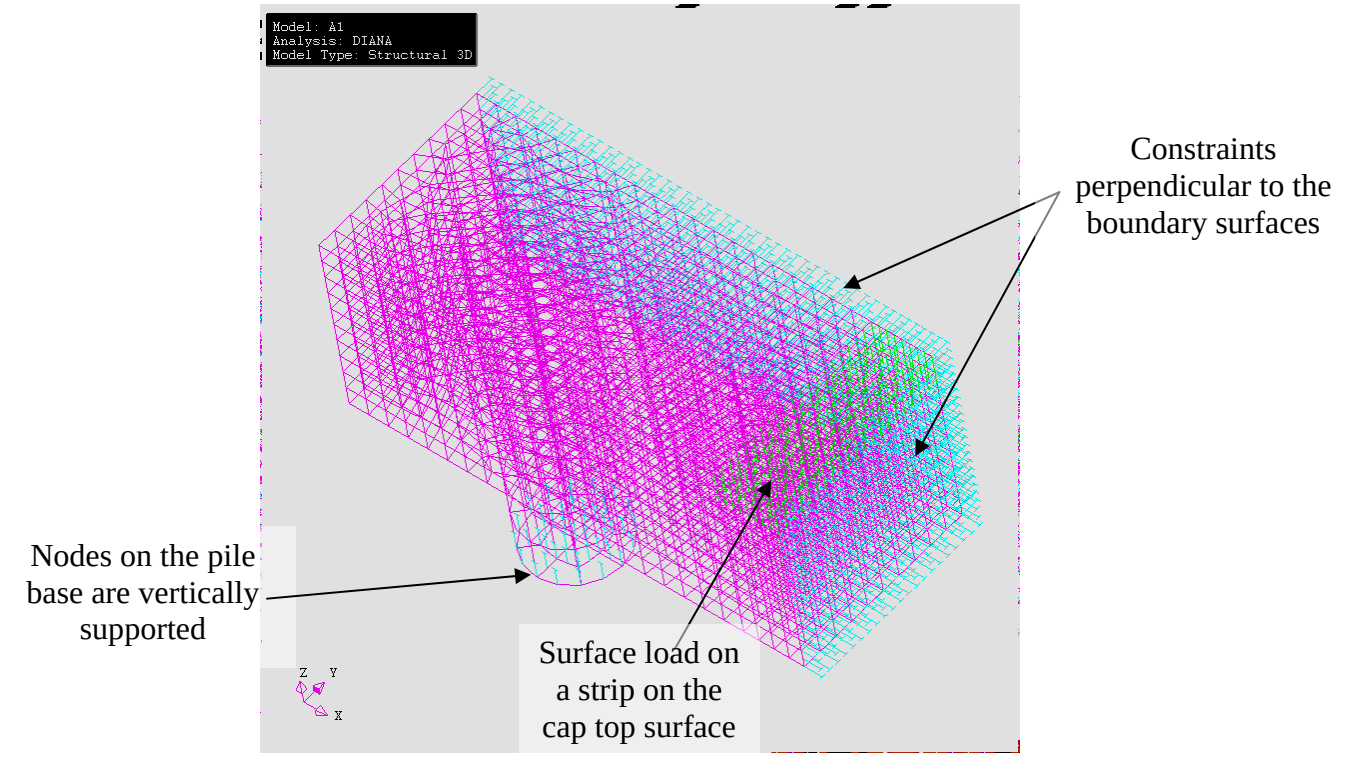

(b) Isometric view

Figure 5.2 The boundary conditions and load conditions of a pile cap model

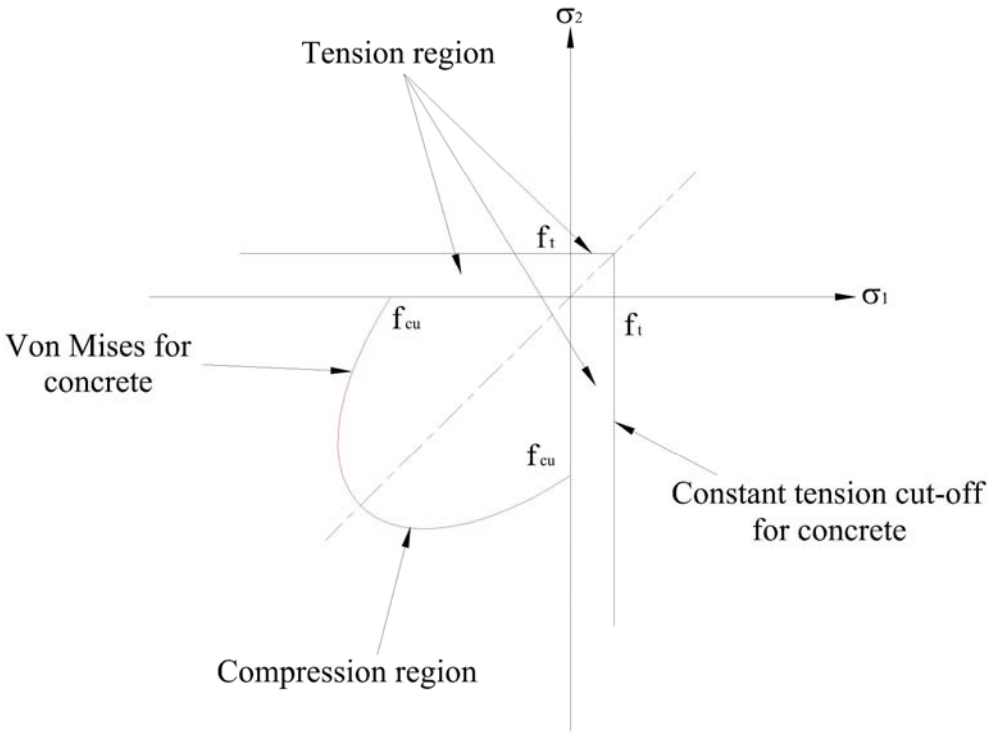

(a) Failure criteria for concrete

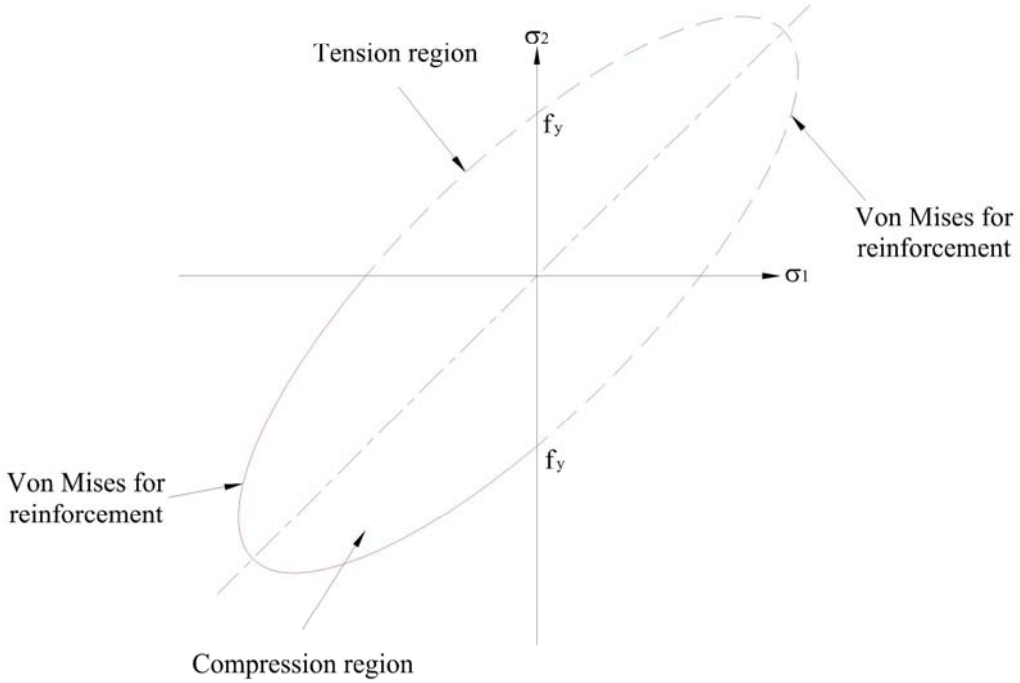

(b) Failure criteria for reinforcement

Figure 5.3 The failure criteria for concrete and reinforcement (not in scale)

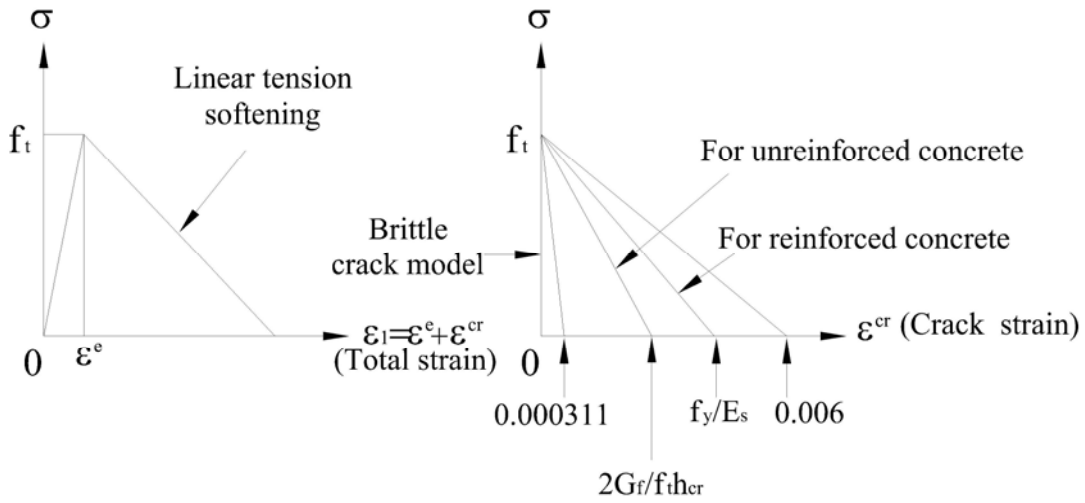

Figure 5.4 The linear tension softening behaviour of concrete after crack appears

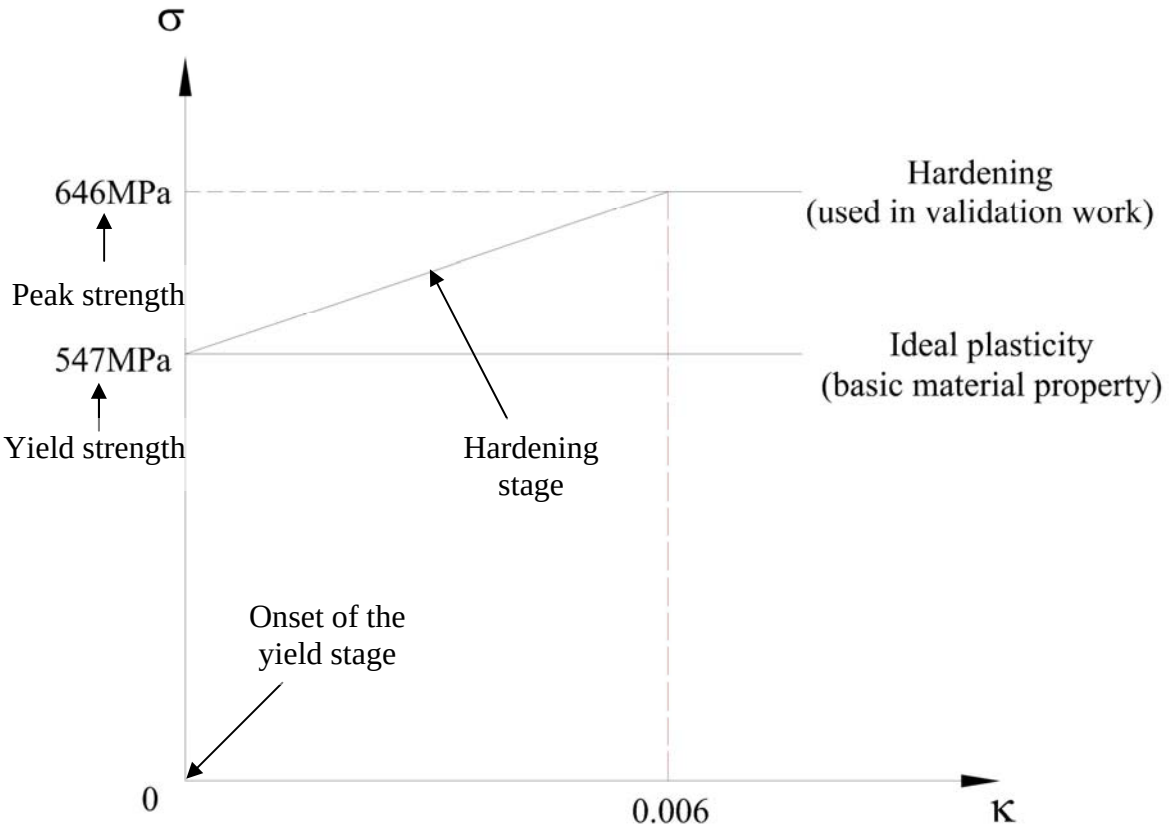

Figure 5.5 Hardening behaviour of reinforcement in both tension and compression regions (κ : internal state variable equivalent to plastic strain) (not in scale)

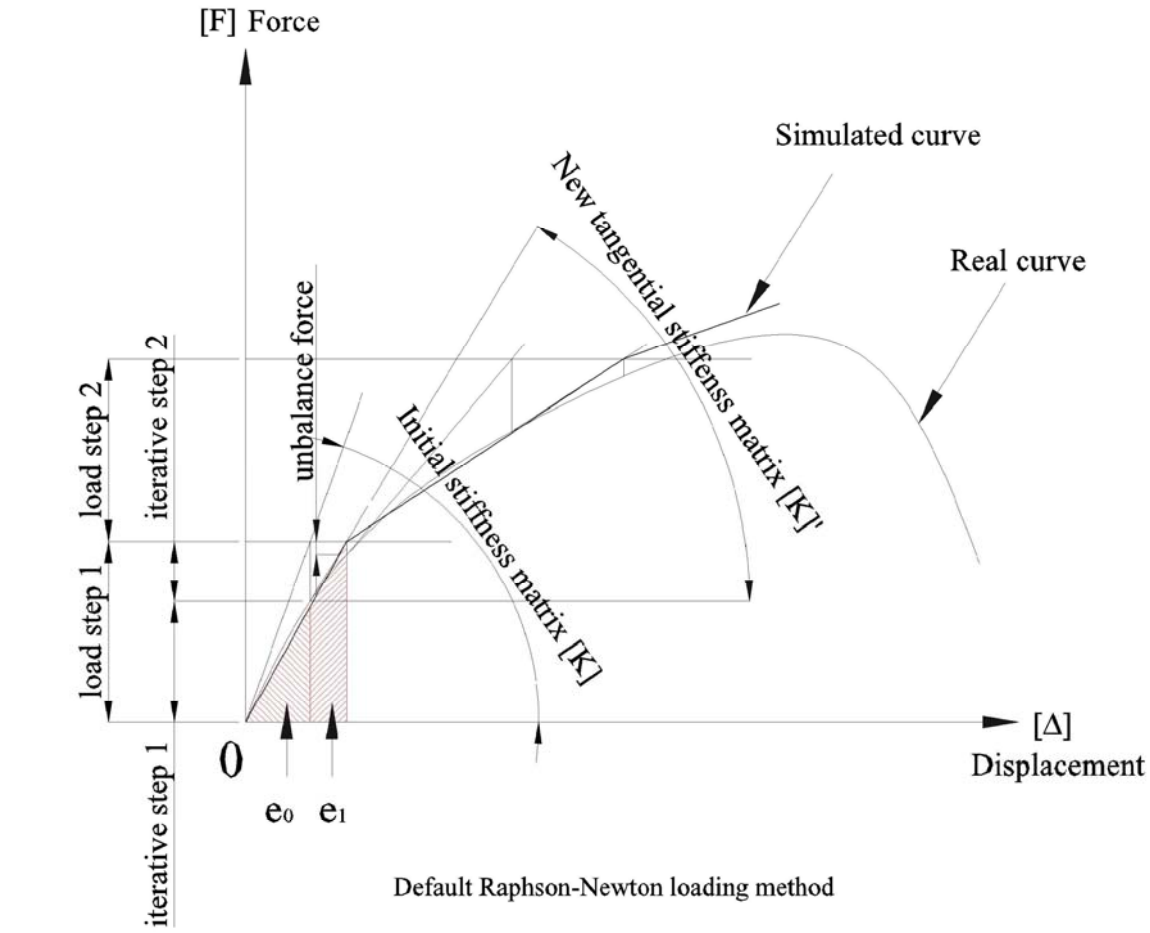

Figure 5.6 Iterative solver

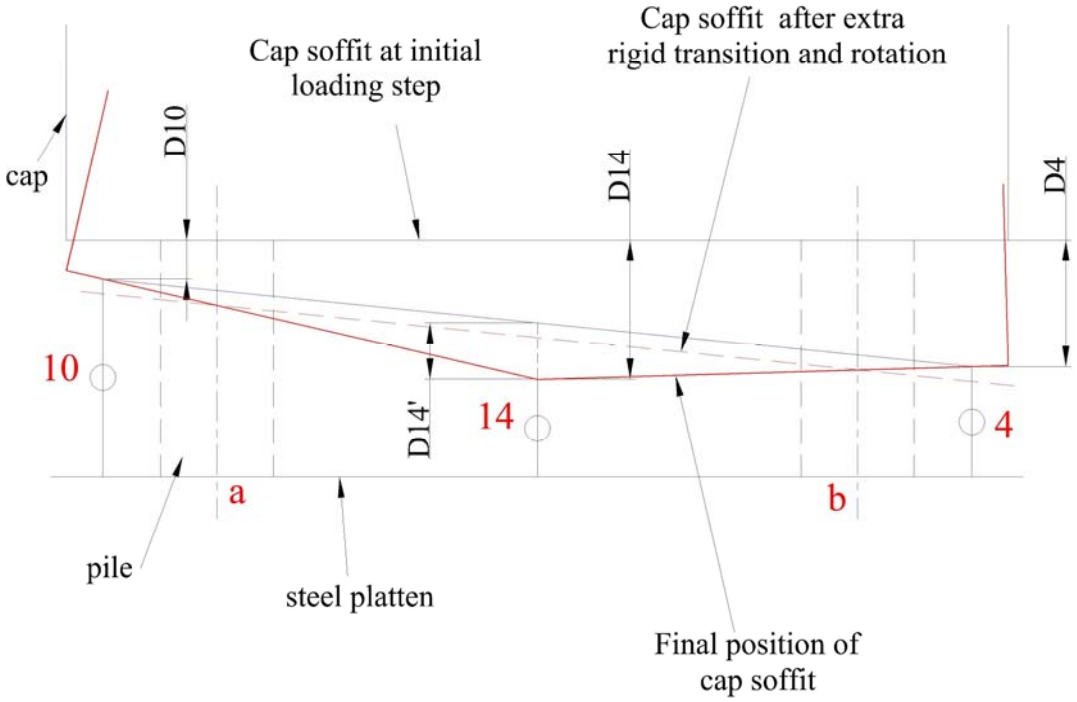

Figure 5.7 The schematic of the calculation of *D*14'

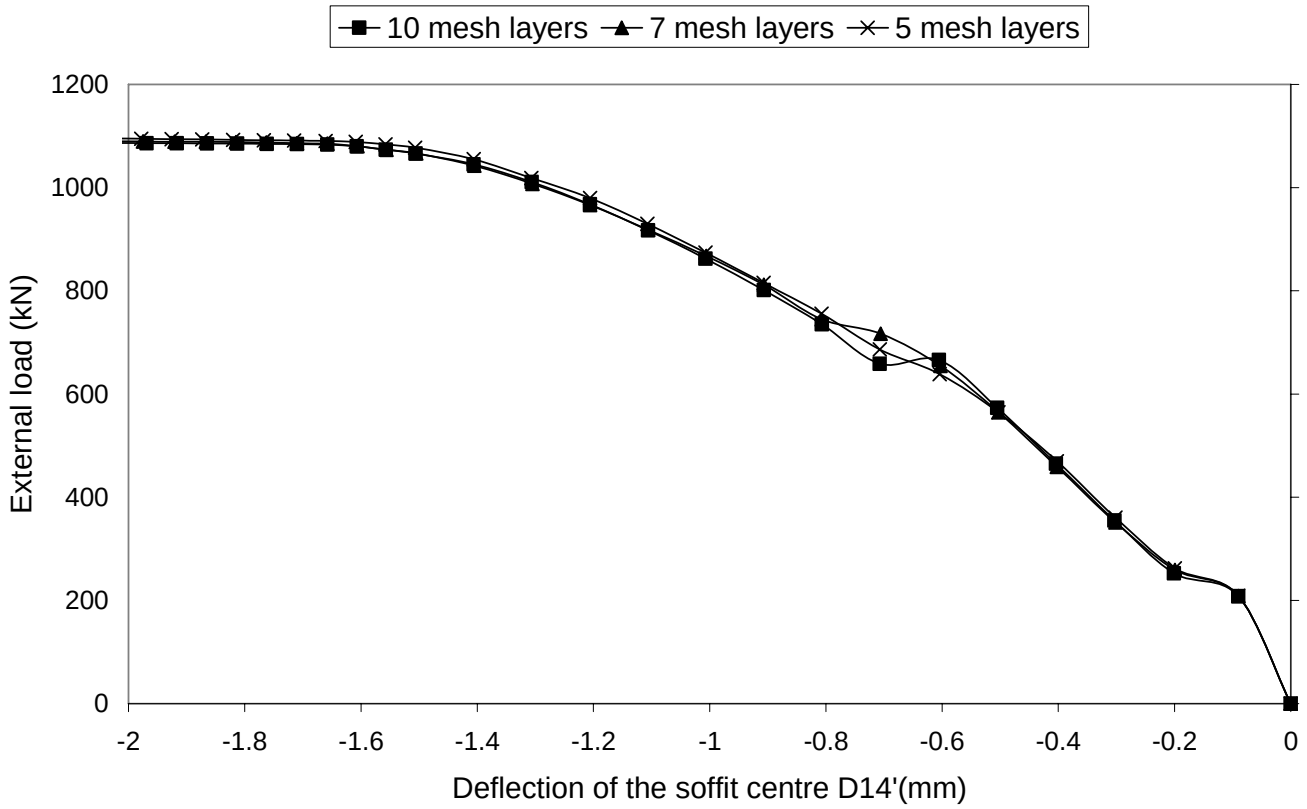

Figure 5.8 Comparison of the load-displacement curves for models with 5, 7 and 10 cap mesh layers (B4A4)

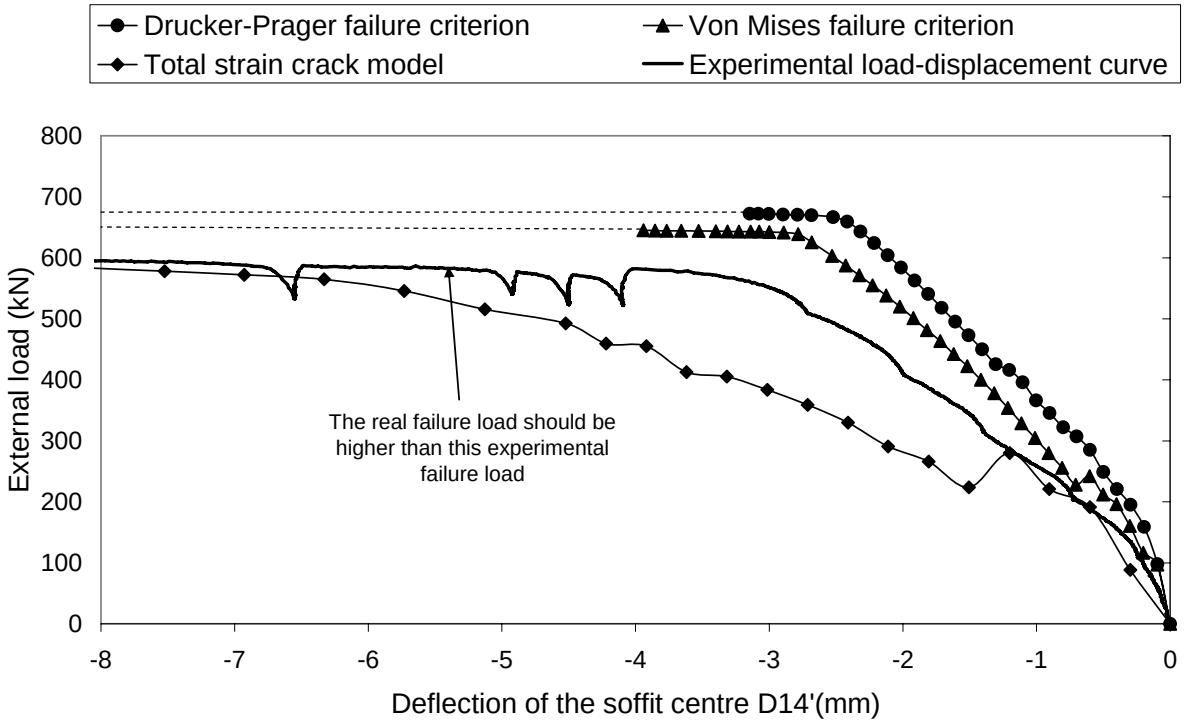

(a) B4A1

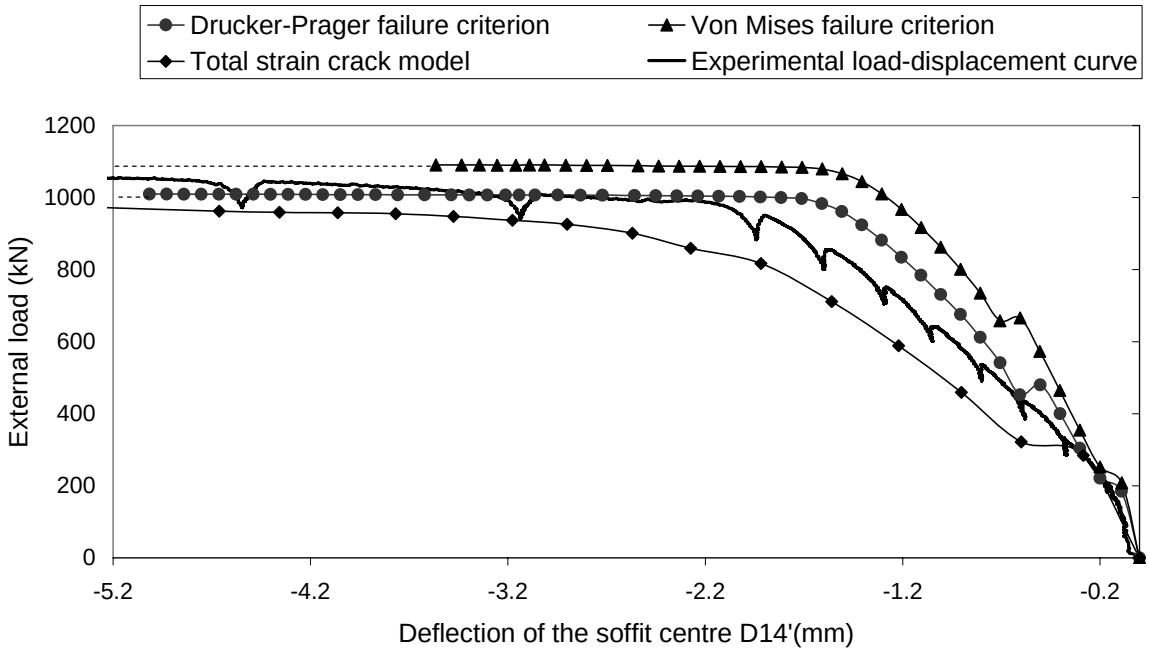

(b) B4A4

Figure 5.9 Comparison of the load-displacement curve among different failure criteria

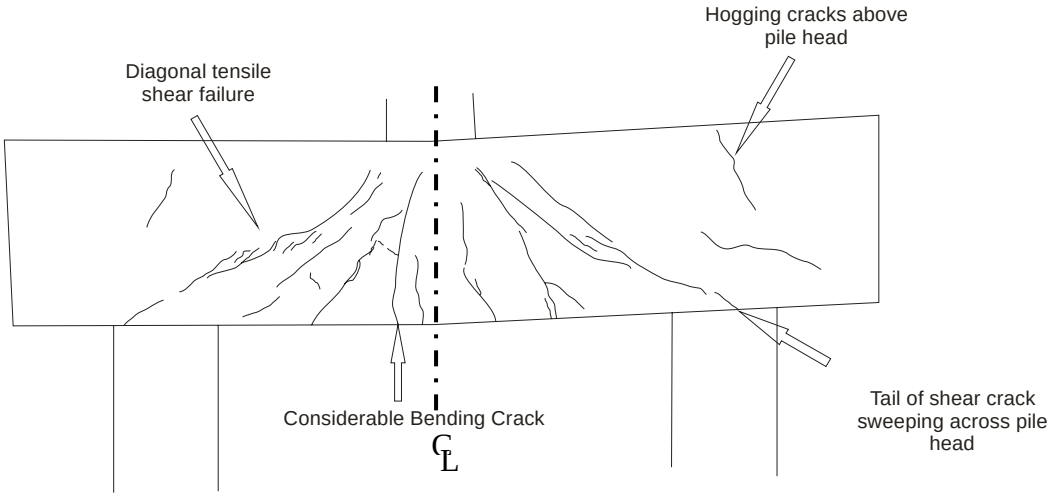

Observed crack pattern

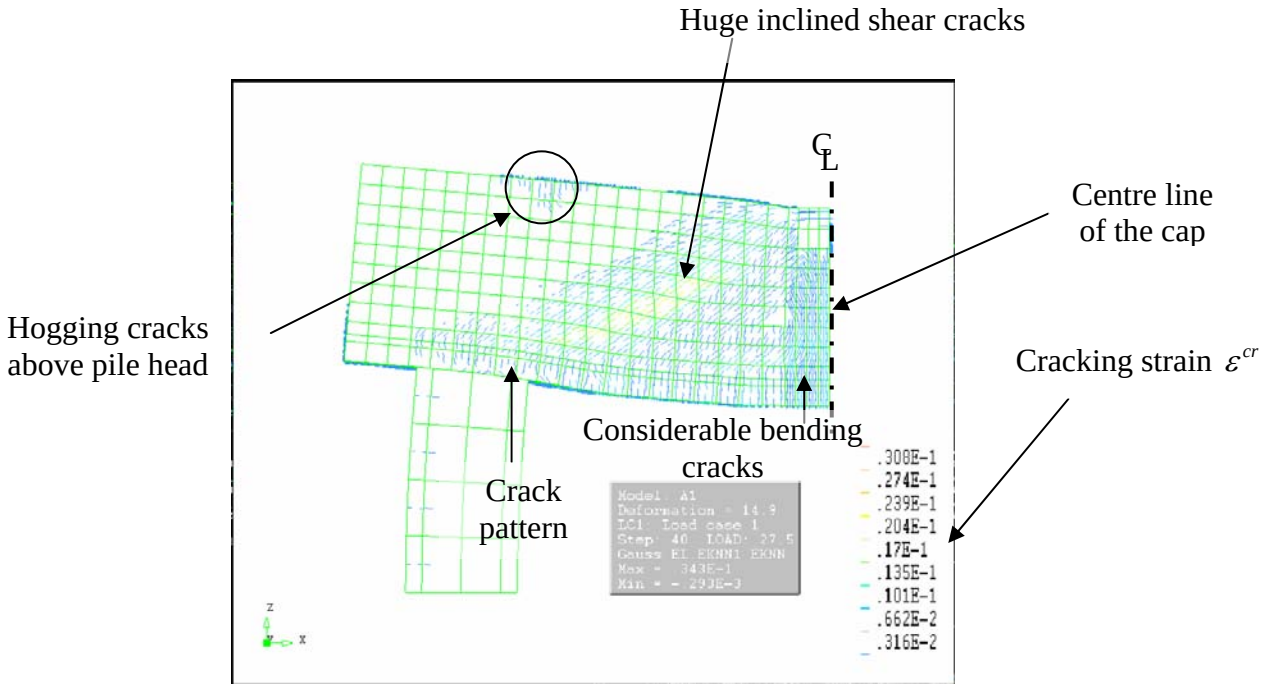

(a) B4A1 front surface

Figure 5.10 Comparison of crack pattern from experiment with cracking strain ε^{cr} and crack pattern from FEA using Von-Mises failure criterion at failure step

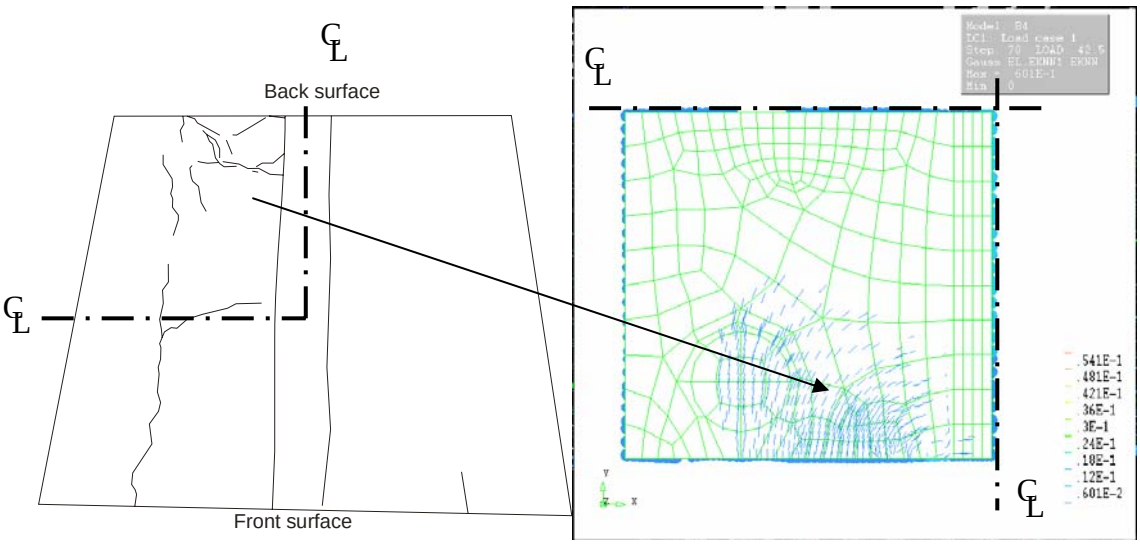

(b) B4B4 top surface

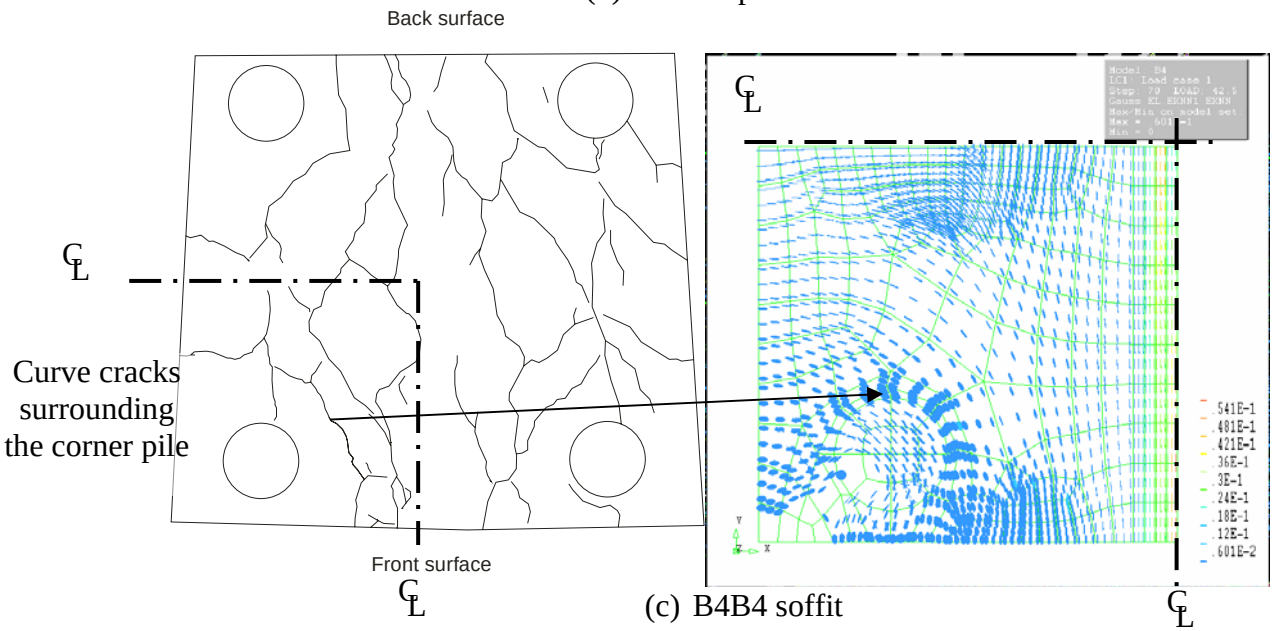

(c) B4B4 soffit

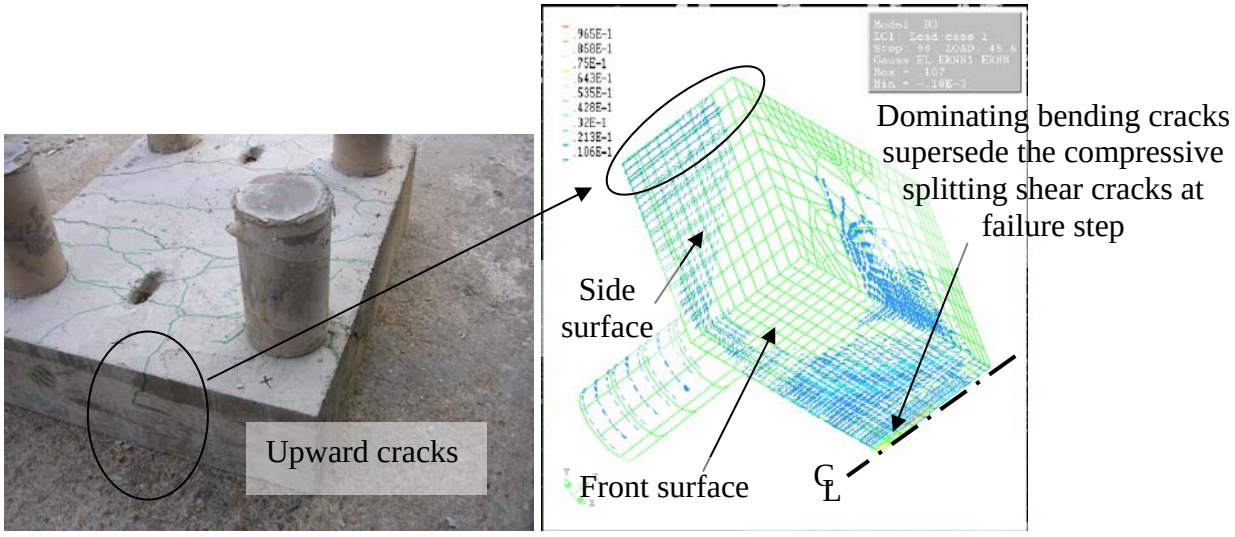

(d)B4B3 side surface

Figure 5.10 Comparison of crack pattern from experiment with cracking strain ε^{cr} and crack pattern from FEA using Von-Mises failure criterion at failure step

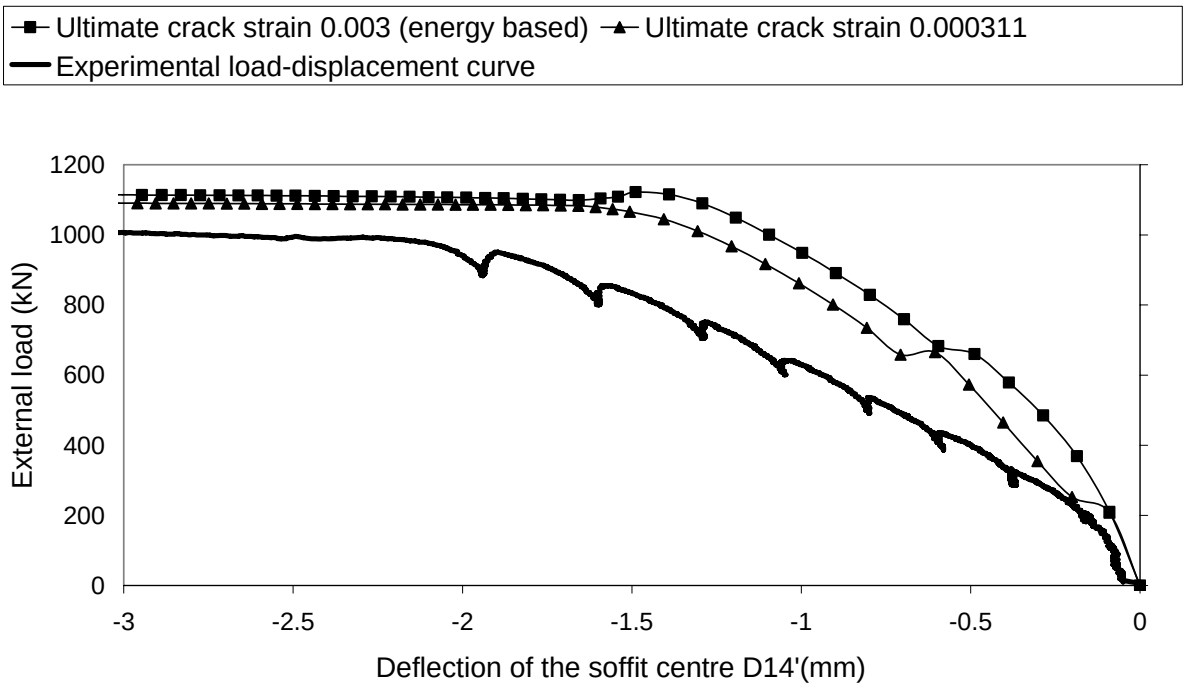

Figure 5. 11 Comparison of the load-displacement curve between different ultimate crack strain ε^{cr} for B4A4

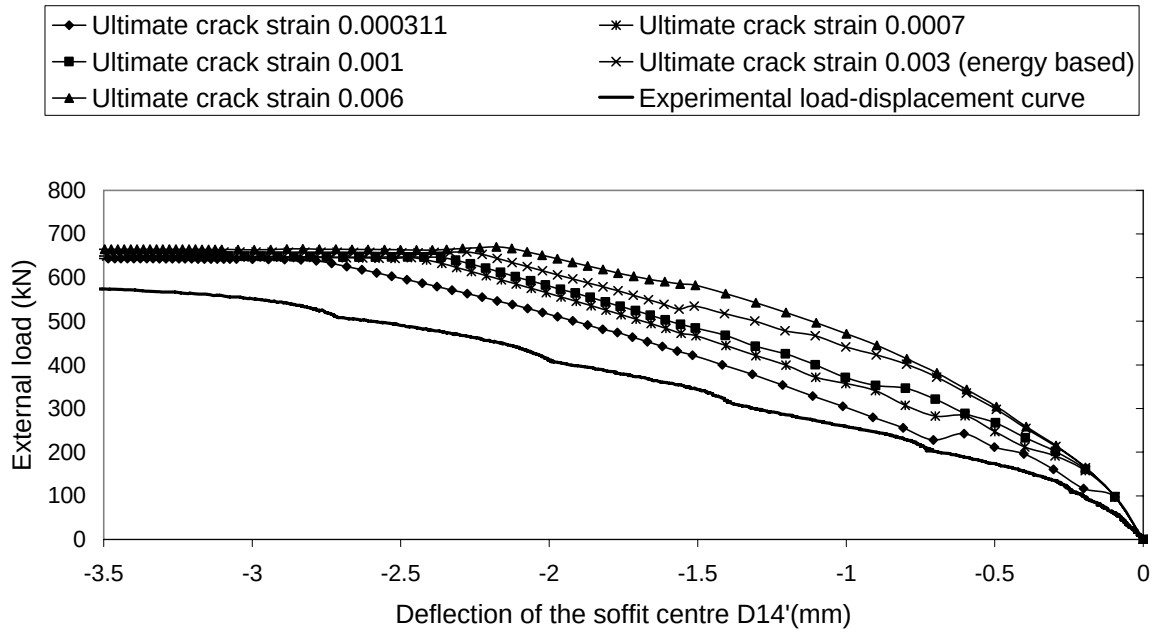

Figure 5. 12 Comparison of the load-displacement curve among different ultimate crack strain ε^{cr} for B4A1

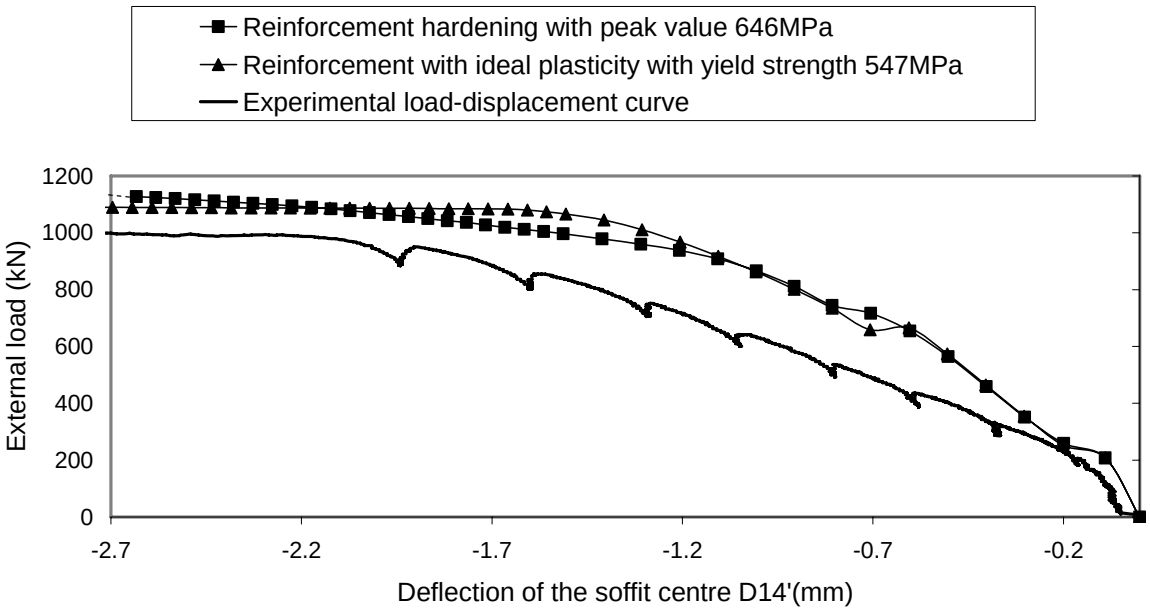

Figure 5.13 Comparison of the load-displacement curve between reinforcement with and without hardening (B4A4)

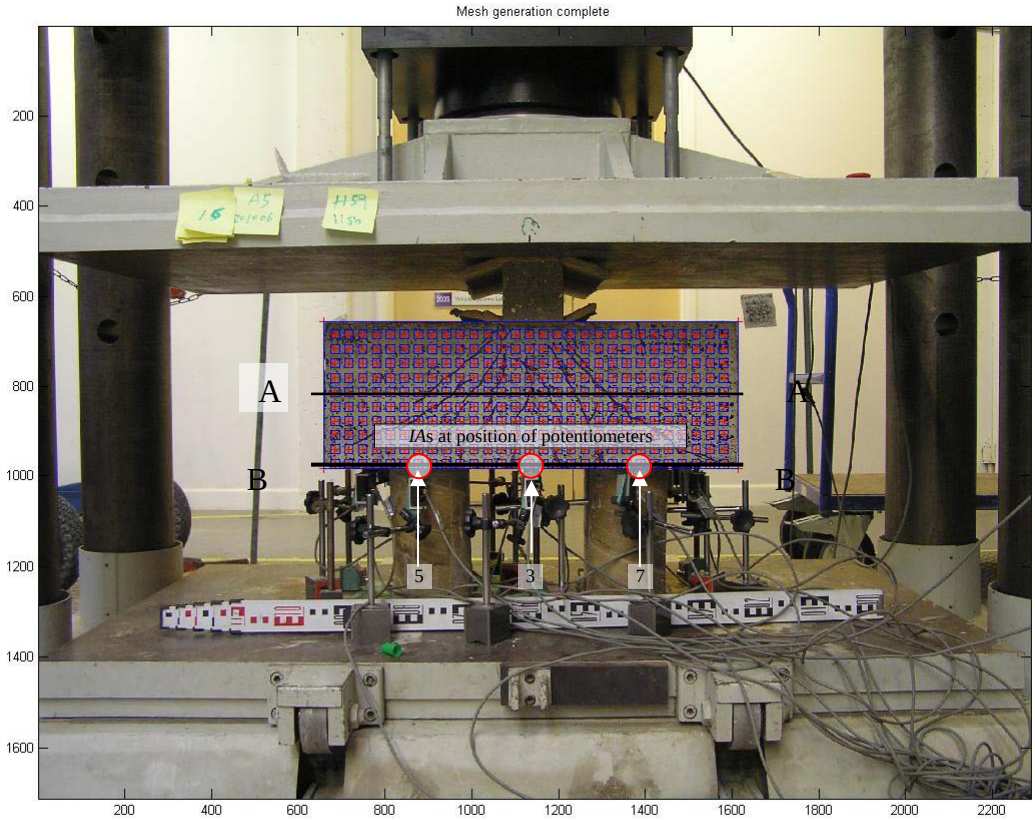

Figure 5.14 Basic *IA* array on B4A5 front surface

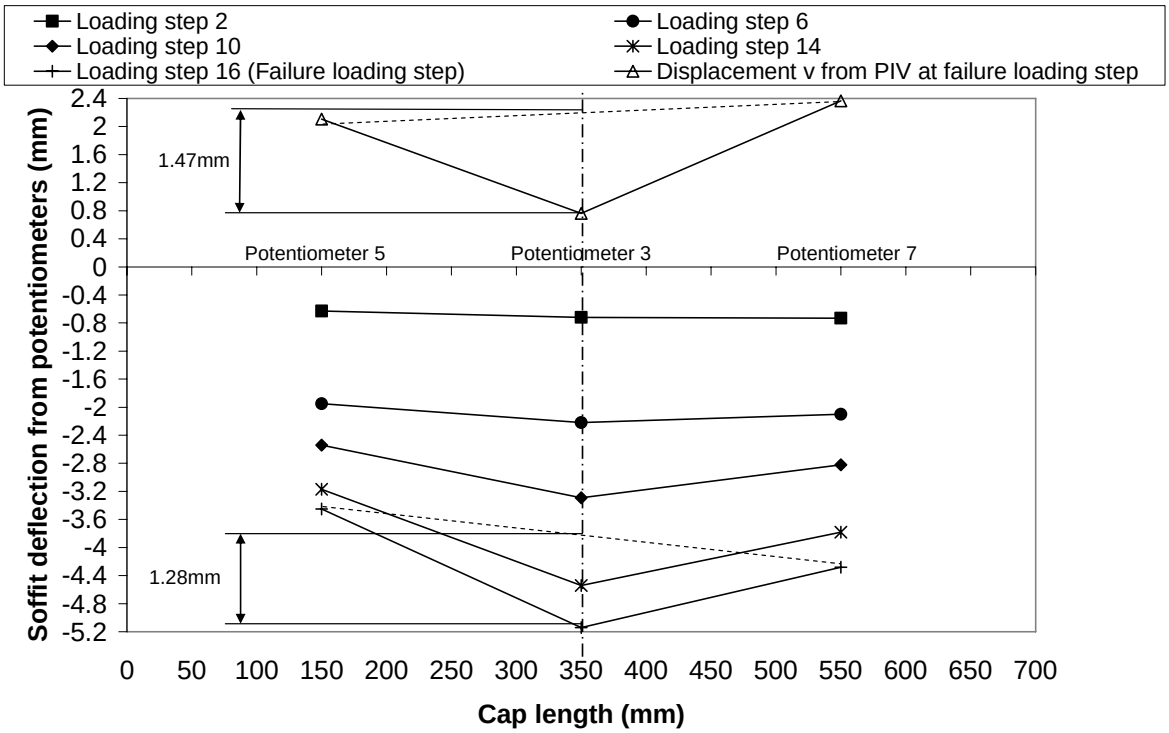

Figure 5.15 Comparison of the vertical displacement between the result from potentiometers near front cap surface and vertical displacement v from PIV (B4A5)

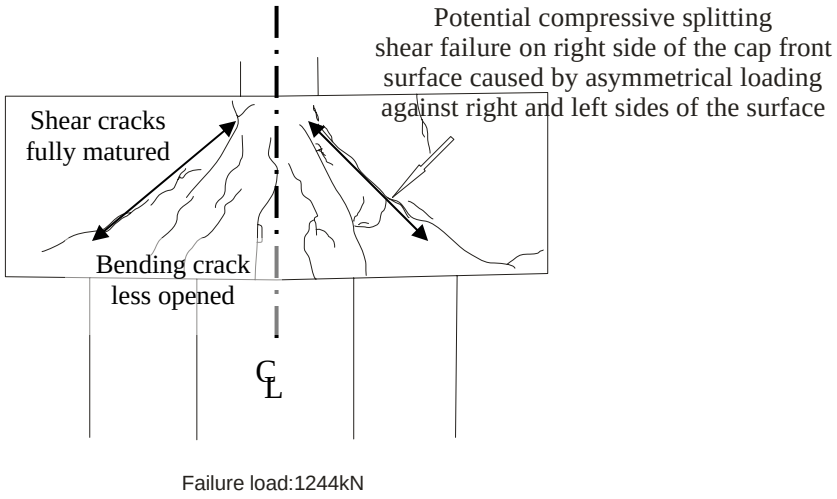

(a) Observed crack pattern in experiment

Figure 5.16 Comparison between the maximum principal strain ε_1 from PIV and crack strain ε^{cr} from FEA for B4A5 at the onset of the yield stage

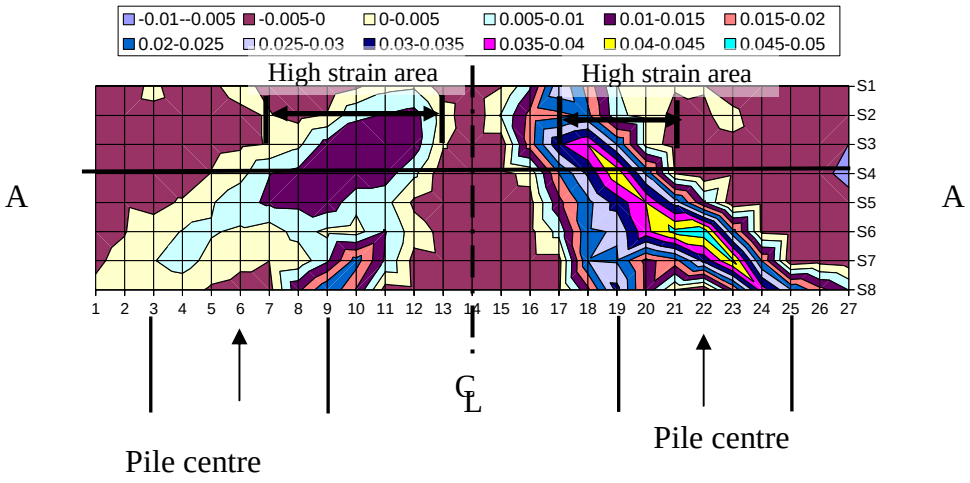

(b) Contour of maximum principal strain ε_1 from PIV

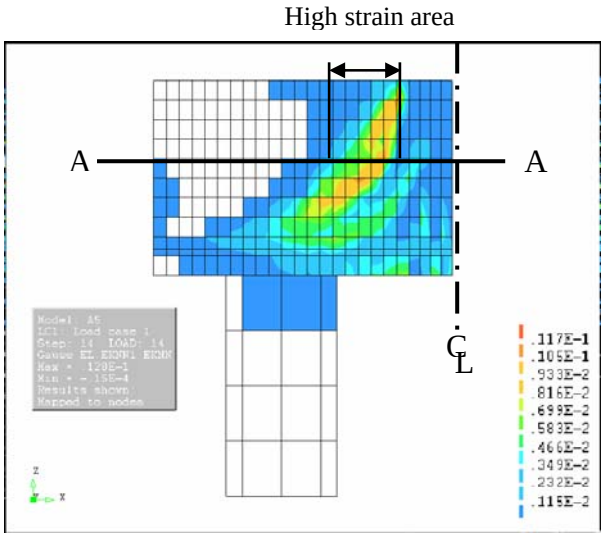

(c). Contour of crack strain ε^{cr} from FEA

Figure 5.16 Comparison between the maximum principal strain ε_1 from PIV and crack strain ε^{cr} from FEA for B4A5 at the onset of the yield stage

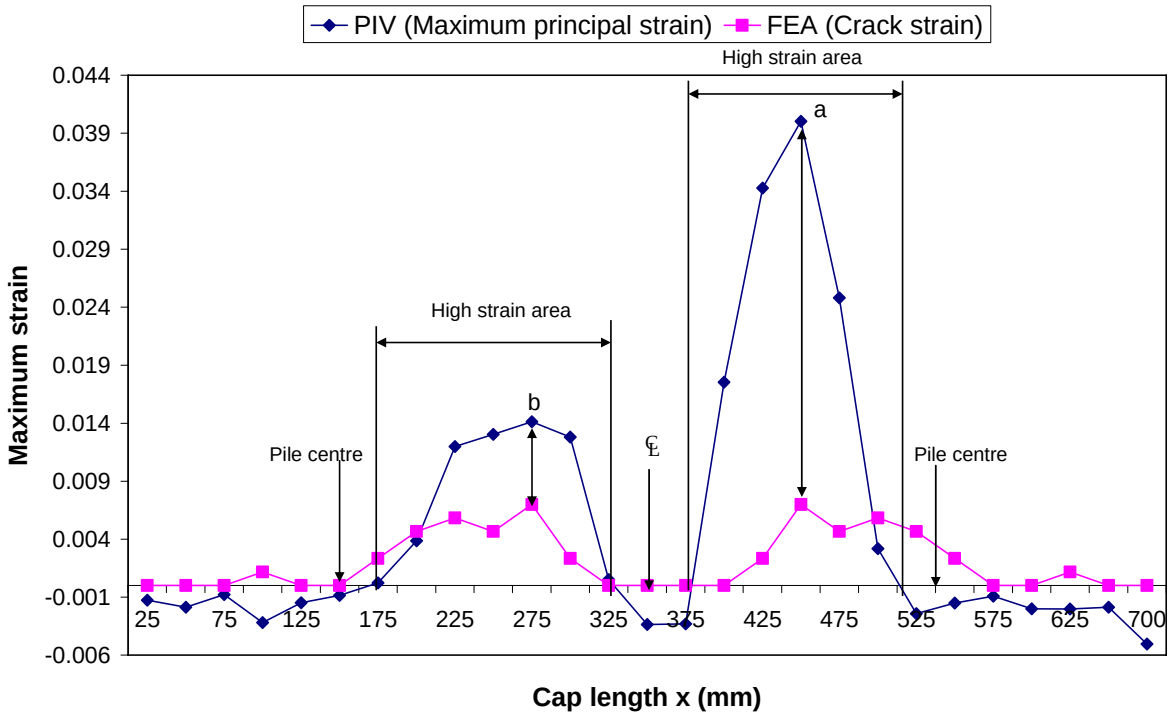

(d)The comparison of the crack strain along $A-A$

Figure 5.16 Comparison between the maximum principal strain ε_1 from PIV and crack strain ε^{cr} from FEA for B4A5 at the onset of the yield stage

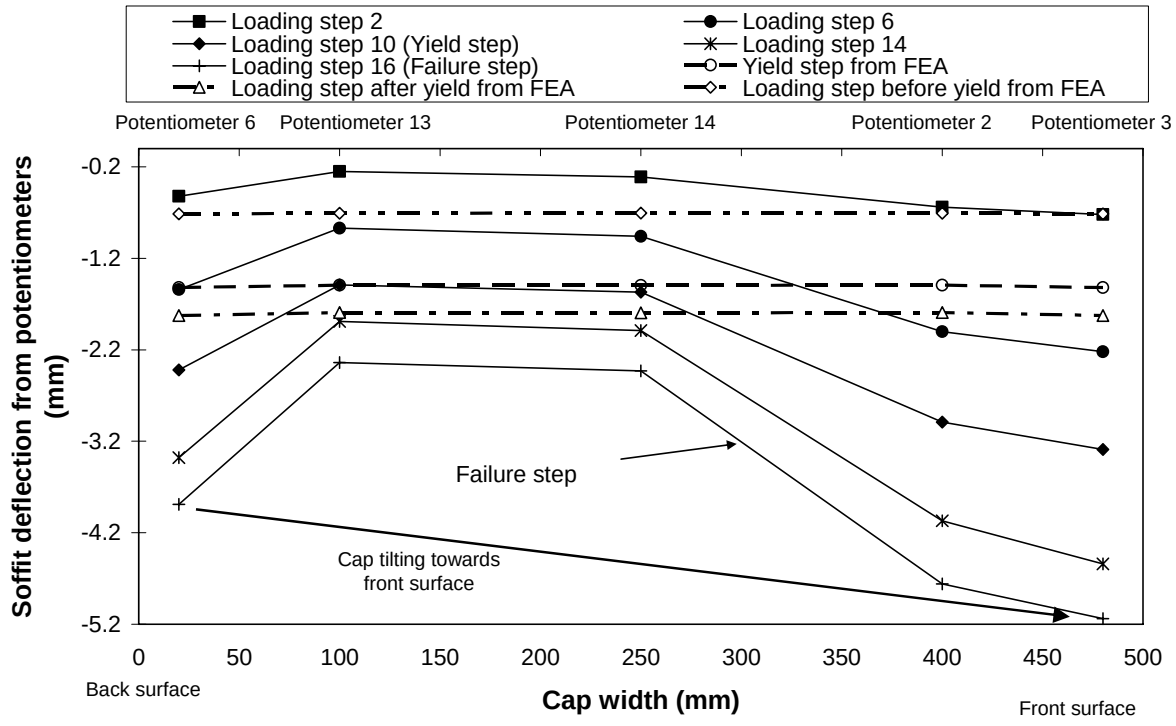

Figure 5.17 Cap soffit deflection along transverse centre line in B4A5

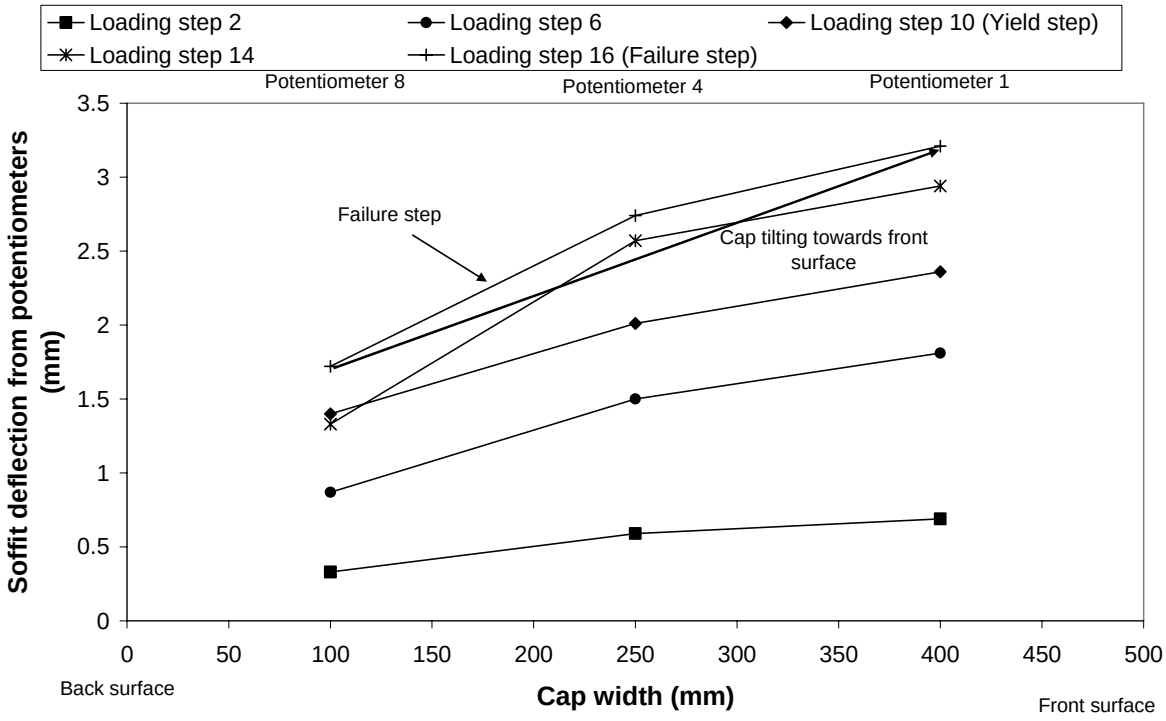

Figure 5.18 Cap soffit deflection along cap side width in B4A5

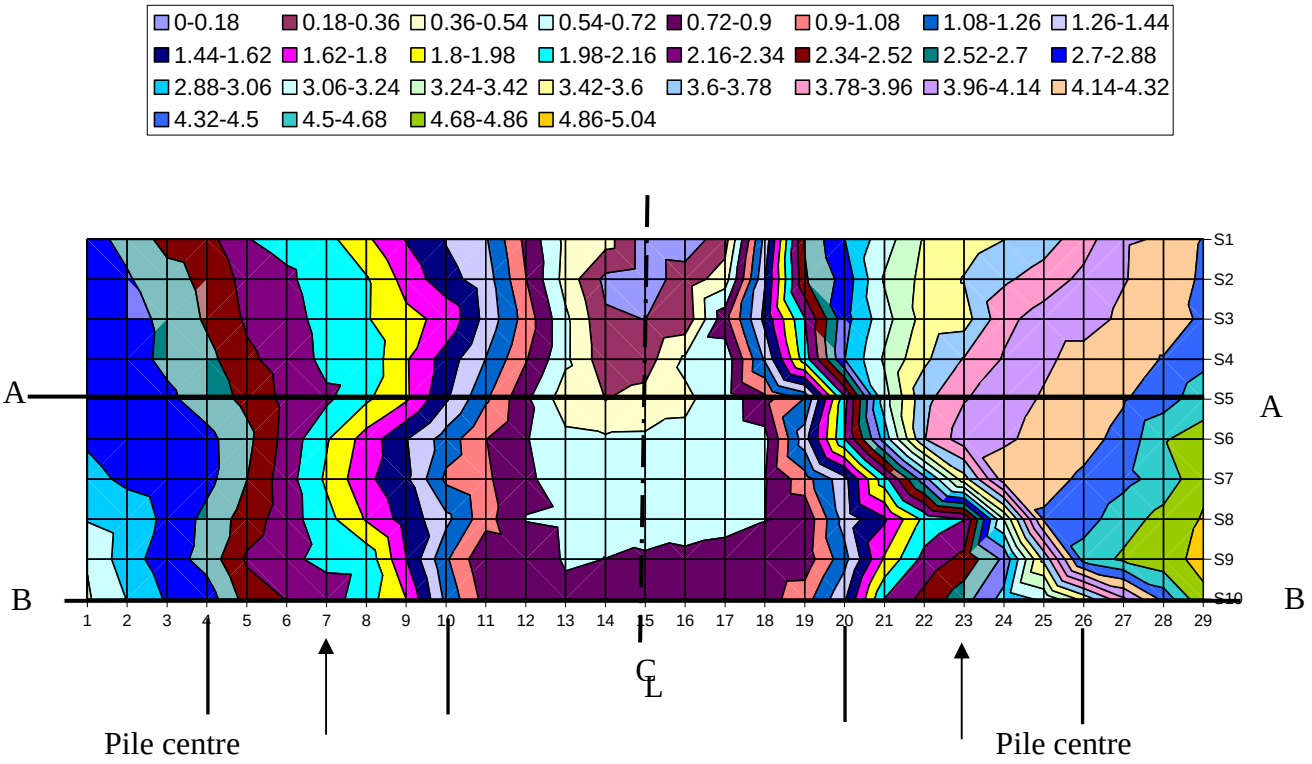

(a) Contour of the resultant displacement d (mm) from PIV

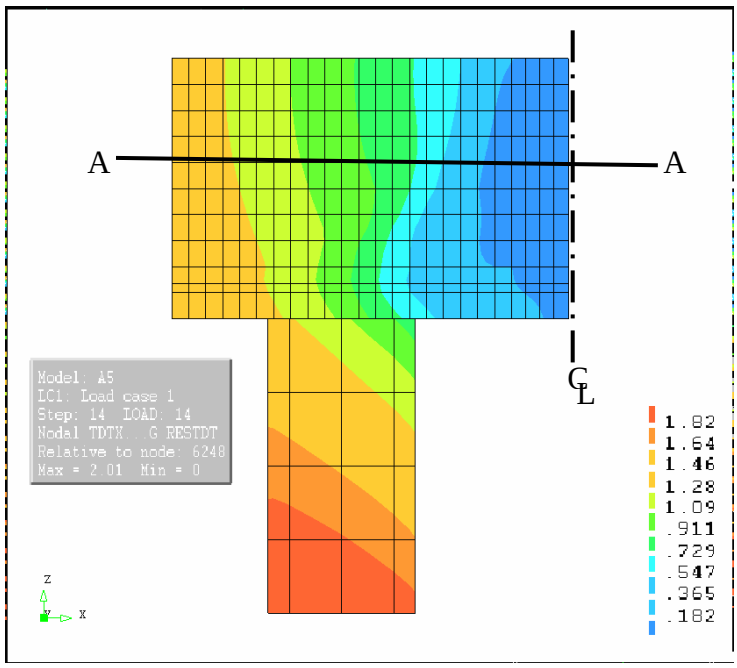

(b) Contour of the resultant displacement d (mm) from FEA

Figure 5.19 Comparison between the resultant displacement d from PIV and FEA for B4A5 at the onset of the yield stage

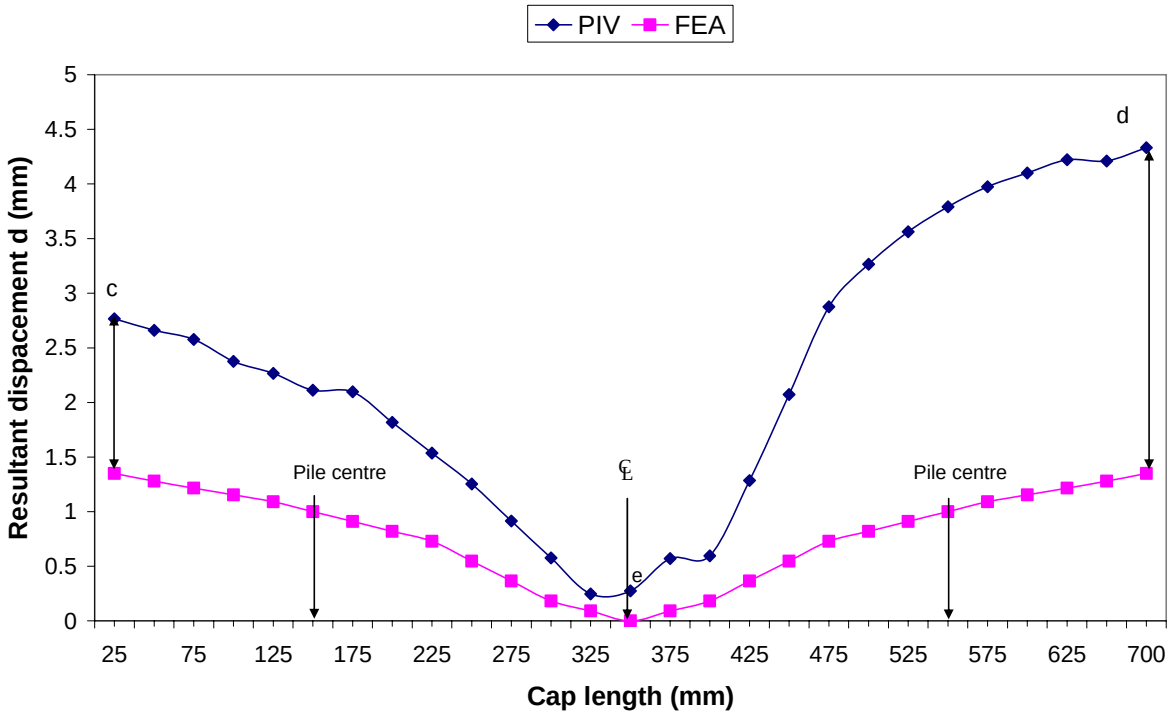

(c) The comparison of the resultant displacement d along $A-A$

Figure 5.19 Comparison between the resultant displacement from PIV and FEA for B4A5 at the onset of the yield stage

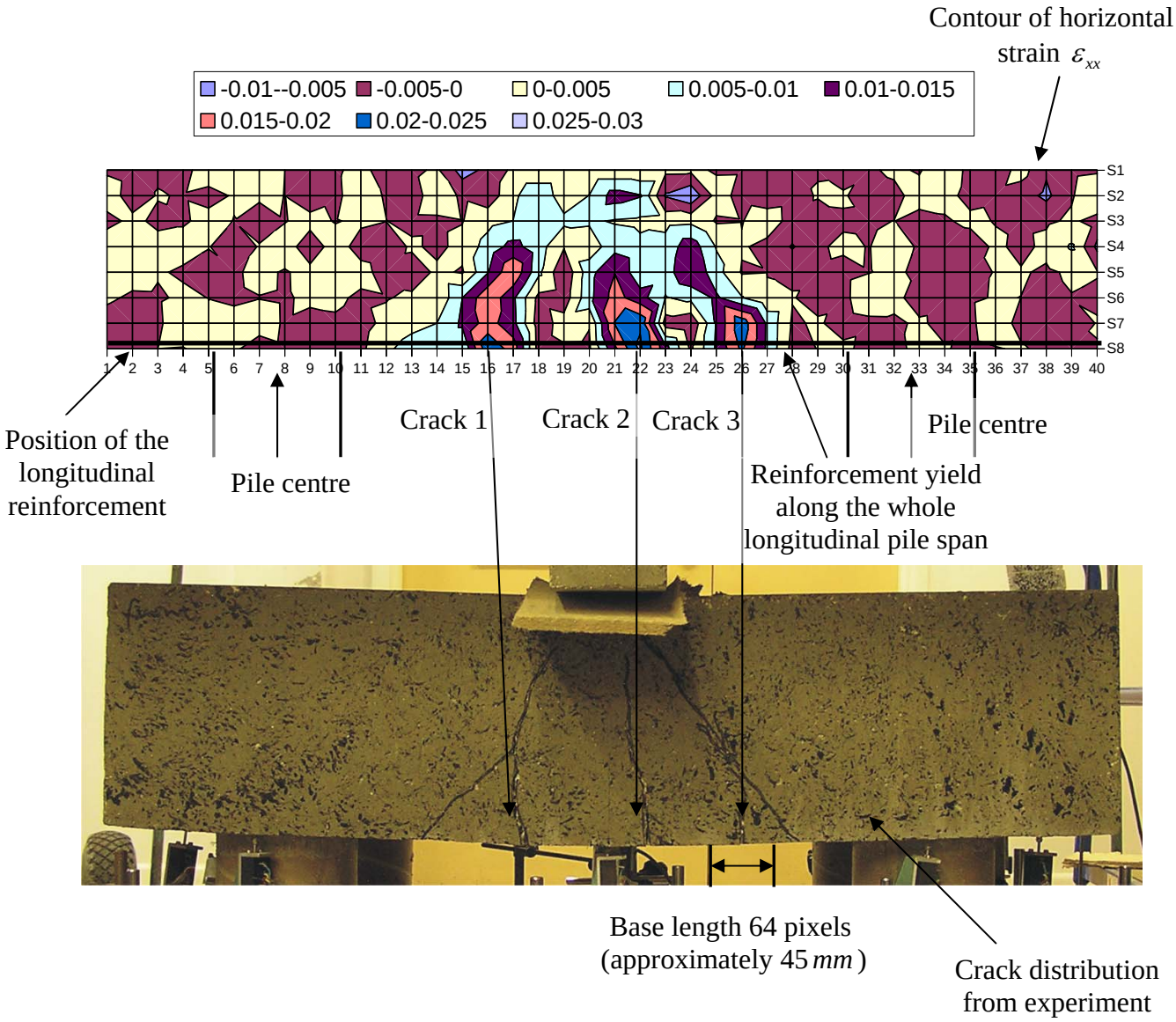

Figure 5.20 Example of the horizontal strain ε_{xx} at the lower end of critical bending cracks and shear cracks at longitudinal reinforcement level from PIV (B4B2)

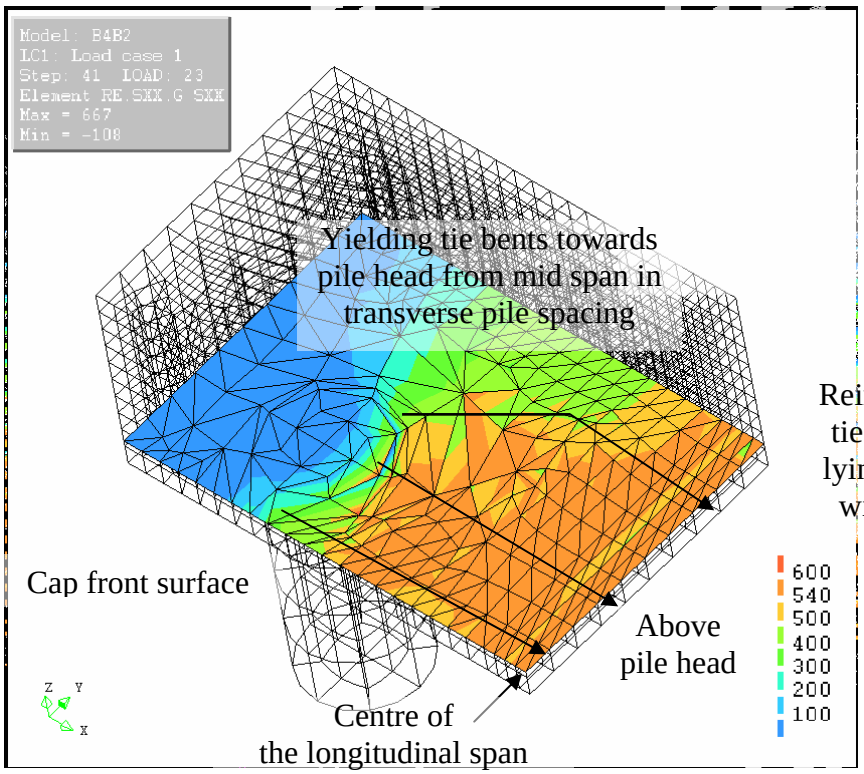

Figure 5.21 σ_{sx} in B4B2 ($n = 3.46$, $\frac{2d}{a_v} = 1.69$) at failure step

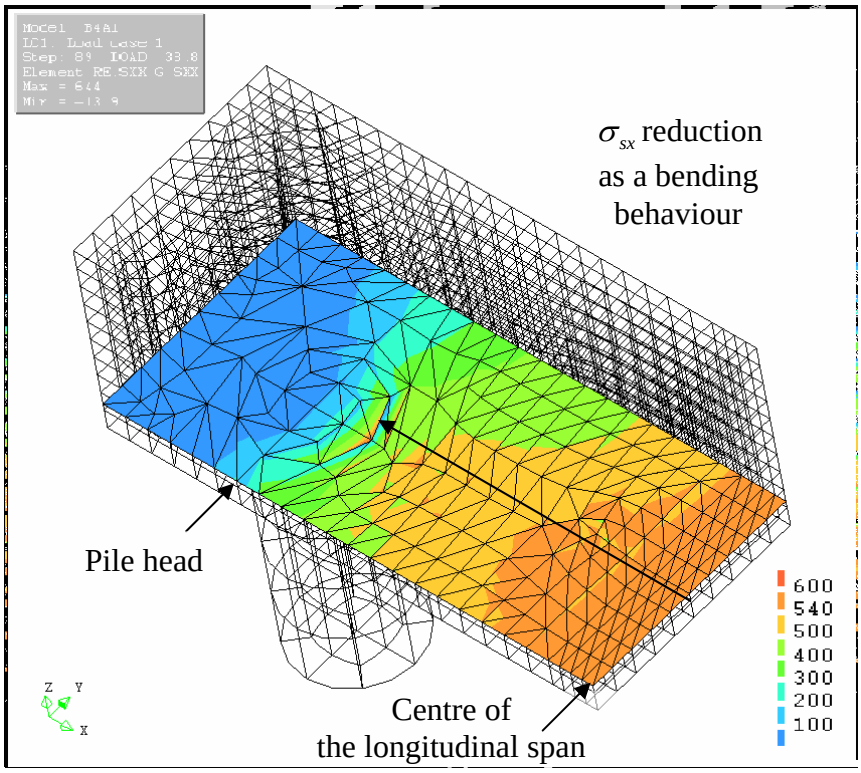

Figure 5.22 σ_{sx} in B4A1 ($n = 2.31$, $\frac{2d}{a_v} = 1.28$) at failure step

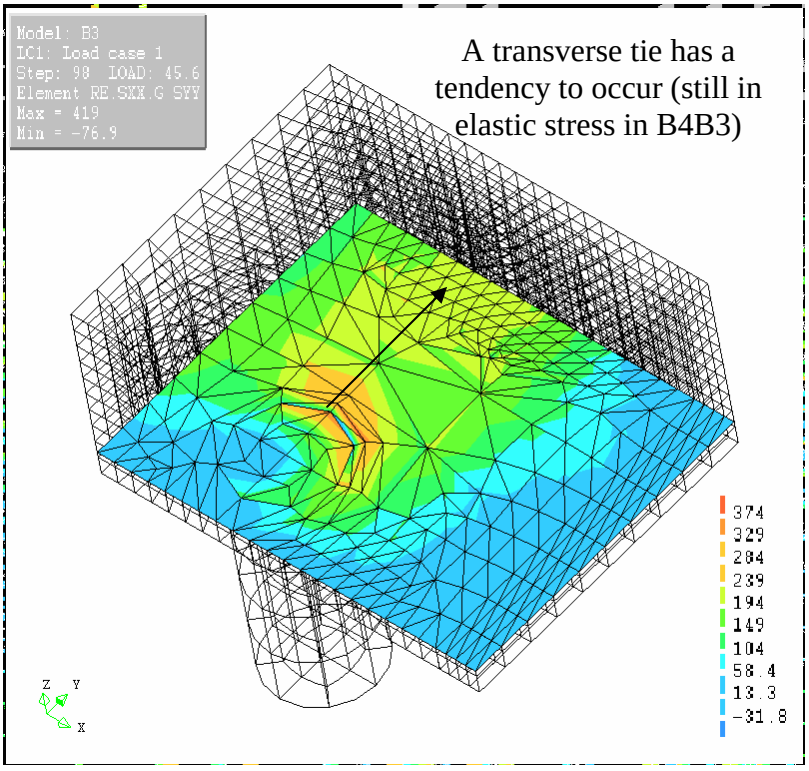

(a) Distribution of σ_{sy}

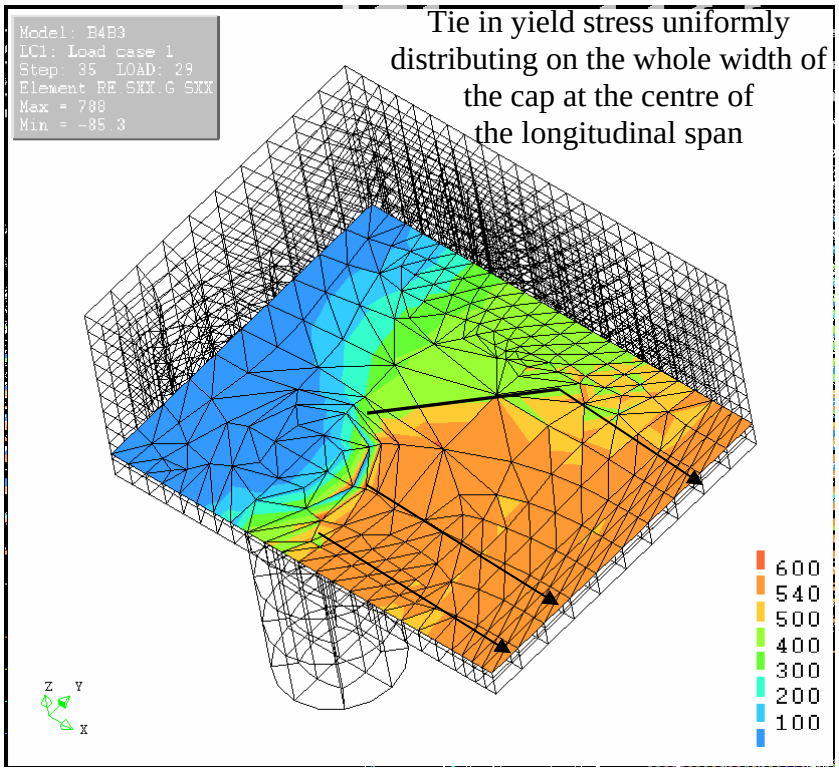

(b) Distribution of σ_{sx}

Figure 5.23 Distribution of σ_{sx} and σ_{sy} in B4B3 ($n = 4.23, \frac{2d}{a_v} = 1.69$) at failure step

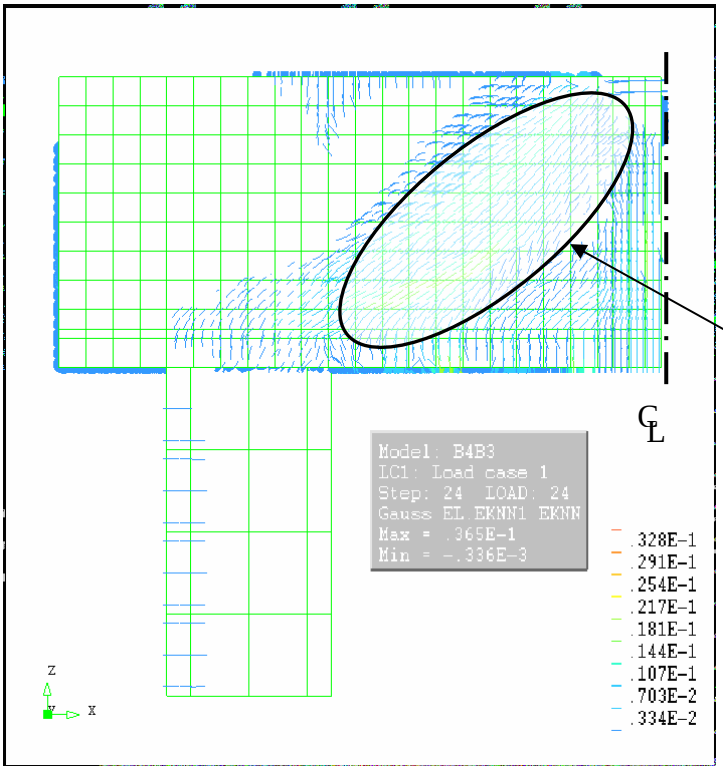

Figure 5.24 The distribution of crack strain ε^{cr} on B4B3 front surface ($n = 4.223$, $\frac{2d}{a_v} = 1.69$) at the onset of yield stage

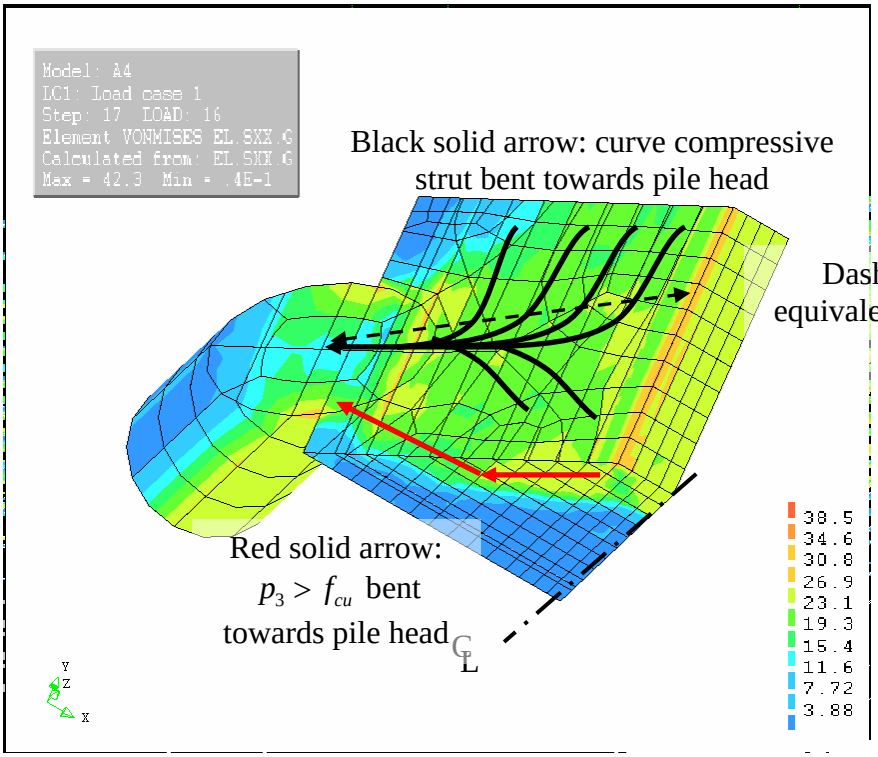

(a) contour of σ_v distribution

Figure 5.25 Strut-and-tie behaviour in B4A4 ($n = 2.31$, $\frac{2d}{a_v} = 2.47$) at the onset of yield stage

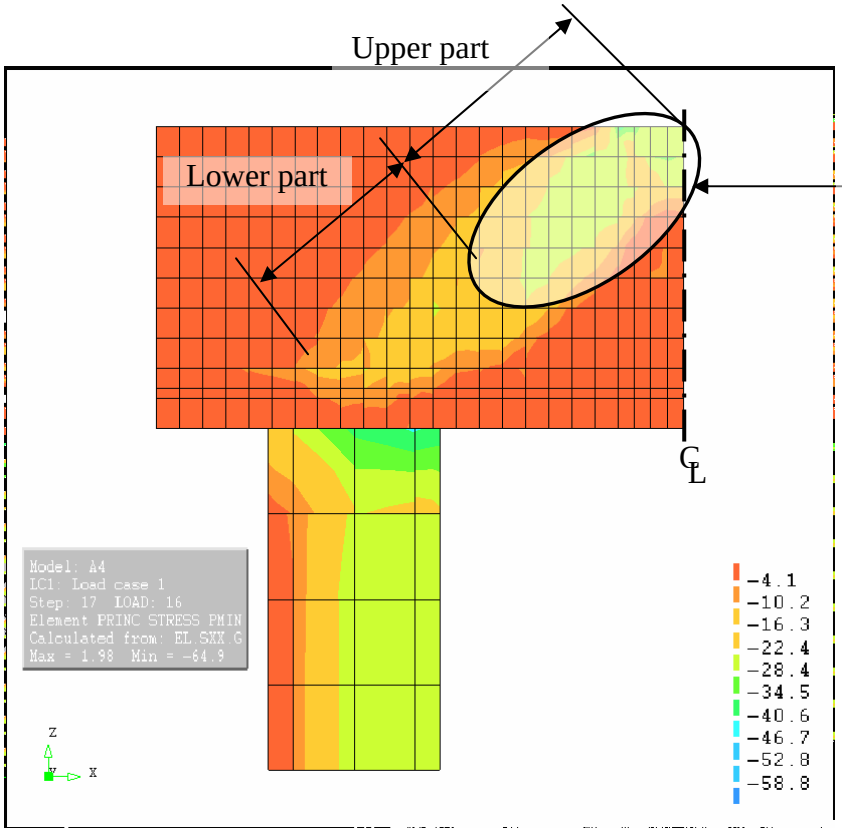

(b) contour of p_3 distribution on front surface

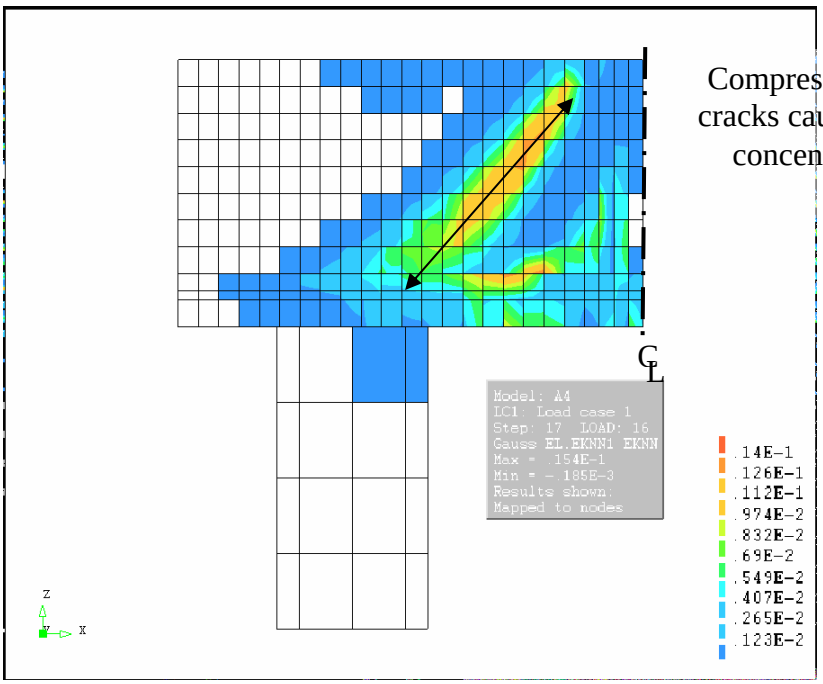

(c) contour of ε^{cr} distribution on front surface

Figure 5.25 Strut-and-tie behaviour in B4A4 ($n = 2.31$, $\frac{2d}{a_v} = 2.47$) at the onset of the yield stage

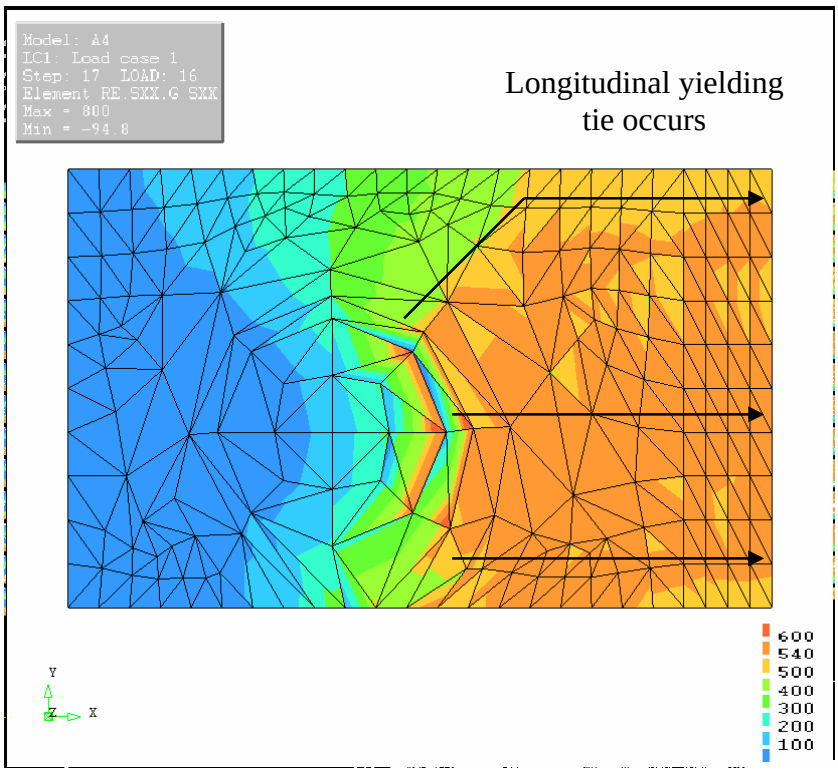

(d) σ_{sx} distribution

Figure 5.25 Strut-and-tie behaviour in B4A4 ($n = 2.31$, $\frac{2d}{a_v} = 2.47$) at the onset of the yield stage

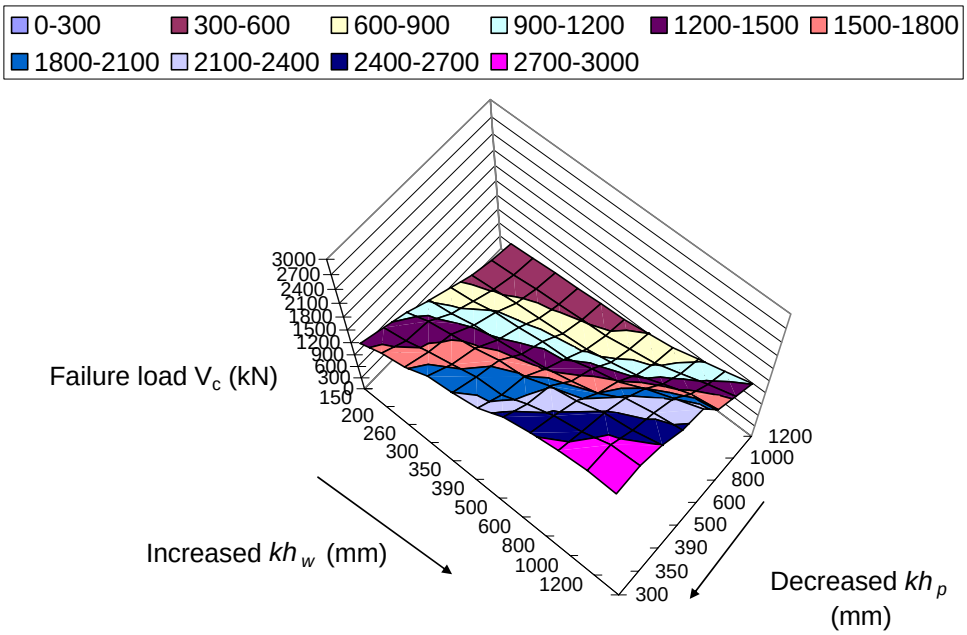

Figure 5.26 The distribution of the failure loads V_c of models in parametric study

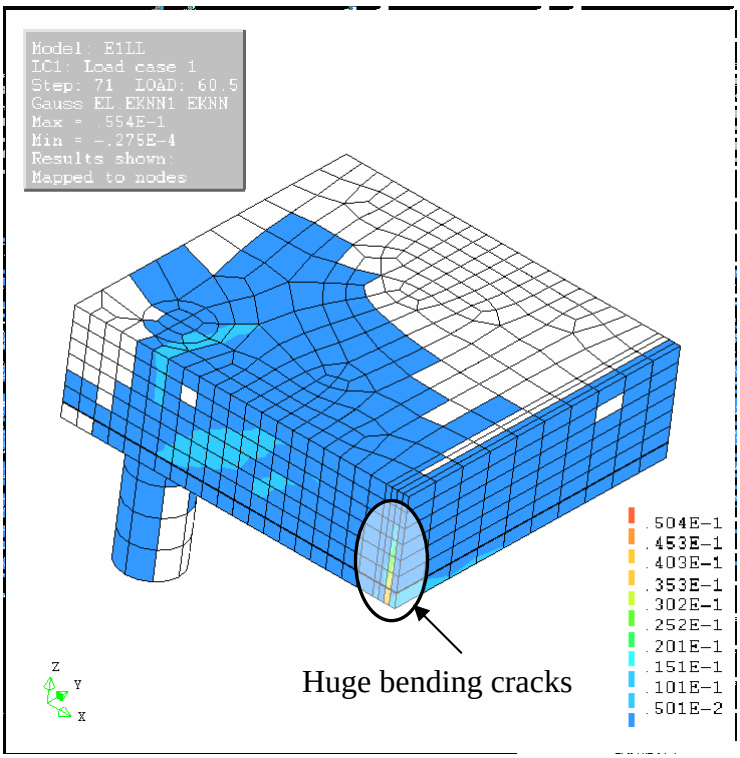

Figure 5.27 Bending failure in terms of the ε^{cr} on the front surface in E1ll ($n = 9.23$, $\frac{2d}{a_v} = 0.78$)

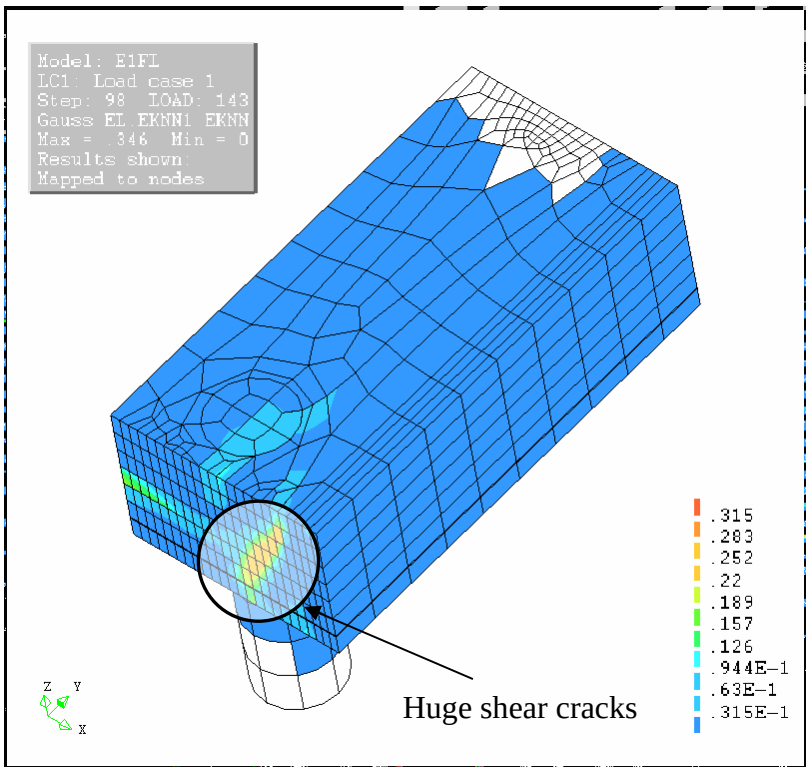

Figure 5.28 Shear failure in terms of the ε^{cr} on the front surface in E1fl ($n = 9.23, \frac{2d}{a_v} = 3.75$)

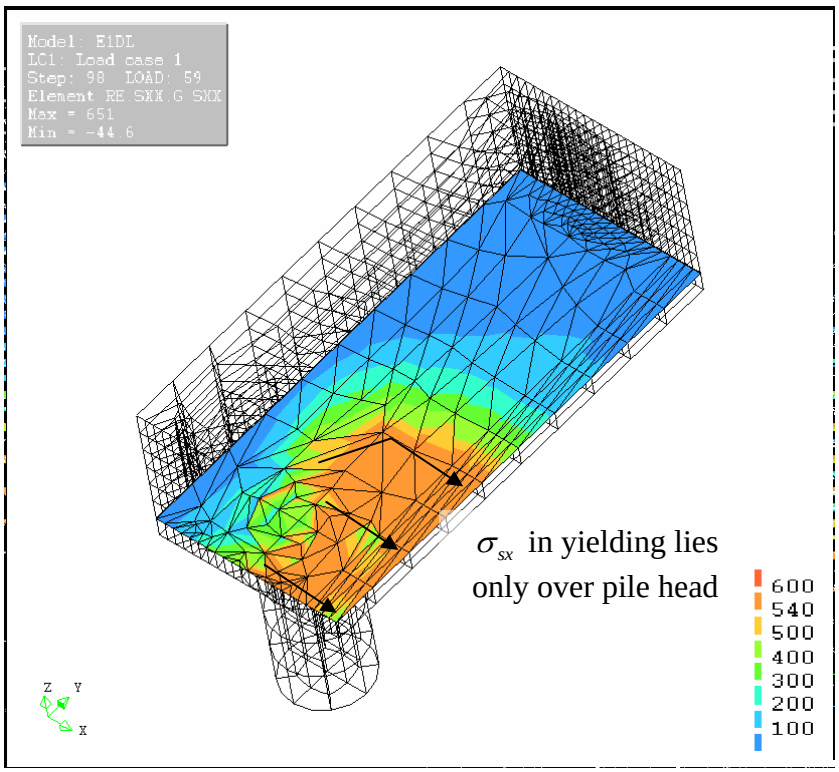

Figure 5.29 σ_{sx} distribution in E1dl ($n = 9.23, \frac{2d}{a_v} = 6.52$) at failure step

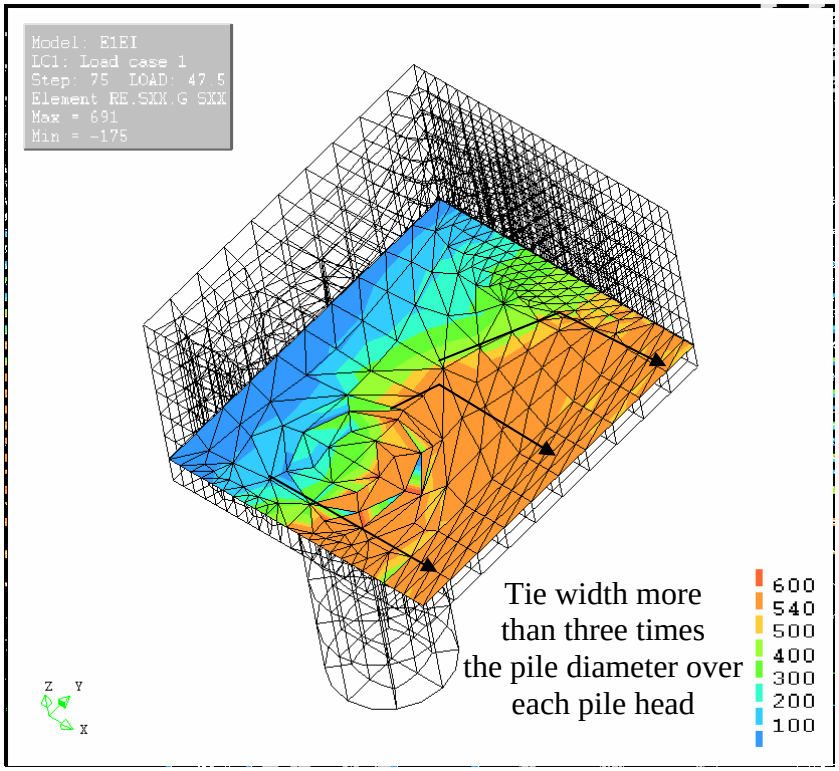

Figure 5.30 σ_{sx} distribution in E1ei ($n = 4.62, \frac{2d}{a_v} = 4.63$) at failure step

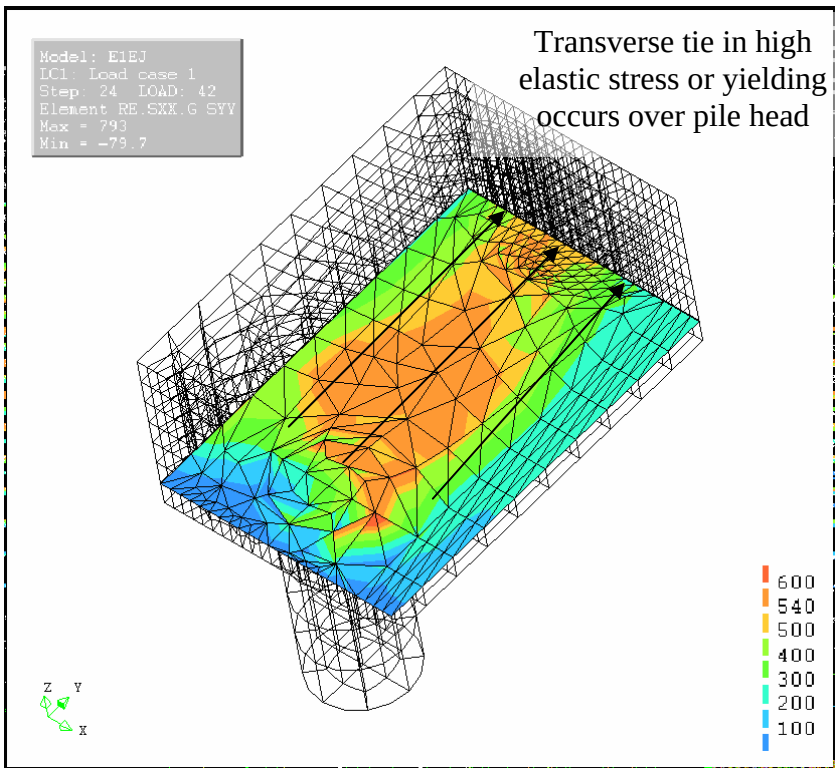

Figure 5.31 σ_{sy} distribution in E1ej ($n = 6.15, \frac{2d}{a_v} = 4.63$) at failure step

Chapter 6 Discussions

6.1 Introduction

In this chapter, the expression of the current bending theory based shear design formulae for pile caps in BS5400 and BS8110 are validated. The inaccuracy of the current design methods including STM is discussed. To validate the expression of the design formulae, the real nominal shear stress v_c calculated from the shear failure load V_c from the experimental samples, numerical models of the experimental samples and models in the parametric study is presented against shear enhancement factor $\frac{2d}{a_v}$ and the shear enhancement application factor A or the ratio of the transverse pile spacing over one pile diameter n. The design v_c from *Eq.*2.5 and *Eq.*2.6 is then validated with the real v_c. To judge the inaccuracy of the current design methods, the modification ratio m, which is defined as the ratio of the failure load of the samples and models in the FEA over the prediction from the design formulae in BS5400 and BS8110 (including STM), is calculated. The distribution of m is plotted against the variation of $\frac{2d}{a_v}$ and A or n.

The feasibility of improving the current bending theory based shear design formulae is studied. More concentration is put on potential improvement to the STM. The influence of load pattern on the shear capacity and shear mechanism of a pile cap is studied by analysing an existing experimental sample from another researcher's work and a model in the parametric study but under a reduced length wall loading.

6.2 The nominal shear stress from experiments and FEA

In order to validate the expression of the design formulae, the partial safety factor γ_m is set as 1.0 and the real strength of materials is adopted. As discussed in Section 3.9.2, some experimental samples should have had a higher shear failure load than observed, either because they failed asymmetrically or because they failed by bending. The trend of the potential higher shear failure load for these samples is expressed by an upward black arrow in Figures 6.1~6.2 and 6.6~6.9. The failure loads of the FEA models of experimental samples are also included in the discussion.

6.2.1 Results from experiments

Since the concrete strength f_{cu} of samples in each series is just slightly different (Table 3.4), in order to correct for this difference, the nominal shear strength can be expressed as $\frac{v_c}{PartI}$ $(=\frac{V_c}{2bd(PartI)})$ (see $Eq.2.5, Eq.2.6$) for the validation. For real v_c obtained from experiments and FEA, *Part I* from BS5400 ($Eq.2.6$) is used.

Figure 6.1 presents the relationship between $\frac{v_c}{PartI}$ and $\frac{2d}{a_v}$ for samples in Batch 3 Series A and Batch 4 Series A, those with constant $n(=\frac{kh_w}{h_p})$ and A but varied $\frac{2d}{a_v}$ (Table 3.3 (b)). It shows that the real $\frac{v_c}{PartI}$ increases linearly with $\frac{2d}{a_v}$, implying that v_c is strongly influenced by the shear enhancement factor. The linear trend is confirmed by the FEA results for samples in Batch 4 Series A as also shown in Figure 6.1. The trends predicted by BS5400 and BS8110 bending theory based shear formulae are also linear. But the real $\frac{v_c}{PartI}$ is much higher than the predictions and the slope of the trend line for real $\frac{v_c}{PartI}$ is also higher than that of the trend lines from British Standards.

Figure 6.2 (a) and (b) show the relationship between $\frac{v_c}{PartI}$ and n or A respectively for samples in Batch 4 Series B, those with constant $\frac{2d}{a_v}$ but varied n or A (Table 3.3 (b)). The real $\frac{v_c}{PartI}$ is much higher than the predictions from British Standards. The results from FEA show that the relationship between $\frac{v_c}{PartI}$ and n or A is likely to be a higher order polynomial. The predictions from BS5400 and BS8110 bending theory based formulae, however, show that this relationship is linear. This indicates that the expression of A in *Part IV* in $Eq.2.5$ and $Eq.2.6$ may be better expressed in a way other than linearly. It can also be seen that $\frac{v_c}{PartI}$ is less influenced by n or A than by $\frac{2d}{a_v}$ (Figure 6.1).

6.2.2 Results from parametric study

Figure 6.3 shows the distribution of v_c varying against $\frac{2d}{a_v}$ and A or n for the 88 models in the parametric study. As shown in Figure 6.3 (a), v_c is more dependent on A or n when $\frac{2d}{a_v}$ is large than when $\frac{2d}{a_v}$ is small. As shown in Figure 6.3 (b), when $\frac{2d}{a_v} = 0.78$, v_c does not vary with A (or n). When $\frac{2d}{a_v} = 6.52$ and n is roughly larger than 3, v_c reduces significantly with increasing n (or decreasing A). This may be because when $\frac{2d}{a_v}$ is large, the proportion of the cap width on which the shear enhancement factor is applied reduces with increasing n, especially when $n > 3$.

Figure 6.3 (c) shows that v_c is more dependent on $\frac{2d}{a_v}$ when n is small (or when A is large). When $n = 1.15$, v_c increases more quickly with increasing $\frac{2d}{a_v}$ than when $n = 9.23$. v_c is almost flat when $n = 9.23$, especially when $\frac{2d}{a_v}$ is larger than 2.47. $\frac{2d}{a_v} = 2.47$ is for models in the E1g series in the parametric study (Table 5.3). This implies that when the pile cap becomes more 2-way *i.e.* when n becomes large, the proportion of the cap width on which the shear enhancement factor is applied decreases with increasing $\frac{2d}{a_v}$, especially when $\frac{2d}{a_v} > 2.47$. The figure also shows that even when $\frac{2d}{a_v} < 1$ where in current British Standards v_c is not required to be enhanced, the shear stress increases with the increasing $\frac{2d}{a_v}$.

The above trends of v_c are in co-ordination with the results from experiments. For example, as shown in Figure 6.1, for Batch 3 Series A ($n = 2$) and Batch 4 Series A ($n = 2.31$), v_c increases significantly with increasing $\frac{2d}{a_v}$ since n is small. As shown in Figure 6.2, for Batch 4 Series B ($\frac{2d}{a_v} = 1.69$), v_c varies insignificantly with A or n since

$\frac{2d}{a_v}$ is small. The distribution of v_c against $\frac{2d}{a_v}$ and A or n follows a complex curve, rather than a 2-way plane as specified by the current bending theory based formulae in British Standards.

BS8110 states that the nominal design shear stress v_c for pile caps must in no circumstances exceed $0.8\sqrt{f_{cu}}$ or $5\,N/mm^2$, even if the caps are reinforced to resist shear. BS5400 has a similar limit, $0.75\sqrt{f_{cu}}$ or $4.75\,N/mm^2$ (Section 2.10.1). These upper limits, normally specified for 1-way spanning RC beams, are for concrete strength f_{cu} below 40 N/mm^2. They prevent the crushing of the concrete in the direction of the maximum principal compressive stress near the concentrated load caused by the high vertical shear force (Mosley *et al*, 1999). The real v_c for experimental samples B4A3, B4A4 and B4A5 ($4.62\,N/mm^2$, $5.29\,N/mm^2$ and $6.25\,N/mm^2$ respectively from experiments) and of models normally with $\frac{2d}{a_v} > 1.89$ in the parametric study exceeds this upper limit. But brittle failure was not observed in the experiments or FEA. This may be because the upper limit is a lower bound to test data from 1-way spanning RC beams (Clarke & Taylor, 1975), not for 2-way spanning pile caps. Considering that the shear mechanism of pile caps is different from 1-way spanning beams, the limit may be improved or not be applied to pile caps.

6.3 Comparison of failure loads with BS8110 and BS5400

In the following sections, the modification ratio m of the actual failure load from experiments and FEA over the predictions from bending theory based shear formulae and STM in BS81110 and BS5400 and from a new STM that will be proposed are expressed as $m_{BS8110b}$, $m_{BS5400b}$, $m_{BS8110S}$, $m_{BS5400S}$ and m_{nSTM} respectively. When calculating v_c using the bending theory based shear formulae in BS8110 and BS5400 for models in the parametric study with shear enhancement factor smaller than 1.0 (Table 5.3), $\frac{2d}{a_v}$ is always taken as 1.0 *i.e. Part V* in *Eq.*2.5 and *Eq.*2.6 is taken equal to 1.0.

6.3.1 STM in British Standards

Before the discussion, the STM in current British Standards is explained in detail. Section 2.5 stated that one prerequisite of the application of STM is that the anchorage of

reinforcement at nodes should be sufficient. Fully bent-up reinforcement passing sufficient distance over the pile head in the experimental pile caps in this research ensures this requirement, such that STM can be applied.

In BS8110, longitudinal reinforcement A_s taken as a yielding tie in STM lies on a cap width which corresponds to that for which the shear enhancement is applied in the bending theory based formula *i.e.* not wider than triple the pile diameter above each pile head (Section 2.10.3). In BS5400, the yielding tie is to be 1.25 times the amount of reinforcement above each pile head but 80% of reinforcement is required to be placed above pile heads. The geometry of the strut-and-tie model is specified as a triangulated form, with the lower nodes lying at the intersections of the centre-lines of the piles with the longitudinal reinforcement and the zenith of the triangulated form lying under the centre of the load area, regardless of the load pattern.

It is difficult to construct a strut-and-tie model at the failure step based on crushing of the inclined concrete strut, because it is difficult to decide the failure criterion for a concrete strut which depends on the strut shape which itself varies with the cap dimensions. The strut-and-tie system is thus deemed to fail when the reinforcement tie yields. The role of the transverse reinforcement tie is vague in current British Standards. In this research, it is assumed that only the longitudinal reinforcement yields.

Figure 6.4 (a) shows such a typical strut-and-tie model in a ¼ pile cap based in British Standards. The STM is constructed on a force balance at the intersection of the pile centre and reinforcement (point A). The compressive force C in the concrete strut linking the zenith and the pile head is balanced by forces in the reinforcement in both directions, $\frac{1}{2} f_y A_s$ and F_s, and a vertical reaction equal to ¼ the external vertical load on the cap $\frac{1}{4}F$. Because the transverse reinforcement remains elastic and thus F_s remains low, it is possible that $\frac{1}{2} f_y A_s$, F_s and $\frac{1}{4}F$ can add up vectorially to oppose the inclined force C with spatial angles α, β, γ (Figure 6.4 (a)), resulting in force equilibrium:

$$\frac{\frac{1}{4}F}{\frac{1}{2} f_y A_s} = \frac{d}{\frac{1}{2} k h_p}$$

Rearrange, and we have the expression of the shear capacity of the pile cap predicted by STM in BS8110 and BS5400:

$$F = \frac{4df_y A_s}{kh_p} \qquad (Eq.6.1)$$

where the calculation of the total area of the longitudinal reinforcement A_s follows the respective rules in BS5400 and BS8110 (Section 2.10.3). *Eq.*6.1 indicates that the shear capacity is independent of the spatial angle of the inclined concrete strut α, β, γ and the force in the transverse reinforcement. In practice, α, β, γ vary with the load pattern. For example, under a full-length wall loading, the vertical force $\frac{1}{4}F$ may move transversely to a new position but still on the centre of the longitudinal span, producing a new concrete strut as shown by a dash line in Figure 6.4 (a). Figure 5.25 (a) implies that the equivalent compressive strut in B4A4 under full-length wall loading points to somewhere between the centre of the cap top and centre of the top front edge rather than the centre of the cap top.

Once the reinforcement in the transverse direction becomes a tie yielding or at high elastic stress, resulting in a transverse force F_s which could ruin the force equilibrium mentioned above, α, β, γ of the inclined concrete strut may also change from the original angles in order to fit a new strut-and-tie system and new force equilibrium leading to a new design formula.

6.3.2 Results from experiments

The comparison of the observed failure loads with the predictions from bending theory based formulae and STM in BS5400 and BS8110 is shown in Table 6.1. The partial safety factor γ_m is taken as 1.0. The real strength of materials is adopted. It can be seen that $m_{BS8110b}$ and $m_{BS5400b}$ are larger than 1.0 for all samples, indicating that the design formulae in BS8110 and BS5400 are conservative. $m_{BS5400b}$ being larger than $m_{BS8110b}$ for all samples implies that BS5400 is more conservative than BS8110. For the samples in Batch 1 and 2, though the real shear capacity was higher than the threshold of the testing machine, $1440\,kN$ (Section 3.7), the predictions from BS5400 and BS8110 are conservatively below $1440\,kN$. For example, for B2A1, the real shear capacity is at least 3.5 times the prediction from BS5400. For samples in Batch 3 and 4 for which the real shear capacity was obtained (Section 3.9.2), $m_{BS5400b}$ and $m_{BS8110b}$ are always above 2.05 and 1.66.

STM in BS8110 (*Eq.*6.1), however, gives a relatively accurate prediction for all the samples. For samples in Batch 3 and 4, $m_{BS8110S}$ is not more than 1.68, implying that strut-and-tie behaviour is close to the physical explanation of the shear behaviour of the

experimental pile caps. This is in line with the observation of the strut-and-tie behaviour from FEA for experimental samples (Section 5.6.3).

Figure 6.5 shows the relationship between $m_{BS8110b}$ and f_{cu} for all samples in Batch 4 from experiments and FEA. The scatter distribution of the dots implies that there is no specific relationship between $m_{BS8110b}$ and the concrete strength.

Figure 6.6 shows the relationship between $m_{BS8110b}$ and the shear enhancement factor $\frac{2d}{a_v}$ for samples in Batch 4 Series A both from experiments and FEA. The graph shows a linear relationship between $m_{BS8110b}$ and $\frac{2d}{a_v}$. Always being higher than 1.0, $m_{BS8110b}$ decreases with the increasing $\frac{2d}{a_v}$. It implies that the BS8110 prediction becomes less conservative as $\frac{2d}{a_v}$ increases.

Figure 6.7 and 6.8 show the relationship between $m_{BS8110b}$ and n, $m_{BS8110b}$ and A for samples in Batch 4 Series B both from experiment and FEA. $m_{BS8110b}$ is always higher than 1. Though the experimental data cannot imply a dependency between $m_{BS8110b}$ and n or A, $m_{BS8110b}$ from FEA shows a $m_{BS8110b}$ relationship in a high order polynomial with both n and A. The conservatism of the current bending theory based design formula varies little with n and A.

On the other hand, $m_{BS8110S}$ always being around 1.0 in Figures 6.6~6.8 shows STM in BS8110 gives a more accurate prediction than the bending theory based formula.

A study to investigate the relationship between $m_{BS8110S}$ and the spatial angle α in the strut-and-tie model (Figure 6.4 (a)) has been done. Variation of α depends on variation of both kh_w and kh_p, and is more physically meaningful than $\frac{2d}{a_v}$ and A or n. Figure 6.9 shows the relationship for samples in Batch 4 Series B, where α varies hugely with the increasing kh_w (Table 3.3). Results both from experiments and FEA are included. A positive linear relationship between $m_{BS8110S}$ and α is presented. When α or kh_w becomes large, $m_{BS8110S}$ increases. The reason is that the STM in BS8110 is only considering a longitudinal yielding tie with a limited width and excluding the influence of the transverse reinforcement. However the truth may be that the width of the longitudinal yielding tie is larger than triple

the pile diameter above each pile head when kh_w is larger than triple the pile diameter *e.g.* B4B3 ($n = 4.23$) (Figure 6.9). Another truth may be that the larger is α or kh_w, the bigger part the transverse reinforcement plays in the strut-and-tie behaviour. This is in line with the implication from the observed crack distributions on cap soffits that the larger the transverse pile spacing, the more transverse reinforcement will be involved in the shear resistance (Section 3.9.1). Figure 5.23 evidences the above truths in the case of B4B3 at its failure step. More evidences from the parametric study are discussed in the next section.

6.3.3 Results from parametric study

In the parametric study, only a few models with low $\frac{2d}{a_v}$ and n behaved nearly 1-way and underwent a pure bending failure, not determined by the combination of the internal bending moment and shear force in both longitudinal and transverse directions. Other models failed relatively 2-way. The failure is actually a combination of both bending failure (longitudinal and/or transverse) and shear failure (on longitudinal and/or transverse cross-sections), even though some seemed like a 1-way bending failure regarding the crack distribution on the cap front surface, *e.g.* E1ll in Figure 5.27 (also see Section 5.8). Therefore, all these failure types can be called 'shear failure' since they cannot be defined as the well-understood 1-way bending failure. The shear failure load can then be compared with the shear prediction from British Standards.

The distribution of $m_{BS8110b}$ for models in the parametric study against $\frac{2d}{a_v}$ and A or n is plotted in Figure 6.10. Ranging from 2.03~3.10, $m_{BS8110b}$ varies with both $\frac{2d}{a_v}$ and A or n. Ranging from 2.09~4.44, $m_{BS5400b}$ distributes in a similar way to $m_{BS8110b}$ but more conservatively. The curve plane of the $m_{BS8110b}$ distribution can be expressed alternatively by the relationships between $m_{BS8110b}$ and $\frac{2d}{a_v}$ for a series of constant n or A (Figure 6.11 (a)), and n for a series of constant $\frac{2d}{a_v}$ (Figure 6.11 (b)). Both relationships are high order polynomials. $m_{BS8110b}$ (the conservatism of BS8110) varies with $\frac{2d}{a_v}$ and n or A, being more apparent with $\frac{2d}{a_v}$ (*cf.* Figures 6.6~6.7). $m_{BS8110b}$ is at its peak value when $\frac{2d}{a_v}$ is

between 1.28 and 2.47 (Figure 6.11 (a)). A similar distribution can be obtained for $m_{BS5400b}$.

Taking the above together with the results for experimental samples described in Section 6.3.2, the reason of the large discrepancy between the real shear capacity of the pile cap and the prediction from the bending theory based design formulae in BS810 and BS5400 could be that the expression of $\frac{2d}{a_v}$ developed from Regan's theory, and A in current formulae, are incorrect and cannot physically explain the shear behaviour of the 2-way spanning pile caps (Section 2.3.1).

Figure 6.12 shows the distribution of $m_{BS8110S}$ varying against $\frac{2d}{a_v}$ and A or n. It shows that for caps with small pile transverse spacing ($A=1$), the prediction from STM matches well with the FEA prediction while for caps with large transverse pile spacing ($A<1$ or $n>3$), the failure load from FEA becomes higher than the STM prediction. This can be explained as follows.

For models with transverse pile spacing larger than three times the pile diameter, the yield stress in longitudinal tie σ_{sx} can actually distribute on the full cap width (such as in E1ei, Figure 5.30) rather than just over triple the pile diameter over each pile head as specified in BS8110. In these models, the stress in the transverse reinforcement σ_{sy} could be very large and even reach yield at the failure step, forming a tie which cannot be neglected, *e.g.* as in E1ej (Figure 5.31). These imply that the concrete strut might change its direction, forming a new strut-and-tie system and disturbing the spatial angle assumed in $Eq.6.1$ which neglects the influence of the transverse reinforcement. These result in the underestimation by current STM for models with large kh_w in the parametric study and for samples with large α in Batch 4 Series B (Figure 6.9). To correct this underestimation, a new STM is suggested to extend the longitudinal tie to the whole cap width while keeping α, β, γ unchanged (see Section 6.4.2).

m_1 is the ratio of the failure load of models in the parametric study over the failure load assumed to be caused by the crushing of concrete under the full-length wall loading, $F_c = f_{cu} \times S$, where $S = h_c \times b$ is the concrete area under wall loading. The distribution of m_1 against $\frac{2d}{a_v}$ and A or n is shown in Figure 6.13. m_1 ranges from 1.12 to 0.18 and decreases with decreasing A and $\frac{2d}{a_v}$. m_1 around 1.0 appears only in models with very

short longitudinal and transverse pile spacing, since in these models the inclined angle of the concrete strut γ (Figure 6.4 (a)) is nearly $90°$ such that the assumed crushing load of the concrete under the wall loading is approximately equal to the crushing load of the compressive concrete strut which fails caps. It indicates that for most models in the parametric study, crushing failure of the concrete under wall loading is not the reason for the failure of the whole structure, which agrees with the experimental observations (Section 3.9.2).

m_2 is the ratio of the longitudinal central resisting bending moment of models when failure happens over the bending capacity predicted by BS8110, M_{FL} (Section 2.3.2), the distribution of which is shown in Figure 6.14 varying against $\frac{2d}{a_v}$ and A or n. The bending formula is taken as the one used for the 1-way spanning RC beam. The bending span is taken as the longitudinal pile spacing. The simply support condition uniformly over the whole cap width is assumed. The wall loading is simplified as a line load without width. The reinforcement across the whole cap width is considered.

Figure 6.14 is the equivalent, for 2-way spanning four-pile caps, to the Kani's valley for 1-way spanning beams (Figure 2.6), *i.e.* to express the failure mode (Table 5.4) by plotting the ratio of the bending moment of the cap when any failure type happens over the nominal bending capacity varying against the key parameters. For pile caps in this research, the key parameters are $\frac{2d}{a_v}$ and A or n while for beams in Kani's research it is $\frac{a_v}{d}$ (Figure 2.6).

In order to compare Figure 6.14 with Kani's valley, $\frac{2d}{a_v}$ is transformed to $\frac{a_v}{d}$, ranging from 0.31~2.56. When A is small or n is large, m_2 increases with the increasing $\frac{a_v}{d}$. Only for pile caps with small transverse pile spacing ($A=1$), m_2 reduces with increasing $\frac{a_v}{d}$ when $0.81<\frac{a_v}{d}<2.56$. This is in line with the trend of Kani's valley for beams. As can be seen in Figure 2.6, when $1<\frac{a_v}{d}<2.5$, m_2 (in Kani's valley $m_2=\frac{M_{CR}}{M_{FL}}$) also reduces with the increasing $\frac{a_v}{d}$. Over most of the curve plane in Figure 6.14, the actual co-ordinates $\left(A,\frac{a_v}{d}\right)$ or $\left(n,\frac{a_v}{d}\right)$ at transitional points (Section 2.3.2) between failure modes, and the

definitions of the failure modes in the pile caps (*e.g.* Table 5.4), are totally different from the 1-way Kani's valley.

Figure 6.14 is a rude equivalent to Kani's valley. It needs to be improved after fully understanding all the failure modes in pile caps varying against key dimensions, and the corresponding mathematical expressions by which the transitional points can be defined. For example, the bending capacity M_{FL} of caps obtained above involves assumptions of the support and load conditions. A real M_{FL} acting as a normalizer is better to be larger than any bending moment corresponding to other failure modes, such that m_2 is always lower than 1.0 rather than the case in Figure 6.14 where m_2 is always larger than 1. M_{FL} may even be defined as other types of resistant capacity rather than the bending capacity. This is not in the scope of this research.

It is evident from Sections 6.2 and 6.3 that the shear strength v_c of the pile cap predicted by the current bending theory based formulae in BS5400 and BS8110 is no longer correct. The distribution of v_c is dependent on $\frac{2d}{a_v}$, A or n in a complex relationship. The actual shear capacity of the pile cap is much higher than predictions from current shear formulae. The current STM in BS8110 gives better prediction but fails to do so when the transverse pile spacing is large. The reason is that the strut-and-tie system assumed is disturbed when the transverse reinforcement plays a greater part in the shear resistance and more longitudinal reinforcement acts as a yielding tie than just lying on a width of maximum three times the pile diameter over each pile head. The shear failure is unlikely to be caused by the crushing of the concrete immediately under the wall loading. It is feasible to produce a design curve plane for 2-way spanning pile caps similar to Kani's valley for 1-way RC beams but varying against key parameters such as $\frac{2d}{a_v}$ and A or n.

6.4 Improvement to standard formulae

In this section, several suggestions are given to improve the current design methods *i.e.* the bending theory based shear formulae and STM. As the shear formulae are semi-empirical, a complex statistical method is required to improve the formulae based on the data obtained from experiments and the parametric study. This is not in the scope of this thesis. So qualitative suggestions are given to improve *Eq.*2.5 and *Eq.*2.6 (Section 2.10.1) and a quantitative method is presented to improve the current STM.

6.4.1 Suggestion to improve current bending theory based shear formulae

Sections 6.2 and 6.3 have already shown that v_c is dependent on A and $\frac{2d}{a_v}$. So the original expression of A and $\frac{2d}{a_v}$ needs to be modified. The ideal modified formula should describe a regression curve plane of the distribution of v_c in Figure 6.3. But a rough method is to subscribe a modification factor to $Eq.2.5$. Figure 6.10 shows $m_{BS8110b}$ from the parametric study ranging from 2.03~3.10. To make the formula conservative, a value of 2.0 is used. The modified $Eq.2.5$ can be expressed as:

$$v_c = \underbrace{\frac{0.79}{\gamma_m} MAX\left(\left(\frac{f_{cu}}{25}\right)^{1/3},1\right)}_{PartI}\underbrace{\left(\frac{100A_s}{bd}\right)^{1/3}}_{PartII}\underbrace{MAX\left(\left(\frac{400}{d}\right)^{1/4},0.67\right)}_{PartIII}\underbrace{\left(2\left(\frac{2d}{a_v}-1\right)A+2\right)}_{PartIV} \quad (Eq.6.2)$$

where A is based in BS8110 and the modification factor 2 is merged into *PartIV* of $Eq.2.5$ in a way to reduce a_v (d is fixed in this research) or increase A.

There is some physical explanation for increasing A as the longitudinal yielding tie and thus the width on which shear enhancement can be applied could be wider than triple the pile diameter over each pile head (Section 2.10.3). But A cannot exceed 1.0, or otherwise the physical meaning is lost.

The physical explanation for reducing a_v is the concern that the real shear span defined as the distance between the central span and the contra-flexural point could be shorter than specified in British Standards *i.e.* the distance between the edge of wall loading and 20% into pile inner edge (Figure 3.16).

But as discussed in Appendix II.2, for all experimental samples $\left|\frac{M_h}{M_s}\right|$ from a frame analysis is relatively small, causing the real shear span to be longer than the current shear span. For instance, as already discussed in Section 3.6, the largest $\left|\frac{M_h}{M_s}\right|$ appearing in B4A1 is $\frac{1}{26.4}$. Thus, the real shear span in B4A1 $a_v = 385mm$, longer than $a_v = 361mm$ specified by British Standards (Section AII.2). Though the frame analysis neglects the influence of the dimensions of the wall loading and pile diameter (Appendix AII.1) which might potentially increase $\left|\frac{M_h}{M_s}\right|$ and is slightly less physical, it still suggests that to reduce a_v to correct

current formulae may lack a physical meaning. Therefore the 'correct' expressions of A and $\frac{2d}{a_v}$ in *PartIV* in an ideal design formula, if obtained using a statistical method similar to the empirical method introduced in Section 2.7, would end up being without physical meaning.

6.4.2 Suggestion to improve current STM

Section 5.8 and Section 6.3.3 have discussed that when the transverse pile spacing is large, the width of longitudinal reinforcement reaching yield could be larger than triple the pile diameter above each pile head and the transverse reinforcement plays an important role in the shear resistance. An ideal STM should consider the deviation of the spatial angles of the concrete compressive strut assumed in *Eq.*6.1 caused by these behaviours. Considering that the shape and strength of the inclined concrete strut are different for different cap dimensions, the precise establishment of such a STM is complex. It is suggested to use one uniform formula for a range of pile caps, constructed on the yielding of the longitudinal tie.

A new STM is therefore proposed, in which 90% of the whole width of the longitudinal reinforcement be considered as a yielding tie to compensate for the neglected contribution of the transverse reinforcement and for the neglected extra longitudinal yielding tie if the tie width is larger than triple the pile diameter over each pile head. This method is especially efficient for caps with large transverse pile spacing. In addition, the inclined concrete strut with α, β, γ links the pile head to a point ¼ the width of the loaded area h_c from the centre of the top surface (Figure 6.4 (b)) for all load patterns, accounting for the width of the wall loading and the pile. The new STM can then be obtained in a similar way to *Eq.*6.1. The shear capacity of pile caps is thus expressed as:

$$F' = \frac{4df_y A_{s90\%}}{kh_p - \frac{h_c}{2}} \qquad (Eq.6.3)$$

where $A_{s90\%}$ is 90% the total area of the longitudinal reinforcement.

The distribution of the modification ratio m_{nSTM} varying against $\frac{2d}{a_v}$ and A or n for the models in the parametric study is shown in Figure 6.15. It shows that compared with $m_{BS8110S}$, m_{nSTM} close to 1.0 covers over a larger area (*cf.* Figure 6.12). In this area, m_{nSTM} (maximum 1.3) is also closer to 1.0 than $m_{BS8110S}$ (maximum 1.5), giving a better prediction. If considering the range of $\frac{2d}{a_v}$ and n of experimental samples represents the practical

range of pile cap dimensions *i.e.* $1.28 < \frac{2d}{a_v} < 3.59$ and $2 < n < 5.38$ (Table 3.3 (b)), the new STM gives a good prediction for practical pile caps, as shown in the area enclosed by the bold line in Figure 6.15. The area enclosed by the bold dashed line is considered as the enlarged practical range of pile cap dimensions where the new STM can also perform well.

In Figure 6.15, one can see that for pile caps in the corner of the curve plane, within the range $n > 3.84$ and $\frac{2d}{a_v} > 1.89$, m_{nSTM} drops sharply below 1.0, failing to predict the shear capacity. In this range, the longitudinal yielding tie may concentrate on the pile head rather than on the whole cap width or 90% of the cap width, for example as shown in Figure 5.29 for E1dl with $n = 9.23$ and $\frac{2d}{a_v} = 6.52$. Though the transverse reinforcement tie at high elastic stress or yielding occurs in this range, for example as shown in Figure 5.31 for E1ej with $n = 6.15, \frac{2d}{a_v} = 4.63$ (also see Table 5.4 (c)), its contribution to the real shear resistance is much less than the reduction caused by the reduction of the longitudinal yielding tie, which makes the real shear capacity of pile caps in this area much less than the prediction from *Eq.*6.3.

*Eq.*6.3 is also applied to predict the shear capacity of the experimental samples in Batch 4 and to be compared with the failure load from the models in FEA. The results are shown in Table 6.1. It shows a general image that the new STM is less conservative than the STM in BS8110, and for most samples the prediction is more accurate than *Eq.*6.1. m_{nSTM} for B4A5 is 0.84. This is because the actual failure load for B4A5 may be higher than the observed failure load $1244\,kN$ in the FEA since B4A5 fails by the pile crushing (Table 3.5). In Batch 4 Series B, the prediction from BS8110 STM is constant at $624\,KN$ for B4B2, B4B3 and B4B4 because the width of the longitudinal tie in *Eq.*6.1 is always triple the pile diameter above each pile head. In the experiments, the shear capacity has a tendency to increase with increasing transverse pile spacing, which is well predicted by *Eq.*6.3 (Table 6.1).

It is clear from the FEA that when the transverse pile spacing is small, such as for samples in Batch 4 Series A, the longitudinal yielding tie lies on the whole cap width (Table 5.4 (b)) rather than 90% of the cap width. The factor of 90% is only to make *Eq.*6.3 prediction conservative, slightly lower than the actual shear capacity.

It needs to be emphasized that the new STM is best applicable to the pile caps studied in

this research. For other pile caps with different concrete strengths, reinforcement ratios, size effects and load patterns, this method may be less applicable.

6.5 The influence of load pattern on a cap's shear mechanism

So far, all results have been for pile caps subject to the full-length wall loading. It is expected that the shear capacity and mechanism may vary with the load pattern, and so in order to study its influence, the shear behaviours of one of Clarke's experimental samples (Section 3.2) under a concentrated load, and a model in the parametric study under a wall loading with reduced length were investigated.

In Clarke's work, three different types of reinforcement layouts were used in 15 samples divided into Series A and B with different size dimensions. All these square samples were subject to a concentrated load of $200mm \times 200mm$. The reinforcement layout in cap A10 was closest to the experimental samples in this research *i.e.* grid reinforcement fully bent up with bobbing up above the pile head in both longitudinal and transverse directions. Therefore, A10 was chosen for comparison. The dimensions and material properties of A10 are shown in Table 6.2 (a), (b) and Table 6.3. The depth of the pile was $150\,mm$.

A FEA was done for A10 based on the principles in Section 5.2~5.3 except the material strengths (Table 6.3). Figure 6.16 shows a comparison of the crack distributions on the ¼ pile cap surfaces at the failure step between the FEA and the experiment. The cracks in the FEA are compatible with the experimental distributions. Table 6.4 is the comparison of the failure load for the experiment and FEA in which the loads are comparable. Both failure modes in FEA and experimental were brittle. The FEA was thus considered as reliable.

Figure 6.17 shows the distribution of stress in longitudinal and transverse reinforcement σ_{sx} and σ_{sy} in A10 at failure step. It is clear that when A10 failed, ties in both directions appeared but were both in the elastic stage (below $400\,MPa$). Though $n=3$ for A10, the longitudinal tie in elastic stress concentrated above the pile head rather than on the whole cap width. However in models with $n=3$ under full-length wall loading in the parametric study, the longitudinal tie yields on the whole cap width (Table 5.4 (b)). Rather than the ductile failure of the pile cap under the full-length wall loading (Section 3.9.1), the brittle punching shear failure of A10 under the concentrated load led to a conical plug of concrete being pushed out (Clarke, 1973). The punching shear cracks both from FEA and experiments are shown in Figure 6.16.

Table 6.5 compares the real failure load of A10 with bending theory based shear formulae in BS8110 and BS5400, the new STM in *Eq.*6.3 and the prediction of the

punching shear failure in BS8110. It is shown that the BS8110 bending theory based formula overestimates the shear capacity of A10 rather than underestimating as for caps under full-length wall loading. On the contrary, the predictions from *Eq.*6.3, BS5400 bending theory based shear formula and BS8110 prediction of punching shear capacity are lower than the real failure load. The underestimation from *Eq.*6.3 is because σ_{sx} was still elastic when the pile cap failed, which defies the assumption in *Eq.*6.3 that pile caps fail by the strut-and-tie system failure after the yielding of the longitudinal reinforcement on 90% the whole cap width at the failure step.

A parametric study model, E1gg (Table 5.3), was used to investigate the shear behaviour of a pile cap under a wall loading with reduced length to the pile inner edge (Figure 6.18). The same iterative solver parameters were used as in E1gg under full-length wall loading (Section 5.7.3) were used. The failure load of E1gg under the wall loading with reduced length is $800\,kN$, less than under full-length wall loading ($1616\,kN$, Table 6.6). It also fails in a brittle way rather than ductile as under full-length wall loading. Figure 6.19 shows the crack distribution on E1gg surfaces at the failure step. Different from the punching shear cracks in Figure 6.16, a large number of compressive splitting shear cracks on the front surface, similar to the normal shear failure in E1gg under a full-length wall loading, are observed. On the left surface, only central bending cracks are observed. However σ_{sx} and σ_{sy} stay below yield stress similar to the behaviour of Clarke's A10 under concentrated load.

Table 6.6 is the comparison of the shear predictions from the different methods. Unlike for A10 failing in punching shear, the prediction by the new STM is higher than the real failure load, while the prediction from BS8110 bending theory based formula and punching shear prediction is lower than the real failure load.

It is clear from the above discussion that the failure mechanism of E1gg under the wall loading with reduced length is neither the punching shear failure as in A10 under concentrated load nor the normal shear failure in E1gg under a full-length wall loading but a mechanism in between these two extreme load patterns.

This section has shown that the shear mechanism and the shear capacity of pile caps and the accuracy of each design method are influenced by the load pattern. The load pattern may cause the shear mechanism to change from a normal shear failure explained by the bending theory based shear formulae to a punching shear failure. Current bending theory based shear formulae, STM and the punching shear prediction for pile caps (*e.g.* at a constant perimeter surrounding the loading lying on 20% the pile diameter inside the inner edge of the piles) do not consider the influence of the load pattern which is not ideal. In other words, the transition

of the shear mechanism of a pile cap under full-length wall loading to the concentrated load is not clearly represented by the current design methods. The cap under full-length wall loading may have a maximum or up limit shear capacity. The shear capacity reduces with reducing length of wall loading ending up with brittle punching shear failure at lowest shear failure load when the cap is under concentred loading.

6.6 Summary

The nominal design shear stress v_c obtained from the experimental samples, FEA models of experimental samples and the models in the parametric study have been compared with the expression of the bending theory based shear formulae in BS8110 and BS5400. Rather than a plane specified by BS8110 and BS5400, real v_c is in a complex relationship with shear enhancement factor $\frac{2d}{a_v}$, shear enhancement application factor A and the ratio of the transverse pile spacing over one pile diameter n. v_c increases with the increasing $\frac{2d}{a_v}$ and A or reducing n. The incorrect expression of *PartIV* in *Eq.*2.5 and *Eq.*2.6 needs to be modified in a way to fit the real relationship between v_c, $\frac{2d}{a_v}$ and A or n. The current upper limit of v_c for 2-way spanning pile caps in British Standards is not applicable.

The modification ratio of the real shear capacity over the predictions from the bending theory based shear formulae in British Standards is a function of $\frac{2d}{a_v}$ and A or n. Always being significantly higher than 1, the modification ratio indicates that both British Standards are conservative because of the incorrect expression of $\frac{2d}{a_v}$ and A.

The shear capacity predicted from the current STM in BS8110 is compared with the real shear capacity from the experimental samples, models in FEA for experimental samples and models in the parametric study. The modification ratio being close to 1 for most samples and models indicates that STM can physically explain the shear behaviour of pile caps and gives better prediction, except for those with large transverse pile spacing for which STM in BS8110 underestimates the shear capacity.

Suggestions to improve the current design methods have been given. A new STM is established in which the longitudinal reinforcement tie across the 90% the whole cap width is

considered and the span of the longitudinal tie is reduced. The pyramid geometry of the strut-and-tie system is remained. The new STM gives better prediction than the current STM in BS8110. This is because for models where transverse reinforcement is either yielding or at high elastic stress, and where the longitudinal yielding tie has a width more than triple the pile diameter above each pile, the increased shear capacity compared to current STM is compensated for by increasing the width of the longitudinal yielding tie in the new STM. The new STM overestimates the capacity of pile caps with very large transverse pile spacing and very short longitudinal pile spacing, but these are deemed not to be practical pile cap dimensions.

An alternative way to improve the design methods is to modify the expression of *PartIV* in *Eq.*2.5 and *Eq.*2.6 by a statistical method based on the available v_c distribution against $\frac{2d}{a_v}$ and A or n from the experimental samples, models in FEA and in the parametric study. The new expression of *PartIV* would lack a physical meaning though.

Another design method suggested to designers is to directly use the $m_{BS8110b}$ distribution in Figure 6.10, firstly proposing A and $\frac{2d}{a_v}$, and then projecting to the curve plane to obtain the modification ratio $m_{BS8110b}$. Finally, the real shear capacity is the current prediction from BS8110 multiplied by the modification ratio.

The shear capacity and shear mechanism are influenced by the load pattern. Under different load patterns, the modification ratios of bending theory based formulae, STM and prediction of punching shear capacity vary. Any ideal design method both for normal shear capacity and punching shear capacity should consider the influence of the load pattern. The current design methods however do not. The cap under full-length wall loading may have maximum shear capacity which reduces with the reducing length of the wall loading. It is expected that the shear capacity of pile caps under load patterns between full-length and concentrated loading can be estimated by interpolation between normal shear capacity when under full-length wall loading and the punching shear capacity when under concentrated loading.

It is possible to construct a design curve plane describing the shear behaviour of 2-way spanning pile caps which is equivalent to the Kani's valley plot for 1-way spanning RC beams, as long as the mathematical expressions for all the failure modes occurring in pile caps varying with key dimensions and thus the co-ordinates of the transitional points are obtained.

Table 6.1 Comparison of observed failure loads with predictions from different design methods ($\gamma_m = 1$, real strength of materials adopted)

Pile cap No.	Observed failure load $V_c\,(kN)$	BS8110 bending theory based prediction (kN)	Observed failure load over BS8110 prediction $m_{BS8110b}$	BS5400 bending theory based prediction (kN)	Observed failure load over BS5400 prediction $m_{BS5400b}$	BS8110 STM prediction $F\,(kN)$	Observed load over BS8110 STM prediction $m_{BS8110S}$	Failure load in FEA (kN)	Observed failure load in FEA over BS8110 STM prediction $m_{BS8110S}$	New STM prediction $F'\,(kN)$	Observed failure load in FEA over new STM prediction m_{nSTM}
B1A1	>1440*	885.0	>1.6	713.9	>2.0	1328.2	>1.1	N/A	N/A	1277.3	N/A
B2A1	>1440*	445.4	>3.2	412.0	>3.5	726.2	>2.0	N/A	N/A	798.1	N/A
B2A2	>1440*	641.2	>2.2	514.5	>2.8	939.8	>1.5	N/A	N/A	1105.1	N/A
B2A3	>1440*	776.9	>1.9	585.3	>2.5	1065.1	>1.4	N/A	N/A	1306.0	N/A
B2A4	>1440*	967.0	>1.5	681.1	>2.1	1228.9	>1.2	N/A	N/A	1596.2	N/A
B3A1	960	383.4	2.50	354.6	2.71	726.2	1.32	N/A	N/A	798.1	N/A
B3A2	1232	554.5	2.22	445.0	2.77	939.8	1.31	N/A	N/A	1105.1	N/A
B3A3	1415	675.0	2.10	508.6	2.78	1065.1	1.33	N/A	N/A	1306.1	N/A
B4A1	592	250.0	2.37	220.4	2.69	615.5	0.96	632	1.03	632.6	1.00
B4A2	548	329.4	1.66	267.3	2.05	757.6	0.72	820	1.08	805.1	1.02
B4A3	919	418.0	2.20	325.3	2.82	895.3	1.03	1008	1.13	984.1	1.02
B4A4	1052	482.9	2.18	361.1	2.91	984.9	1.11	1064	1.08	1107.0	0.96
B4A5	1244	700.4	1.78	468.5	2.66	1231.1	0.99	1244	1.01	1476.1	0.84
B4B1	622	293.9	2.12	231.3	2.69	528.8	1.18	605	1.14	562.5	1.07
B4B2	713	370.5	1.92	306.4	2.33	623.9	1.14	812	1.30	731.3	1.11
B4B3	769	402.2	1.91	339.3	2.27	623.9	1.23	924	1.48	843.8	1.10
B4B4	1048	454.2	2.31	367.2	2.85	623.9	1.68	1040	1.67	1012.5	1.03

* Failure did not happen and the shear failure load was higher than the threshold of the testing machine 1440 kN.

Table 6.2 Dimensions and reinforcement arrangement of Clarke's A10

(a)

Pile cap No.	Pile cap depth h (mm)	Effective depth $d\,(mm)$	Pile cap length l (mm)	Pile cap width b (mm)	Pile diameter $h_p\,(mm)$	Longitudinal pile spacing $kh_p\,(mm)$	Transverse pile spacing $kh_w\,(mm)$	Side length of square concentrated loading $h_c\,(mm)$
A10	450	405	950	950	200	600	600	200

(b)

Pile cap No.	Reinforcement ratio $\rho\,(\%)$	Ratio of transverse pile spacing over pile diameter $n\left(=\frac{kh_w}{h_p}\right)$	Shear enhancement factor $\frac{2d}{a_v}$	Shear enhancement application factor A	
				BS8110	BS5400
A10	0.204	3.00	5.79	1	0.42

Table 6.3 Concrete and reinforcement properties

Pile cap No.	28 days concrete characteristic cube strength (N/mm^2)	Real cube compressive strength at 28 days or on the day of test $f_{cu}\,(N/mm^2)$	Reinforcement diameter (mm)	Reinforcement mean yield strength f_y (N/mm^2)
A10	32.2	30.2	10	510

Table 6.4 Comparison of the failure load (kN) of A10 between FEA and experiment

	Clarke's A10
FEA	1404
Experiment	1520

Table 6.5 Comparison of the real failure load of A10 under concentrated loading with different predictions ($\gamma_m = 1$)

	Observed load (kN)	Failure load in FEA (kN)	New STM (kN)	BS8110 bending theory based prediction (kN)	BS5400 bending theory based prediction (kN)	BS8110 punching capacity of pile cap (kN)
A10	1520	1404	1168	2274	1251	1275

Table 6.6 Comparison of the real failure load of E1gg under a wall loading with reduced length with different predictions ($\gamma_m = 1$)

	Failure load in FEA (kN)	New STM (kN)	BS8110 bending theory based prediction (kN)	BS5400 bending theory based prediction (kN)	BS8110 punching capacity (kN)	E1gg under full-length wall loading (kN)
E1gg	800	1378	613	447	664	1616

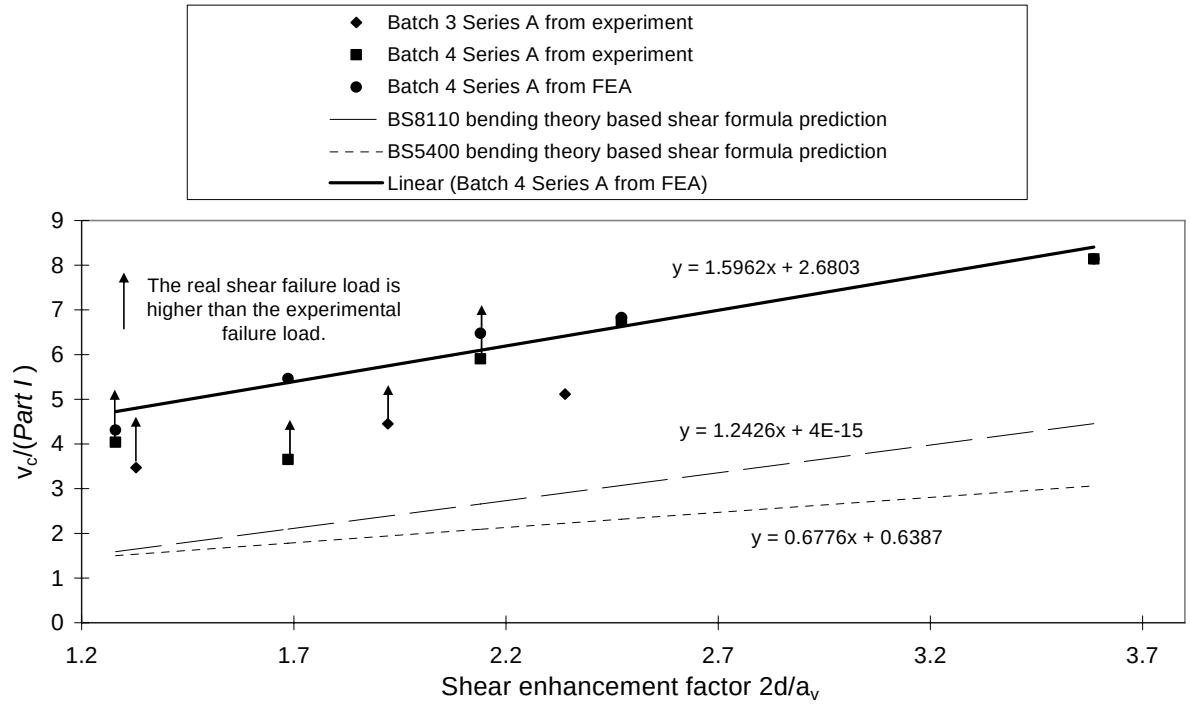

Figure 6.1 The relationship between $\frac{v_c}{PartI}$ and $\frac{2d}{a_v}$ of samples in Batch 3 Series A ($n = 2$) and Batch 4 Series A ($n = 2.31$)($\gamma_m = 1$)

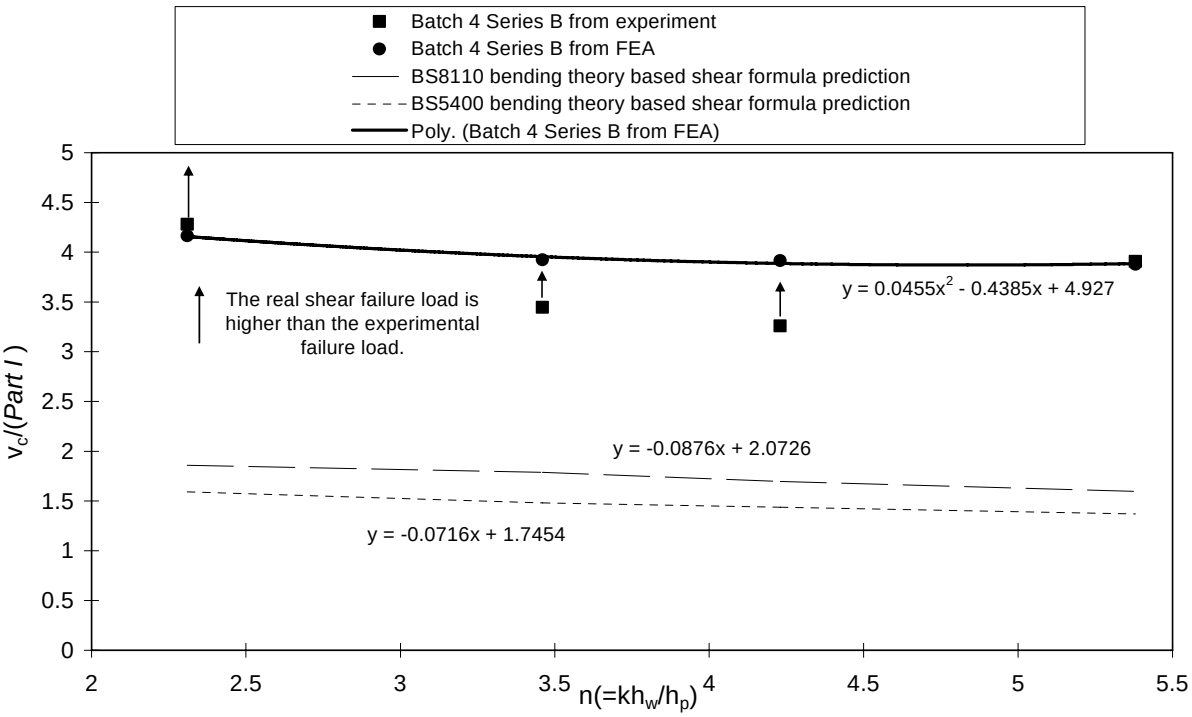

(a) The relationship between $\frac{v_c}{PartI}$ and n

Figure 6.2 The relationship between $\frac{v_c}{PartI}$ and A or n for samples in Batch 4 Series B ($\frac{2d}{a_v} = 1.69$)($\gamma_m = 1$)

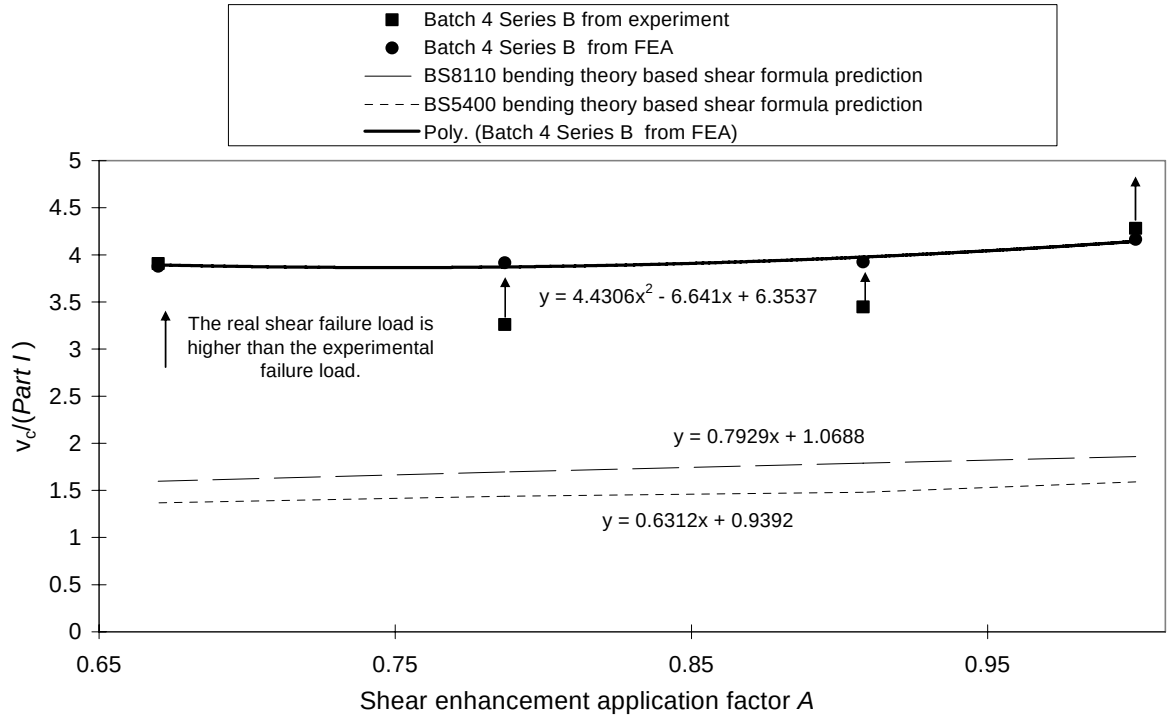

(b) The relationship between $\frac{v_c}{PartI}$ and A

Figure 6.2 The relationship between $\frac{v_c}{PartI}$ and A or n for samples in Batch 4 Series B ($\frac{2d}{a_v}=1.69$)($\gamma_m=1$)

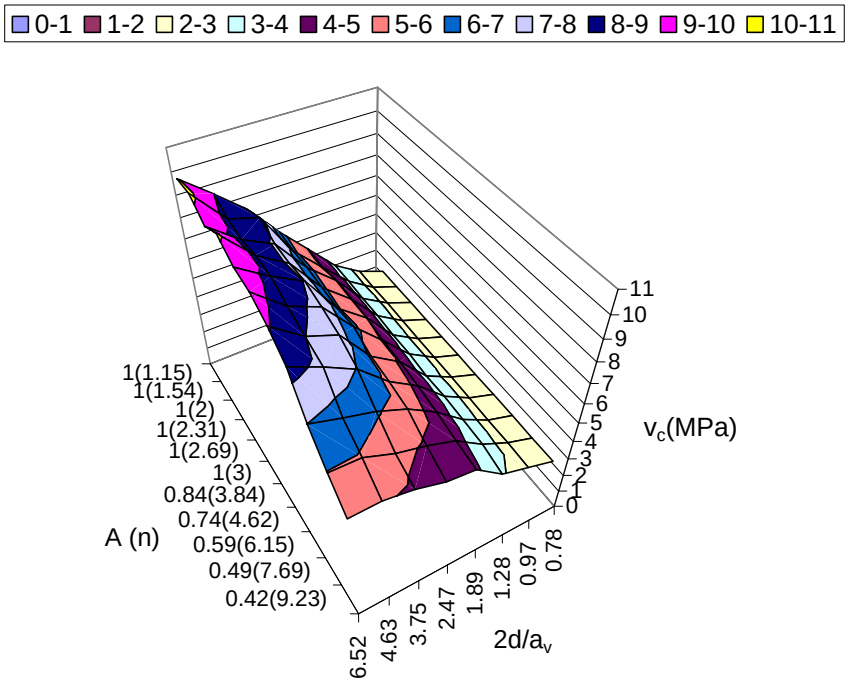

(a) The distribution of v_c as a whole

Figure 6.3 The distribution of v_c for 88 models in parametric study ($\gamma_m=1$)

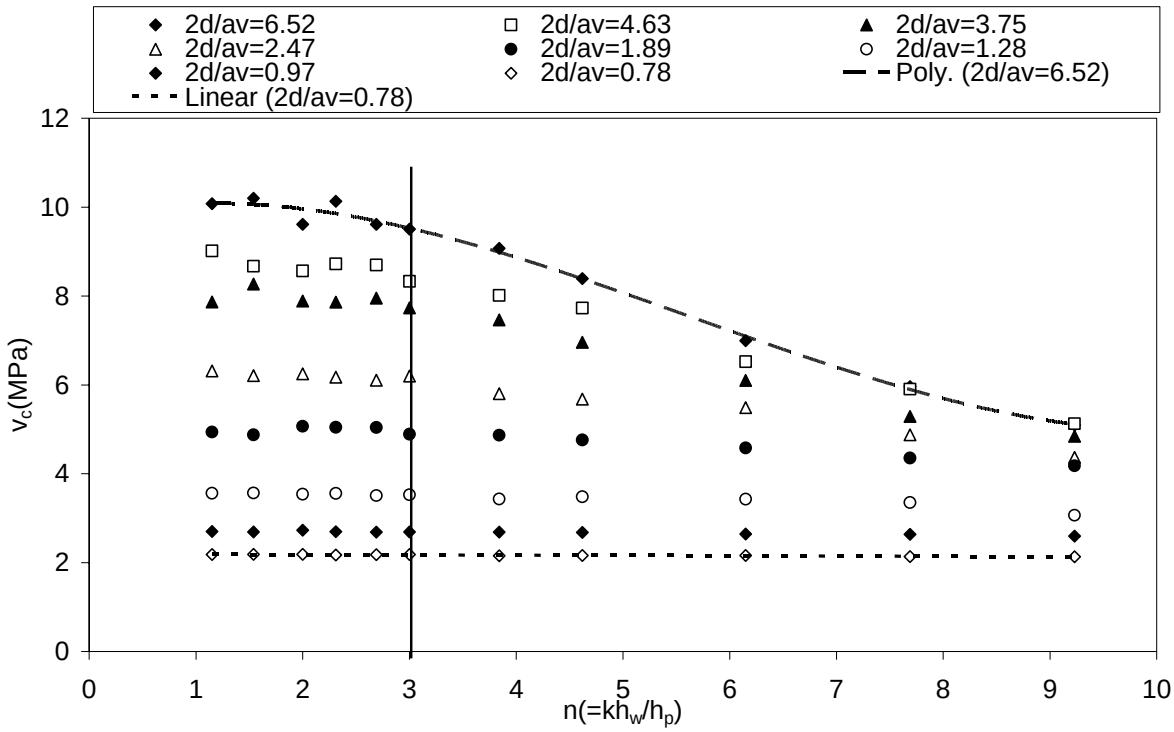

(b) The relationship between v_c and n subject to different $\frac{2d}{a_v}$

Figure 6.3 The distribution of v_c for 88 models in parametric study ($\gamma_m = 1$)

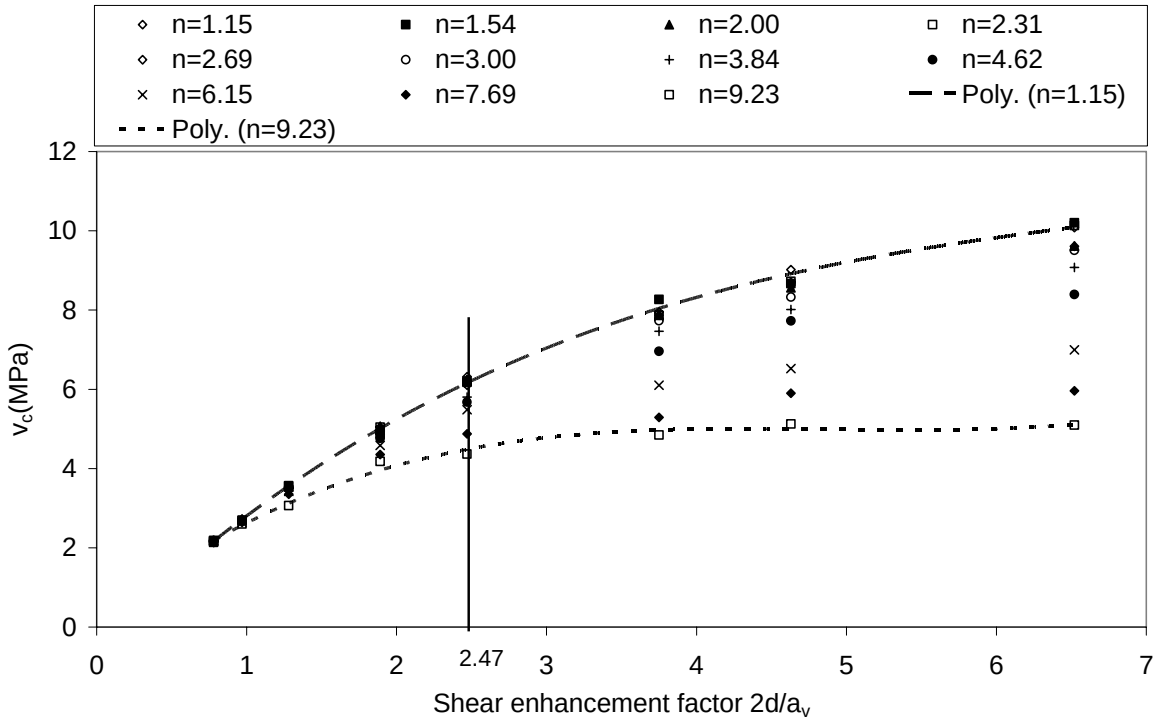

(c) The relationship between v_c and $\frac{2d}{a_v}$ subject to different n

Figure 6.3 The distribution of v_c for 88 models in parametric study ($\gamma_m = 1$)

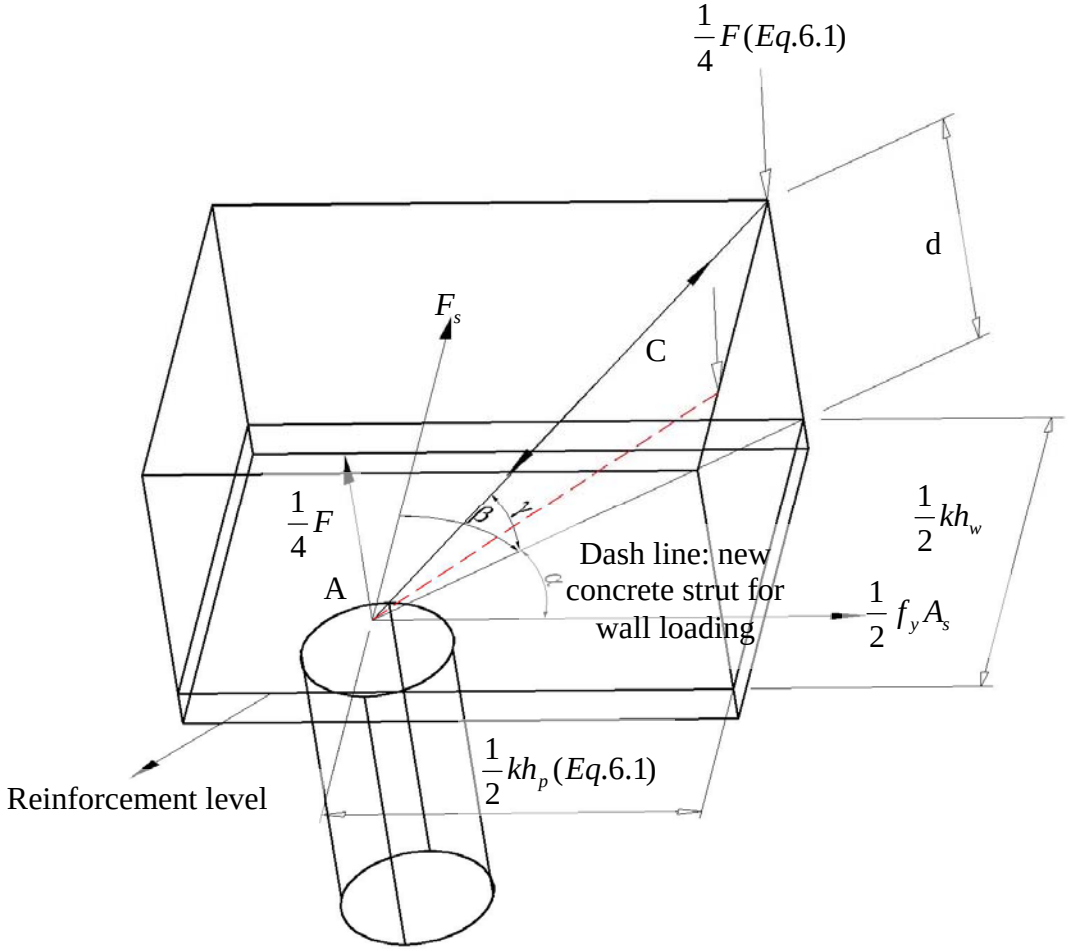

(a) STM currently used in BS8110 and BS5400

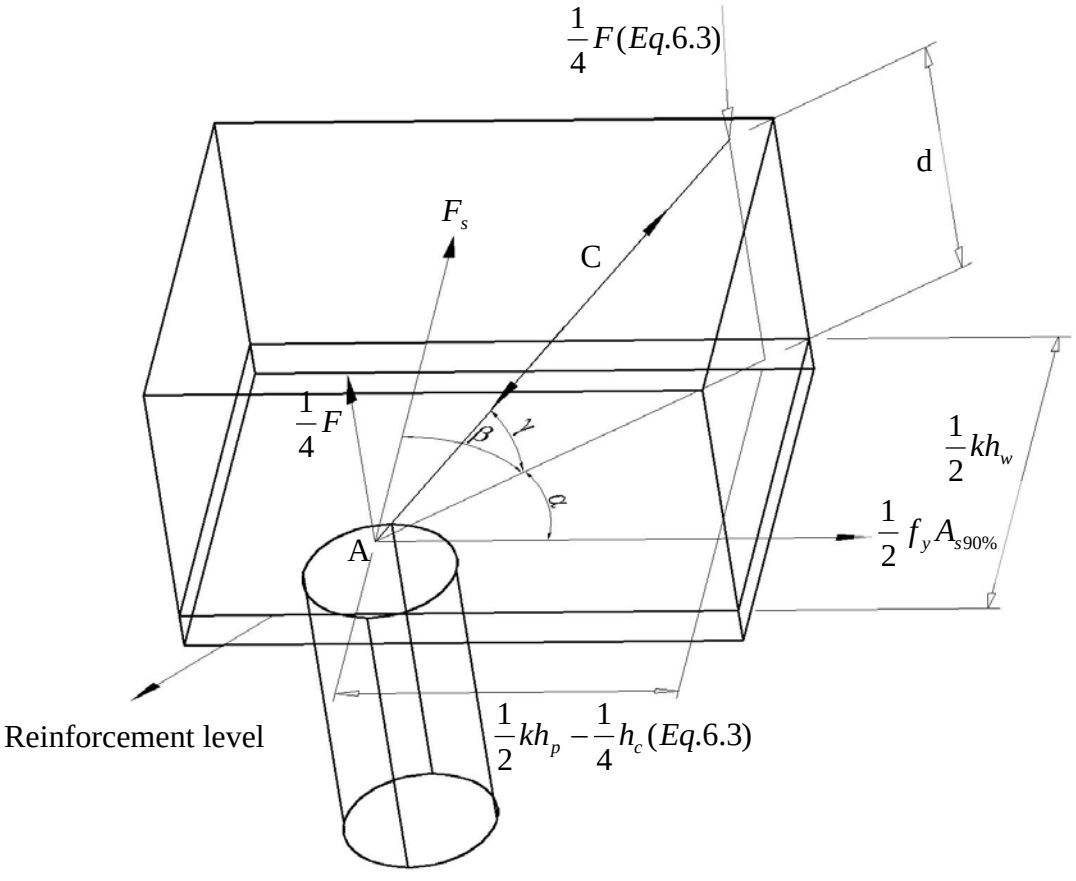

(b) New STM

Figure 6.4 Strut-and-tie model in ¼ pile cap

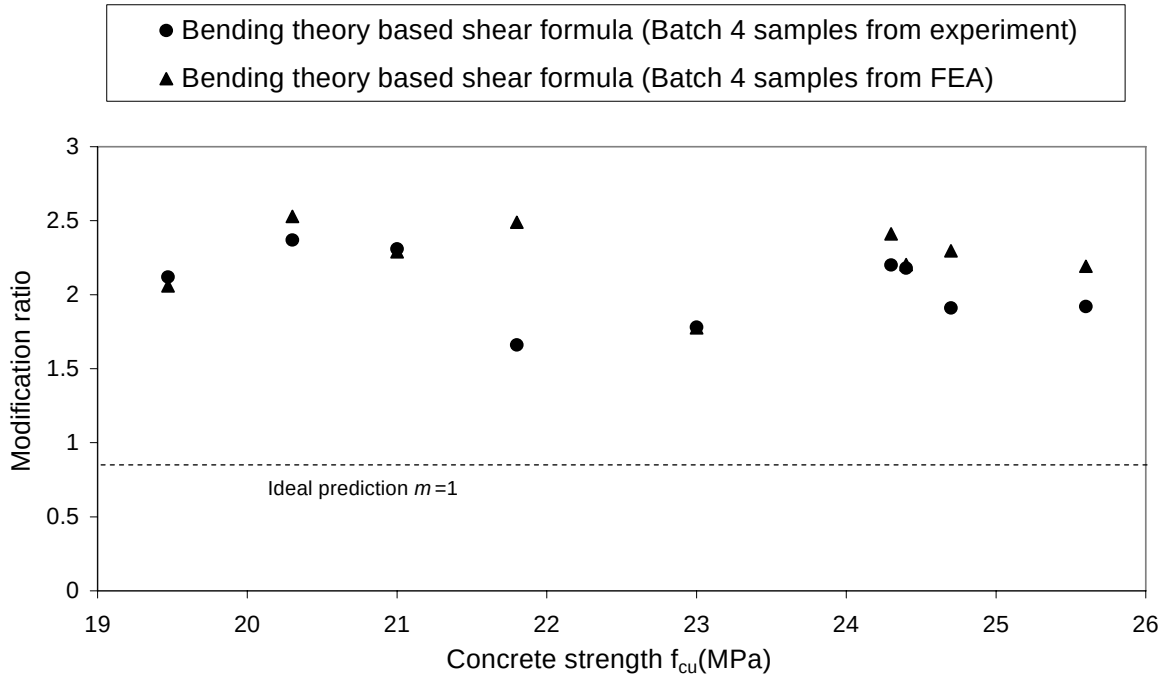

Figure 6.5 The relationship between $m_{BS8110b}$ and f_{cu} ($\gamma_m = 1$)

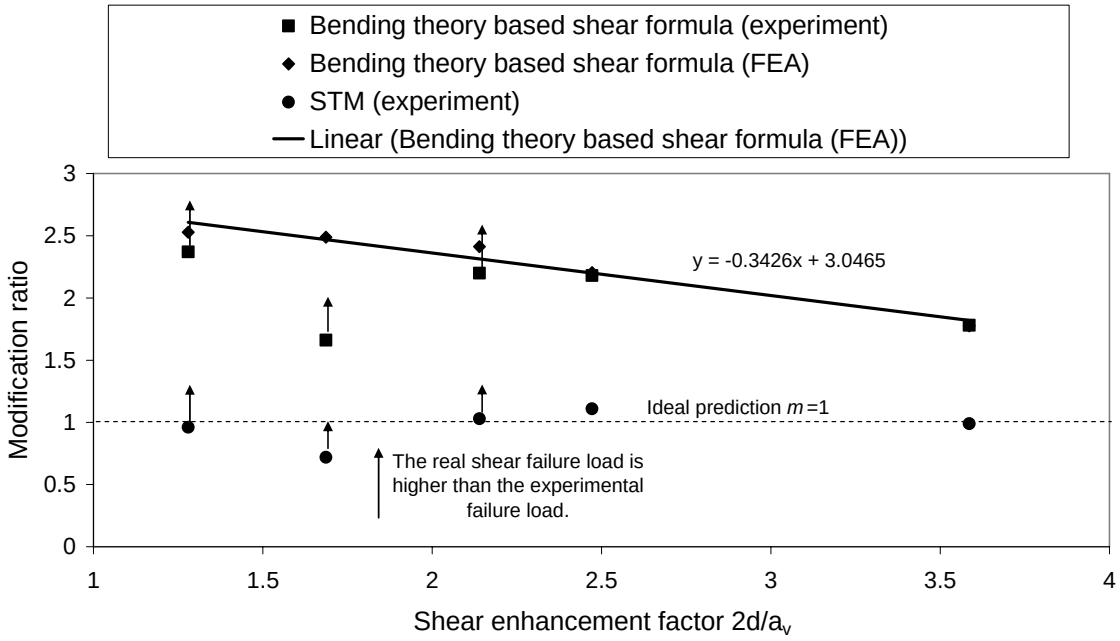

Figure 6.6 The relationship between $m_{BS8110b}$ and $\frac{2d}{a_v}$, $m_{BS8110S}$ and $\frac{2d}{a_v}$ for samples in Batch 4 Series A ($n = 2.31$) ($\gamma_m = 1$)

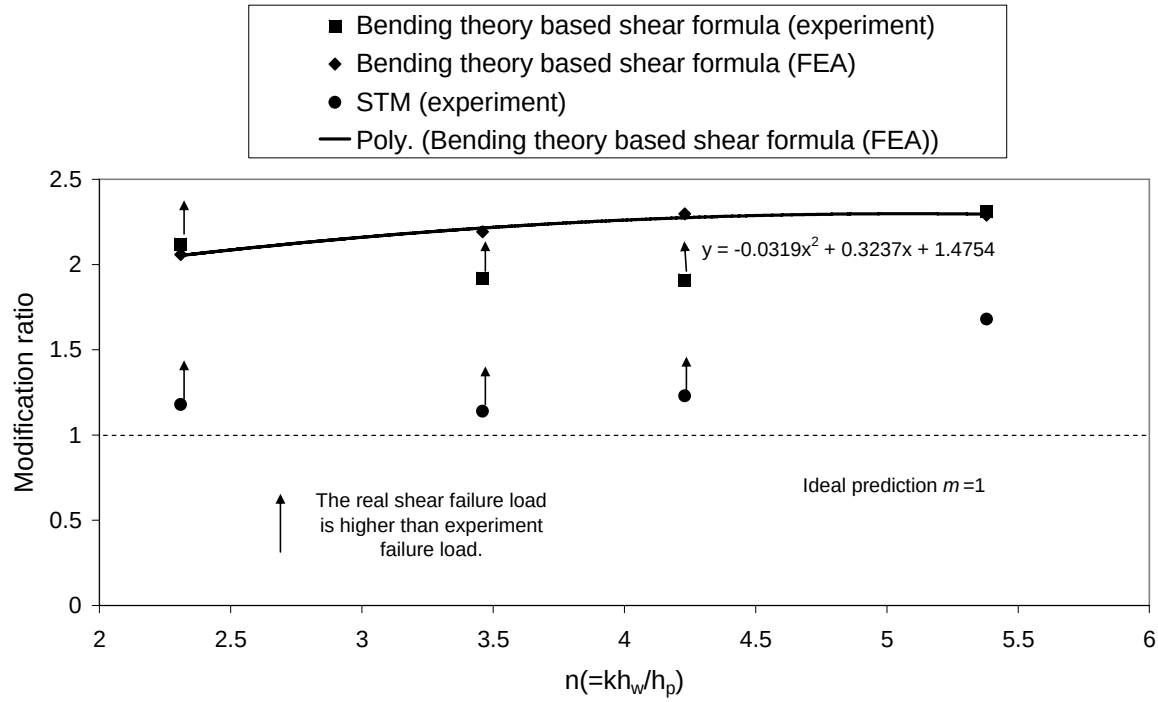

Figure 6.7 The relationship between $m_{BS8110b}$ and n, $m_{BS8110S}$ and n for samples in Batch 4 Series B ($\frac{2d}{a_v} = 1.69$) ($\gamma_m = 1$)

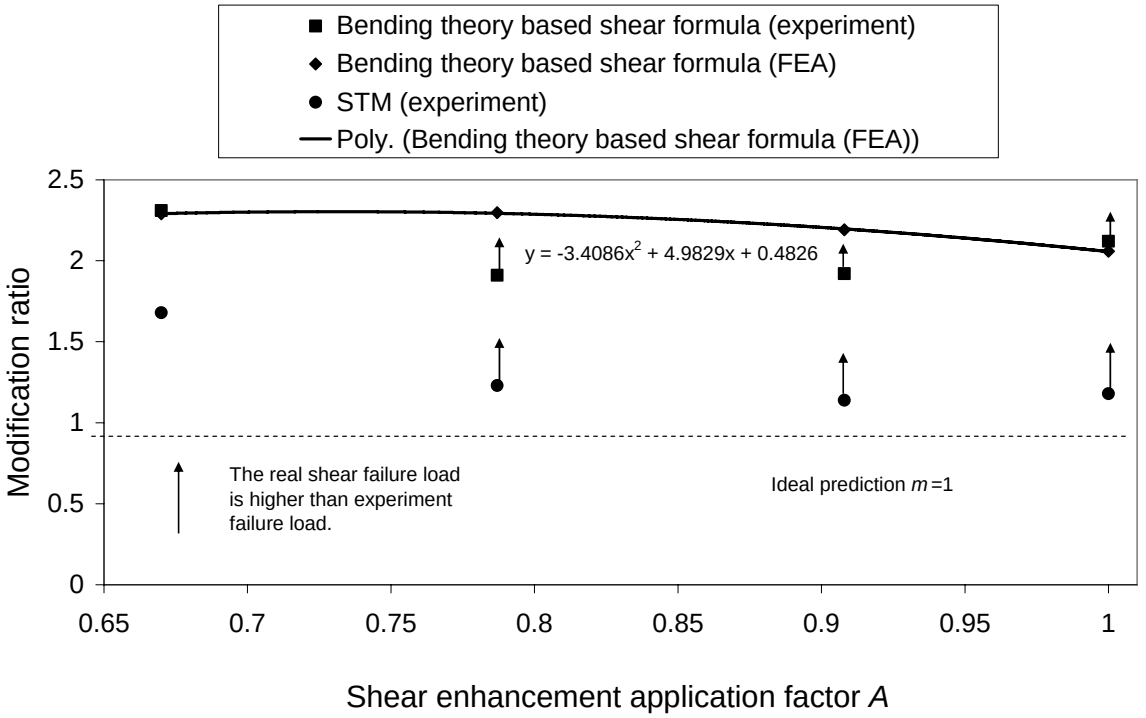

Figure 6.8 The relationship between $m_{BS8110b}$ and A, $m_{BS8110S}$ and A for samples in Batch 4 Series B ($\frac{2d}{a_v} = 1.69$) ($\gamma_m = 1$)

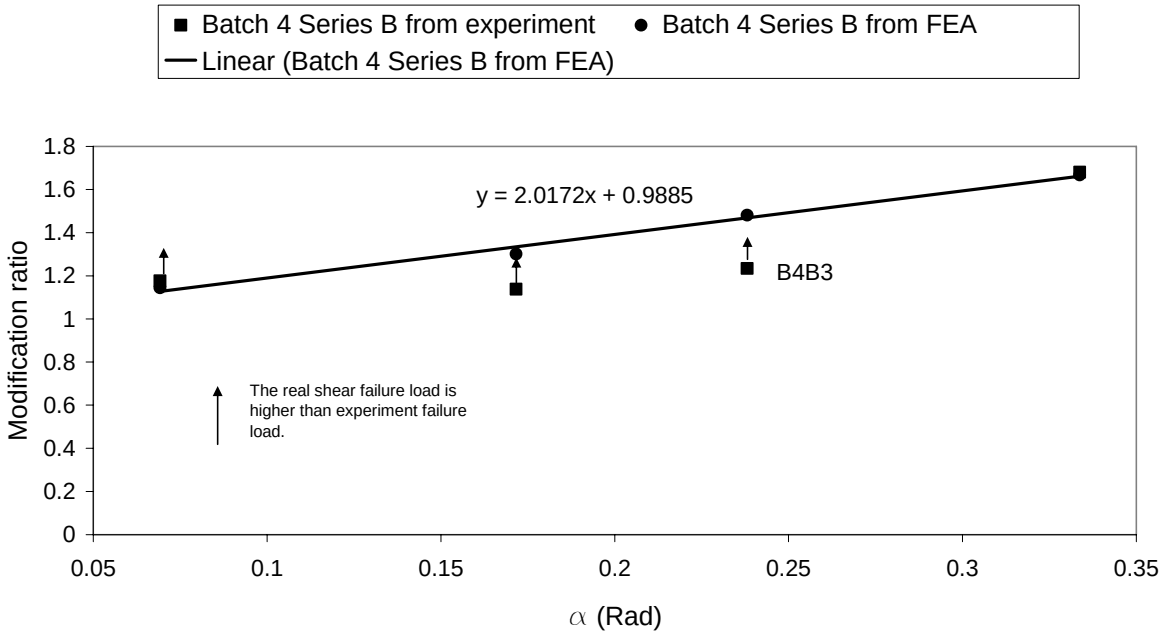

Figure 6.9 The relationship between $m_{BS8110S}$ and the space angle of the concrete strut α for samples in Batch 4 Series B ($\frac{2d}{a_v} = 1.69$) ($\gamma_m = 1$)

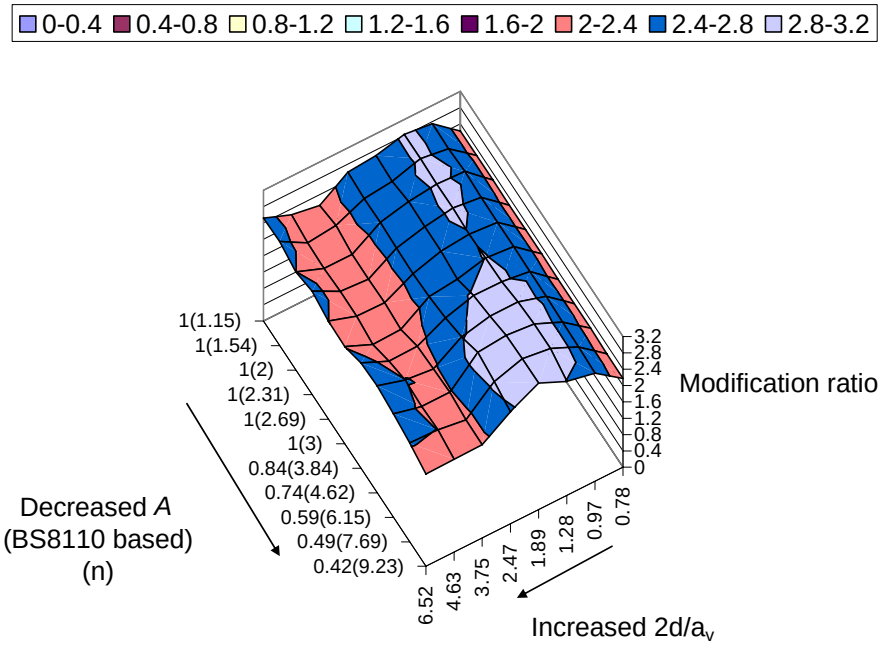

Figure 6.10 Distribution of $m_{BS8110b}$ for models in parametric study

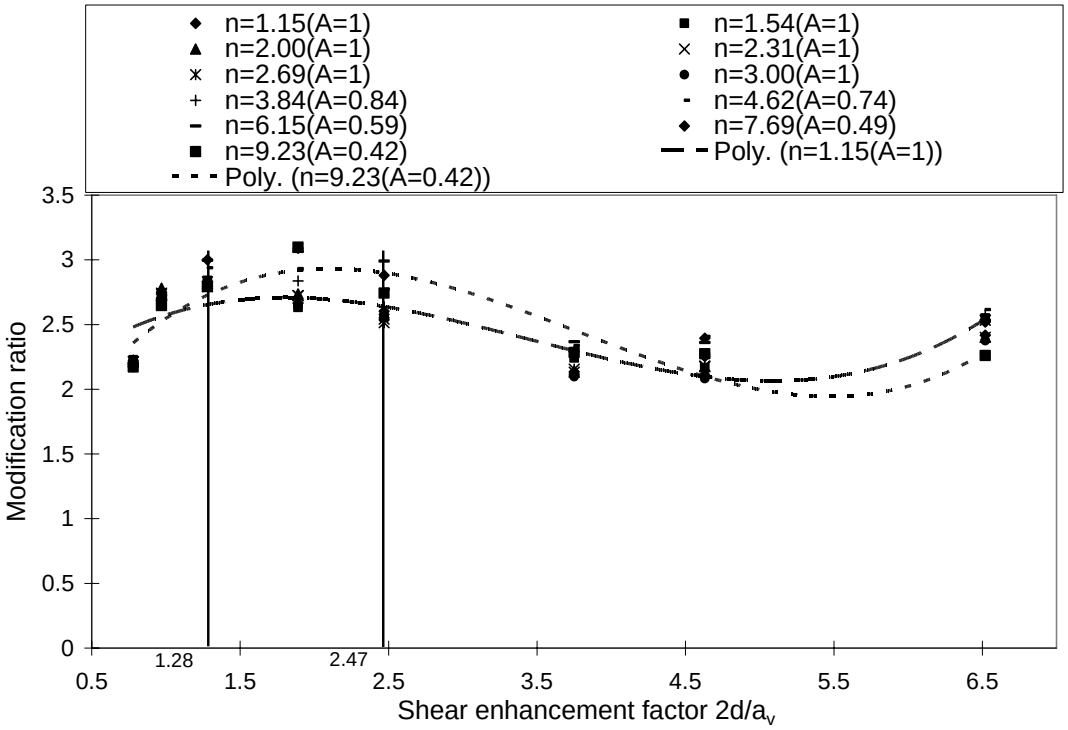

(a) Relationship between $m_{BS8110b}$ and $\frac{2d}{a_v}$

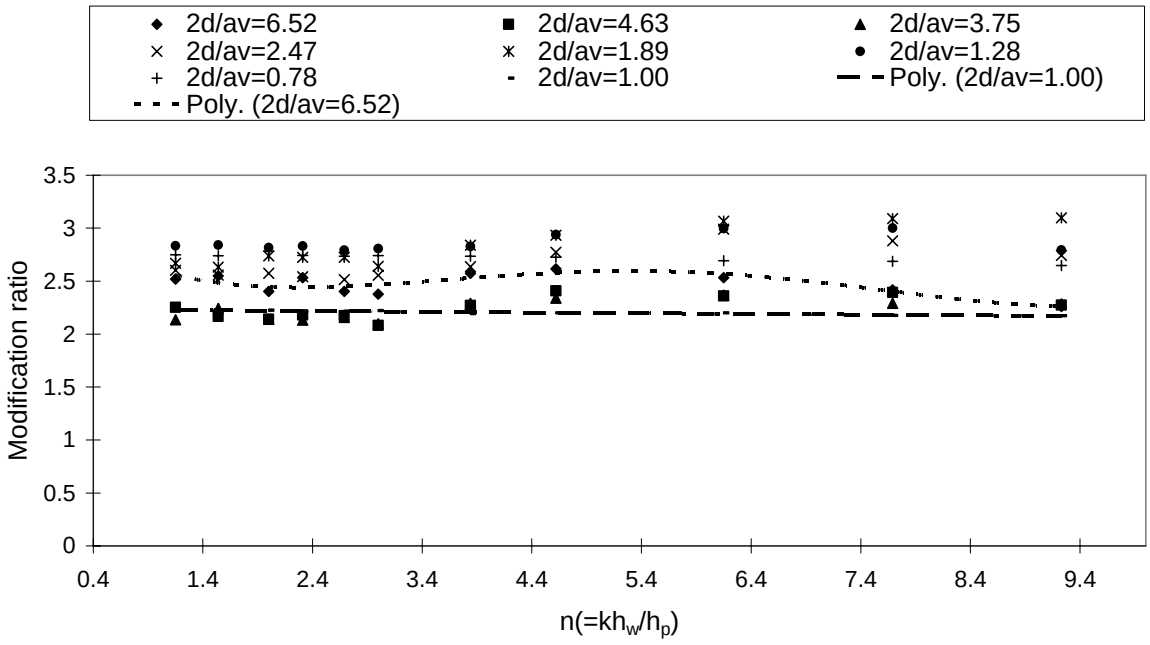

(b) Relationship between $m_{BS8110b}$ and n

Figure 6.11 Relationship between $m_{BS8110b}$ and $\frac{2d}{a_v}$, between $m_{BS8110b}$ and n for models in parametric study

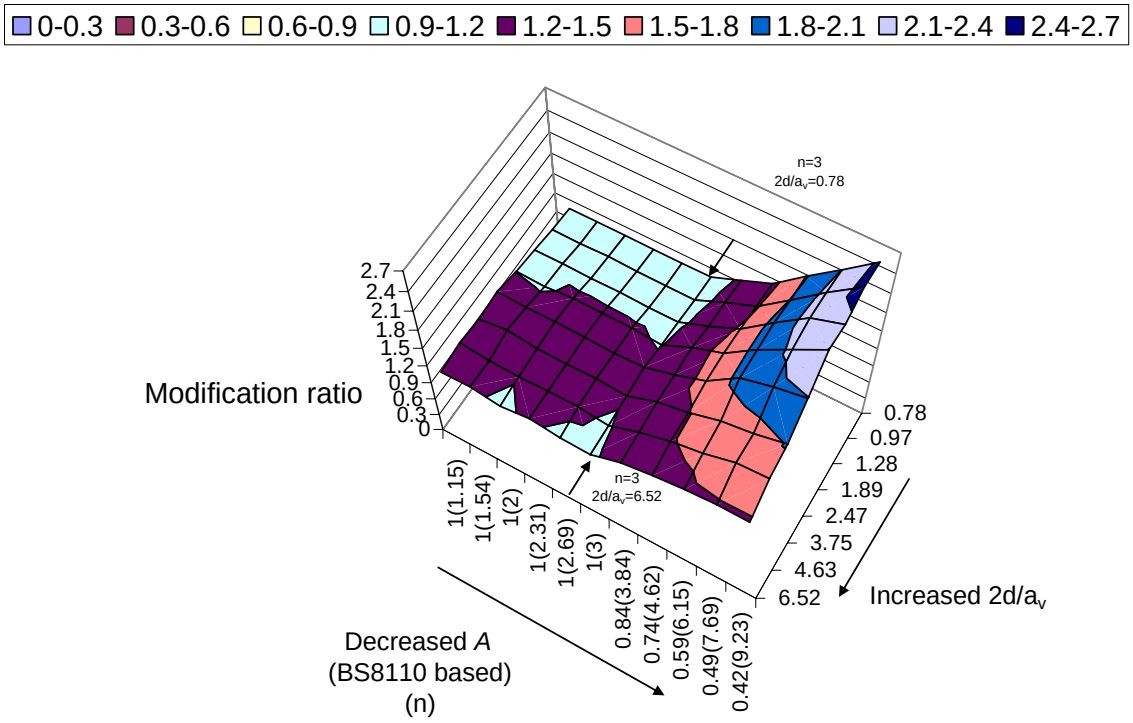

Figure 6.12 Distribution of $m_{BS8110S}$ for models in parametric study

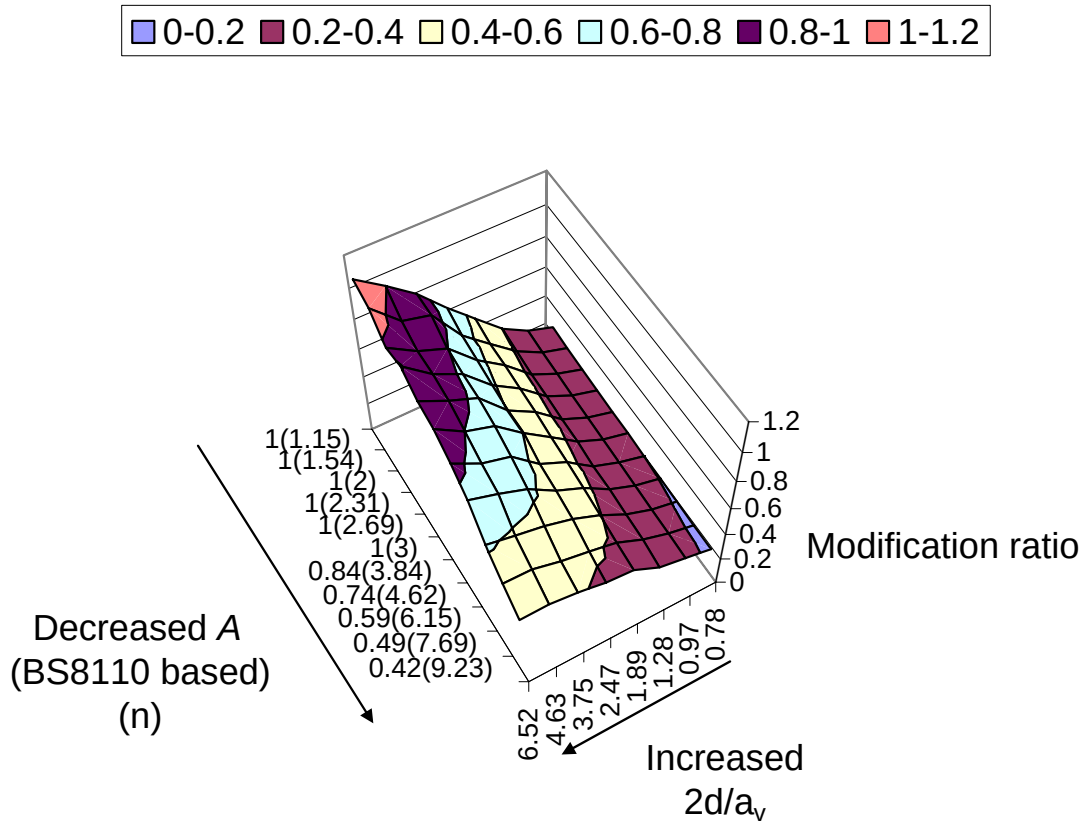

Figure 6.13 Distribution of m_1 for models in parametric study

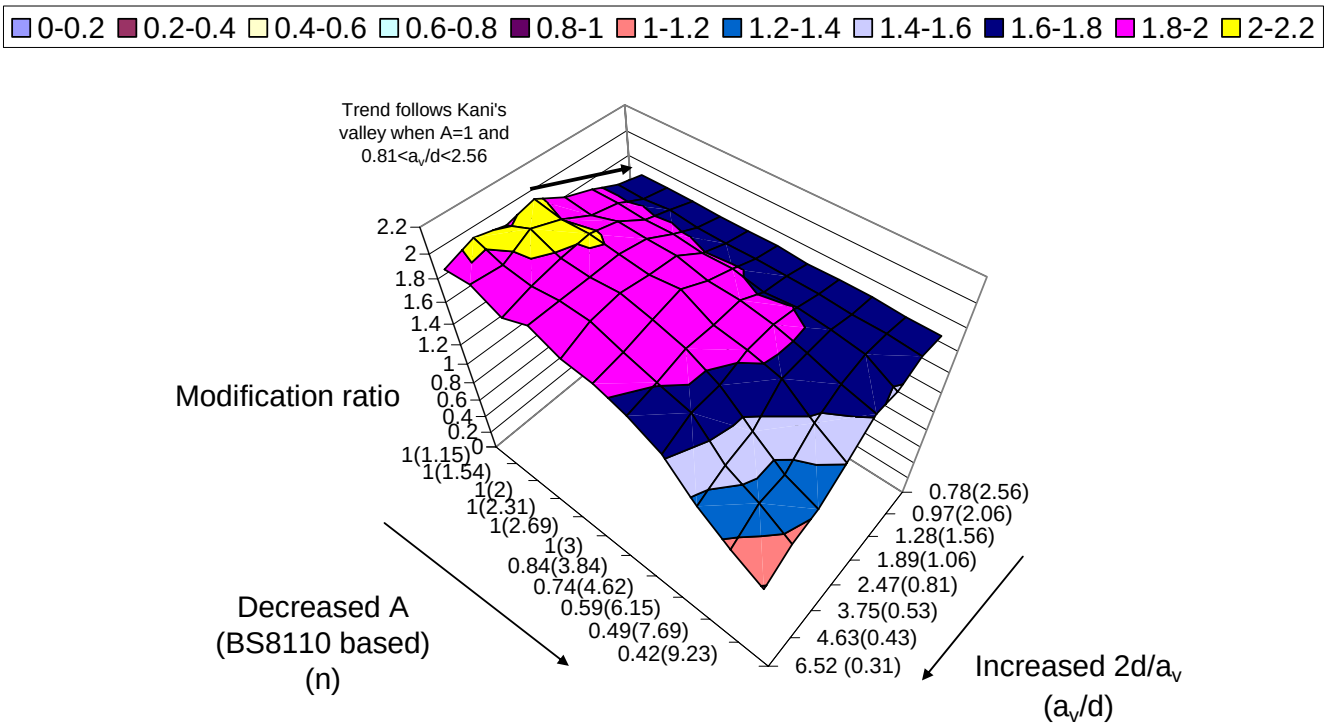

Figure 6.14 Distribution of m_2 for models in parametric study

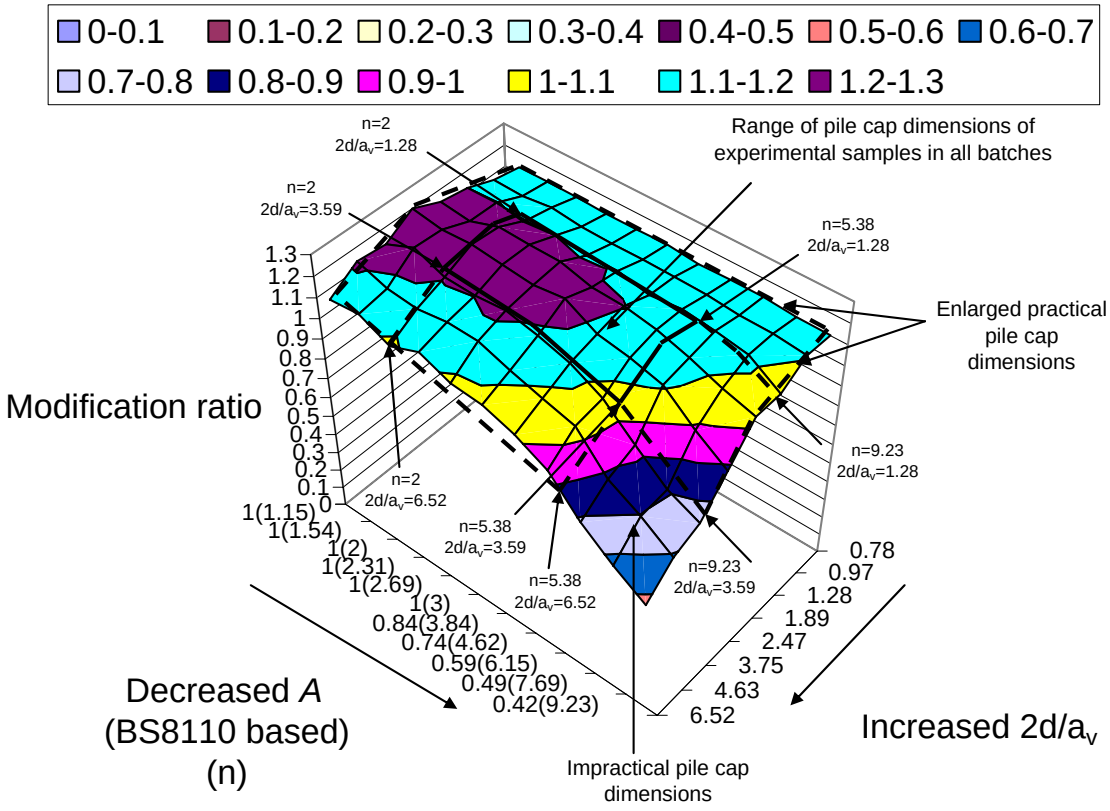

Figure 6.15 Distribution of m_{nSTM} for models in parametric study

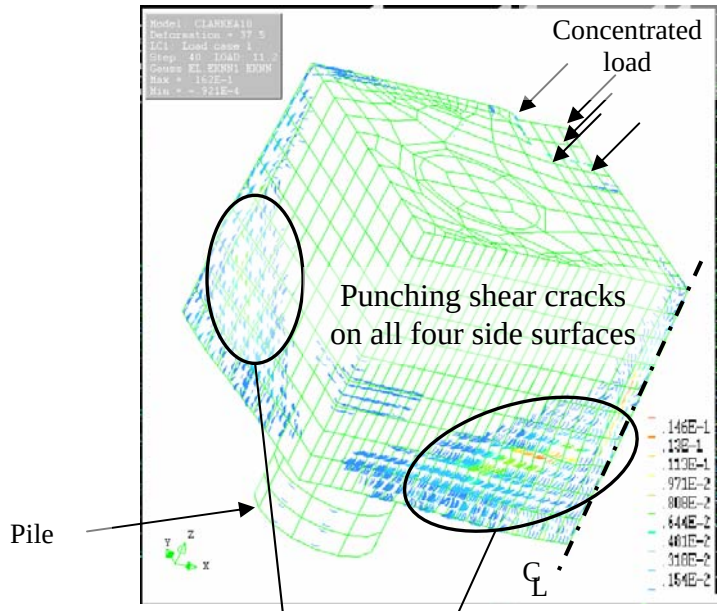

Crack distribution ε^{cr} on surfaces of ¼ A10 from FEA

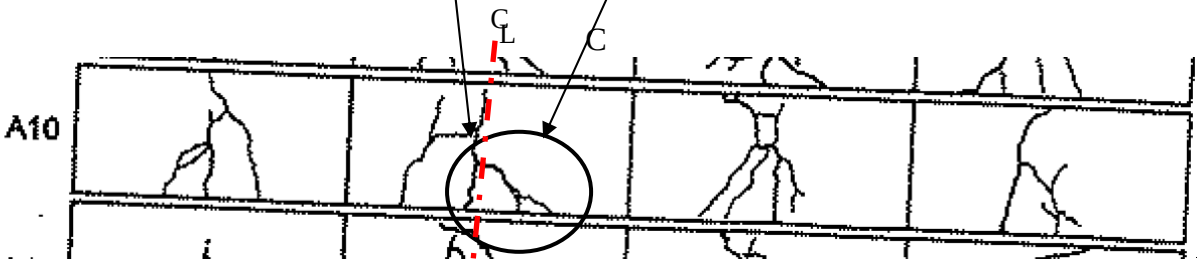

Crack distribution on A10 surfaces from experiment (Clarke, 1973)

Figure 6.16 Comparison of the crack distribution on surfaces of ¼ A10 ($n = 3$, $\frac{2d}{a_v} = 5.79$) at failure step between FEA and experiment

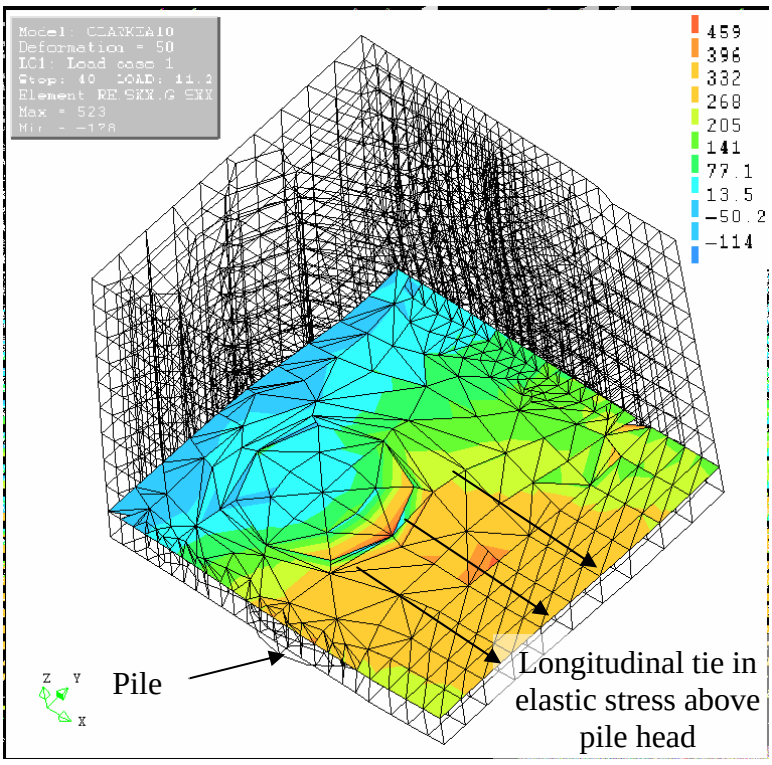

(a) σ_{sx} distribution

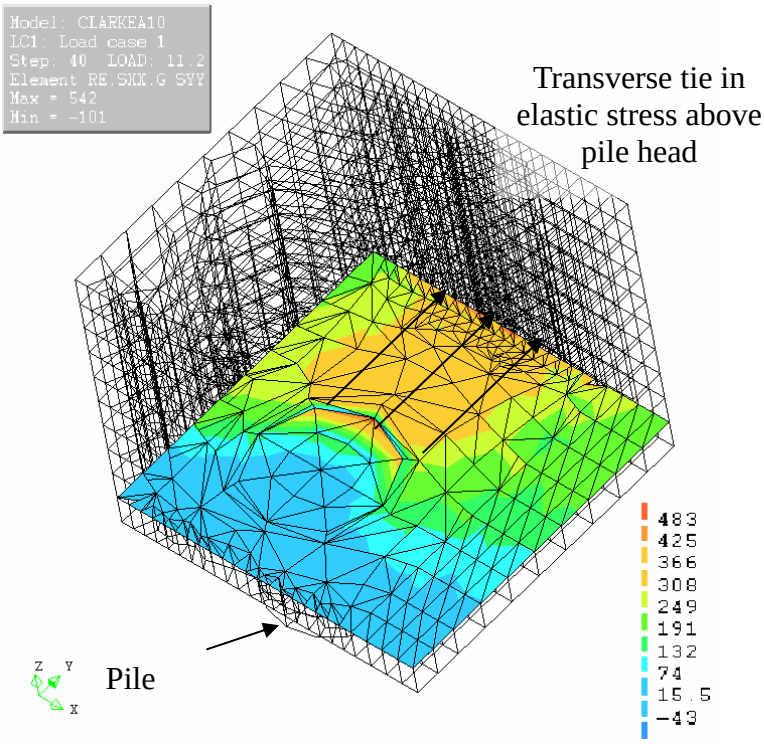

(b) σ_{sy} distribution

Figure 6.17 The distribution of σ_{sx} and σ_{sy} in ¼ A10 ($n = 3$, $\frac{2d}{a_v} = 5.79$) at failure step

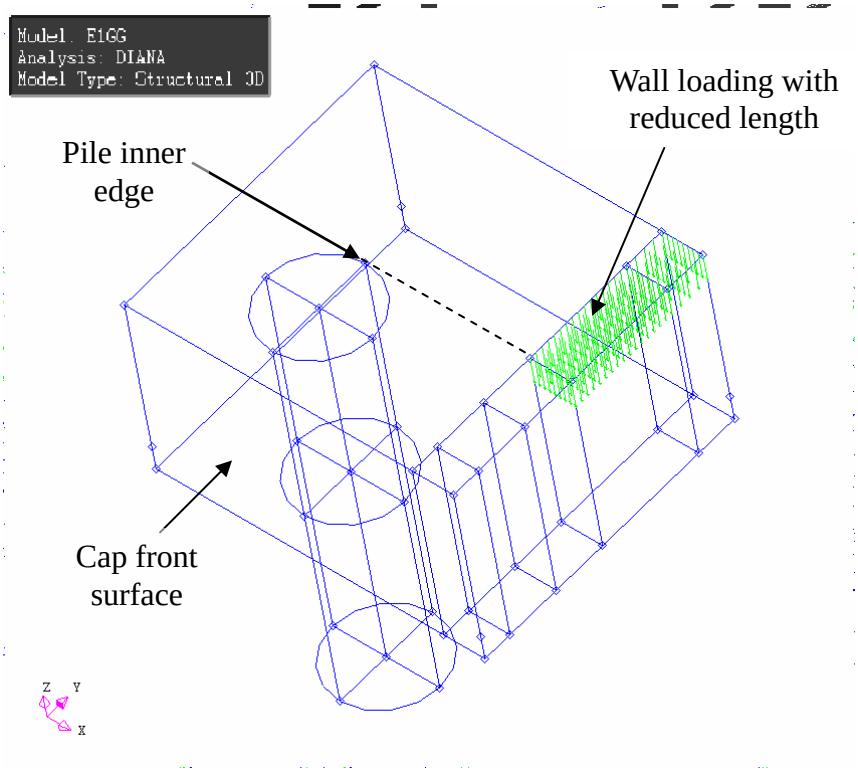

Figure 6.18 Wall loading with reduced length to E1gg

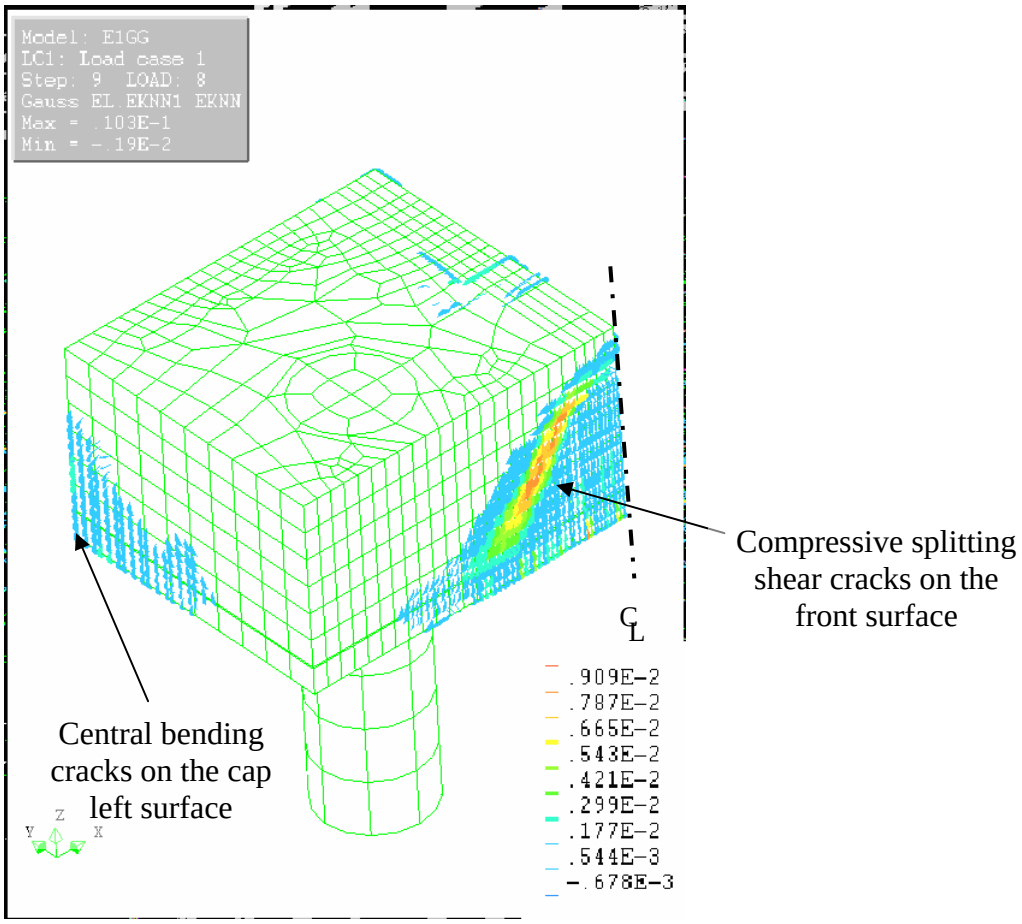

Figure 6.19 Crack distribution in E1gg ($n = 3.84$, $\frac{2d}{a_v} = 2.47$) under a wall loading with reduced length at failure step

Chapter 7 Conclusions and future works

7.1 Synopsis of research

There is an unjustifiable and illogical discrepancy between the predictions of the shear capacity of reinforced concrete pile caps from current bending theory based shear design formulae in BS8110 and BS5400. The research aim of this thesis is therefore to investigate the real shear capacity and shear failure mechanism of pile caps under full-length wall loading.

This research started with a literature review of various existing shear theories and design methods for 1-way spanning RC beams to learn how the shear formulae for 2-way spanning pile caps in the British Standards arose over time. Then 17 simplified and reduced scaled pile cap samples *i.e.* square cap supported by four piles were tested under a full-length wall loading to obtain the real shear capacity of the pile caps. Non-linear FEA for experimental samples was carried out in parallel with the laboratory work. Having been validated with the experimental results, the results from FEA were used to further recognize the shear behaviour and mechanism of the experimental samples. Finally, a parametric study covering a wider range of pile cap dimensions was carried out using FEA to enrich the laboratory work.

A photogrammetry, PIV, combined with a commercial digital camera and a Matlab based software GeoPIV8, was used to obtain the full-field displacement and strain distribution on the cap concrete front surface, replacing the traditional strain gauges which are uneconomical in labour and time cost. The purpose of the technology was twofold. Firstly, the distributions were used to validate the FEA results. Secondly, the results supplied evidences of the shear mechanism of pile caps. An error analysis for the technique was carried out.

By the research, the reason of the discrepancy between the two shear design formulae was obtained. The inaccuracy of design methods in BS8110 and BS5400 was validated. The shear mechanism of pile caps was studied. Suggestions to improve the current shear design formulae and a new STM to better predict the shear capacity of pile caps were given. The influence of load patterns on the shear mechanism and shear capacity of pile caps was studied.

7.2 Conclusions

7.2.1 Shear failure mechanisms and shear capacities of RC pile caps

The shear failure mechanism of experimental pile cap samples, based on the observation of the crack distribution on front and back cap surfaces and the stress and strain in

reinforcement in the longitudinal direction, is mainly the compressive splitting shear failure. The shear failure mechanism is deemed as 2-way especially when the transverse pile spacing is large, proved by the appearance of the bending cracks perpendicular to the bending cracks linking the front and back surface on the cap soffit.

The shear mechanism in the experimental samples can be envisaged as a strut-and-tie behaviour leading to the final compressive splitting shear failure. The physical explanation of the cap width on which the shear enhancement factor is applied in the bending theory based shear design formulae should also be associated with this behaviour. The concrete strut linking the loaded area and the pile head and the longitudinal reinforcement yielding tie constitute the strut and tie system. In the strut-and-tie system, the longitudinal yielding tie could cover the whole cap width even when the transverse pile spacing is larger than triple the pile diameter. When the transverse pile spacing is large, the transverse reinforcement plays an important role in the shear mechanism. These behaviours are not considered in the current STM and shear design formulae.

The failures in all the experimental samples are ductile after critical shear cracks on front and back surfaces appeared, rather than the brittle shear behaviour seen in 1-way spanning RC beams. One reason for this is because under the full-length wall loading, the ductile transverse reinforcement takes effect especially when the transverse pile spacing is large.

The shear failure mechanism of the pile cap models in the parametric study varies with the shear enhancement factor $\frac{2d}{a_v}$, the shear enhancement application factor A (the ratio of the cap width on which $\frac{2d}{a_v}$ applies over the total cap width) or the ratio of the pile transverse spacing over one pile diameter n. In these models, when the shear enhancement factor $\frac{2d}{a_v}$ is lower than 3.75, central bending cracks dominate the front surface of the cap at the failure step. With increasing $\frac{2d}{a_v}$, shear cracks replace the central bending cracks when caps fail. When $\frac{2d}{a_v}$ is low, the longitudinal reinforcement yielding tie does not occur. With increasing $\frac{2d}{a_v}$, the longitudinal yielding tie occurs. Apart from some pile caps with $n > 3.84$ and $\frac{2d}{a_v} < 0.97$ where the longitudinal yielding tie may centred on the each pile

head with width less than triple the pile diameter, the width of the longitudinal reinforcement is larger than three times the pile diameter above each pile head when $n > 3$. With the increasing transverse pile spacing, the stress in the transverse reinforcement increases and the transverse reinforcement begins to play an important role in the shear resistance. When $n > 2.31$, the transverse tie in high elastic stress and even yielding stress occurs.

The shear capacity of experimental pile caps, models in FEA for experimental pile caps and in parametric study under full-length wall loading increases with decreasing longitudinal pile spacing and with increasing transverse pile spacing. The nominal shear strength v_c increases with the increasing $\frac{2d}{a_v}$ and with reducing n or increasing A.

The upper limit of v_c in BS8110 and BS5400 to avoid the brittle failure of the concrete under the loading area may no longer be applicable in the pile cap. The limit should be improved or whether it is still applicable to the pile cap needs to be studied.

The shear capacity and the shear mechanism of pile caps are influenced by the load pattern. Once the full-length wall loading reduces to a concentrated load, the nominal shear failure in the cap under full-length wall loading gradually changes to the punching shear failure and the failure load gradually reduces. Pile caps under full-length wall loading may have up limit shear capacity. This is not considered in the bending theory based shear design formulae for the normal shear failure, the punching shear design formula for the punching shear failure (*e.g.* at a constant perimeter surrounding the loading lying on 20% the pile diameter inside the inner edge of the piles) and STM in British Standards, which is not reasonable.

Under full-length wall loading, the shear failure may be suppressed by the longitudinal central bending failure if the reinforcement ratio reduces. The reinforcement ratio has more influence on the bending capacity than on the shear capacity of pile caps.

7.2.2 Validity of current bending theory based design formulae

The current shear design formulae for pile caps are incorrect. The correct v_c is in a complex relationship with $\frac{2d}{a_v}, A$ or n rather than a plane as specified in standards. For pile caps under full-length wall loading, both BS8110 and BS5400 are very conservative. BS5400 is more conservative than BS81110. The level of the conservatism depends on

$\frac{2d}{a_v}$, A or n. For BS8110, the modification ratio can be as high as 3.20. For BS5400, the maximum modification ratio obtained is 4.44.

The current shear design formulae for pile caps were developed from the bending theory based semi-empirical formula for 1-way spanning RC beams. The poor prediction and the unjustifiable discrepancy between BS8110 and BS5400 result from the following reasons:

- The shear behaviour in 1-way spanning deep beams represented by the shear enhancement factor $\frac{2d}{a_v}$ may not appear in pile caps with large depth-shear span ratio. In other words, the shear behaviour of the two faces of the critical shear crack rotating apart as assumed in Regan's theory, may be replaced by the behaviour of a compressive concrete strut. As a result, the expression of $\frac{2d}{a_v}$ in *PartIV* of *Eq.*2.5 and *Eq.*2.6 no longer applies to pile caps. This causes the poor prediction of the design formulae;
- The behaviour of transverse reinforcement is not considered in the current shear design formulae. This causes the poor prediction of the design formulae especially when the transverse pile spacing is large;
- The current expression of A in the formulae is empirical when 1-way shear design formulae were developed for 2-way spanning pile caps, and has been developed independently in BS8110 and BS5400. This causes both the poor prediction of the design formulae and the discrepancy between BS8110 and BS5400.

The expression of the concrete strength f_{cu} and size effect in current design formulae are other sources of the discrepancy between BS8110 and BS5400 but in less influence. For pile caps under wall loading with reduced length, the current design formulae are even less applicable since longitudinal shear behaviour of caps is not close to the 1-way beam shear behaviour.

7.2.3 Improved design methods for RC pile caps

Compared with the bending theory based design formulae, the current STM in BS8110 gives relatively accurate prediction but fails to predict the shear capacity of pile caps with large transverse pile spacing. A new STM redefining the width of the longitudinal reinforcement tie gives better prediction especially for those pile caps with large transverse

pile spacing. The new STM assumes 90% of the longitudinal reinforcement on the whole cap width to be a tie in the strut-and-tie system. This considers the fact that when the transverse pile spacing becomes large, the assumption of the maximum three times the pile diameter as the width of the longitudinal yielding tie above each pile head in BS8110 is conservative and the transverse reinforcement plays an important role in the shear resistance. The new STM also slightly reduces the span of the longitudinal tie to represent the appearance of the width of the wall loading and pile diameter. The pyramid geometry of the strut-and-tie system is remained. The new STM can apply to pile caps with practical dimensions. Only for some impractical pile caps within $n > 5.38$ and $\frac{2d}{a_v} > 3.59$, the new STM fails to predict and overestimates the shear capacity.

The current bending theory based formulae can be improved by a statistical method based on the distribution of the nominal shear stress v_c varying against $\frac{2d}{a_v}, A$ or n obtained from the experiments and the parametric study. The new expression of $\frac{2d}{a_v}$ and A by the statistical method is likely to lack physical explanation.

The curve plane of the modification ratio for BS8110 varying against $\frac{2d}{a_v}, A$ or n can be used for shear designing. Once $\frac{2d}{a_v}, A$ or n are proposed, the designer can read off the modification ratio from the curve plane and the real shear capacity is the BS8110 prediction multiplied by the modification ratio.

The shear capacity of pile caps under wall loading with reduced length may be obtained by interpolation between the maximum shear capacity when under full-length wall loading obtained in this research and the lowest punching shear capacity when under concentrated loading currently predicted by British Standards.

7.2.4 Lesson learned from the application of the digital PIV and numerical modelling procedures

The optical method PIV with a single commercial digital camera under a natural light source or incandescent light can be applied to the full-field displacement measurement on the reinforced concrete surface. The displacement on the concrete surface can be directly read by this technique. Then the strain on the concrete surface can be calculated. The horizontal

concrete strain at the reinforcement level can be obtained and be considered as the strain on the reinforcement close to the cap front surface which replaces the traditional method of attaching strain gauges on the reinforcement. The quality of the PIV results depends on the camera resolution, the character of the features on the concrete surface, software achieving the technique and the size of the interrogation area *etc*. The idea to validate the displacement and strain distribution on the concrete surface from a non-linear FEA for RC structures with the PIV results has been proved to be feasible. Regarding the validation of strain on the concrete surface, digital PIV can replace the traditional strain gauge and people can benefit from the advantage in the full-field measurement and the huge labour and cost saved. In addition, the full-field displacement as a way to validate the FEA is new to the traditional validation work.

Concrete creep has an influence on the validation between PIV and FEA. In order to reduce the influence, it is necessary to reduce the creep or measure the creep accumulated during the experiment if possible or to model the concrete time effect in FEA. The asymmetric loading also influences the validation since the displacement and strain measured by PIV may increase or reduce because of the extra tilting of the pile cap back and forth and right and left. This makes the validation less valuable since the experiment is not as perfect as the model in FEA. The asymmetric loading should be avoided to make the validation work.

Regarding the non linear FEA for RC structures, a reasonable choice of iterative solver methods and a clever judgement of the failure load and failure mode can give successful prediction for a series of models without any real experimental result to be validated against. This can avoid amount of laboratory work and largely reduce the cost in the research.

7.3 Recommendations for future works

- In the 2-way spanning pile cap, the failure mechanism is no longer able to be simply defined as shear failure or bending failure. More comprehensive definitions of failure mechanisms need to be constructed which vary with the cap dimensions. For instance, when the transverse pile spacing is large and the longitudinal pile spacing is medium, the shear mechanism can be defined as a combination of a longitudinal shear failure and transverse bending failure. But the extent of the longitudinal shear failure (*i.e.* how much of the cap width the critical shear crack cuts through), the extent of the transverse bending failure (*i.e.* how much of the cap length the critical transverse bending crack cuts through) and how these two failure mechanisms interact with each other in the middle of the cap need to be investigated. If all the failure modes in pile caps varying with key cap dimensions can be fully understood and be mathematically

expressed, an equivalent curve plane for 2-way spanning pile caps to Kani's valley for 1-way spanning RC beams can be obtained which connects the failure modes with the failure loads;

- Though this research indicates that an improved STM can better predict the shear capacity of pile caps, a more refined strut-and-tie system for each individual cap is suggested to be established rather than just modifying a general formula. For example, the inclination of the concrete strut really depends on the level of the stress in the longitudinal and transverse reinforcement ties. It is most likely that the strut does not point to the centre of the cap top surface. In cases where the reinforcement in both longitudinal and transverse directions do not reach yield, it is the concrete strut that determines the strut-and-tie capacity (such as Clark's A10), rather than the reinforcement as is assumed in the new STM suggested in this research. Therefore the behaviour of the concrete strut *i.e.* the softening behaviour and the compressive strength which depends on the shape of the strut becomes the focus in future study;

- In addition to $\frac{2d}{a_v}, A$ or n, the shear capacity of pile caps is influenced by many other parameters. The models in the parametric study only vary in cap dimensions, setting other parameters fixed. Among these parameters, the influence of the concrete and reinforcement strength, reinforcement ratio, the size effect and the load pattern need to be investigated. The ultimate aim is to construct an ideal three dimensional design-chart for pile caps which should be a cluster of curve planes, each of which is similar in shape to the v_c distribution in Figure 6.3(a) which is a typical design chart for four-pile caps under full-length wall loading without shear reinforcement when $f_{cu} = 25MPa$, $f_t = 2.5MPa$, $f_y = 547MPa$, $\left(\frac{400}{d}\right)^{1/4} = 1.19$ and $\frac{100A_s}{bd} = 1.137$ in both longitudinal and transverse directions. Different curve planes correspond to different parameters *e.g.* the ratio of the length of the wall loading over the transverse pile spacing or concrete and reinforcement strengths or reinforcement ratio or a combination among them. An example of this type of design-chart is the one for a column subject to combined bending and direct-compression which is a cluster of curves corresponding to different reinforcement ratios.

- An improved PIV with less random errors can be used to trace the strain distribution along the cross section at the tip of a critical shear crack and the relative movement of interrogation areas along compressive splitting shear cracks on the cap front surface.

This is to investigate whether the Regan's theory, claiming that the critical shear crack rotates apart causing the shear failure of deep RC beams, is still applicable to pile caps. Therefore a comprehensive understanding of the validity of the bending theory based formulae in current British Standards and the method to improve the formulae can be obtained.

References

ACI Committee 445 (1998). "ACI Committee 445 on Shear and Torsion Recent Approaches to Shear Design of Structural Concrete." *Journal of Structural Engineering ASCE*, 1375-1417.

Adebar, P., Kuchma, D., and Collins, M. P. (1990). "Strut-and-tie Models for the Design of Pile Caps: an Experimental Study." *ACI Structural Journal*, 87(1), 81-92.

Adebar, P., and Zhou, L. (1996). "Design of Deep Pile Caps by Strut-and-Tie Models." *ACI Structural Journal*, 93(1), 56-64.

Ashour, A. F. (2000). "Shear Capacity of Reinforced Concrete Deep Beams." *Journal of Structural Engineering ASCE*, 1045-1052.

Ashour, A. F., and Morley, C. T. (1994). "The Numerical Determination of Shear Failure Mechanisms in Reinforced-concrete Beams." *The Structural Engineer*, 72(24), 395-400.

Ashour, A. F., and Morley, C. T. (1996). "Effectiveness Factor of Concrete in Continuous Deep Beams." *Journal of Structural Engineering ASCE*, 169-178.

Bazant, Z. P. (1983). "Crack Band Theory for Fracture of Concrete." *Materials et Constructions*, 16, 155-177.

Belvot, J., and Fremy, R. S. (1967). "Semelles Sur Pieux." *l'Institut Technique du Baˆtiment et des Travaux Publics*, 20(230), 223-295.

Bloodworth, A. G., Jackson, P. A., and Lee, M. M. K. (2001). "The Strength of Reinforced Concrete Pile Caps." *ICE Proceedings Structures and Buildings* 149(4), 1-13.

Bond, D. (1979). "Computer Aided Design of Concrete Structures Using Isoparametric Finite Elements and Non-linear Optimization." *Proceedings of Institution of Civil Engineers Part 2*, 67, 785-800.

Bowles, J. E. (1988). "Foundation Analysis and Design" *McGraw-Hill, Singapore*.

British Standard Institution (1972). "CP110 Code of Practice for the Structural Use of Concrete " *BSI, London*.

British Standard Institution (1990). "BS 5400-4 Steel, Concrete and Composite Bridges-Part 4: Code of Practice for Design of Concrete Bridges." *BSI, Milton Keynes*.

British Standard Institution (1997). "BS 8110-1 Structural Use of Concrete-Part 1: Code of Practice for Design and Construction." *BSI, Milton Keynes*.

British Standard Institution (2000). "BS 8666 Specification for Scheduling, Dimensioning, Bending and Cutting of Steel Reinforcement for Concrete." *BSI, Milton Keynes*.

Cao, J., and Bloodworth, A. G. (2007). "Shear Capacity of Reinforced Concrete Pile Caps." *Proceedings of the IABSE Symposium Weimar, Sept 19-21 2007*.

Chan, T. K., and Poh, C. K. (2000). "Behaviour of Precast Reinforced Concrete Pile Caps." *Construction and Building Materials*, 14, 73-78.

Chen, W. F. (1982). "Plasticity in Reinforced Concrete" *McGraw-Hill, New York*.

Chu, T. C., Ranson, W. F., Sutton, M. A., and Peters, W. H. (1985). "Applications of Digital-Image-Correlation Techniques to Experimental Mechanics." *Experimental Mechanics*, 232-244.

Cladera, A., and Mari, A. R. (2004a). "Shear Design Procedure for Reinforced Normal and High-strength Concrete Beams Using Artificial Neural Networks. Part I: Beams without Stirrups." *Engineering Structures*, 26, 917-926.

Cladera, A., and Mari, A. R. (2004b). "Shear Design Procedure for Reinforced Normal and High-strength Concrete Beams Using Artificial Neural Networks. Part II: Beams with Stirrups." *Engineering Structures*, 26, 927-936.

Clarke, J. L. (1973). "Behaviour and Design of Pile Caps with Four Piles, Technical Report." *Cement and Concrete Association, Wexham Springs*, 124-136

Clarke, J. L., and Taylor, H. P. J. (1975). "Web crushing-a review of research Technical Report 42.509 " *Cement and Concrete Association*, 16.

Coates, R. C., Coutie, M. G., and Kong, F. K. (1980). "Structural Analysis " *Chapman and Hall, London*.

Collins, M. P. (1978). "Toward a Rational Theory for RC Members in Shear." *Journal of Structure Division, ACSE*, 104(4), 649-666.

Collins, M. P., Mitchell, D., Adebar, P., and Vecchio, F. J. (1996). "A General Shear Design Method." *ACI Structural Journal*, 93(1), 36-45.

Comite Euro-International du Beton (1990). "CEB-FIP Model Code 1990" *Thomas Telford Services Ltd. London*.

Concrete Reinforcing Steel Institution (1978). "CRSI Handbook 3rd Edition "

DANTEC DYNAMICS (2006) "Basic of 3D Digital Image Correlation." http://www.dantecdynamics.com/Default.aspx?ID=24. [accessed March 2006].

DIANA. (2005). "Standard DIANA course Tutorials and exercises."

DIANA, TNO Building and Construction Research Department of Computational Mechanics (2002). "DIANA Finite Element Analysis User's manual Release 8.1."

Fafitis, A., and Won, Y. H. (1994). "Nonlinear Finite Element Analysis of Concrete Deep Beams." *Journal of Structural Engineering, ASCE*, 120(4), 1202-1220.

Gambarova, P. G. (1981). "On Aggregate Interlock Mechanism in Reinforced Concrete Plate with Extensive Cracking." *IABSE Colloquium*, 105-134.

Gomes, R. B., and Regan, P. E. (1999). "Punching Resistance of RC Flat Slabs with Shear Reinforcement." *Journal of Structural Engineering ASCE*, 684-692.

Hartl, H., and Sparowitz, L. (2000). "The 3D Computational Modelling of Reinforced and Prestressed Concrete Structures " *Bergmeister K. (ed.) Proceedings of the 3rd International PhD Symposium in Civil Engineering*, 2, 69-79.

Hoang, L. C., and Nielsen, M. P. (1998). "Plasticity Approach to Shear Design." *Cement and Concrete Composites*, 20, 437-456.

Hobbs, N. B., and Stein, P. (1957). "An Investigation into the Stress Distribution in Pile Caps with Some Notes on Design." *Proceedings of the Institution of Civil Engineers*, 7, 599-628.

Hsu, T. T. C. (1993). "Unified Theory of Reinforced Concrete", *CRC Press, Boca Raton, FL*.

Hsu, T. T. C. (1998). "Unified Approach to Shear Analysis and Design." *Cement and Concrete Composites*, 20, 419-435.

Huang, H. T., Fieldler, H. E., and Wang, J. J. (1993a). "Limitation and Improvement of PIV Part I: Limitation of Conventional Techniques Due to Deformation of Particle Image Patterns." *Experiments in Fluids*, 15, 168-174.

Huang, H. T., Fieldler, H. E., and Wang, J. J. (1993b). "Limitation and Improvement of PIV Part II: Particle Image Distortion, a Novel Technique." *Experiments in Fluids*, 15, 263-273.

Hung, P. C., and Voloshin, A. S. (2003). "In-plane Strain Measurement by Digital Image Correlation." *Journal of Brazilian Society of Mechanical Sciences and Engineering*, XXV(3), 215-221.

Hwang, S. J., and Lee, H. J. (2000). "Analytical Model for Predicting Shear Strengths of Exterior Reinforced Concrete Beam-column Joints for Seismic Resistance." *ACI Structural Journal*, 97(1), 35-44.

Hwang, S. J., Lu, W. Y., and Lee, H. J. (2000a). "Shear Strength Prediction for Deep Beams." *ACI Structural Journal*, 97(3), 367-376.

Hwang, S. J., Lu, W. Y., and Lee, H. J. (2000b). "Shear Strength Prediction for Reinforced Concrete Corbels." *ACI Structural Journal*, 543-552.

Jenkins, W. M. (1999). "A Neural Network for Structural Re-analysis." *Computers and Structures* 72, 687-698.

Jensen, J. F. (1982). "Discussion of 'An Upper-bound/Rigid-plastic Solution for the Shear Failure of Concrete Beams without Shear Reinforcement' by Kemp K.O. and Al-Safi M.T." *Magazine of Concrete Research*, 37, 100-104.

Jeppsson, J. (2000). "Contact-free Monitoring of Cracked Concrete." *Structural Concrete*, 3, 133-141.

Johansson, M. (2000). "Nonlinear Finite-Element Analyses of Concrete Frame Corners." *Journal of Structural Engineering, ASCE*, 190-199.

Kani, G. N. J. (1964). "The Riddle of Shear Failure and Its Solution." *Journal of The American Concrete Institute*, 61(4), 441-467.

Keown, P., Cleland, D. J., Gilbert, S. G., and Sloan, D. (2006). "Shear in Reinforced Concrete Continuous Beams." *The Structural Engineer*, 8, 24-28.

Keown, P. G. (2000). "Investigation of the Shear Characteristics of Reinforced Concrete Continuous Beams." *Queen's University, Belfast*, PhD Thesis.

Kim, J. I., Kim, D. K., Feng, M. Q., and Yazdani, F. (2004). "Application of Neural Networks for Estimation of Concrete Strength." *Journal of Materials in Civil Engineering, ASCE*, 257-264.

Kong, F. K. (1990). "Reinforced Concrete Deep Beams", *Blackie Glasgow and London Van Nostrand Reinhold*.

Kotsovos, M. D. (1987). "Shear Failure of Reinforced Beams." *Engineering Structures*, 9, 32-38.

Kotsovos, M. D., and Pavlovic, M. N. (1997). "Size Effects in Structural Concrete: a Numerical Experiment." *Computers and Structures*, 64(1-4), 285-295.

Kupfer, H. B. (1973). "Behaviour of Concrete under Biaxial Stresses." *Journal of the Engineering Mechanics Division, ASCE*, 99, 852-866.

Kwak, H. G., and Filippou, F. C. (1990). "Finite Element Analysis of Reinforced Concrete Structures Under Monotonic Loads." *UCB/SEMM-90/14*, Department of Civil Engineering University of California, Berkeley, California.

Lampert, P., and Thurlimann, B. (1968). "Torsion Tests of Reinforced concrete Beams." Bericht No.6506-2,Institute fur Baustatik, ETH, Zurich, Switzerland.

MacLeod, I. A. (2005). "Modern Structural Analysis Modelling Process and Guidance" *Thomas Telford Limited, London*

Martin-Perez, B., and Pantazopoulou, S. J. (2001). "Effect of Bond, Aggregate Interlock and Dowel Action on the Shear Strength Degradation of Reinforced Concrete." *Engineering Structures* 23, 214-227.

Masahiro, S., Jiro, F., Naoki, M., and Kenji, K. (2003). "Ultimate Shear Strength of Pile Caps." *Technical Memorandum of Public Works Research Institute*, 3920, 355-368.

Millard, S. G., and Johnson, R. P. (1985). "Shear Transfer in Cracked Reinforced Concrete." *Magazine of Concrete Research*, 37(130), 3-15.

Morsch, E. (1902). *Der Eisenbetonbau, seine Anwendung und Theorie, 1st ed.*, Wayss and Freytag, A.G., Im Selbstverlag der Firma, Neustadt a.d. Haardt, Germany, 1902.

Mosley, W. H., Bungey, J. H., and R.Hulse. (1999). *Reinforced Concrete Design*, Palgrave Macmillan.

Nielsen, M. P. (1967). "On Shear Reinforcement in Reinforced Concrete Beams." *Bygingsstatiske Meddelelser, Copenhagan, Denmark*, 38(2), 33-58.

Nissen, I. (1987). "Risverzahnung des Betons-gegenseitige Risuferverschiebugen und ubertragbare Krafte." *University of Munich*.

Park, H., and Klingner, R. E. (1997). "Nonlinear Analysis of RC Members Using Plasticity with Multiple Failure Criteria." *Journal of Structural Engineering ASCE* 643-651.

Phillips, D. V., and Zienkiewicz, O. C. (1976). "Finite Element Non-linear Analysis of Concrete Structures." *Proceedings of the Institution of Civil Engineers, Part 2*, 61(Mar), 59-88.

Qu, Z., Lu, X. Z., Ye, L. P., and Chen, J. (2006). "Application of the Digital Photogrammetry in the Studies." *Journal of Building Structures*, 936-939.

Raffel, M., C.Willert, and J.Kompenhans. (1998). "Particle Image Velocimetry", *Springer*.

Rebeiz, K. S. (1999). "Shear Strength Prediction for Concrete Members." *Journal of Structural Engineering ASCE* 301-308.

Regan, P. E. (1971). "Shear in Reinforced Concrete-an Analytical Study." Report to the Construction Industry Research and Information Association, Imperial College, London.

Regan, P. E. (1993). "Research on Shear: a Benefit to Humanity or a Waste of Time?" *The Structural Engineer*, 71(19), 337-347.

Regan, P. E. (1998). "Depth Factors for Shear in Concrete Bridges A review of Literature for the Highways Agency." *University of Westminster*.

Regan, P. E. (1999). "Depth Factors for Shear in Concrete Bridges Report on Beam Tests for the Highways Agency." *University of Westminster*.

Regan, P. E., and Yu, C. W. (1973). "Limit State Design of Structural Concrete" *A Halsted Press Book, John Wiley & Sons, New York.*

Ritter, W. (1899). "Die bauweise hennebique." *Schweizerische Bauzeitung*, 33(7), 59-61.

Robinson, J. R., and Demorieux, J. M. (1972). "Essais de Traction-compresion sur Modeles d'ame de Poutre en Beton Arme In: IRABA Report Part I." Institut de Recherches Appliquees du Beton de L'ame, Paris, France.

Rombach, G. A. (2004). "Finite Element Design of Concrete Structure: Practical Problems and Their Solution" *Thomas Telford Limited, London*.

Ruddle, M. E., Rankin, G. I. B., and Long, A. E. (2003). "Arching-action-flexural and Shear Strength Enhancements in Rectangular and Tee Beams." *Proceedings of the Institution of Civil Engineers, Structures & Buildings* 156(1), 63-74.

Russo, G., Somma, G., and Mitri, D. (2005). "Shear Strength Analysis and Prediction for Reinforced Concrete Beams without Stirrups." *Journal of Structural Engineering ASCE*, 66-74.

Sabins, G. M., and Gogate, A. B. (1984). "Investigation of Thick Slab (Pile Cap) Behaviour." *ACI Journal*, 1, 35-39.

Sanad, A., and Saka, M. P. (2001). "Prediction of Ultimate Shear Strength of Reinforced-concrete Deep Beams Using Neural Networks." *Journal of Structural Engineering ASCE*, 818-828.

Sato, Y., Tadokoro, T., and Ueda, T. (2004). "Diagonal Tensile Failure Mechanism of Reinforced Concrete Beams." *Journal of Advanced Concrete Technology* 12(1), 327-341.

Srinivasan, V., Radhakrishnan, S., Zhan, X., Subbarayan, G., Baughn, T., and Nguyen, I. "High Resolution Characterization of Materials Used in Packages Through Digital Image Correlation." *IPACK2005,ASME InterPACK'05*, San Francisco,California,USA.

Sutton, M. A., Wolters, W. J., Peters, W. H., Ranson, W. F., and McNeill, S. R. (1983). "Determination of Displacements Using an Improved Digital Correlation Method." *Image and Vision Computing* 1(3), 133-139.

Tan, K. H., Tong, K., and Tang, C. Y. (2001). "Direct Strut-and-tie Model for Prestressed Deep Beams." *Journal of Structural Engineering ASCE*, 1076-1084.

Taylor, G. D. (2000). "Materials in Construction: an Introduction", *Longman*.

Vecchio, F., and Collins, M. P. (1981). "Stress-strain Characteristics of Reinforced Concrete in Pure Shear Final report." IABSE Colloquium on Advanced Mechanics of Reinforced Concrete, Delft, Netherland.

Vecchio, F. J., and Collins, M. P. (1986). "The Modified Compression-Field Theory for Reinforced Concrete Elements Subjected to Shear." *ACI Journal*, 83(6), 925-933.

Vidosa, F. G., Kotsovos, M. D., and Pavlovic, M. N. (1991a). "Three-dimensional Non-linear Finite-element Model for Structural Concrete Part 1:Main Features and Objectivity Study." *Proceedings of the Institute of Civil Engineers Part 2*, 91, September, 517-544.

Vidosa, F. G., Kotsovos, M. D., and Pavlovic, M. N. (1991b). "Three-dimensional Non-linear Finite-element Model for Structural Concrete Part 2: Generality Study." *Proceedings of the Institute of Civil Engineers Part 2*, 91, September, 545-560.

Walraven, J. C. (1981). "Fundamental Analysis of Aggregate Interlock." *Journal of Structures Division, ACSE*, 108, 2245-2270.

White, D. J. (2002). "An Investigation into the Behaviour of Pressed-in Piles", PhD Thesis," University of Cambridge.

White, D. J., and Bolton, M. D. (2004). "Displacement and Strain Path During Plane-strain Model Pile Installation in Sand." *Geotechnique*, 54(6), 375-397.

White, D. J., Randolph, M., and Thompson, B. (2005). "An Image-based Deformation Measurement System for the Geotechnical Centrifuge." *IJPMG-International Journal of Physical Modelling in Geotechnics*, 1-12.

White, D. J., Take, W. A., and Bolton, M. D. (2001). "Measuring Soil Deformation in Geotechnical Models Using Digital Images and PIV Analysis." *10th International Conference on Computer Methods and Advances in Geomechanics*, 997-1002.

Yan, H. T. (1954). "Bloom Base Allowable in the Design of Pile Caps." *Civil Engineering and Public Works Review*, 49(575), 493-495.

Zararis, P. D. (2003). "Shear Compression Failure in Reinforced Concrete Deep Beams." *Journal of Structural Engineering ASCE* 544-553.

Zernike, F. (1934). "Beugungstheorie des Schneidenverfahrens und seiner verbesserten Form, der Phasenkontrastmethode." *Physica 1*, 689-704, 1934.

Zienkiewicz, O. C. (1971). "The Finite Element Method in Engineering Science." *McGraw-Hill,London*.

Zienkiewicz, O. C., and Taylor, R. L. (2000). "Finite Element Method: Volume 2, Solid Mechanics Fifth edition." *Butterworth Heinemann*.

Appendix I Principle of digital PIV and PIV error analysis

AI.1 Introduction

Chapter 4 has already introduced the procurement of the full-field displacement and strain distribution on concrete surface using digital PIV with GeoPIV8. In this Appendix, the principle of the digital PIV with a single digital camera and how it is achieved in GeoPIV8 are presented.

An estimation of the system and random errors of the technique is introduced. It starts with an introduction of the experiment arrangement to obtain data for the error analysis. It moves on to describe the errors in a measurement for a designed uniform displacement from GeoPIV8. The fake or the 'dummy strain' on the concrete surface, caused by the errors when the pile cap is not loaded, is introduced. The way to reduce the random error in displacement and strain and a simplified method to eliminate the system error in displacement are then presented.

AI.2 Principle of digital PIV

In the technique, the displacement vectors pointing to single-pixel precision or unit pixel precision are derived by tracing the movement of a series of sub-sections on a target area (Section AI.2.1) in two sequential digital photos captured by CCD (charge-coupled device) in a digital camera using a statistical correlation method (Section AI.2.2). The two photos represent a cap under two different loading steps. The more accurate sub-pixel displacement vectors are obtained by interpolating peak and sub-peak displacement vectors (Section AI.2.3).

AI.2.1 Target area

As shown in Figure AI.1 (a), the target area or the investigated area is the front concrete surface of the cap. In two sequential digital photos of the target area, the first one is divided into an array of square interrogation areas (IA) as shown in Figure AI.1 (a). A series of square search areas are then established, the centre of each of which is located at the centre of an IA (*e.g.* $IA1$, Figure AI.1 (a)) in the co-ordinates system of the first photo. Then the centre of $IA1$ can move by each pixel position in the second photo within the boundaries of a search area having the same centre location and size as in the first photo (Figure AI.1 (b)). In the second photo, an IA array is also constructed, with each IA the same size as $IA1$, taking each pixel position within the boundaries of the search area as the centre of an IA. Correlation of the pixel tricolour values is then carried out between $IA1$ in the first photo and every IA

trialed in the second photo to find a maximum correlation value implying the displacement vector of $IA1$ (Section AI.2.2).

AI.2.2 Correlation method

Among different correlation methods, Normalized Cross-Correlation (NCC) is the most popular with digital PIV. NCC is a statistical method to calculate the correlation level between two variables. The basic formula of NCC is shown below:

$$R(i,j)=\frac{\sum_{i=0}^{N}\sum_{j=0}^{N}\left(\left(I(x+i,y+j)-\bar{I}\right)\left(I'(x'+i,y'+j)-\bar{I}'\right)\right)}{\sqrt{\sum_{i=0}^{N}\sum_{j=0}^{N}\left(I(x+i,y+j)-\bar{I}\right)^2}\sqrt{\sum_{i=0}^{N}\sum_{j=0}^{N}\left(I'(x'+i,y'+j)-\bar{I}'\right)^2}} \qquad (Eq.AI.1)$$

where I and I' are functions of the summation of the value of the tricolour value (red, green and blue, each ranging between 0 to 255) in each pixel unit in $IA1$ in the first photo and each IA within the search area in the second photo respectively (White, 2002); $\bar{I}$ and $\bar{I}'$ are the mean value of I and I' over all the pixel units in $IA1$ and an IA in first and second photos. As shown in Figure AI.1 (b), i, j are the abscissa and ordinate in the local co-ordinates system established about a same origin in $IA1$ and an IA in the second photo.

In pixel units, (x, y) and (x', y') are co-ordinates of the origin point of an $IA1$ in the first photo and a trial IA in the second photo in a global co-ordinates system set in the first photo (Figure AI.1 (a)). $(x+i, y+i)$ and $(x'+i, y'+i)$ imply two pixels in the same position relative to the origin of local co-ordinates in respective interrogation areas. N or IA size is the number of pixels along a horizontal and vertical side of an IA (*i.e.* totally N^2 pixel units in one IA).

$R(i,j)$ is the correlation coefficient used to estimate the correlation level. I for $IA1$ is to be correlated with I' for every trial IA in the search area in the second photo (Section AI.2.1). The displacement vector for $IA1$ at pixel level then points from the $IA1$ centre in the first photo to an trial IA centre in the second photo where the correlation value $R(i,j)$ reaches its peak (Figure AI.1 (b)).

Figure AI.1 (c) shows an example of I of an $IA1$ of $3\times3 pixels$ $(N=3)$ in the first photo being correlated with the I' of other three trial IAs (IAa, IAb and IAc) in the second photo. Finally, the displacement vector at pixel level points from $IA1$ centre to the centre of

IAa in the second the photo, in which R^2 or $|R|$ is maximum showing a peak correlation level compared to other two trial interrogation areas IAb and IAc.

AI.2.3 Sub pixel interpolation

It is most likely that the true displacement vector of $IA1$ is not an exact number of pixels, which means the displacement vector obtained based on the peak correlation coefficient $R(i, j)$ in *Eq.AI*.1 needs to be improved to a reasonable accuracy.

The solution is firstly to determine a peak correlation coefficient and several sub-peak correlation coefficients and their corresponding IA locations at pixel level. Then a high order interpolation is applied (Section AI.3) to obtain the true (statistically speaking) peak correlation coefficient corresponding to a location at sub-pixel level where the true displacement vector in points.

By repeating the process described in Sections AI.2.1~AI.2.3 for every $IA1$ in the target area in the first photo, the full-field displacement distribution on the concrete front surface can then be obtained, which is further used to calculate the full-field strain distribution.

AI.3 GeoPIV8 achieving digital PIV

GeoPIV8 (White, 2004) is a MatLab based software implementing the principles of digital PIV in a style suited for the analysis of geotechnical tests. It supplies a friendly interface to execute the analysis and to present the output of the displacement vector.

In defining the target area, a flexible input is allowed in GeoPIV8. The IA spacing and the size of IA and search area (Figure AI.1 (a)) can be defined by the user, so that depending on different situations, especially on the different crack distributions, the user can adjust these parameters in order to obtain the optimal output (Section 4.3.5).

GeoPIV8 uses NCC (Section AI.2.2) as the correlation method. It also applies a Digital Fourier Transform (DFT) to simplify the calculation of *Eq.AI*.1 (White, 2002). This is essentially to transform the spatial correlation to a frequency domain correlation and is proved to be the most economic in the CPU time cost (Raffel, 1998).

GeoPIV8 adopts 2-dimensional spatial Hermite bicubic surface interpolation (White, 2002 & 2005) to search for the true displacement vector at sub-pixel level (Section AI.2.3). As shown in Figure AI.1 (d), totally five displacement vectors at pixel level, including the displacement vector with the peak correlation coefficient from *Eq.AI*.1 and the other four

vectors with sub-peak correlation coefficients surrounding it corresponding to five *IA* locations at pixel level, are required for the interpolation. The true displacement vector at sub-pixel level is pointing towards the location in the search area corresponding to the true peak correlation coefficient interpolated on the bicubic surface (Figure AI.1 (d)).

AI.4 Errors in uniform displacement

AI.4.1 Test arrangement to obtain data for the error analysis

The data for the system and random error analysis was obtained by a pre-test, analyzing the displacement vectors on the cap surface in several separate uniform vertical displacements given by the testing machine to every pile cap in Batch 4 without being loaded before the main experiment began. The real displacement was read by the testing machine or by a suitably located dial gauge (Section 4.3.6) .

For simplicity, only the uniform displacements in B4B3, which was given the maximum vertical displacement among all the pile caps, are discussed in this Appendix. The real displacement given was $V' = -5.5477\ pixel$ and $U' = 0\ pixel$ (Section 4.3.7).

Different combinations of *IA* size and the size of the search area were tried to test how these parameters influenced the errors in PIV results. The *IA* spacing was kept as 32 $pixels$. In Sections AI.4.2 and AI.4.3, the basic *IA* array with basic *IA* size $20 \times 20\ pixels$ and basic size of the search area $10 \times 10\ pixels$ was taken.

The co-ordinate system and the basic *IA* array for the PIV pre-test for B4B3 is shown in Figure AI.2.

AI.4.2 System and random errors in displacement analyzed by digital PIV

An important statement here is that the random error of PIV results based on a typical *IA* size and size of search area mentioned in this research is obtained from a population of PIV results for a bunch of *IA*s in an *IA* array rather than the population of the PIV results for ONE *IA* in multiple shoots. This is to emphasize the random error caused by the unique distribution of the features on the concrete surface (Section 4.3.4), leaving the other causes of random error such as the errors in different shoots unimportant.

The vertical and horizontal displacements from digital PIV in pixel units for B4B3 in the pre-test are shown in Figure AI.3. Referring to Figure AI.2, there are totally 10 horizontal series and 42 columns (or 42 position number) of *IA*s in the target area of B4B3. In the front view (Figure AI.3 (b), (d)), only two horizontal series (Series 5 and Series 6, Figure AI.2) of

the IA array in the middle of the target area are given a trend line or a regression line to make the figures easy to read.

As shown in Figure AI.3 (b), the random error is in the form of the oscillation of the PIV results against the trend lines. Two causes of the random error are considered: 1. Random or the unique pattern of surface features from manual painting (Section 4.3.4) in different IAs; 2. PIV techniques such as the correlation method, interpolation method and the low resolution of the digital camera relevant to the GeoPIV8 accuracy (Section 4.3.8).

In Figure AI.3 (b), the difference between the trend line and the real displacement value implies the system error. The linear distribution of the system error shown in AI.3 (b) for the horizontal displacement $U^{'}$ and the parabolic distribution of the system error shown in Figure AI.3 (d) for the vertical displacement $V^{'}$ are caused by the distortion of camera lens.

AI.4.3 Dummy strain

Following the above section, strain $\varepsilon_{xx}, \varepsilon_{zz}$ (*Eq.*4.1) over 64 *pixels* base length can be obtained from the pre-test. The strain distributions are shown in Figure AI.4. Because in reality, there was no strain on the concrete surface, in this analysis the strain caused by the system and random errors is named as 'dummy strain'.

It can be seen that the system and random errors of the strain distribution appears in the similar way against the trend line to the errors in the displacement in Section AI.4.2. The system errors causing the dummy strain are the result of the non-zero high order derivative of the distortion function of the camera lens, rather than being directly caused by the lens distortion.

AI.4.4 A method to reduce the random error in displacement and strain

The influence of the IA size and the size of the search area on the random error in $U^{'}, V^{'}$, $\Delta U^{'}, \Delta V^{'}$ (the relative displacement $U^{'}, V^{'}$ of two neighbouring IAs) and $\varepsilon_{xx}, \varepsilon_{zz}$ was investigated by means of the standard deviation (STD) of the PIV results.

This was achieved by investigating the normal density distribution of PIV results with various IA sizes (20 *pixels*, 40 *pixels* and 60 *pixels*) and various sizes of the search area (10 *pixels* and 60 *pixels*). The mean value of the PIV results measuring the system error, STD of the normal distribution measuring the random error and the IA number n (population of the sample space) with different IA sizes and sizes of search area are listed in Table AI.1.

Figure AI.5 is an example of the normal distribution with the basic *IA* size (Section AI.4.1) and basic size of the search area.

The variation of the STD against various *IA* size is given in Figure AI.6. It can be seen that STD of $U^{'},V^{'}$, $\Delta U^{'},\Delta V^{'}$ and $\varepsilon_{xx},\varepsilon_{zz}$ decreases with a gradually decreased rate with increasing *IA* size when the size of search area is fixed . From Table AI.1, the STD of $U^{'},V^{'}$, $\Delta U^{'},\Delta V^{'}$ and $\varepsilon_{xx},\varepsilon_{zz}$ vary little when the size of the search area changes and *IA* size is fixed. For vertical displacement $V^{'}$, the minimum precision GeoPIV8 can reach towards the random features on B4B3 front surface is close to 0.02 *pixels*.

It is concluded that other than increasing the resolution of the digital camera, the most efficient way to reduce the random error in displacement and strain is to increase the *IA* size though it costs more time for the computer to process.

AI.4.5 A simplified method to eliminate the system error in displacement

As explained in Section AI.4.1, the real displacement can be read from the testing machine. So the ratio of the real displacement over the displacement with system error from digital PIV can be calculated. The ratio theoretically varies with the lens distortion (the trend line of the displacement from PIV with system error is not horizontal, see Figure AI.3 (b), (d)) and with the magnitude of the real displacement. For simplicity, the deviation ratios r_u, r_v representing the ratio of the real horizontal and vertical displacements over the mean value of $U^{'},V^{'}$ from PIV for all *IA*s, were introduced.

The r_v finally used was taken as the mean value of r_v from all combinations of sizes of *IA* and search area appearing in Section AI.4.4 (Table AI.2). Then it was assumed r_v does not change with the magnitude of the real displacement and the position of the *IA* studied. Table AI.2 shows the mean value of r_v used. The mean value of r_v changes little with different sizes of the search area or with different *IA* sizes. Also, r_v used is close to 1 which implies that the ratio can be neglected.

On the other hand, r_u was unattainable since no horizontal displacements can be given by the testing machine. So it was assumed that $r_u = r_v$. The application of r_u and r_v to eliminate the system error was to multiply this ratio with the displacement from PIV of each *IA* which is introduced in Section 4.3.7.

AI.5 Summary

The most important advantage of the digital PIV with GeoPIV8 is that it gives a flexible choice to determine the size of the target area, *IA* size, *IA* spacing and the size of the search area such that the issue of the appearance of the cracks on concrete can be solved and the errors can be reduced.

System error in displacement caused by the lens distortion and the random error in displacement and strain caused by the methodology of the technique towards the random artificial features on the concrete surface make the PIV results less reliable. Though an ideal method to tackle the system errors is to construct a validation matrix (White, 2000) and to use a digital camera with higher resolution which decisively improves PIV performance, simplified methods to reduce the random error by increasing the *IA* size and to eliminate the system error by introducing the ratio of the real displacement over the mean value of PIV results were introduced. A professional digital PIV should include a parallel laser light source. In this research, the 15 *Hz* incandescent light in the laboratory was applied. The frequency of the incandescent light might influence the PIV results and introduces new errors, but this was not considered in the research.

Table AI.1 Mean value and STD of $U^{'}, V^{'}, \Delta U^{'}, \Delta V^{'}, \varepsilon_{xx}, \varepsilon_{zz}$ for B4B3 (Real $V^{'} = -5.5477$ *pixels*, real $U^{'} = 0$ *pixels*) with different *IA* sizes and sizes of the search area

IA size (*pixel*)	Size of search area (*pixel*)	$U^{'}$ (*pixel*)			$V^{'}$ (*pixel*)		
		Mean	STD	IA number *n*	Mean	STD	IA number *n*
20	10	-0.150094	0.0685487	420	-5.91694	0.0432152	420
20	60	-0.148278	0.0689537	420	-5.91605	0.0432197	420
40	10	-0.150675	0.0545488	420	-5.91676	0.0263482	420
40	60	-0.150217	0.0527212	420	-5.91822	0.0257143	420
60	10	-0.151664	0.0528609	420	-5.91771	0.0220514	420
60	60	-0.149878	0.0535010	420	-5.91688	0.0224614	420

IA size (*pixel*)	Size of search area (*pixel*)	$\Delta U^{'}$ (*pixel*)			$\Delta V^{'}$ (*pixel*)		
		Mean	STD	IA number *n*	Mean	STD	IA number *n*
20	10	-0.000542	0.0691511	418	-5.60E-05	0.0533797	418
20	60	-0.000584	0.0682302	418	-5.47E-05	0.0534733	418
40	10	-0.000768	0.0440942	418	-0.000105882	0.0262714	418
40	60	-0.000890	0.0426503	418	-0.000126975	0.0246105	418
60	10	-0.000972	0.0402734	418	8.99E-06	0.0172840	418
60	60	-0.000957	0.0400200	418	-2.66E-07	0.0170459	418

IA size (*pixel*)	Size of search area (*pixel*)	ε_{xx}			ε_{zz}		
		Mean	STD	IA number	Mean	STD	IA number *n*
20	10	-8.47E-06	0.001080490	418	-8.75E-07	0.000834058	418
20	60	-9.13E-06	0.001066100	418	-8.54E-07	0.000835520	418
40	10	-1.20E-05	0.000688972	418	-1.65E-06	0.000410490	418
40	60	-1.39E-05	0.000666411	418	-1.98E-06	0.000384539	418
60	10	-1.52E-05	0.000629271	418	1.40E-07	0.000270063	418
60	60	-1.50E-05	0.000625312	418	-4.16E-09	-5.87E-27	418

Table AI.2 Various mean value of deviation ratio r_v

(a) Mean value of deviation ratio r_v (varying with the size of search area)

Varying size of search area(*pixel*)	10	60	Mean r_v used
Fixed *IA* size(*pixel*)	20,40,60	20,40,60	
B4A1	1.020	1.020	1.020
B4A2	0.949	0.948	0.949
B4A3	1.003	1.007	1.005
B4A4	0.903	0.959	0.931
B4A5	0.923	0.926	0.925
B4B2	0.988	0.988	0.988
B4B3	0.936	0.936	0.936

(b) Mean value of deviation ratio r_v (varying with the IA size)

Varying *IA* size (*pixel*)	20	40	60	Mean r_v used
Fixed size of search area(*pixel*)	10, 60	10, 60	10, 60	
B4A1	1.020	1.020	1.020	1.020
B4A2	0.948	0.949	0.948	0.949
B4A3	1.002	1.007	1.006	1.005
B4A4	0.876	0.958	0.958	0.931
B4A5	0.923	0.926	0.925	0.925
B4B2	0.988	0.988	0.988	0.988
B4B3	0.936	0.936	0.936	0.936

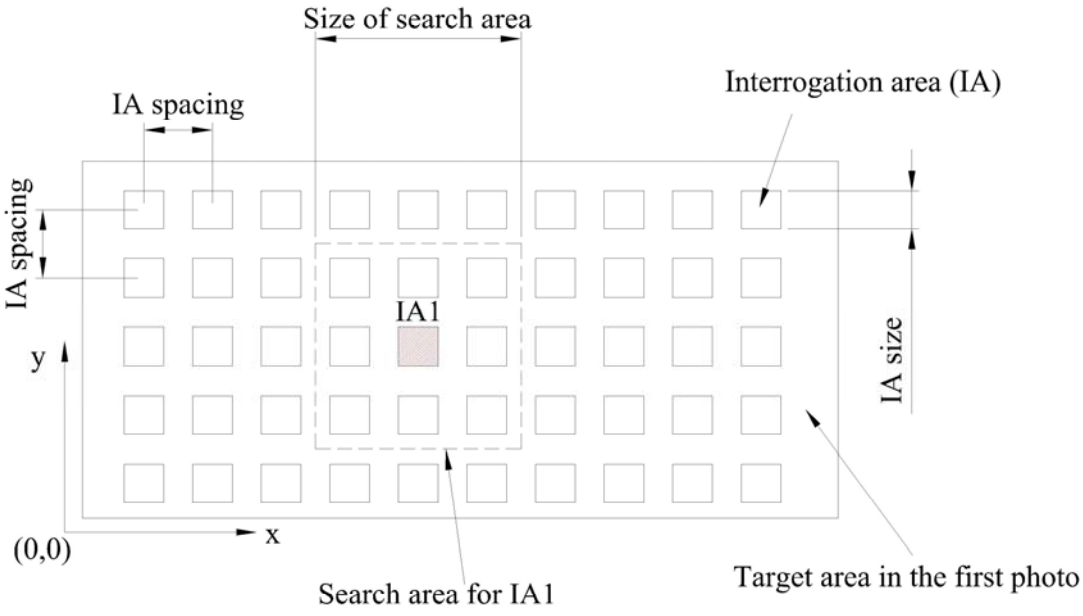

(a) Target area and IA array in the first photo

Figure AI.1 PIV principles

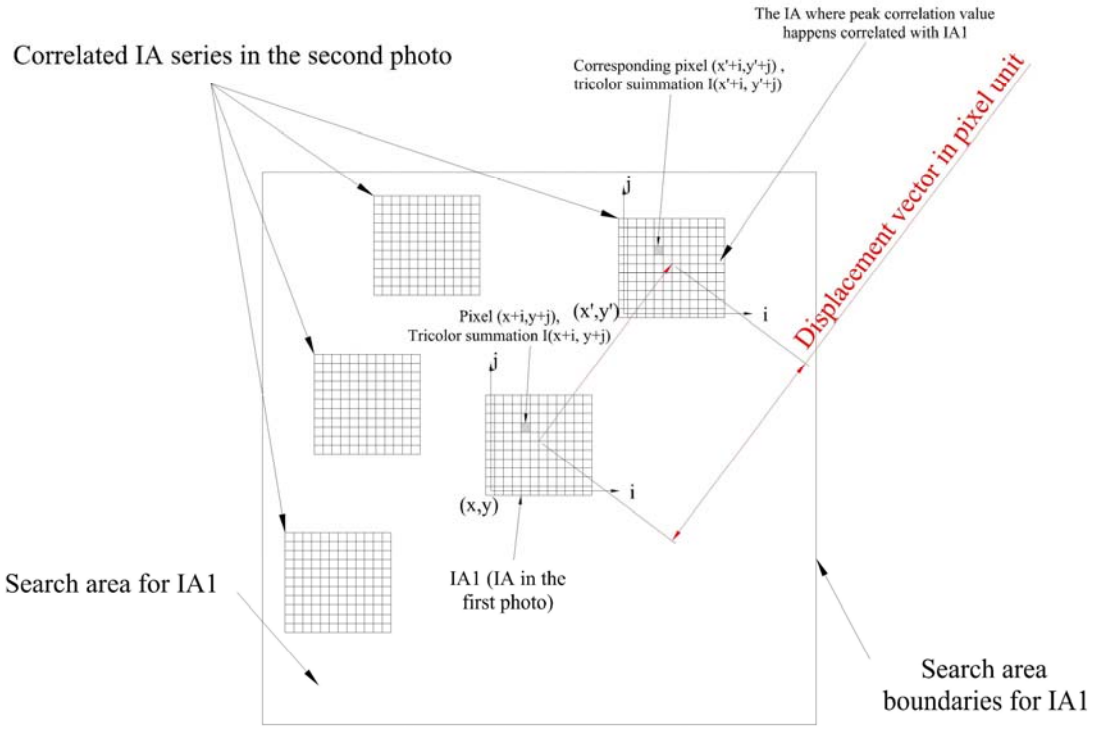

(b) The NCC applied in the second photo to obtain the displacement vector of $IA1$ in pixel unit

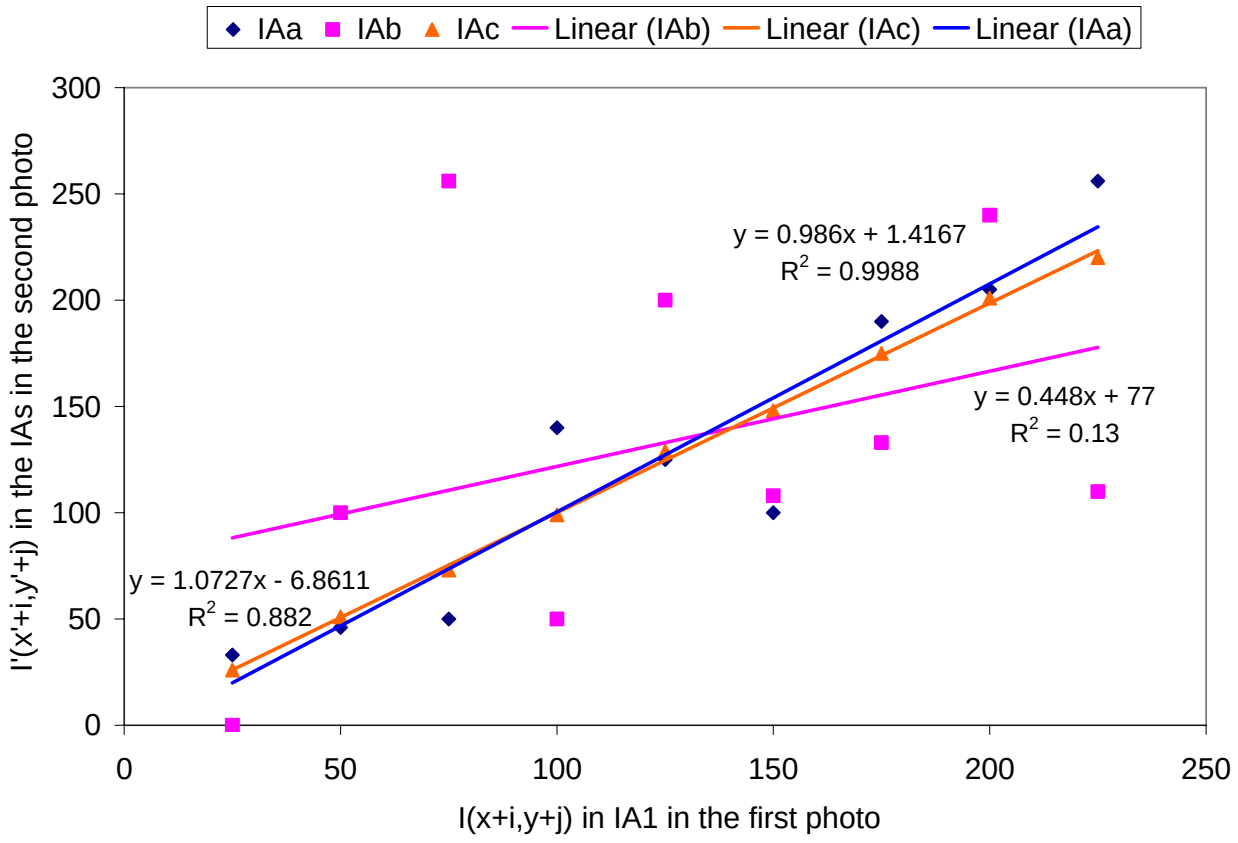

(c) The correlation between $3\times3 pixels$ IA1 in the first photo and 3 $3\times3 pixels$ IAs in the second photo

Figure AI.1 PIV principles

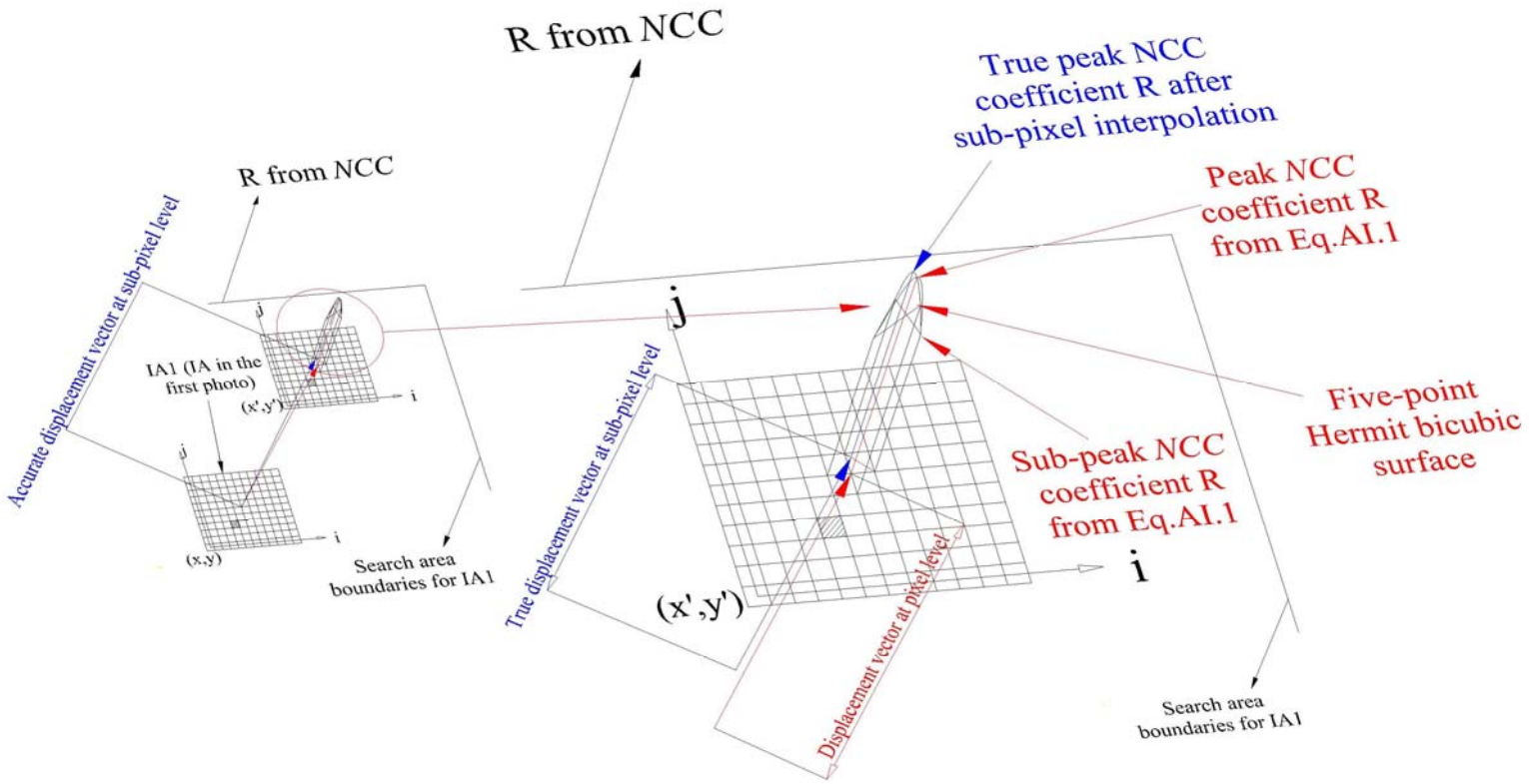

(d) Sub-pixel interpolation in GeoPIV8

Figure AI.1 PIV principles

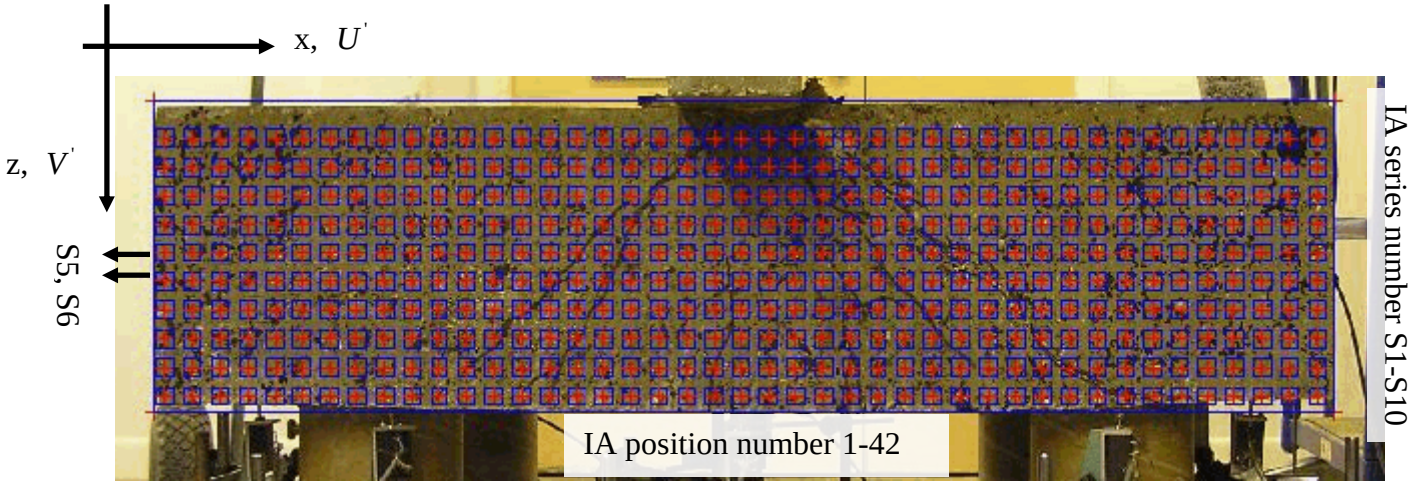

Figure AI.2 Co-ordinates system and basic IA array in PIV pre-test for B4B3

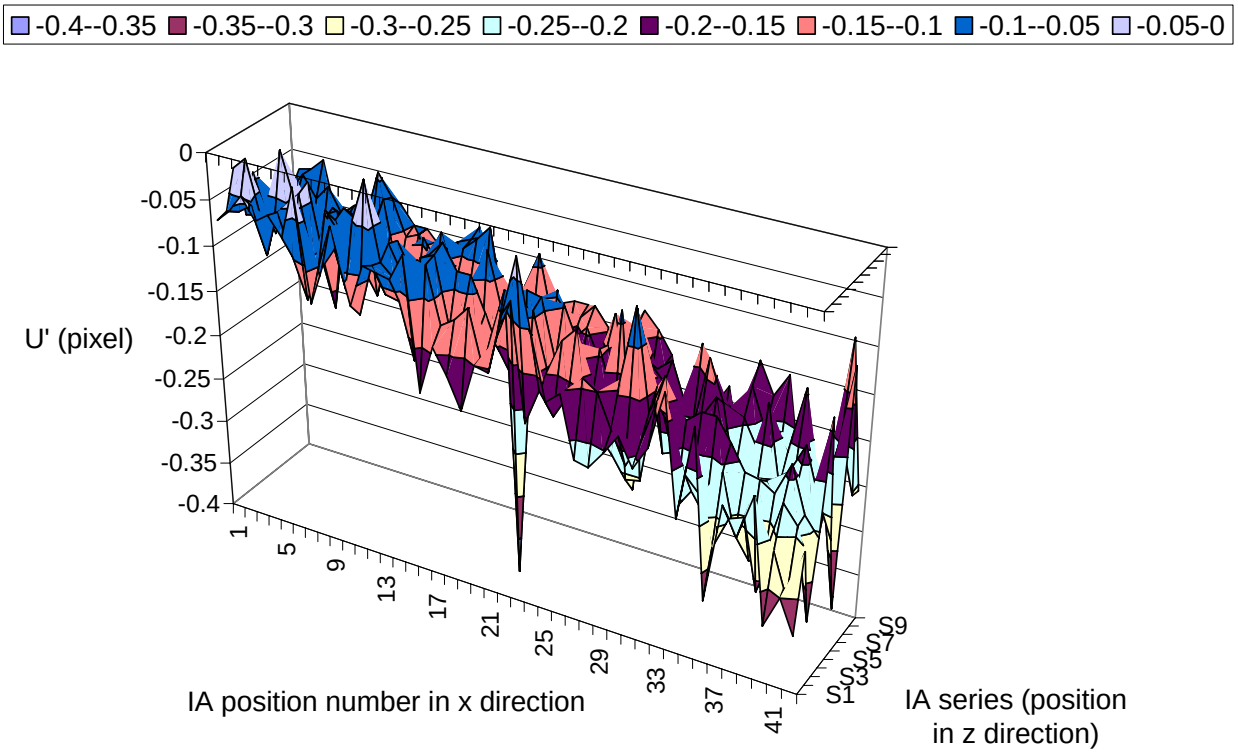

(a) Isometric representation of errors in horizontal displacement U' against IAs

Figure AI.3 Errors in uniform displacement from digital PIV in pre-test for B4B3

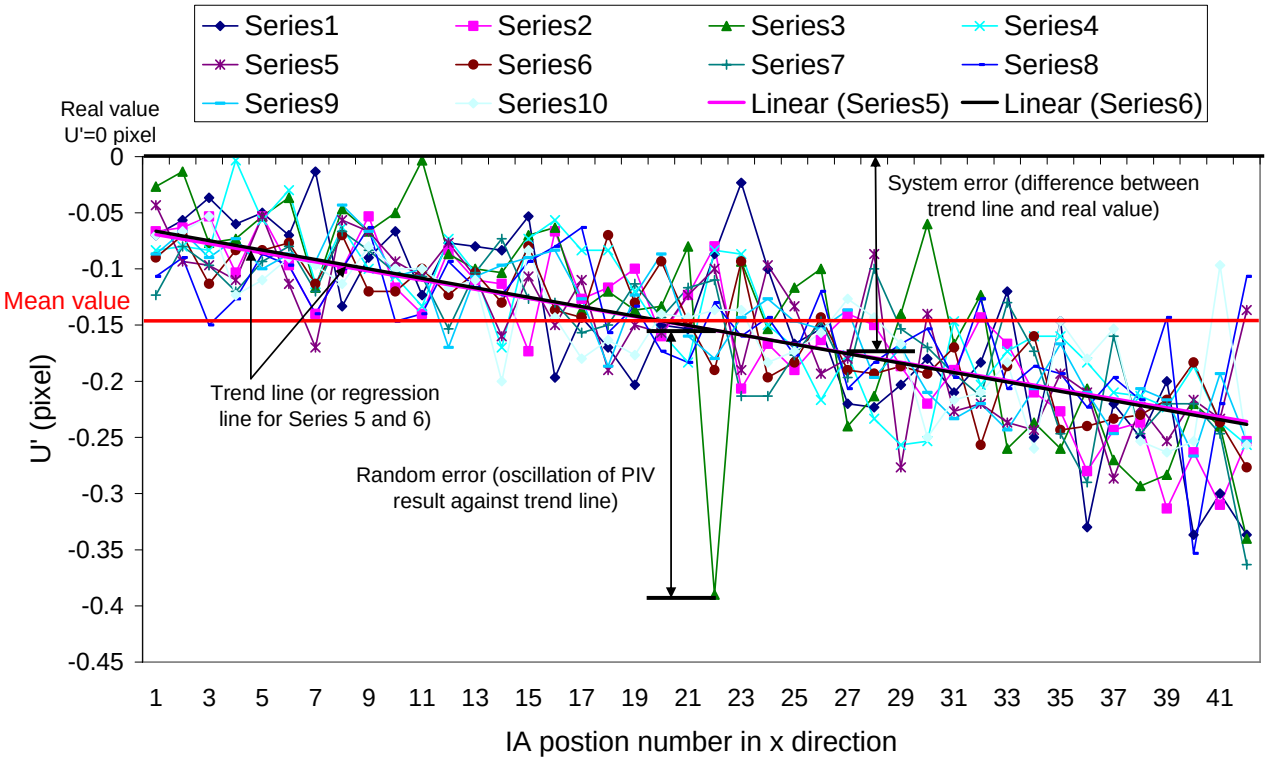

(b) Variation of errors in horizontal displacement U' against IA positions

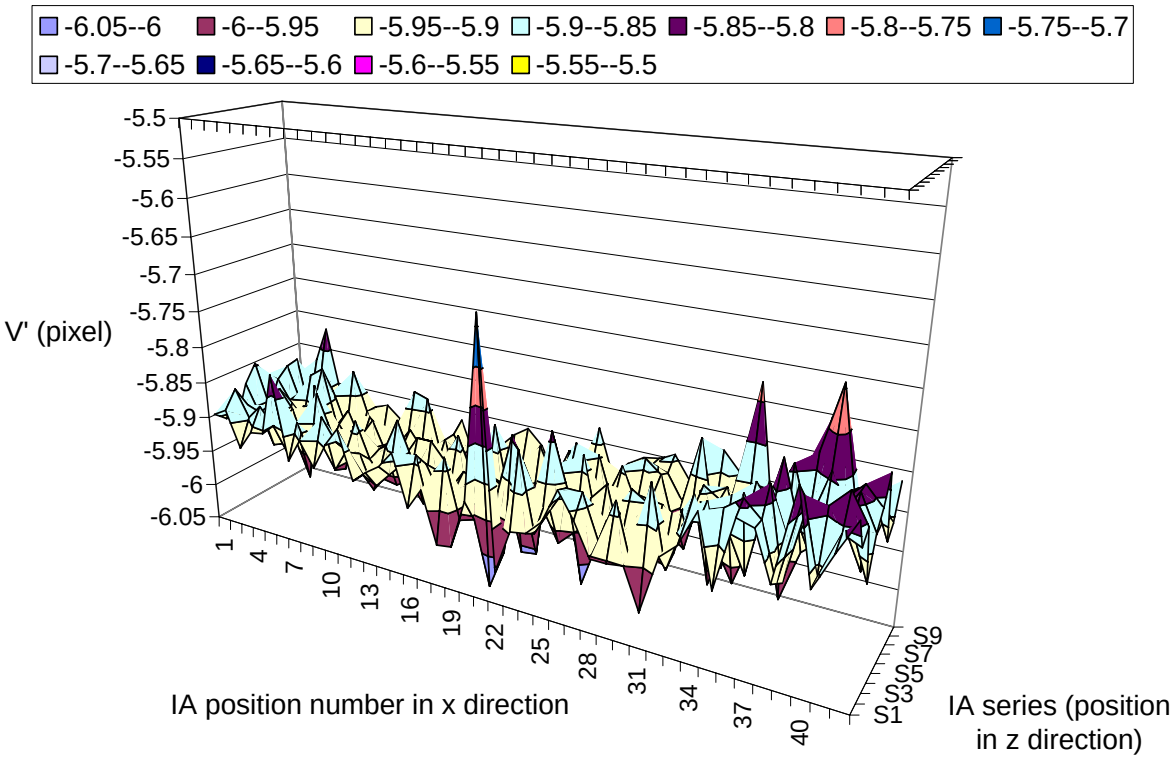

(c) Isometric representation of errors in vertical displacement V' against IA positions

Figure AI.3 Errors in uniform displacement from digital PIV in pre-test for B4B3

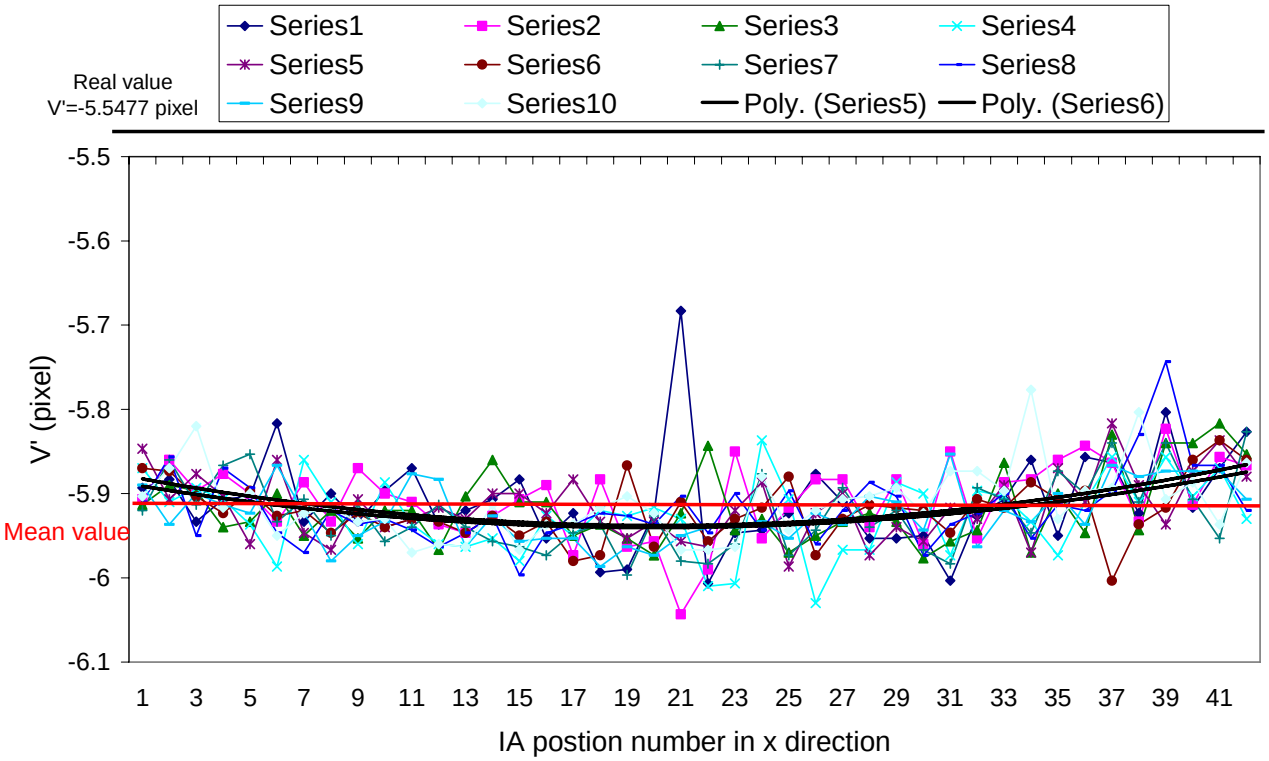

(d) Variation of errors in horizontal displacement V' against IA positions

Figure AI.3 Errors in uniform displacement from digital PIV in pre-test for B4B3

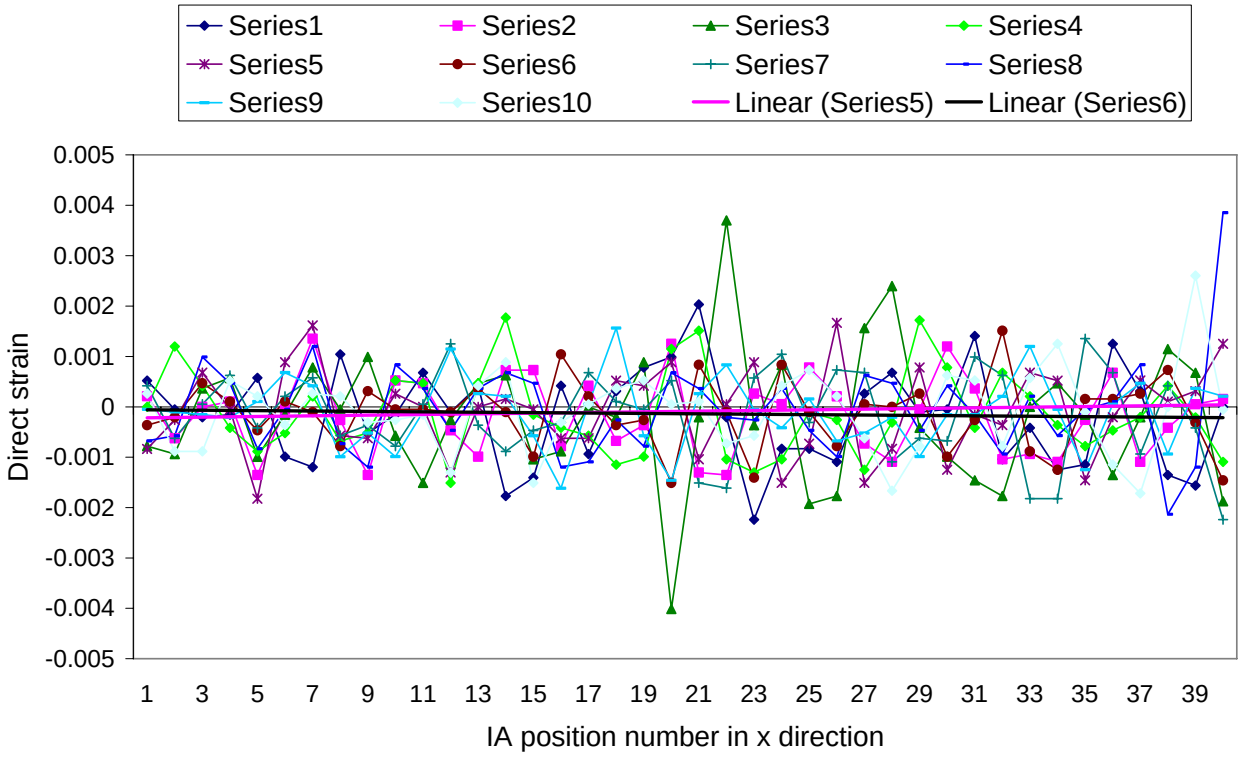

(a) Errors in ε_{xx} (Real value $\varepsilon_{xx}=0$)

Figure AI.4 Dummy strain (error in strain calculation) from digital PIV in pre-test in B4B3

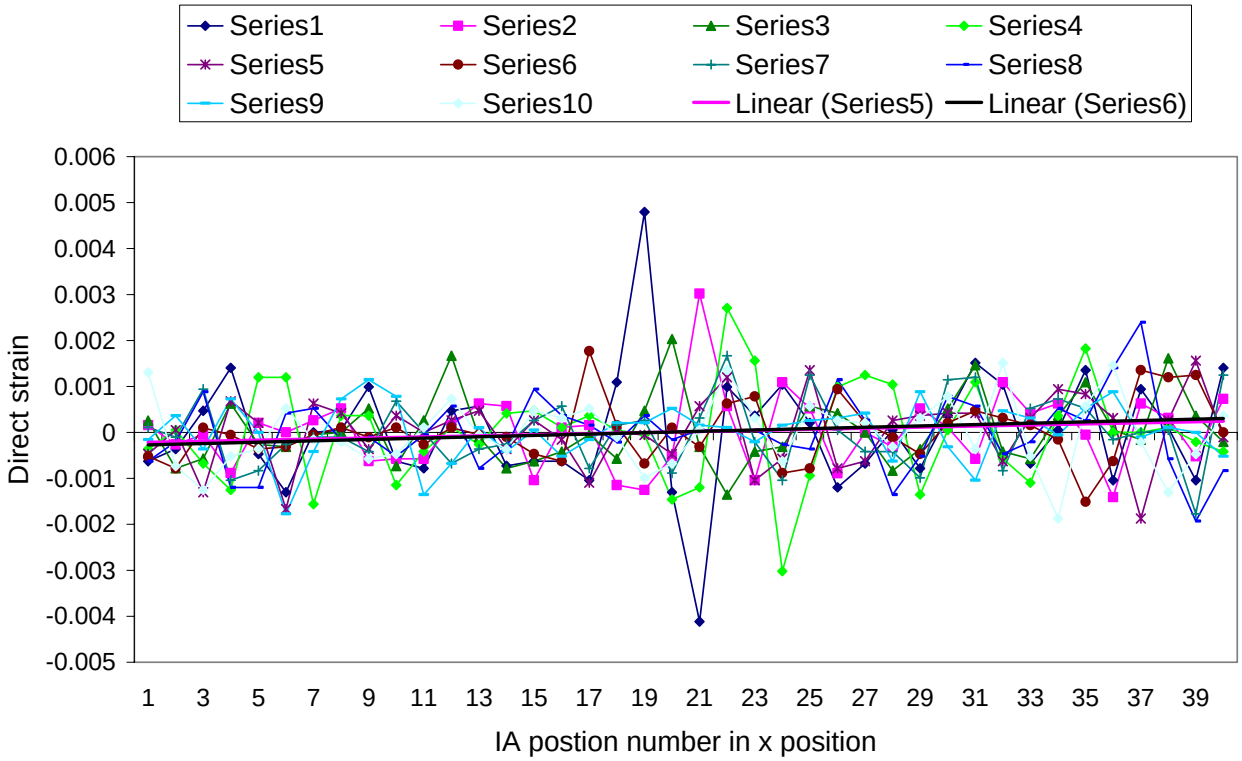

(b) Errors in ε_{zz} (Real value $\varepsilon_{zz} = 0$)

Figure AI.4 Dummy strain (error in strain calculation) from digital PIV in pre-test in B4B3

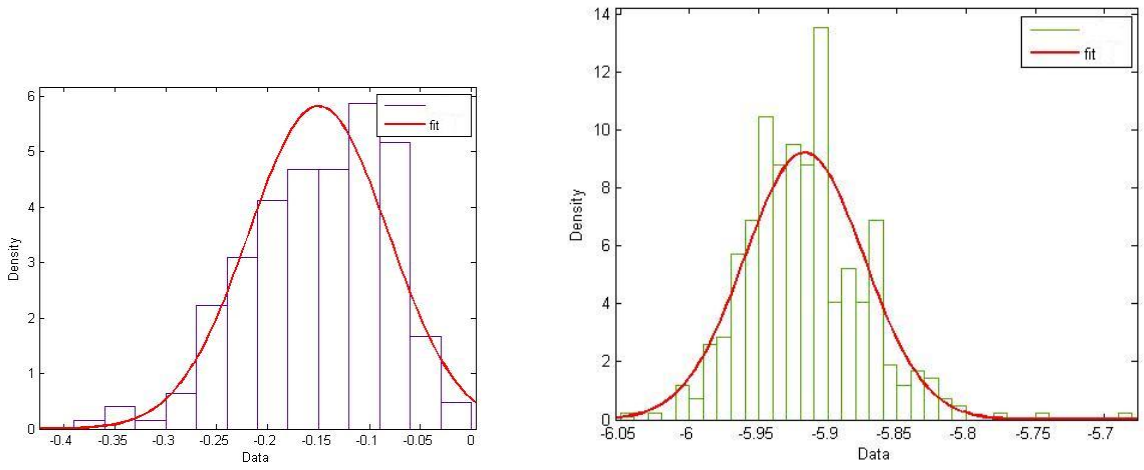

U' V'

Figure AI.5 Normal distribution of U', V' measured using the basic IA size and basic size of search area in B4B3 (population of the sample space $n = 420$)

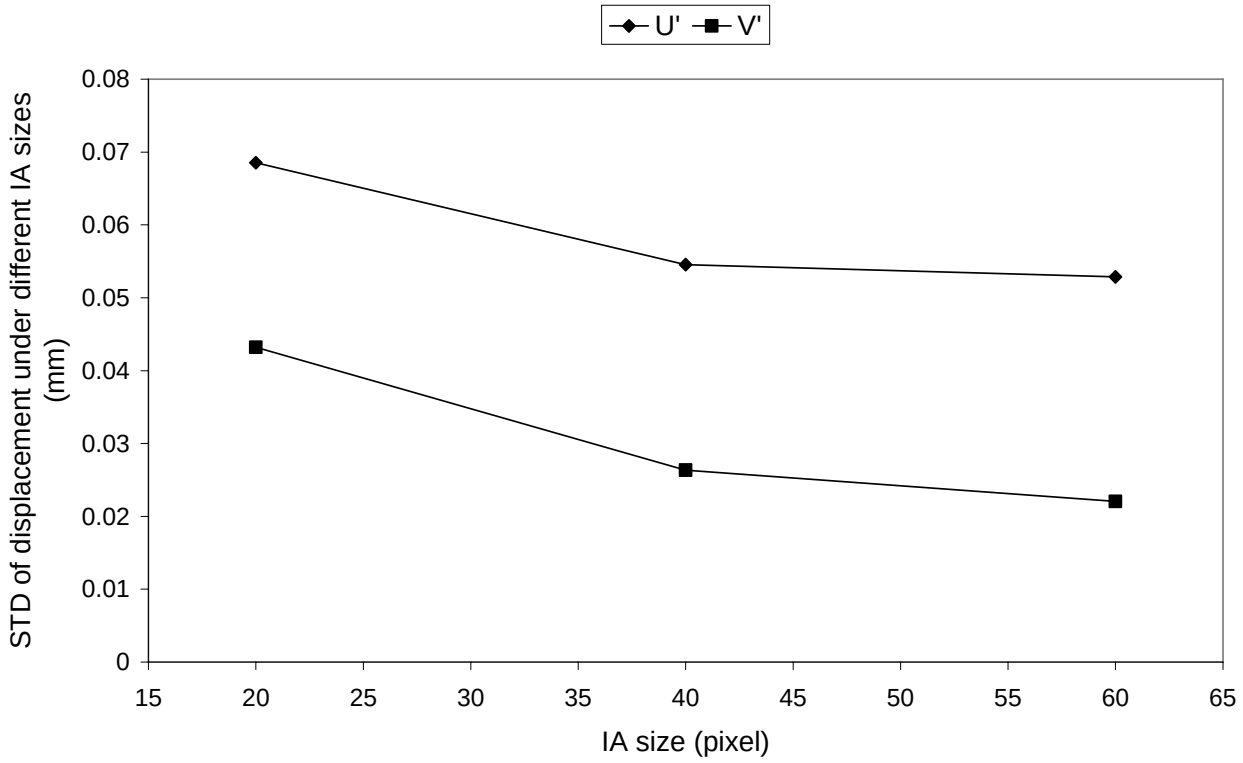

(a) $U^{'}, V^{'}$

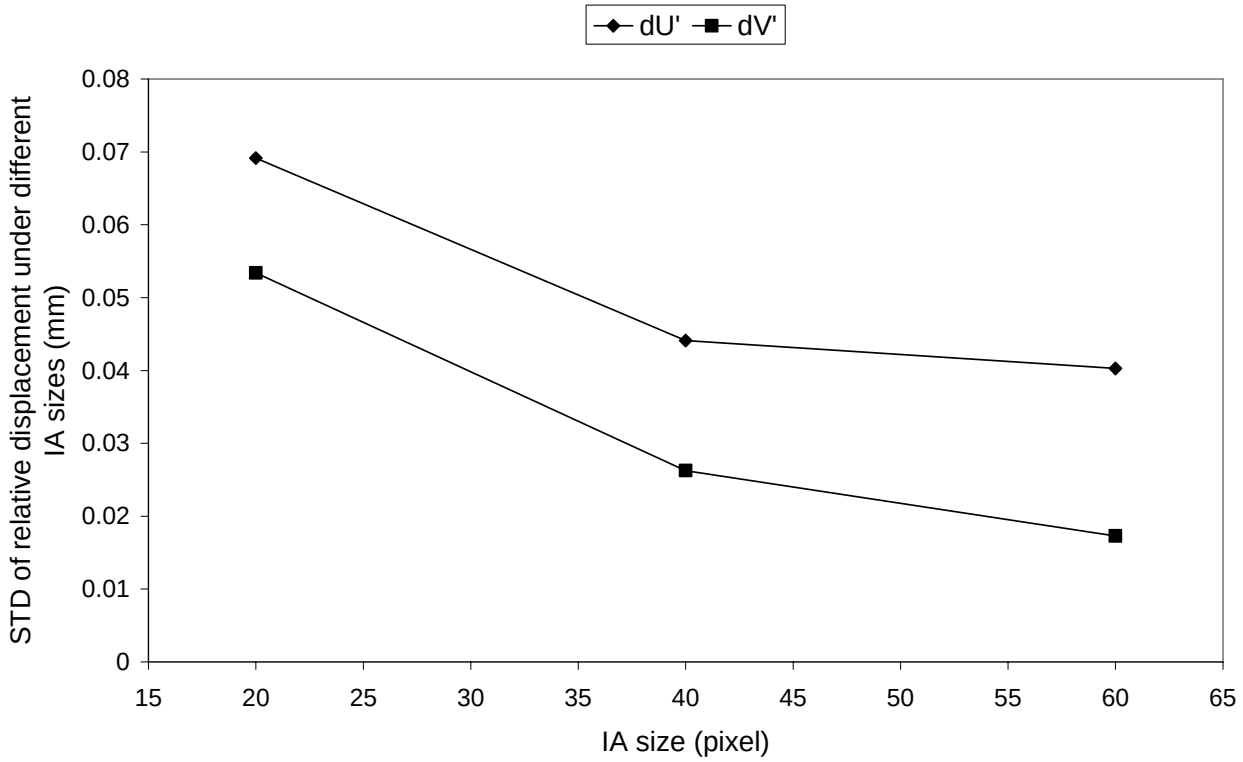

(b) $\Delta U^{'}, \Delta V^{'}$

Figure AI.6 Variation of STD of $U^{'}, V^{'}, \Delta U^{'}, \Delta V^{'}$ and $\varepsilon_{xx}, \varepsilon_{zz}$ with various IA size (Size of search area 10 pixels)

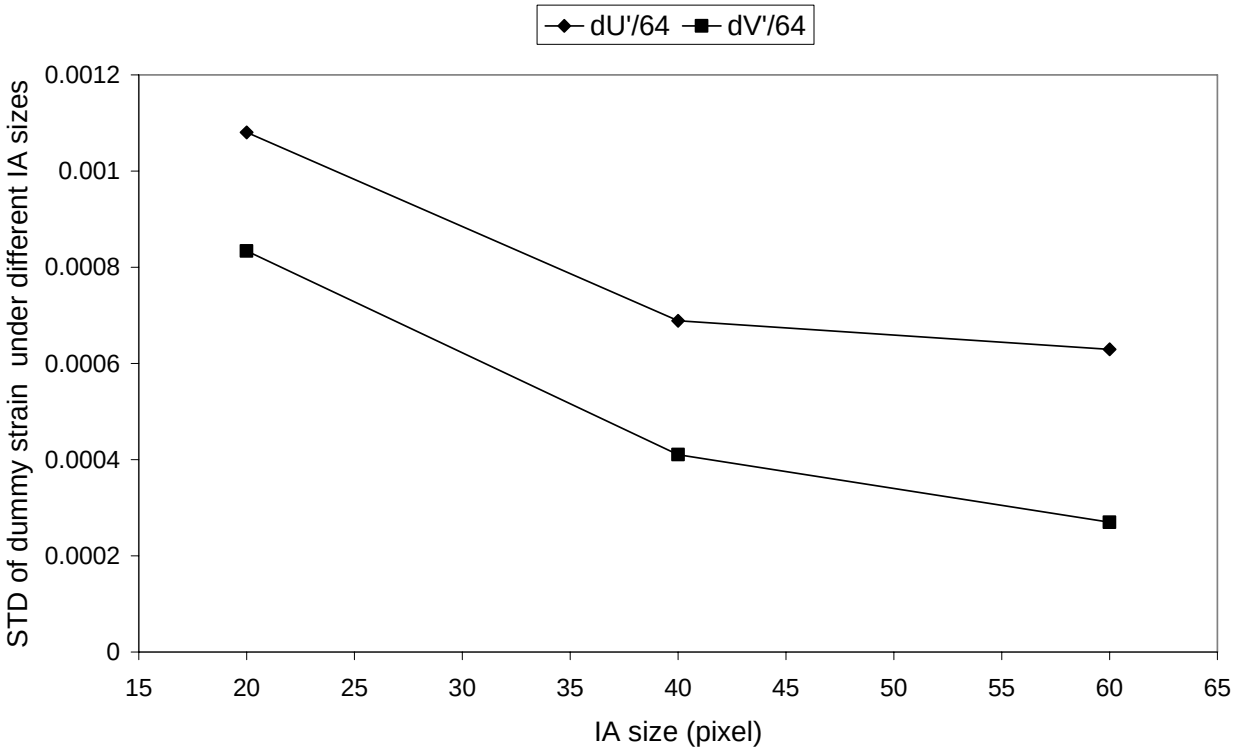

(c) $\varepsilon_{xx}, \varepsilon_{zz}$

Figure AI.6 Variation of $U^{'}, V^{'}, \Delta U^{'}, \Delta V^{'}$ and $\varepsilon_{xx}, \varepsilon_{zz}$ with various IA size (Size of search area 10 pixels)

Appendix II Frame analysis for the pile cap samples in experiments

AII.1 A general frame analysis for pile caps

In order to investigate the influence of the hogging moment above the pile head on the shear capacity of the pile cap which is caused by the experimental pile condition (Section 3.6), a frame analysis has been done to obtain the ratio of the hogging moment above the pile head over the sagging moment at the central span of the pile cap.

The pile cap is a non-linear RC structure and bears cracks. It is not strictly suitable for a linear elastic frame analysis. Also, the width and depth of the cap and the diameter of the pile make the frame analysis less accurate since the simplified 1-way bar members without thickness cannot fully represent the behaviour of the pile cap. So several assumptions have been made:

(i) The RC pile cap is elastic even towards the maturing of the cracks;

(ii) The influence of the dimensions of the pile, cap and wall loading is neglected;

(iii) The bar members are simplified into an in-plane frame (Figure AII.1);

(iv) The joint point of the horizontal bar member representing the cap and the vertical bar member representing the pile is at the half the total depth of the cap (Figure AII.1);

(v) The axial deformation of the bar members is not considered *i.e.* the energy absorbed in elongation or contraction by axial force in the members is neglected;

(vi) The influence of the shear deformation of the cross section of the bar elements is not considered.

The Young's modulus, the length of the bar members and the second moment of the cross section of the bar members representing the cap and the pile are E_1, l_1, I_1 and E_2, l_2, I_2 respectively (Figure AII.1). Sign convention is that the positive moment is always at the tension fibre of the bar element.

Based on the symmetric character of the pile cap, one quarter in-plane frame model is finally analysed which is shown in Figure AII.1. The support condition at the pile base is only to release the horizontal displacement (Section 3.6). Therefore the frame is an indeterminate structure with one redundant restraint.

As assumed above, since the axial and shear deformation is neglected, the following analysis only considers the flexural deformation of the bar elements caused by the bending moment. As shown in Figure AII.2, the one quarter frame is reduced to a determinate frame

by releasing the moment f at the joint b between horizontal and vertical members. A positive unit moment 1 corresponding to f is applied on the reduced frame. The distribution of bending moment m_1 under the unit moment 1 on the determinate frame is shown in Figure AII.2. Under a concentrated external load $\frac{F}{4}$ (Figure AII.1), where F is the external load to the whole pile cap, the distribution of bending moment m_0 on the determinate frame is shown in Figure AII.2.

Based on the stiffness method, the condition that the relative rotation of the two cross sections at joint b is always zero is represented as:

$$f \times f_{11} + f_{10} = 0$$

where

$$f_{11} = \int_a^b \frac{m_1 m_1}{E_2 I_2} dl + \int_b^c \frac{m_1 m_1}{E_1 I_1} dl = \frac{1 \times l_2 \times 1}{E_2 I_2} + \frac{1 \times l_1 \times 1}{E_1 I_1} = \frac{l_2}{E_2 I_2} + \frac{l_1}{E_1 I_1}$$

is the relative rotation of the two cross sections at the joint b of the determinate frame under the unit moment 1,

$$f_{10} = \int_a^b \frac{m_1 m_0}{E_2 I_2} dl + \int_b^c \frac{m_1 m_0}{E_1 I_1} dl = 0 + \frac{\frac{1}{2} \times l_1 \times \frac{F}{4} l_1 \times 1}{E_1 I_1} = \frac{\frac{F}{4} l_1^2}{2 E_1 I_1}$$

is the relative rotation of the two cross sections at the joint b of the determinate frame under the external force $\frac{F}{4}$, and l is the co-ordinates of the length of the bar elements.

The composite cross section of reinforcement and concrete is equalized to the cross section made up of pure concrete but with same bending capacity to the original such that $E_1 = E_2 = E_c$, where E_c is the Young's modulus of concrete and I_1, I_2 are the second moments of the equivalent transformed concrete cross section. Then,

$$f = \frac{-f_{10}}{f_{11}} = -\frac{\frac{F}{4} l_1^2 I_2}{2\left(l_1 I_2 + l_2 I_1\right)}$$

The distribution of the bending moment M_1 caused by f on the determinate frame is shown in Figure AII.2. Combined with the distribution of the bending moment M_0 caused by the external force $\frac{F}{4}$ on the determinate frame, the distribution of the total moment M on the indeterminate frame is obtained as shown in Figure AII.2.

As shown in Figure AII.2, the sagging moment at the central span

$$M_s = \frac{F}{4} l_1 + f$$

i.e.

$$M_s = \frac{F}{4} l_1 - \frac{\frac{F}{4} l_1^2 I_2}{2(l_1 I_2 + l_2 I_1)} = \frac{F}{4} l_1 \frac{l_1 I_2 + 2 l_2 I_1}{2(l_1 I_2 + l_2 I_1)}$$

and the hogging moment above the pile head

$$M_h = f = -\frac{\frac{F}{4} l_1^2 I_2}{2(l_1 I_2 + l_2 I_1)}$$

The ratio of the absolute value of the hogging moment over the sagging moment is therefore

$$\left|\frac{M_h}{M_s}\right| = \frac{\frac{F l_1^2 I_2}{2(l_1 I_2 + l_2 I_1)}}{F l_1 \frac{l_1 I_2 + 2 l_2 I_1}{2(l_1 I_2 + l_2 I_1)}} = \frac{l_1 I_2}{l_1 I_2 + 2 l_2 I_1} = \frac{1}{1 + 2\left(\frac{l_2}{l_1}\right)\left(\frac{I_1}{I_2}\right)} \qquad (Eq.AII.1)$$

AII.2 A frame analysis for B4A1

To obtain the ratio $\left|\frac{M_h}{M_s}\right|$ for B4A1, the second moment I_1, I_2 of the equivalent transformed concrete cross section of the bar members must be calculated.

The real cross-sections of the cap and the pile and the equivalent transformed concrete cross-sections in B4A1 are shown in Figure AII.3. The equivalent concrete cross-sections replace the reinforcement area with an enlarged concrete area of $\frac{E_s}{E_c}$ times of the original area of Young's modulus E_c . It is assumed that Young's modulus of reinforcement $E_s = 210000 MPa$ and of concrete $E_c = 28000 MPa$ (Section 5.3) resulting in $\frac{E_s}{E_c} = 7.5$.

The equivalent concrete cross sections are shown in Figure AII.3. $I_1 = 26.21 \times 10^7 mm^4$ and $I_2 = 1.937 \times 10^7 mm^4$ for the cap and pile respectively. The neutral axis of the equivalent cross sections is also shown in Figure AII.3. In addition, for B4A1, $l_1 = 400 mm, l_2 = 375 mm$ (Table 3.3). Substitute I_1, I_2, l_1, l_2 into $Eq.AII.1$,

$$\left|\frac{M_h}{M_s}\right| = \frac{1}{1 + 2 \times \left(\frac{375}{400}\right)\left(\frac{26.21 \times 10^7}{1.937 \times 10^7}\right)} = \frac{1}{26.4}$$

The real shear span defined by the contra-flexure point determined by $\frac{M_h}{M_s}$ is shown in Figure 3.16. From the frame analysis, the shear span for B4A1

$$a_v = l_1 \times \left(\frac{\frac{1}{\left|\frac{M_h}{M_s}\right|}}{\frac{1}{\left|\frac{M_h}{M_s}\right|}+1} \right) = 385.4mm$$

From current British Standards, $a_v = \frac{800}{2} - \frac{130}{2} + 130 \times 0.2 = 361mm$ though (Section 2.10.1).

AII.3 The influence of the shear deformation of the cross section of the pile cap on the distribution of the bending moment

The above analysis neglects the shear deformation in the cap. As the cap under wall loading bears high vertical shear force, the influence of the shear deformation of the cross section of the pile cap on $\left|\frac{M_h}{M_s}\right|$ is studied.

The distribution of the shear force s_0, s_1 of the determinate frame under the concentrated external load $\frac{F}{4}$ and unit moment 1 at joint b respectively are shown in Figure AII.4. G_1, l_1, A_1 and G_2, l_2, A_2 are the shear modulus, the length and the cross section area of the bar members representing the cap and the pile respectively.

It is clear from the Figure AII.4 that under the unit moment 1, the shear force s_1 is constantly 0 along the members implying that the shear force caused by the external load $\frac{F}{4}$ and the released bending moment f at joint b does not contribute any work to the relative rotation of the two cross sections at joint b *i.e.* the shear force and the shear deformation occurred in the pile cap do not influence the distribution of the bending moment and $\left|\frac{M_h}{M_s}\right|$.

This is mathematically expressed as:

$$f_{10}^{s} = \kappa_2 \int_a^b \frac{s_1 s_0}{G_2 A_2} dl + \kappa_1 \int_b^c \frac{s_1 s_0}{G_1 A_1} dl = 0$$

$$f_{11}^{s} = \kappa_2 \int_a^b \frac{s_1 s_1}{G_2 A_2} dl + \kappa_1 \int_b^c \frac{s_1 s_1}{G_1 A_1} dl = 0$$

where f_{10}^{s}, f_{11}^{s} are the relative rotation of the two cross sections at joint b caused by the shear force from external $\frac{F}{4}$ and the released bending moment f at joint b, both of which are 0 implying zero flexural deformation at joint b in the determinate frame. κ_1, κ_2 are the shape factors representing the average shear deformation of the cross sections of the cap and pile.

It is evident that it is only under the support condition assumed in this research that the shear force and shear deformation do not influence the distribution of the bending moment. It might influence once the support condition is changed.

The result of $\left|\frac{M_h}{M_s}\right|$ for B4A1 in Section AII.2 was verified by a professional software SAM for the calculation of the properties of the cross-section and by STAAD for the calculation of the frame analysis. The distribution of the bending moment of the same frame of ¼ the pile cap of B4A1 under $\frac{F}{4} = 1 \times 10^5 N$ analyzed by STAAD is shown in Figure AII.5. It can be seen the ratio $\left|\frac{M_h}{M_s}\right| = \frac{1.215 kNm}{36.285 kNm} = \frac{1}{29.86}$ which is close to the manual calculation $\left|\frac{M_h}{M_s}\right| = \frac{1}{26.4}$ (Section AII.2).

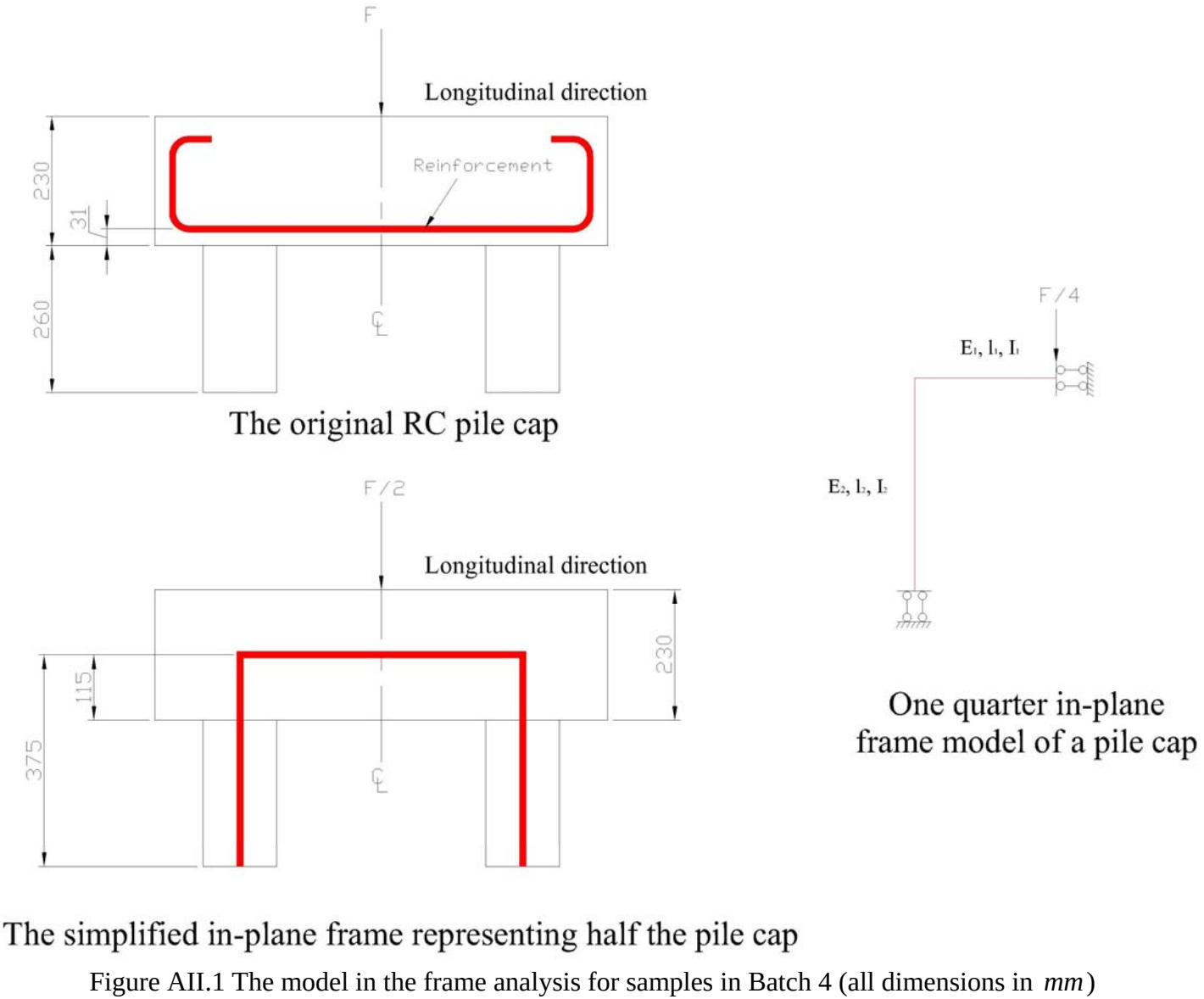

Figure AII.1 The model in the frame analysis for samples in Batch 4 (all dimensions in *mm*)

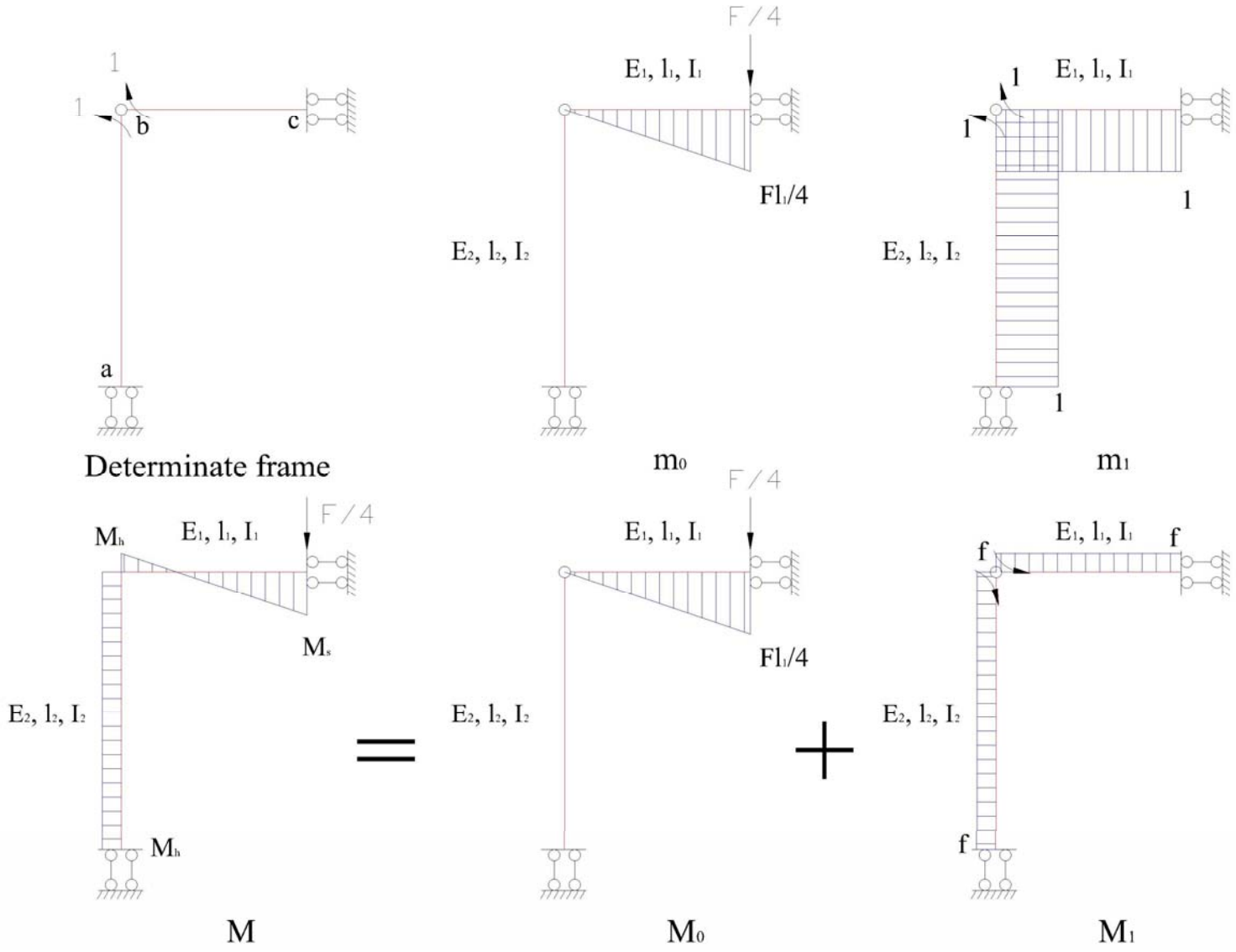

Figure AII.2 Bending moment in the determinate and indeterminate frames of ¼ the pile cap

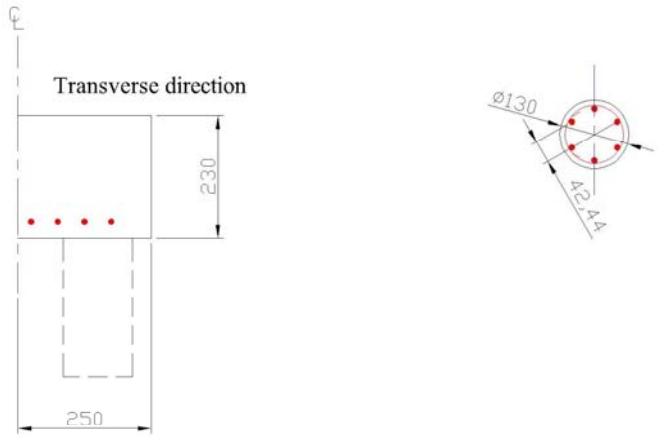

Cap Pile

The cross section of the cap and pile in real situation

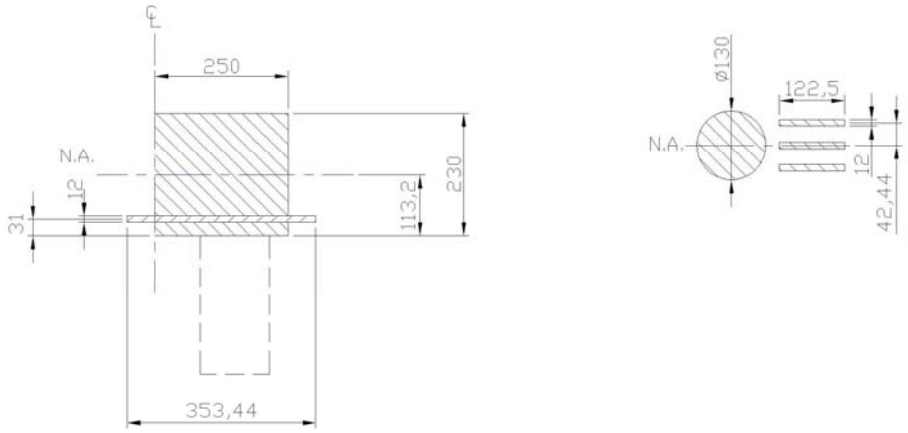

Cap I_1 Pile I_2

Equivalent concrete cross section

Figure AII.3 The equivalent transformed concrete cross sections in ¼ B4A1 (all in *mm*)

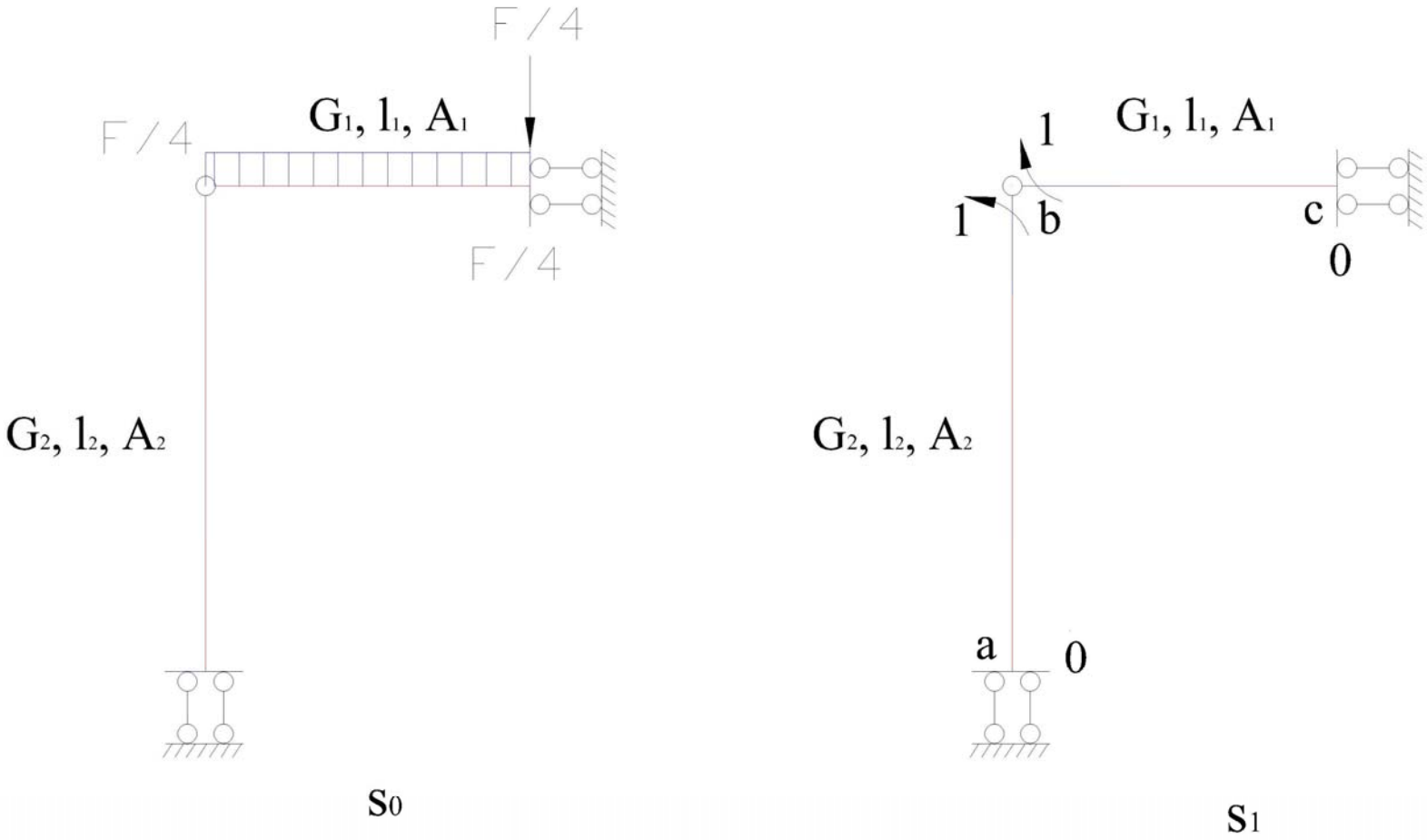

Figure AII.4 The shear force in the determinate frame of ¼ the pile cap

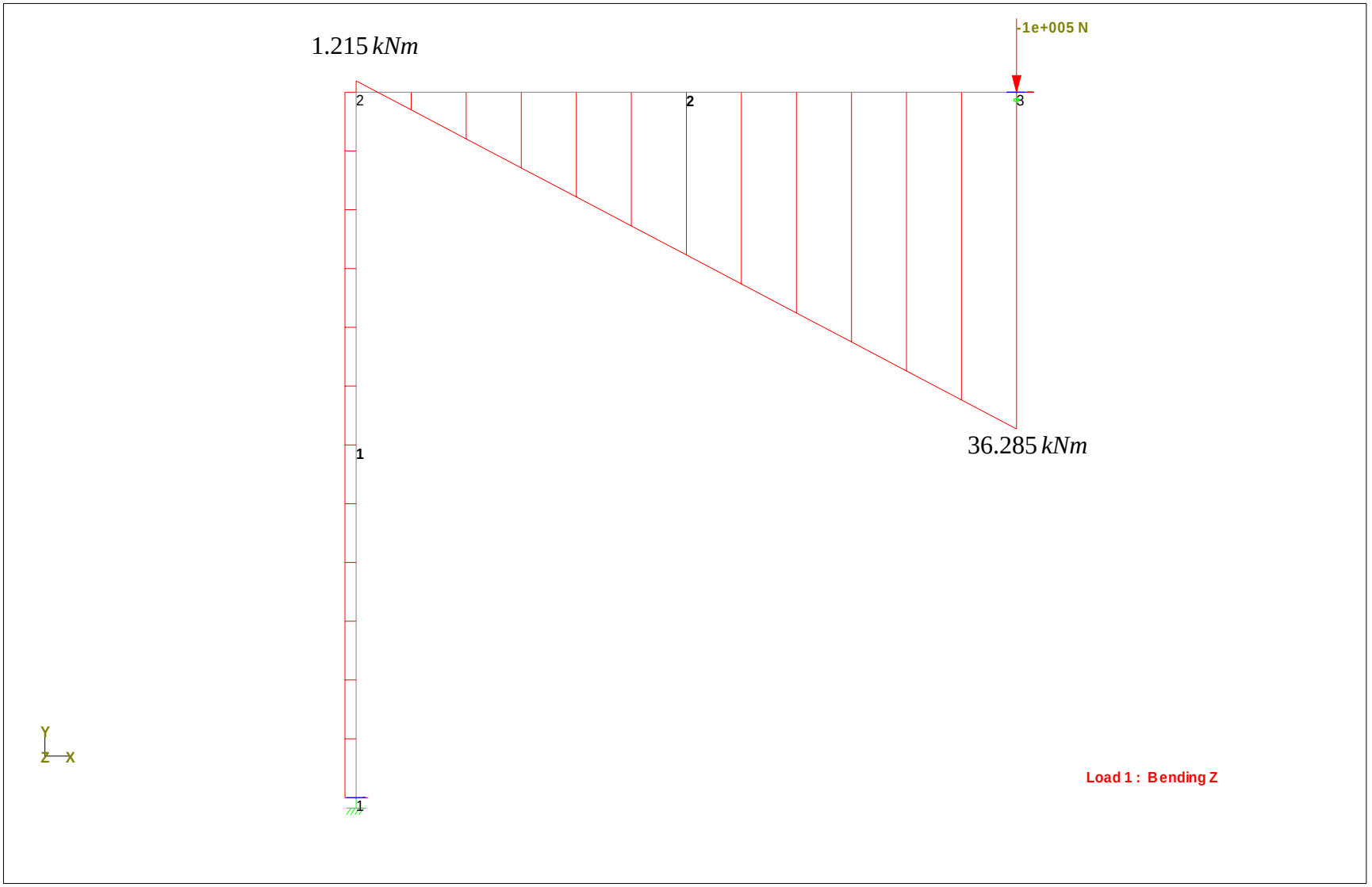

Figure AII. 5 The distribution of the bending moment of the ¼ pile cap B4A1 under $\frac{F}{4} = 1 \times 10^5 N$ from STAAD

Appendix III Crack distributions of pile cap samples at failure step

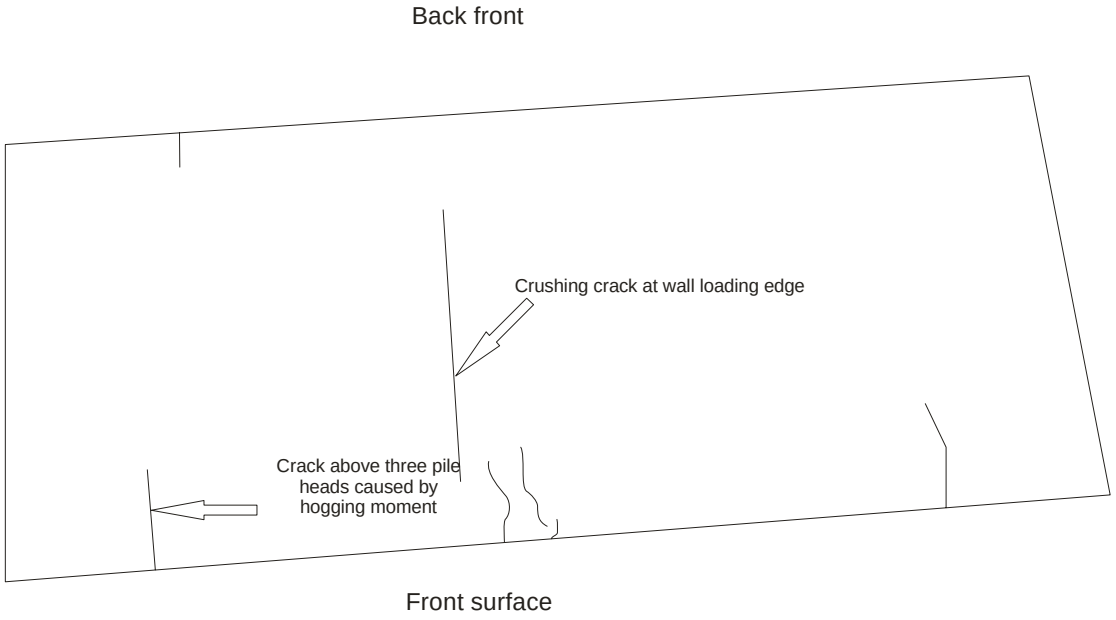

B3A1 Top surface

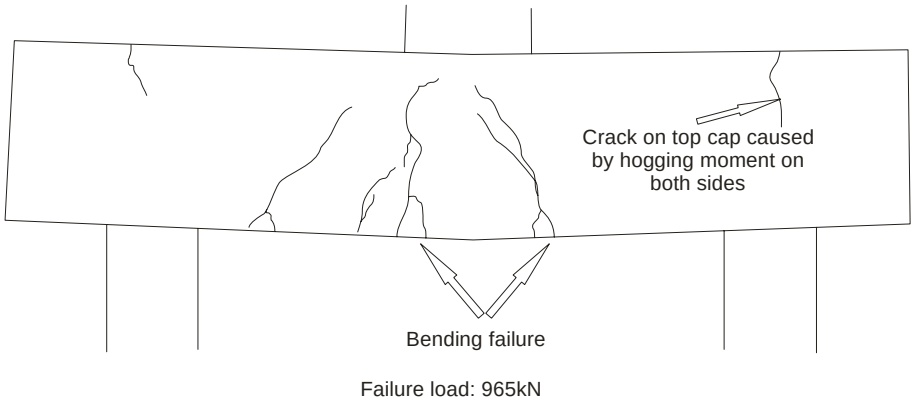

B3A1 Front surface

Figure AIII Crack distribution (continued)

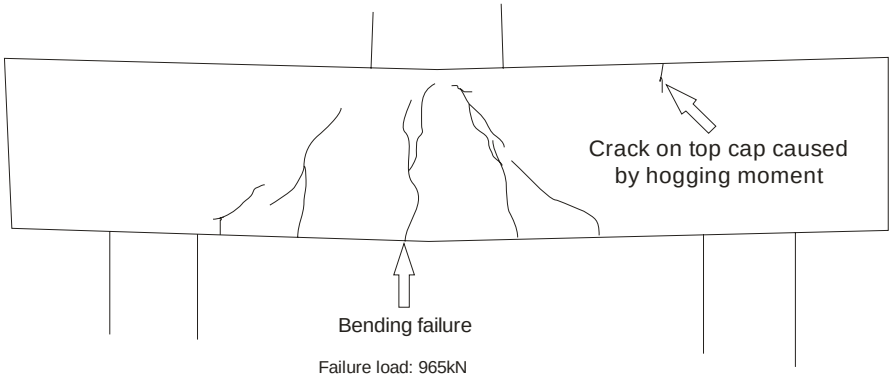

B3A1 Back surface

Back surface

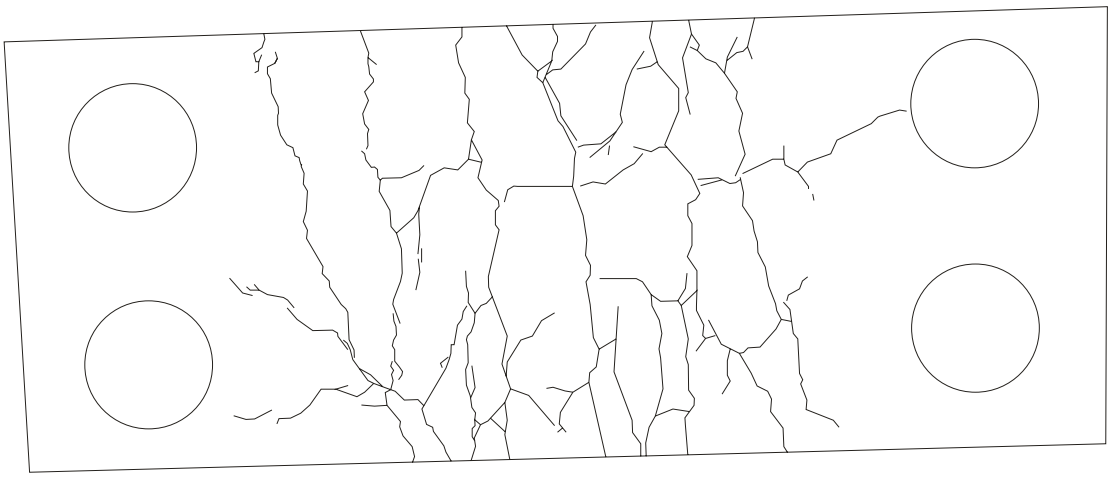

Front surface

B3A1 Cap soffit

Figure AIII Crack distribution (continued)

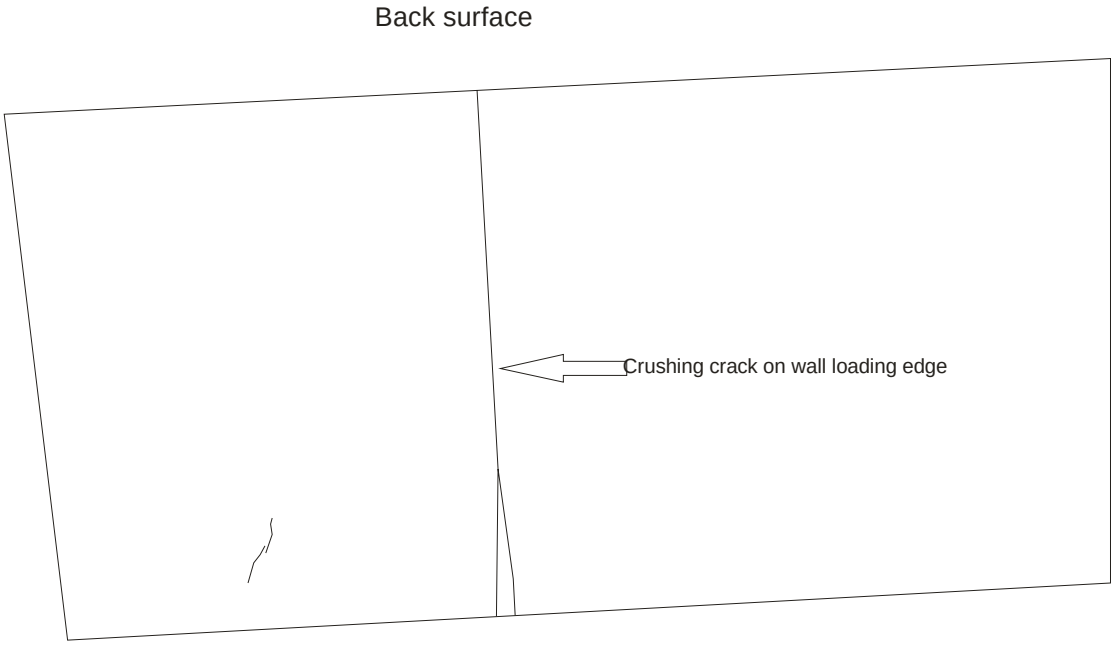

B3

B3A2 Top surface

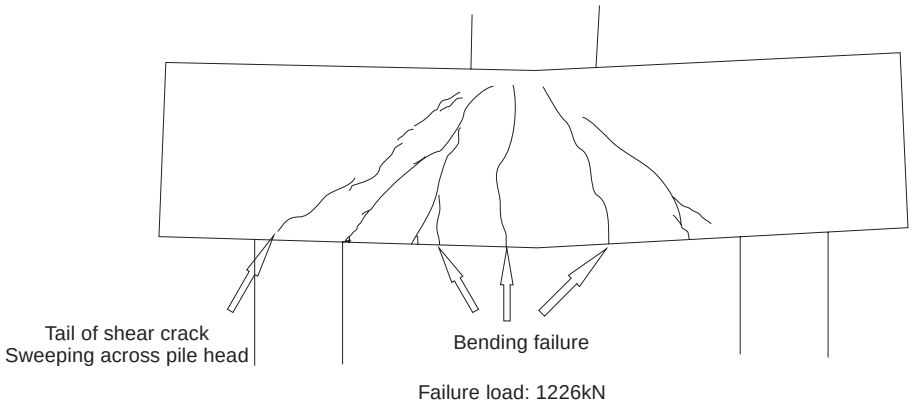

B3A2 Front surface

Figure AIII Crack distribution (continued)

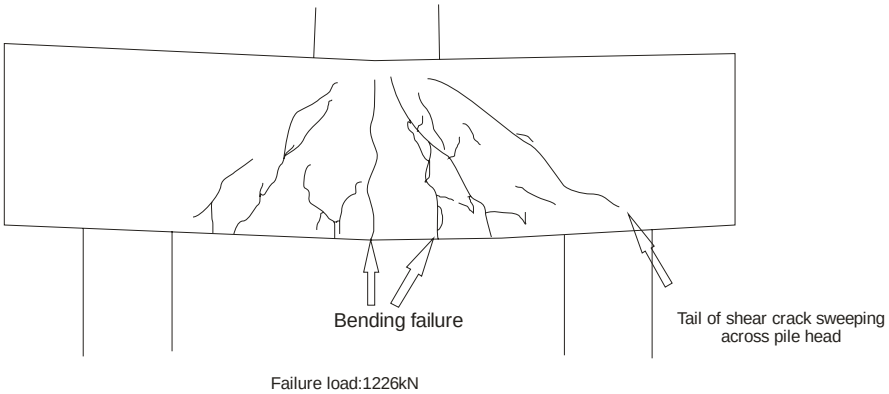

B3A2 Back surface

Back surface

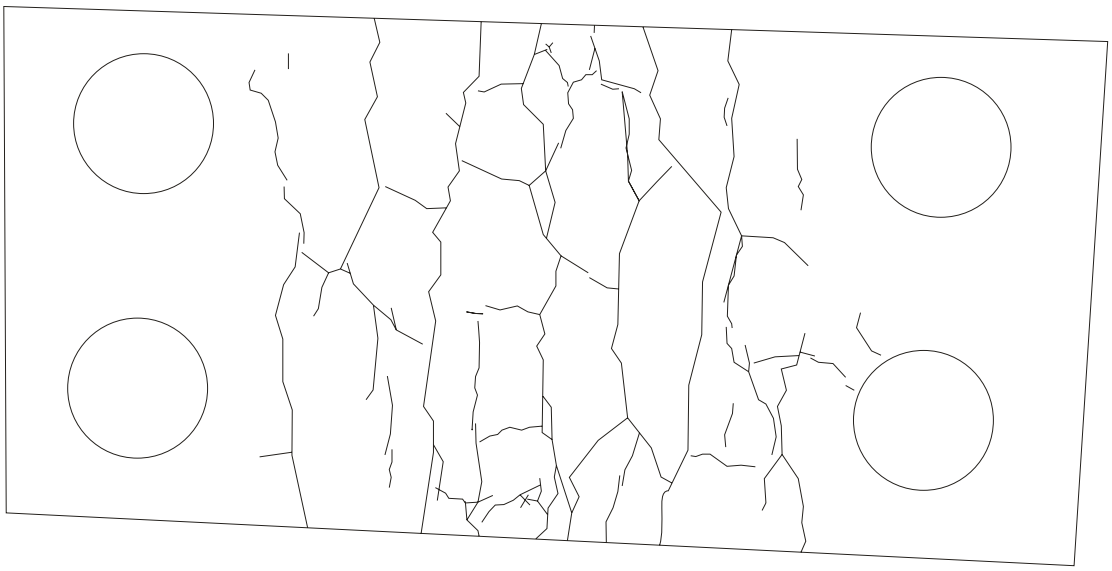

Front surface

B3A2 Cap soffit

Figure AIII Crack distribution (continued)

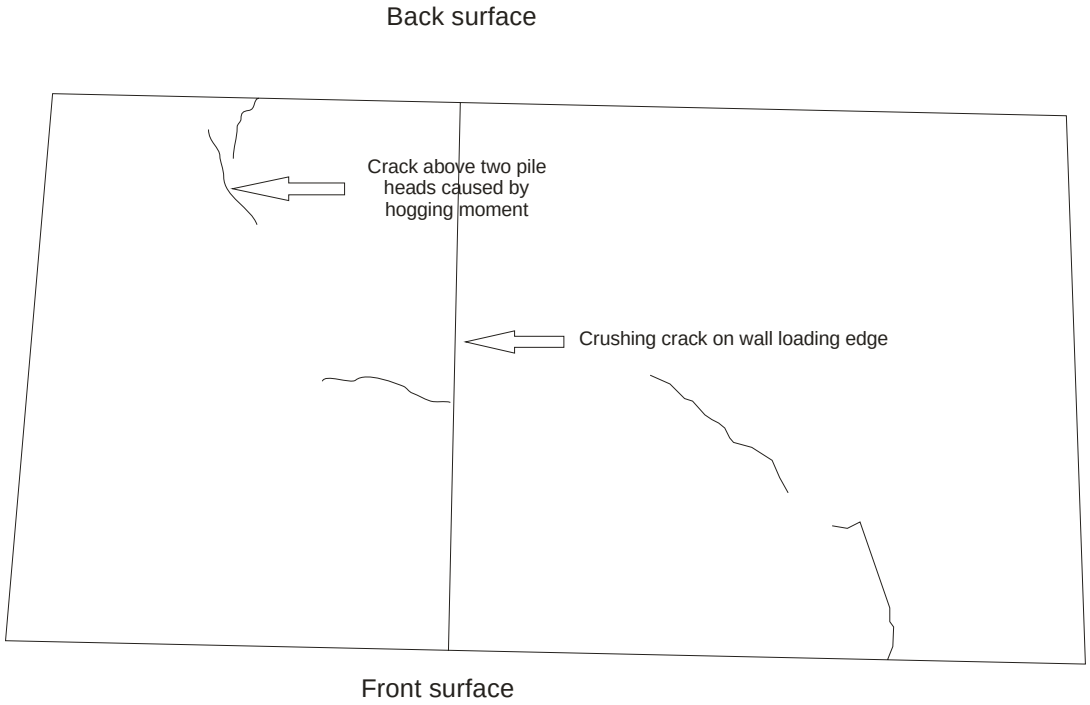

B3A3 Top surface

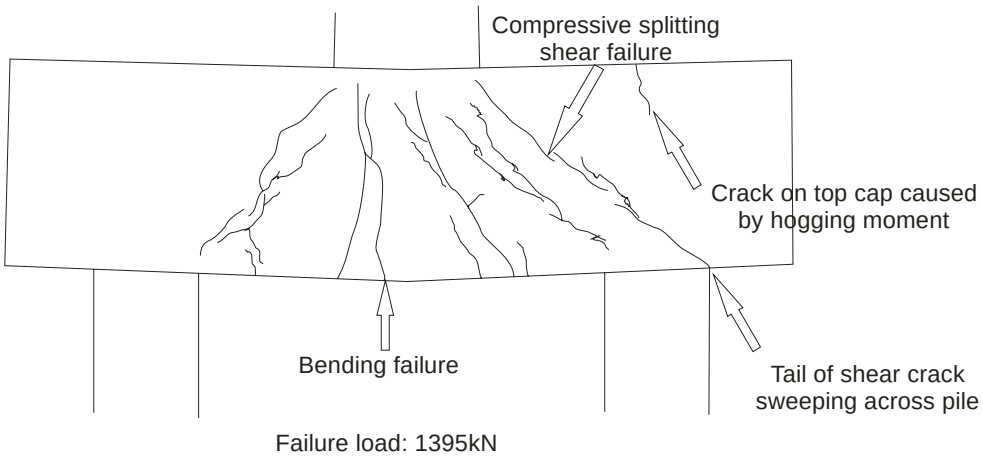

B3A3 Front surface

Figure AIII Crack distribution (continued)

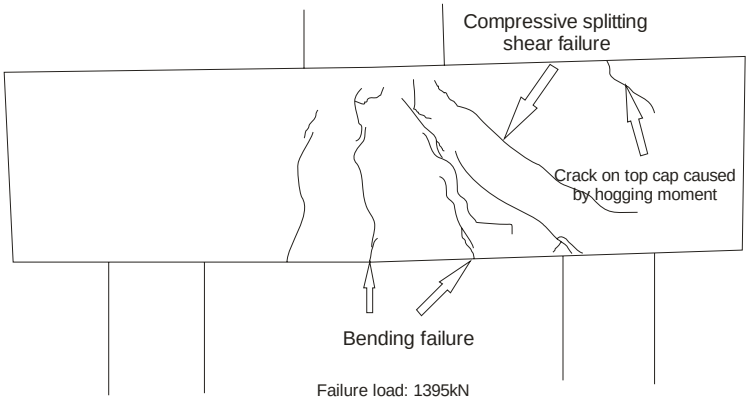

B3A3 Back surface

Back surface

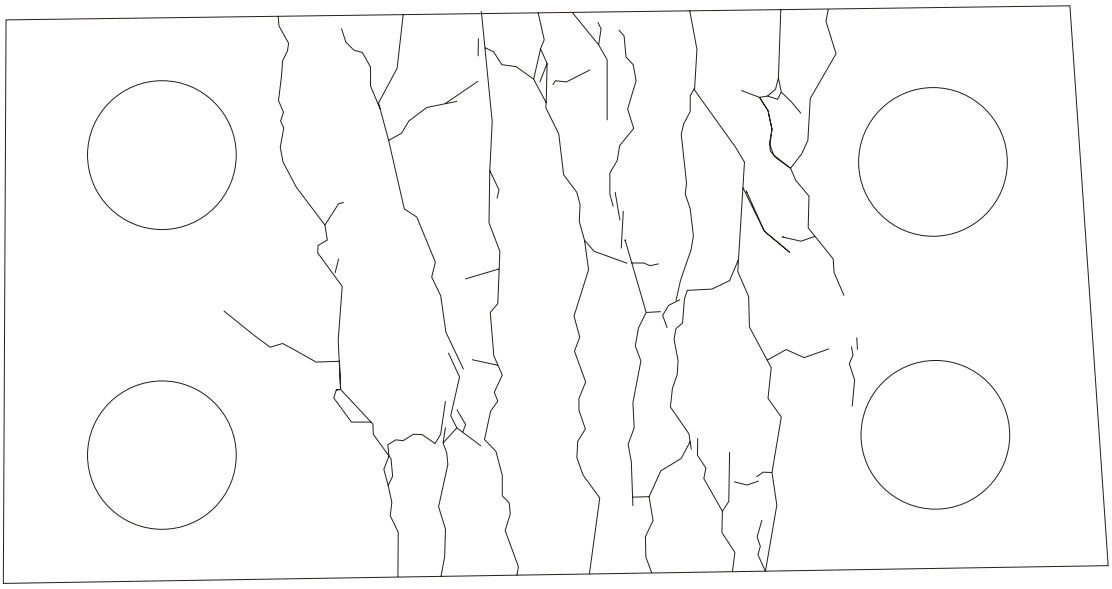

Front surface

B3A3 Cap soffit

Figure AIII Crack distribution (continued)

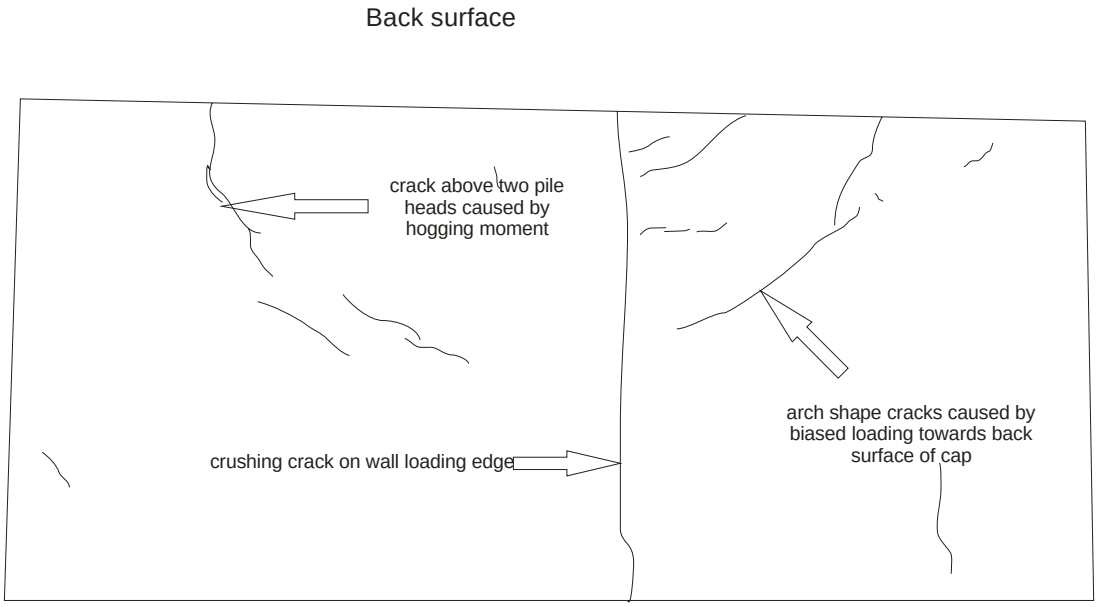

B4A1 Top surface

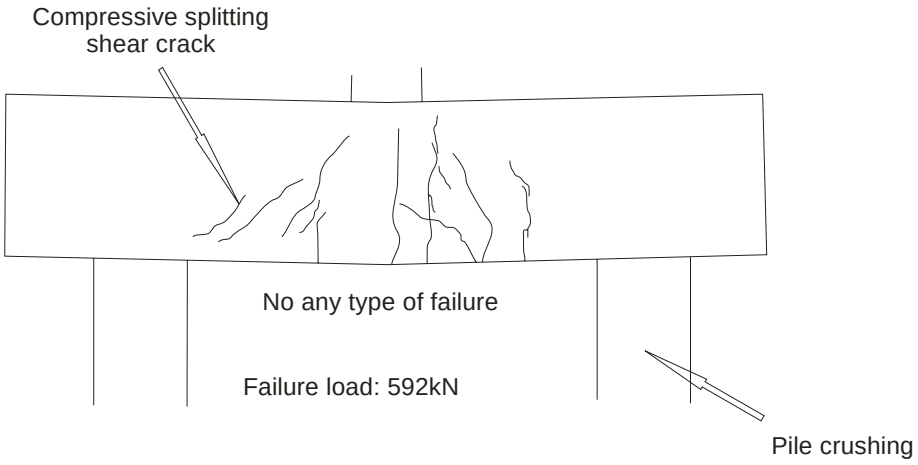

B4A1 Front surface

Figure AIII Crack distribution (continued)

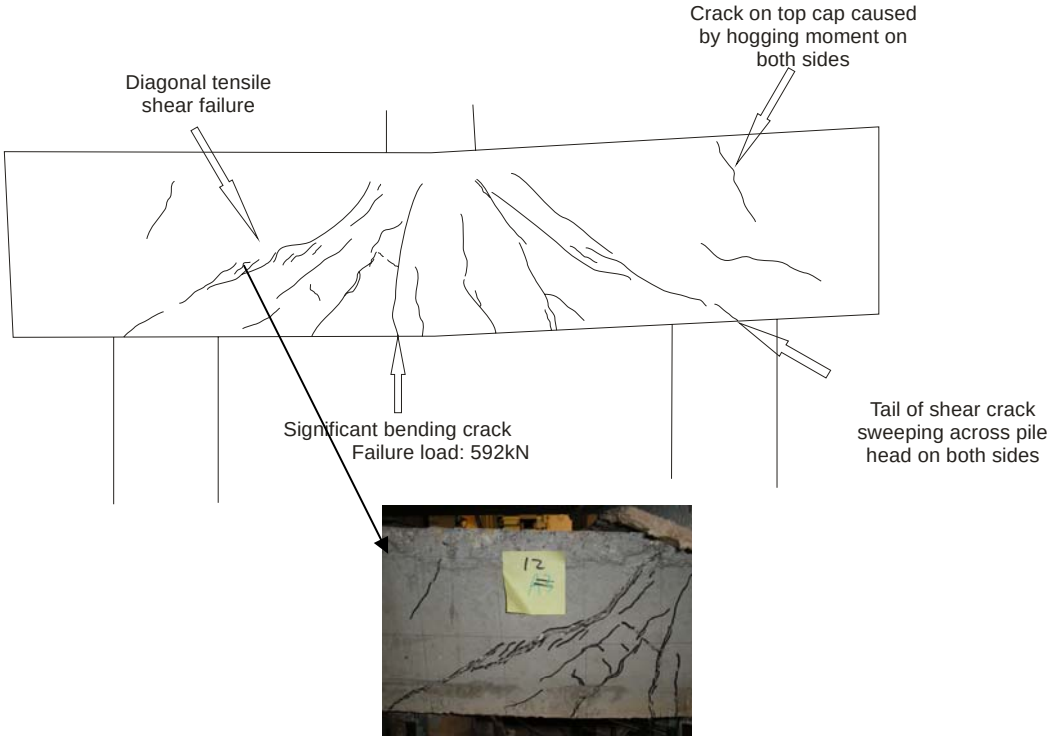

B4A1 Back surface

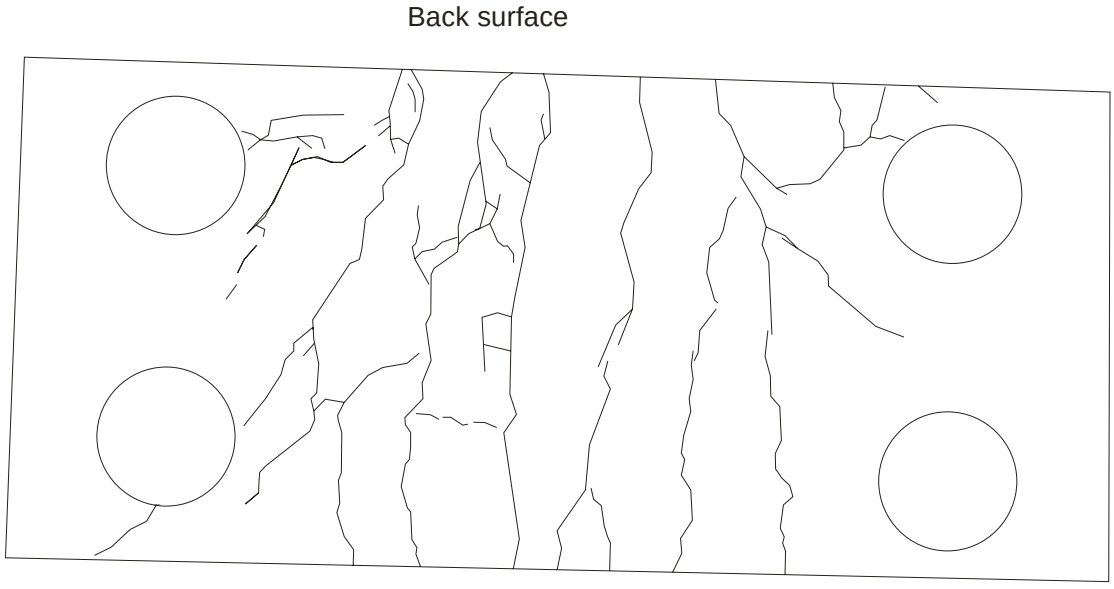

B4A1 Cap soffit

Figure AIII Crack distribution (continued)

Back surface

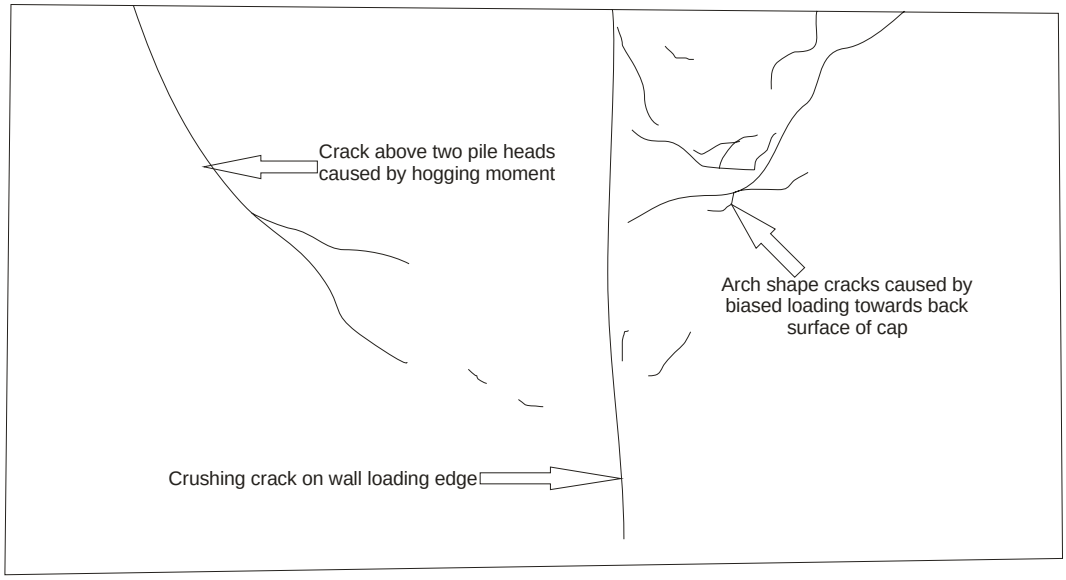

Front surface

B4A2 Top surface

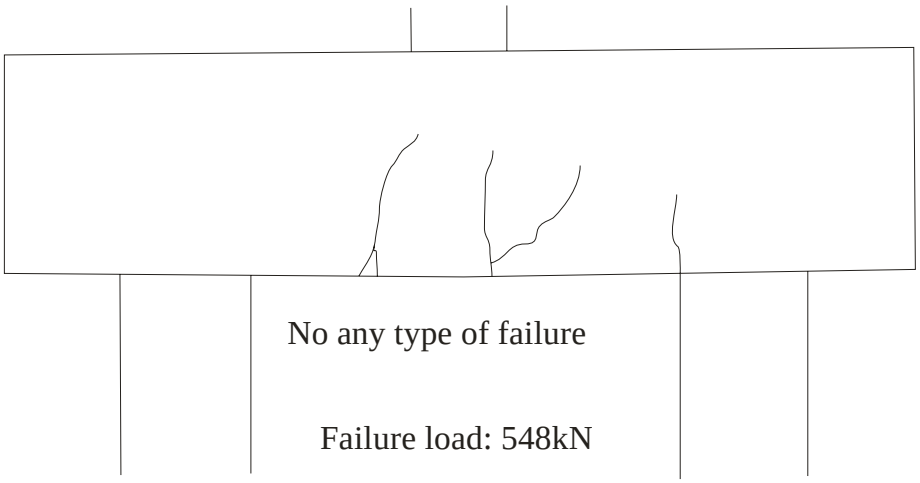

B4A2 Front surface

Figure AIII Crack distribution (continued)

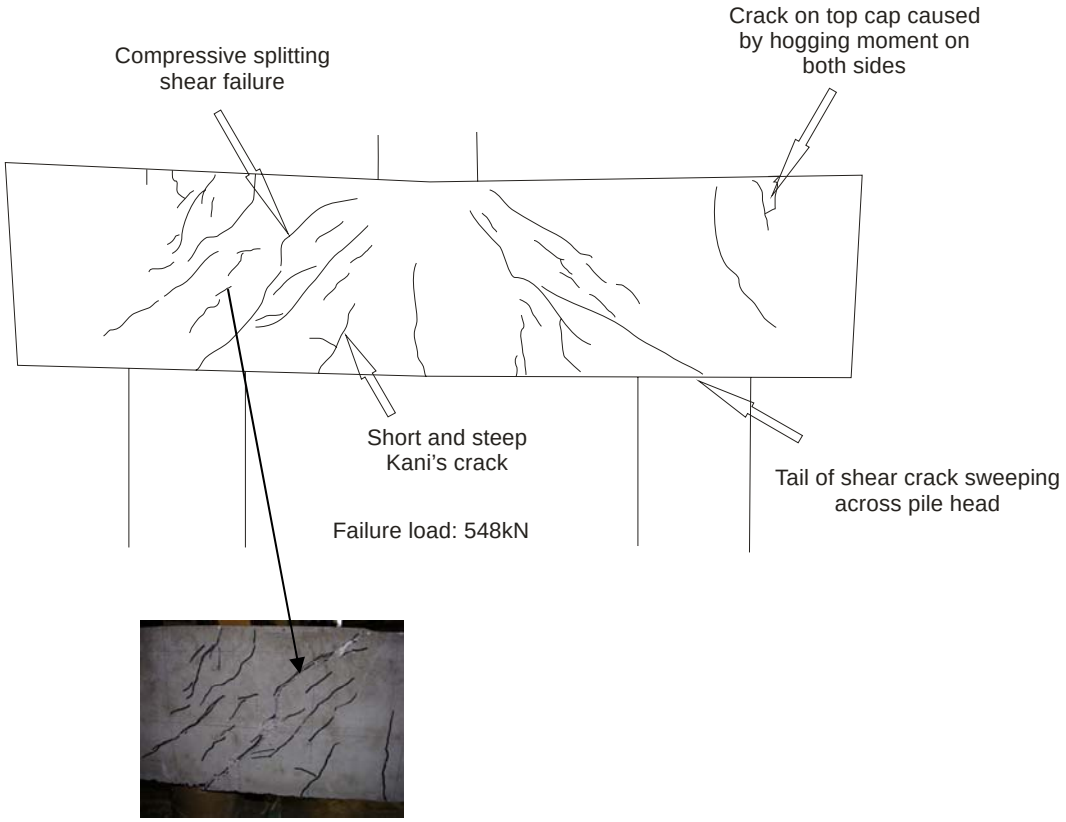

B4A2 Back surface

Back surface

Front surface

B4A2 Cap soffit

Figure AIII Crack distribution (continued)

Back surface

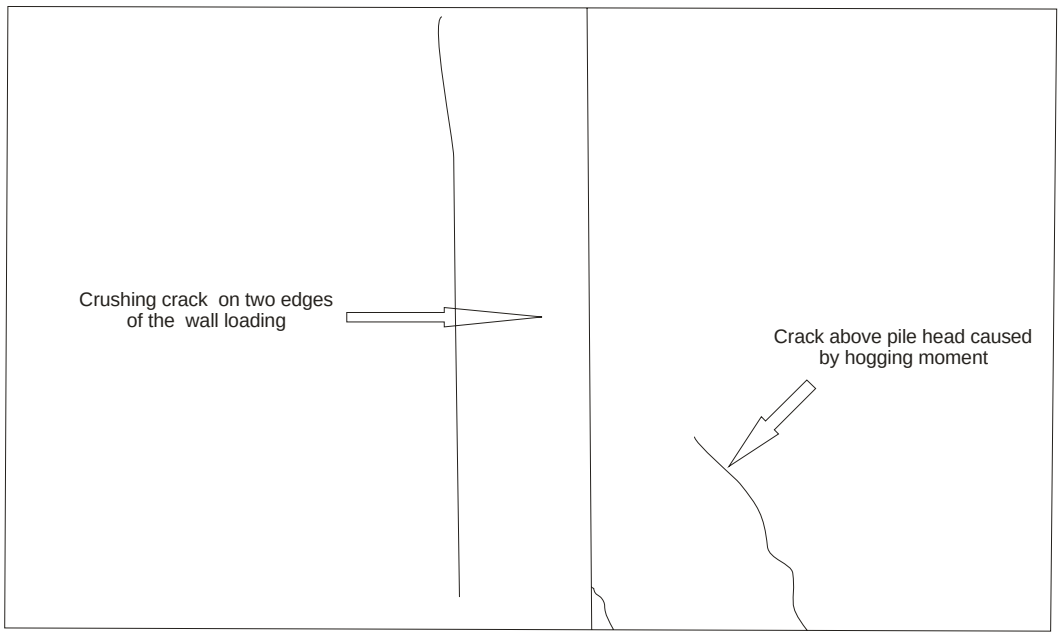

Front surface

B4A3 Top surface

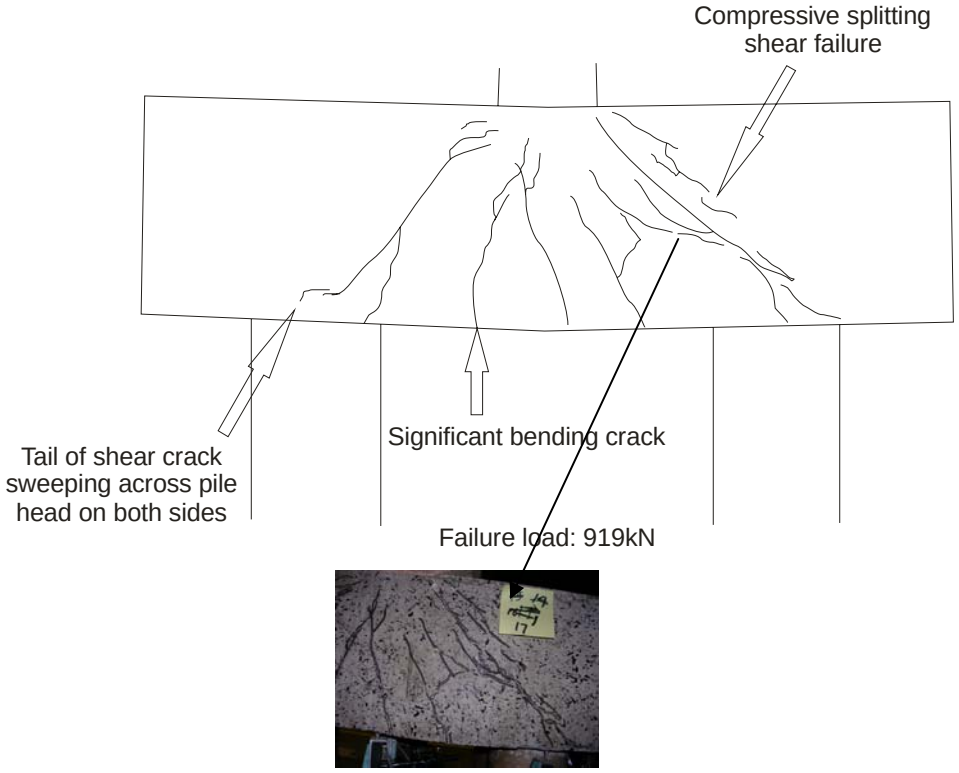

B4A3 Front surface

Figure AIII Crack distribution (continued)

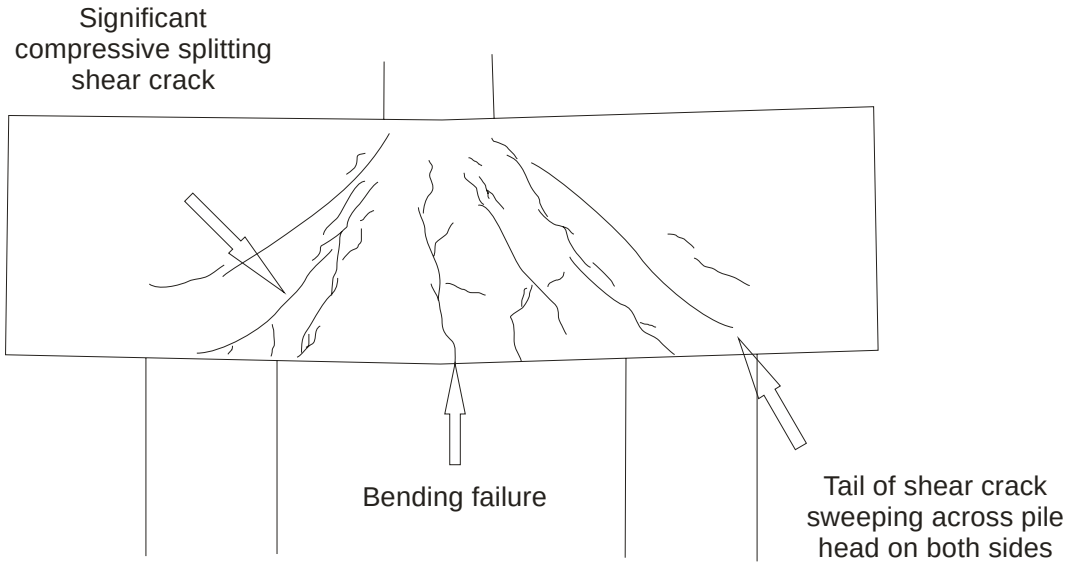

Failure load: 919kN

B4A3 Back surface

Back surface

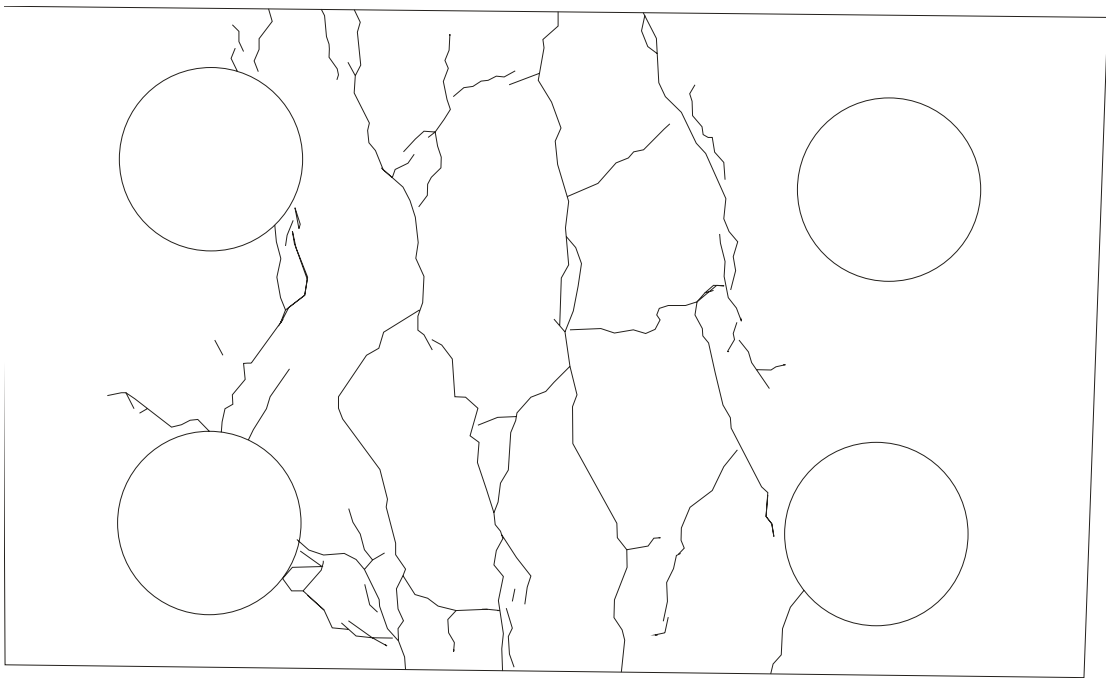

Front surface

B4A3 Cap soffit

Figure AIII Crack distribution (continued)

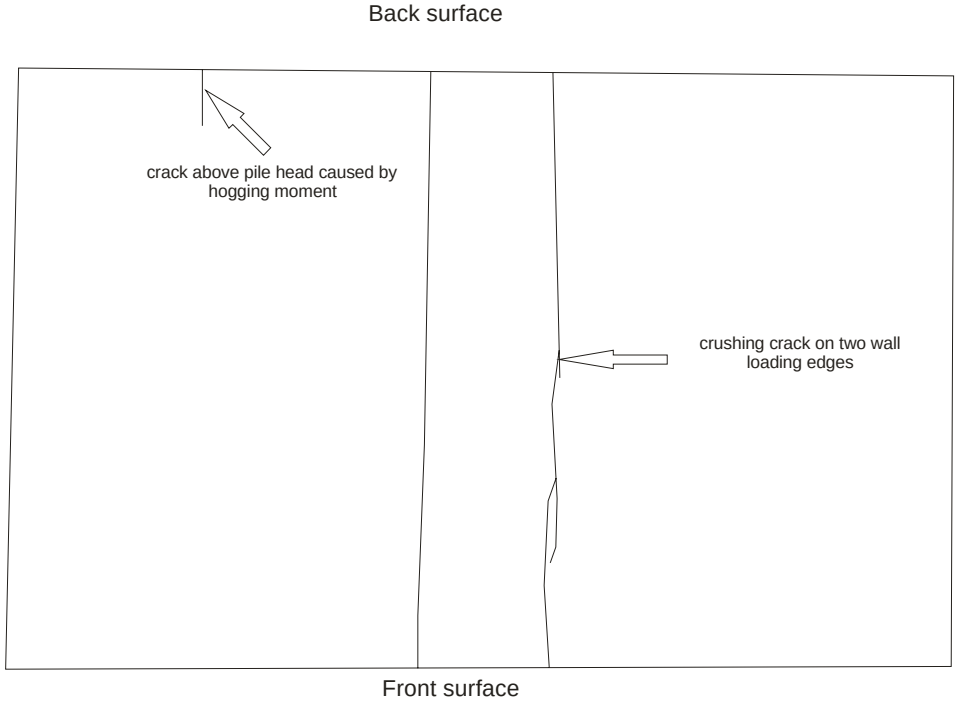

B4A4 Top surface

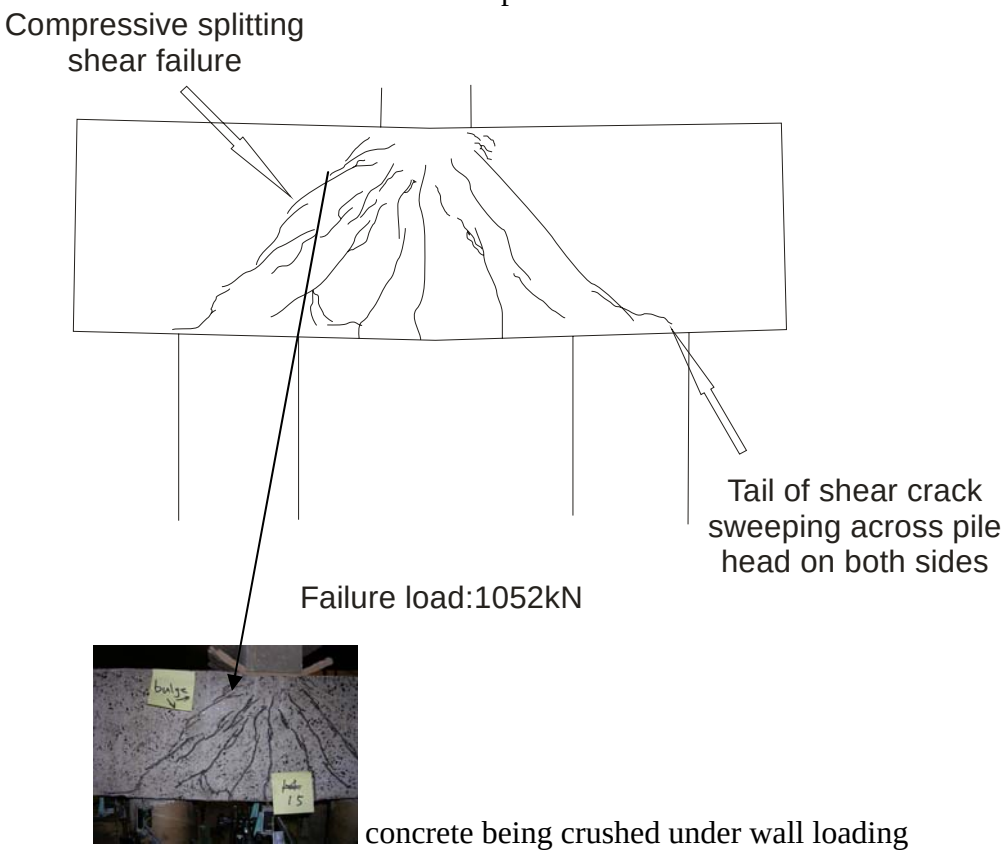

B4A4 Front surface

Figure AIII Crack distribution (continued)

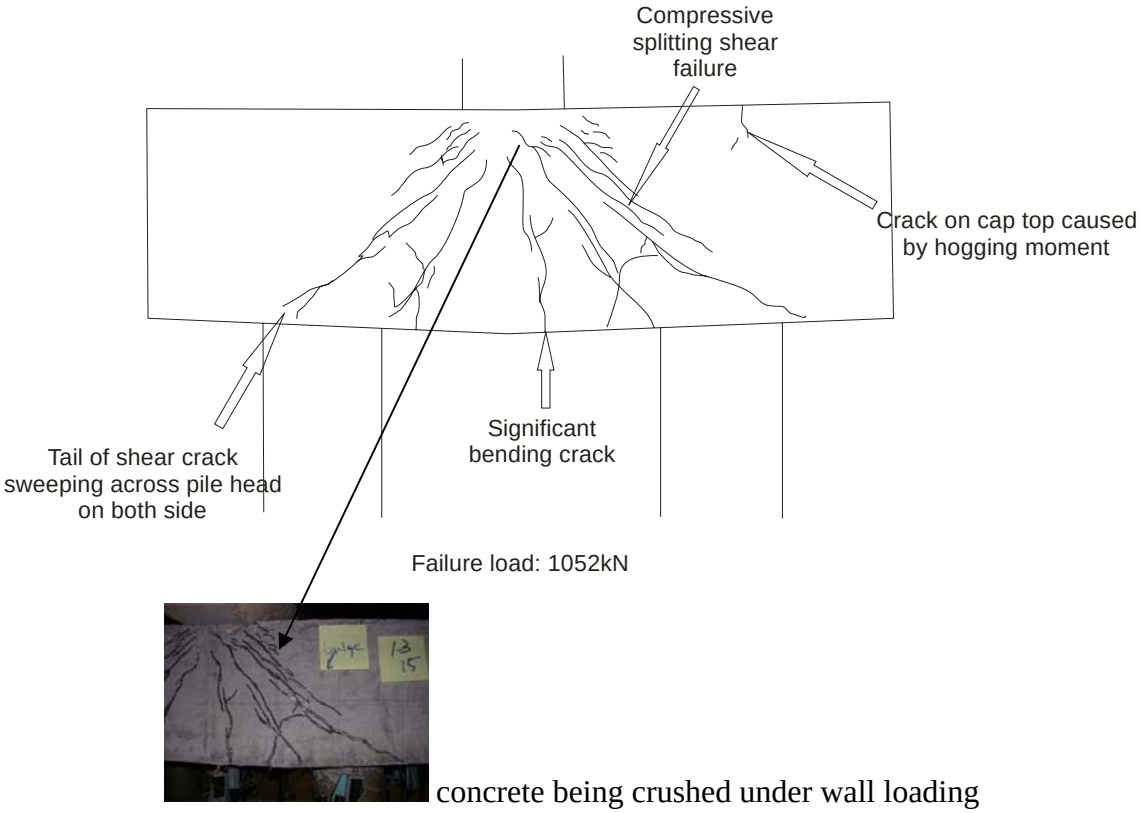

concrete being crushed under wall loading

B4A4 Back surface

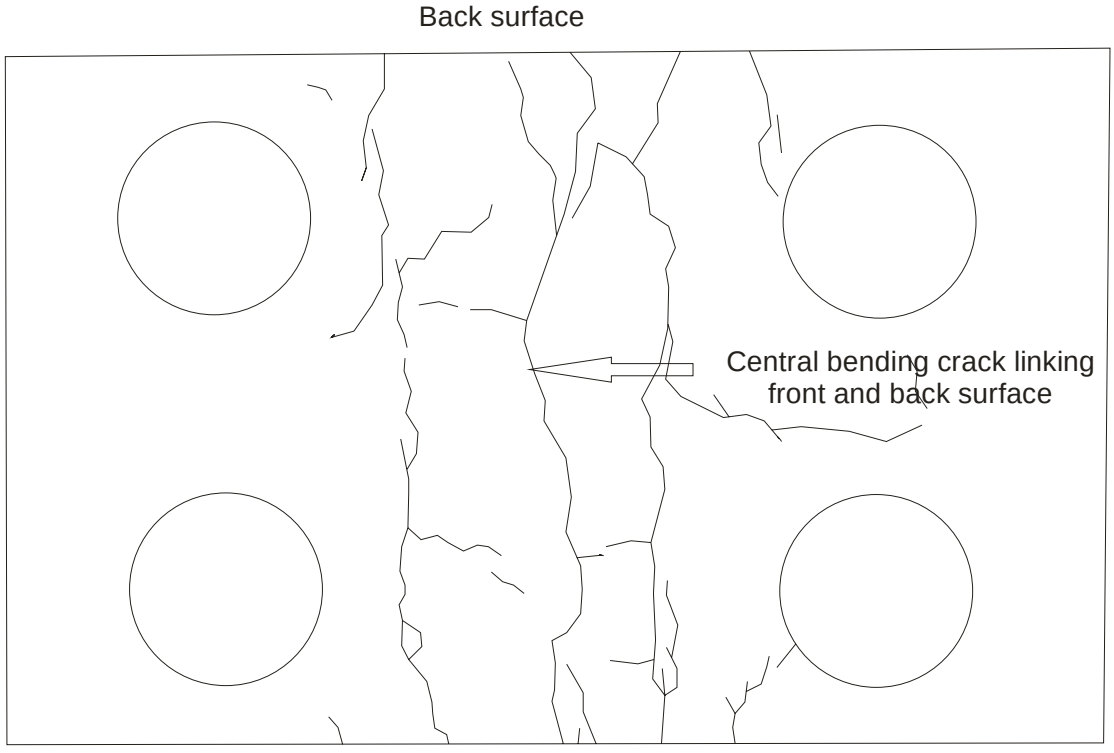

B4A4 Cap soffit

Figure AIII Crack distribution (continued)

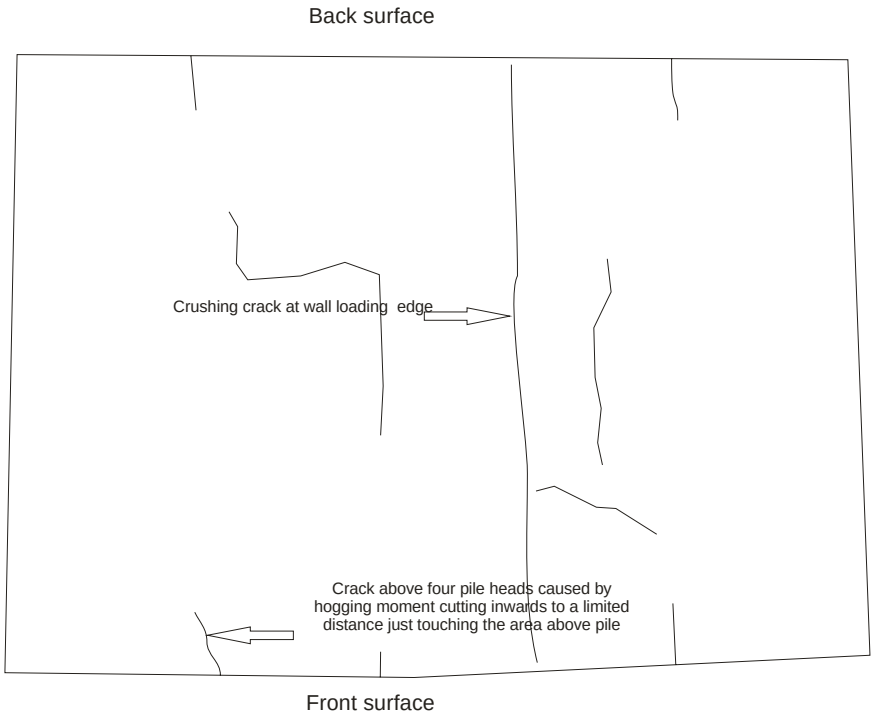

B4A5 Top surface

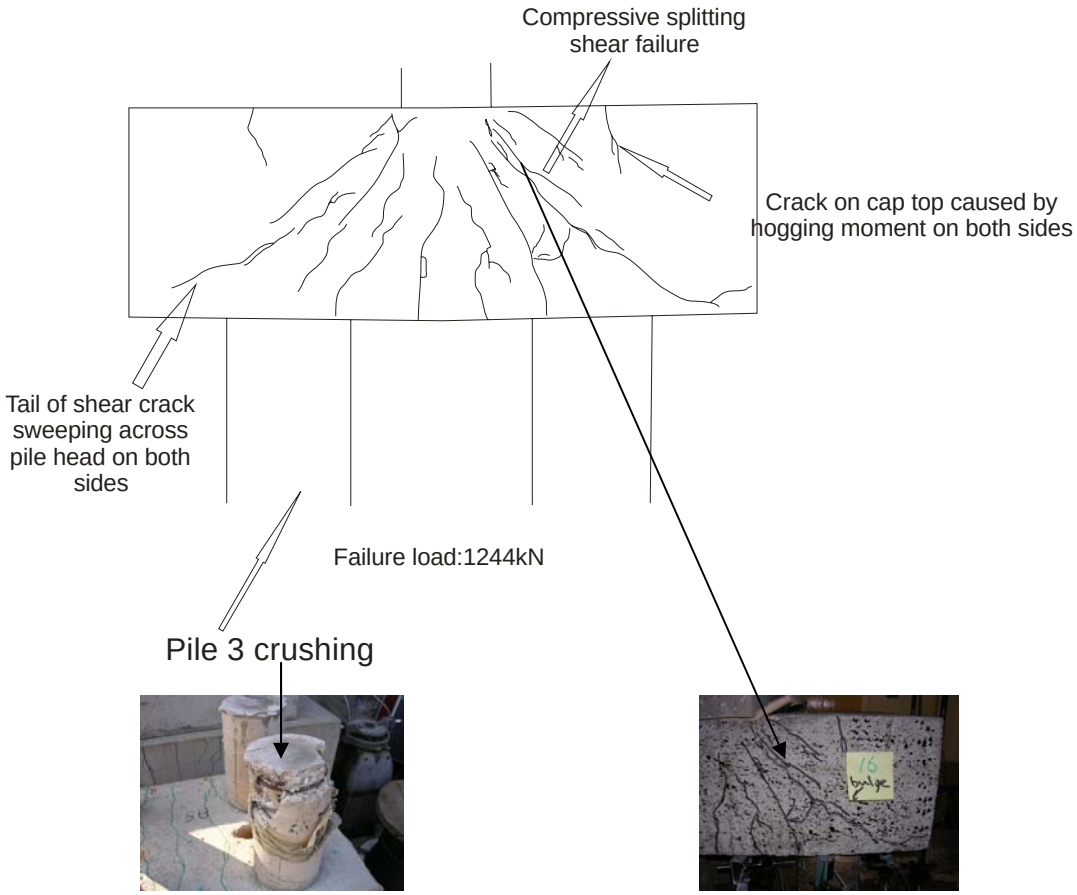

B4A5 Front surface

Figure AIII Crack distribution (continued)

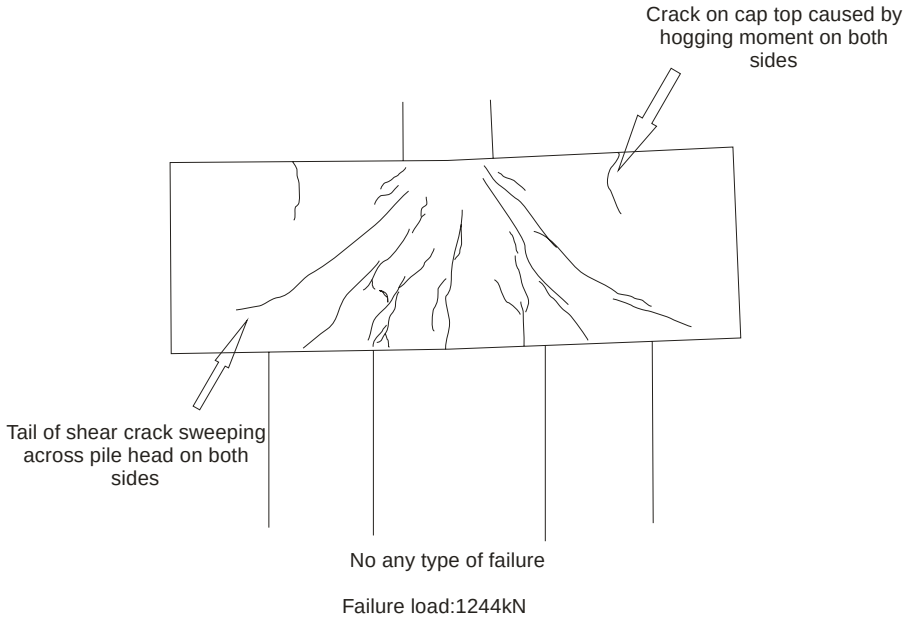

B4A5 Back surface

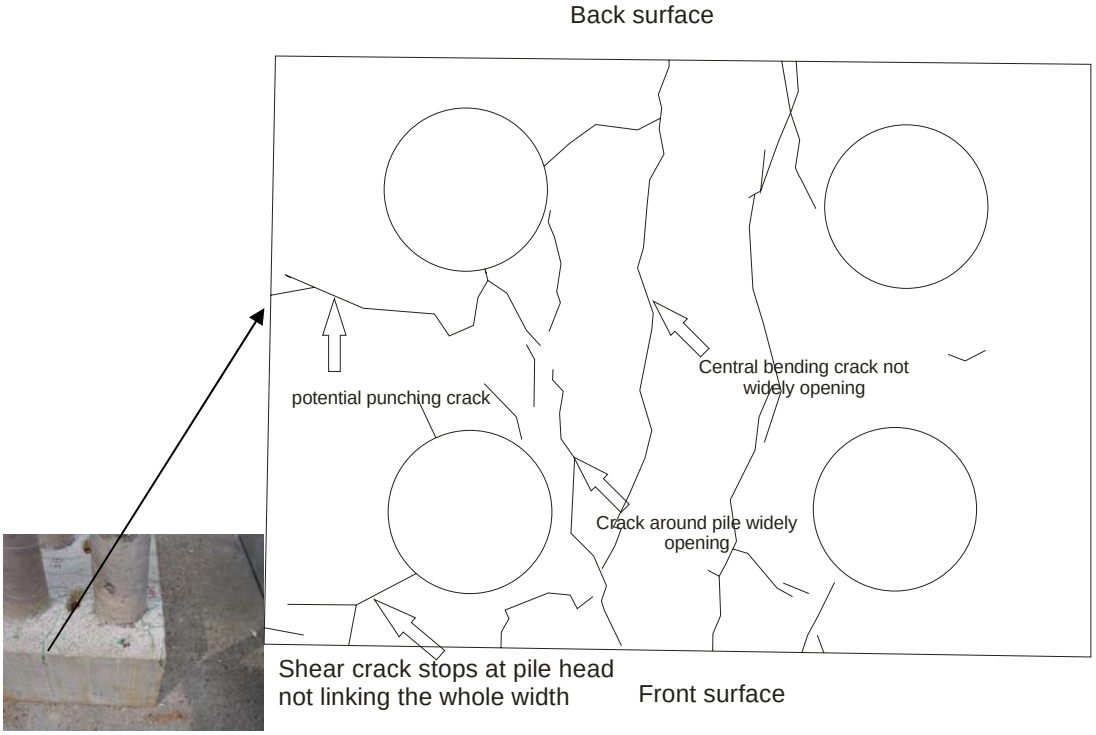

Punching crack on right surface

B4A5 Cap soffit

Figure AIII Crack distribution (continued)

Back surface

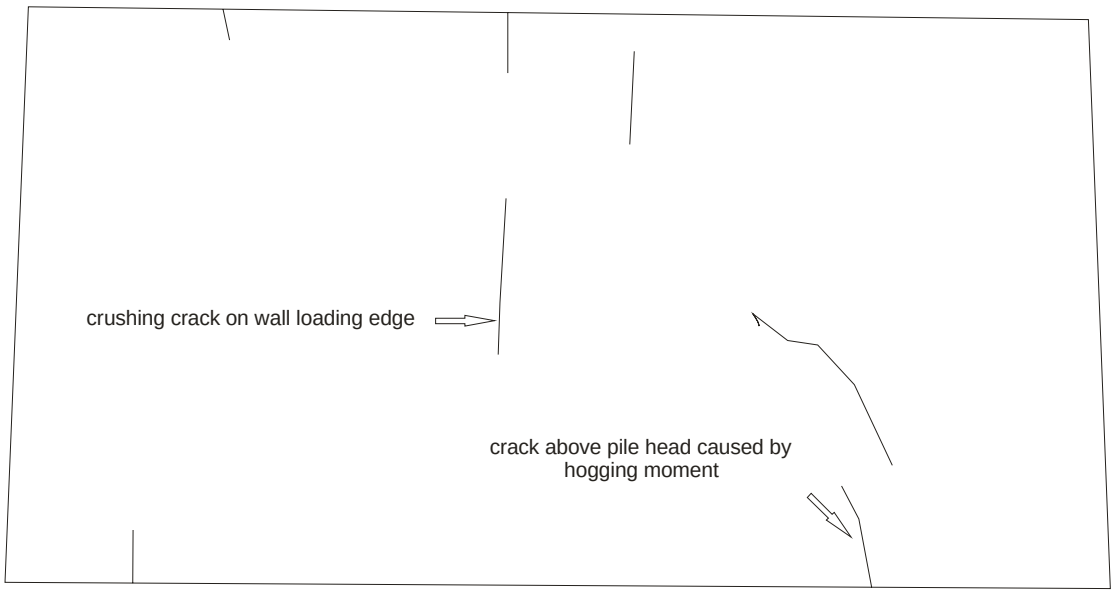

Front surface

B4B1 Top surface

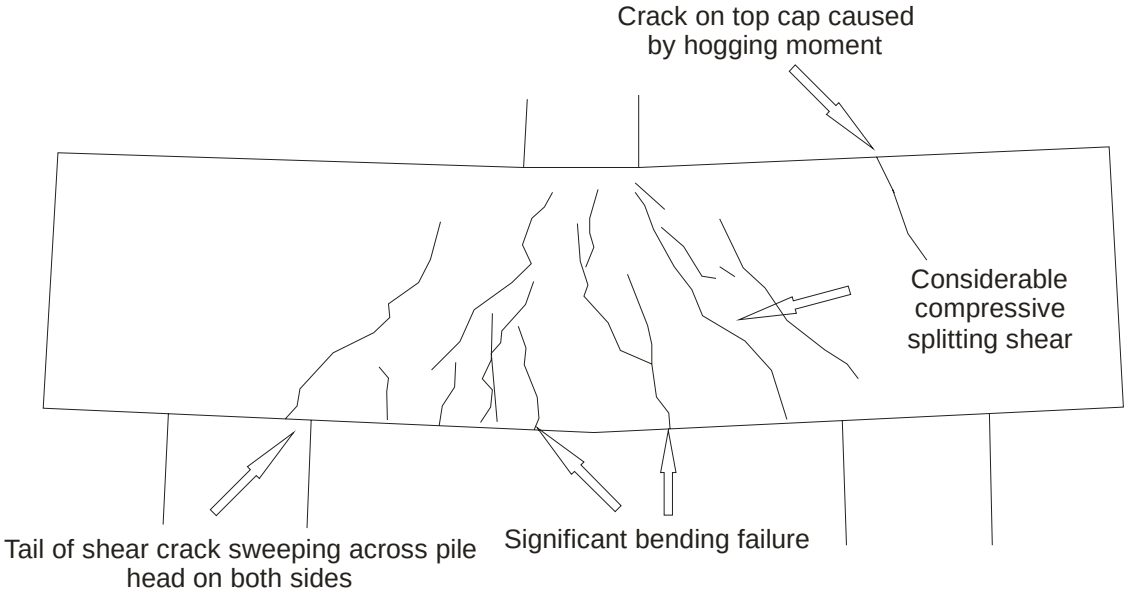

B4B1 Front surface

Figure AIII Crack distribution (continued)

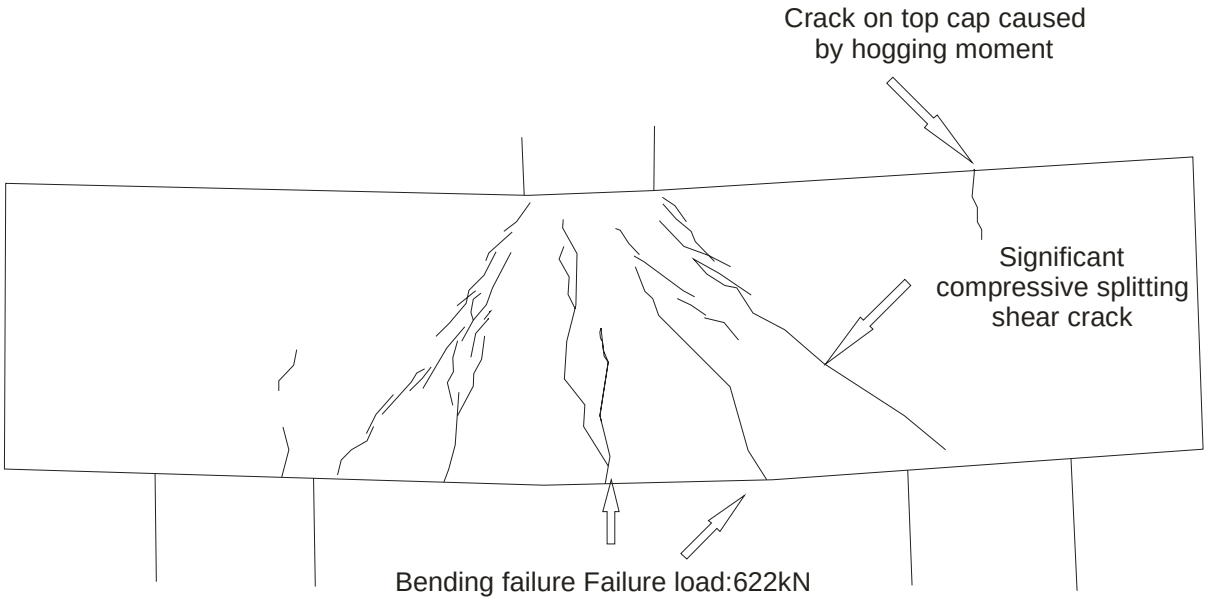

B4B1 Back surface

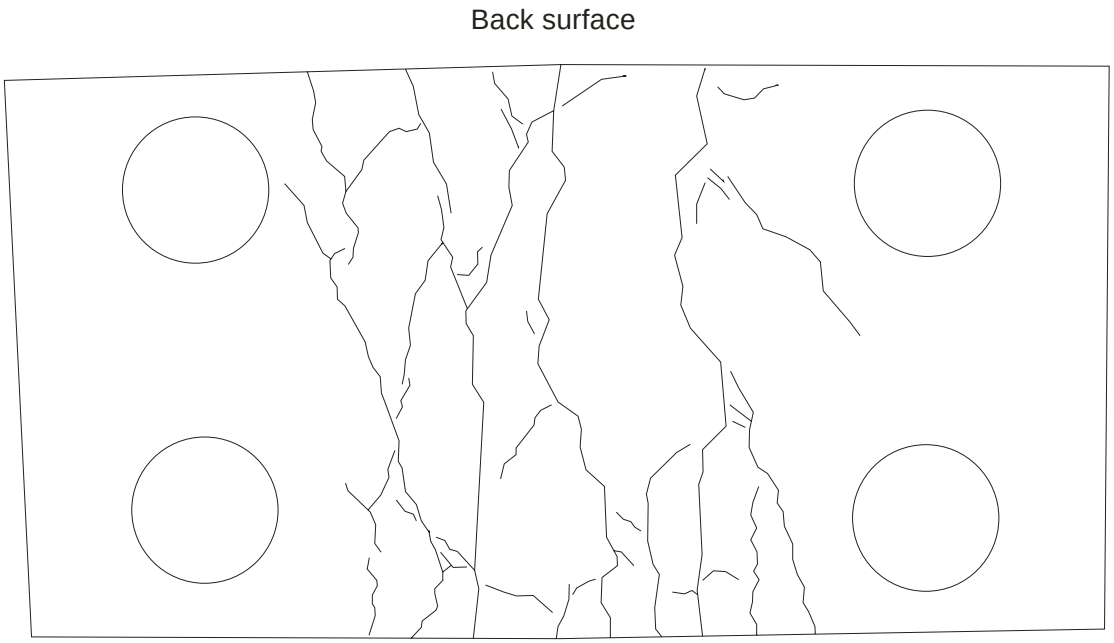

B4B1 Cap soffit

Figure AIII Crack distribution (continued)

B4B2 Top surface

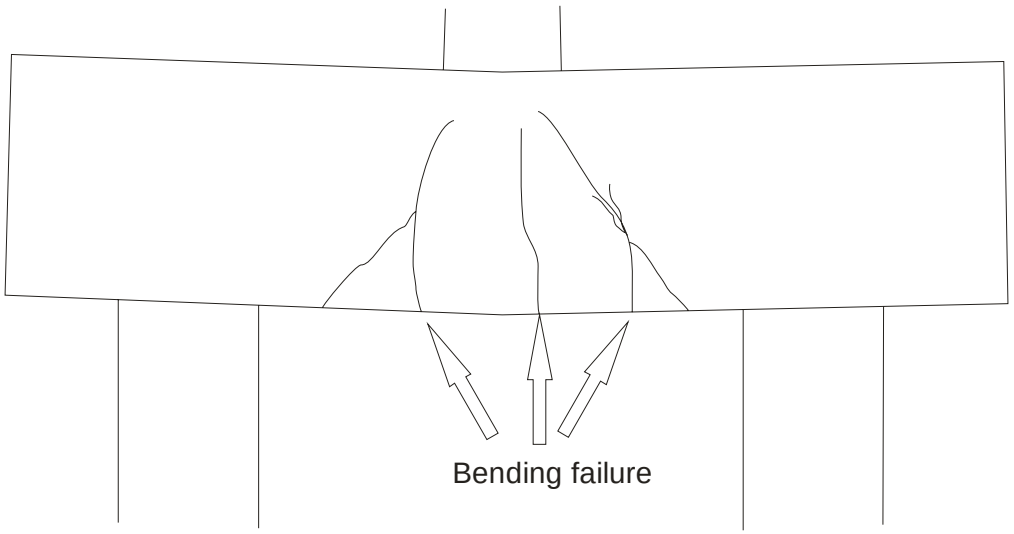

Failure load:713kN

B4B2 Front surface

Figure AIII Crack distribution (continued)

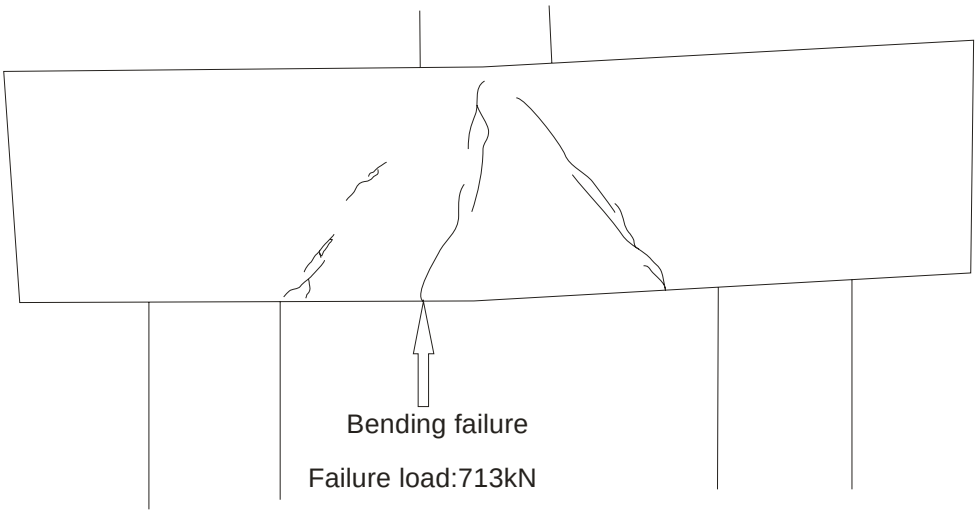

B4B2 Back surface

Back surface

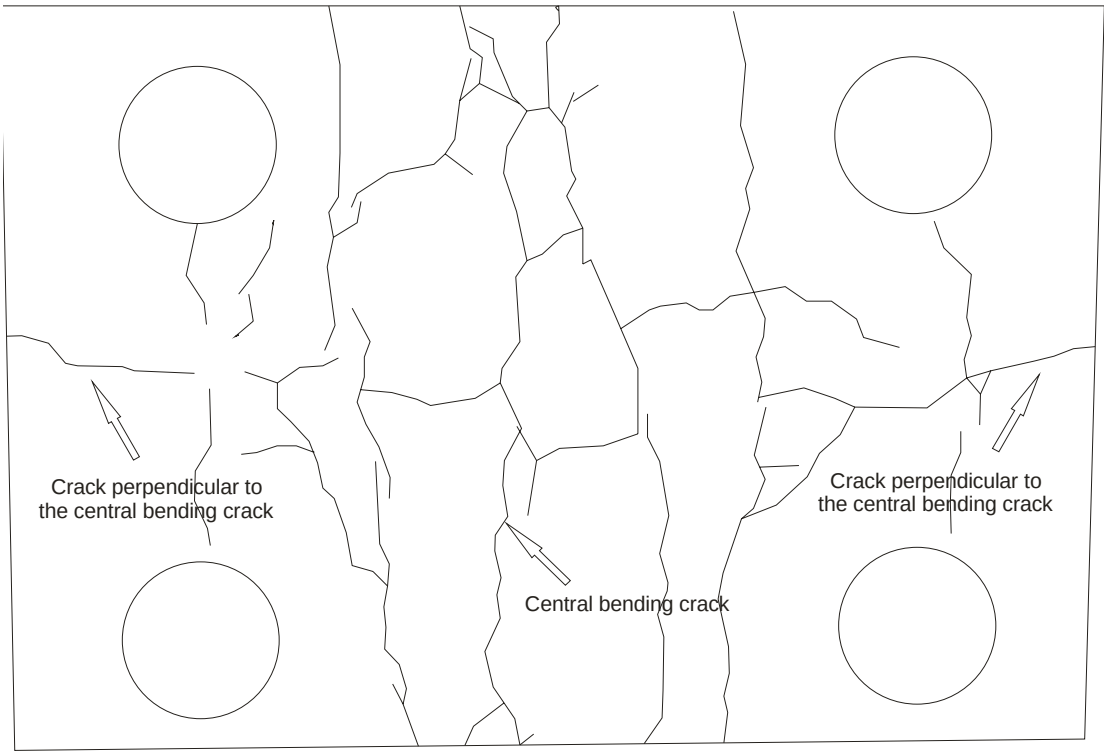

Front surface

B4B2 Cap soffit

Figure AIII Crack distribution (continued)

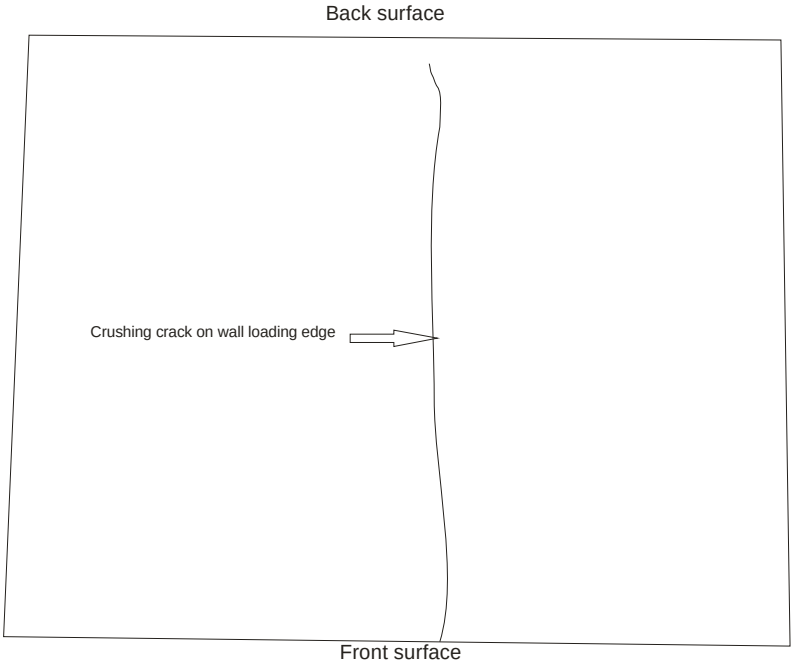

B4B3 Top surface

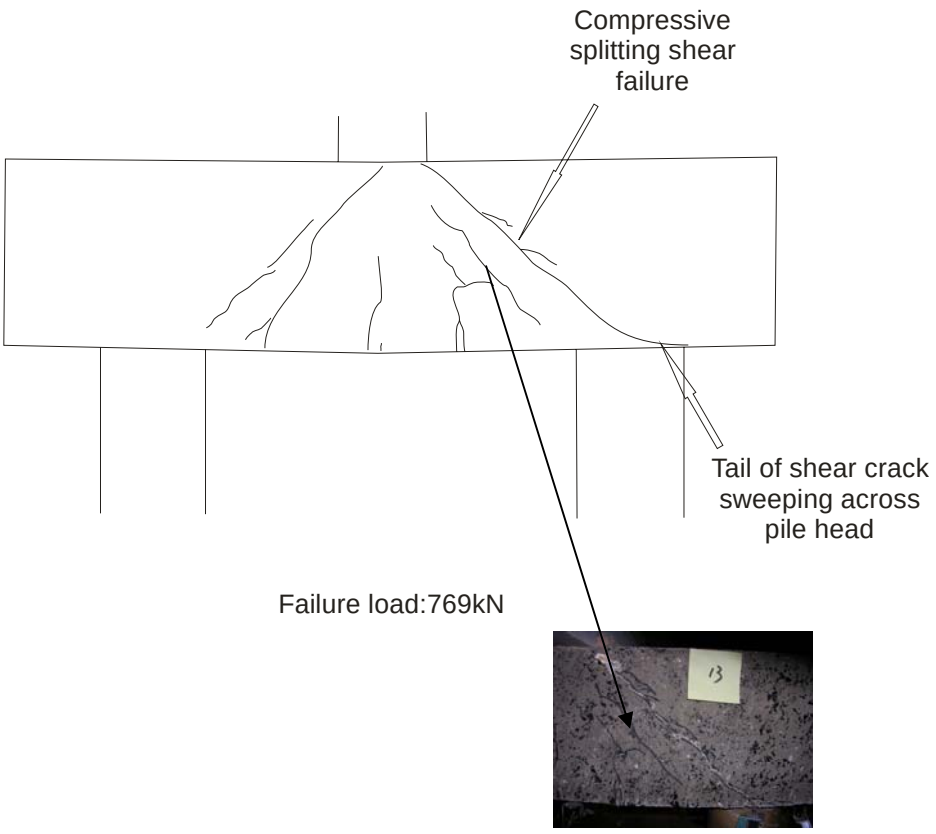

B4B3 Front surface

Figure AIII Crack distribution (continued)

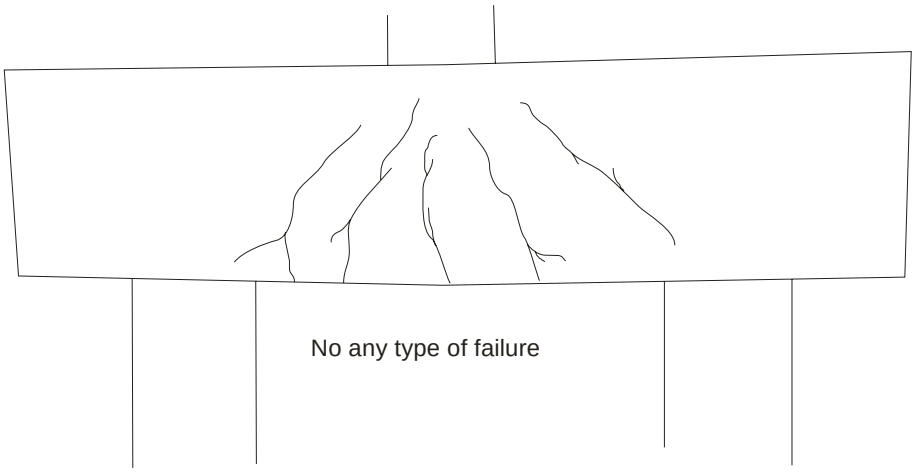

Failure load:769kN

B4B3 Back surface

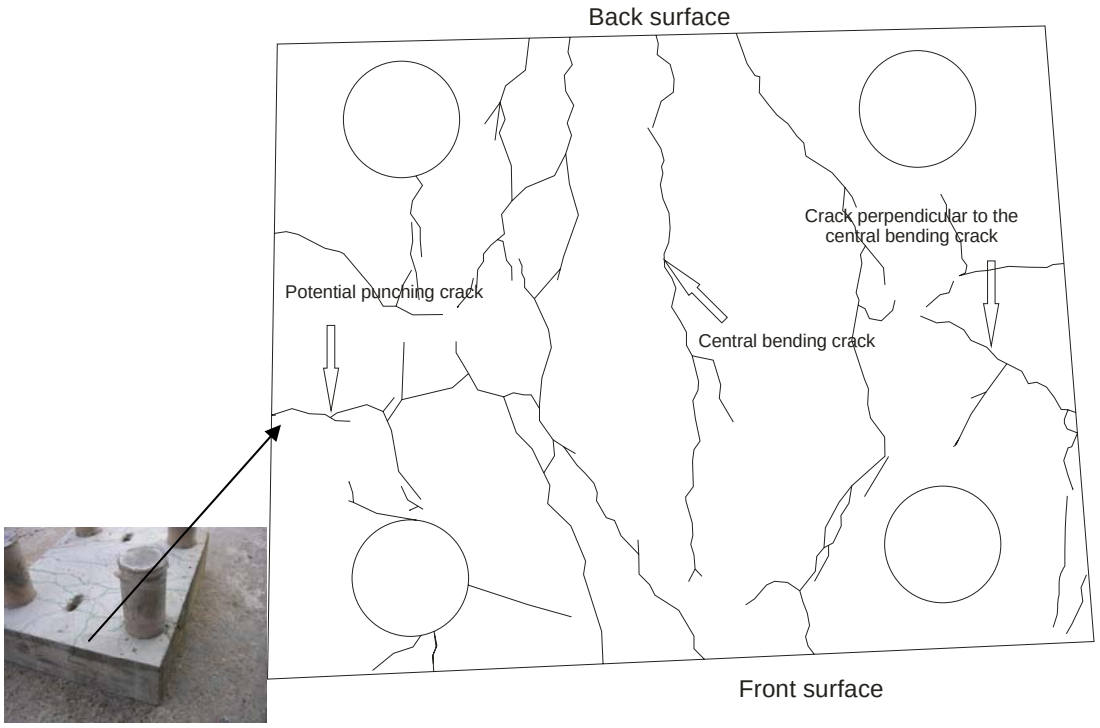

Punching crack on right surface

B4B3 Cap soffit

Figure AIII Crack distribution (continued)

B4B4 Top surface

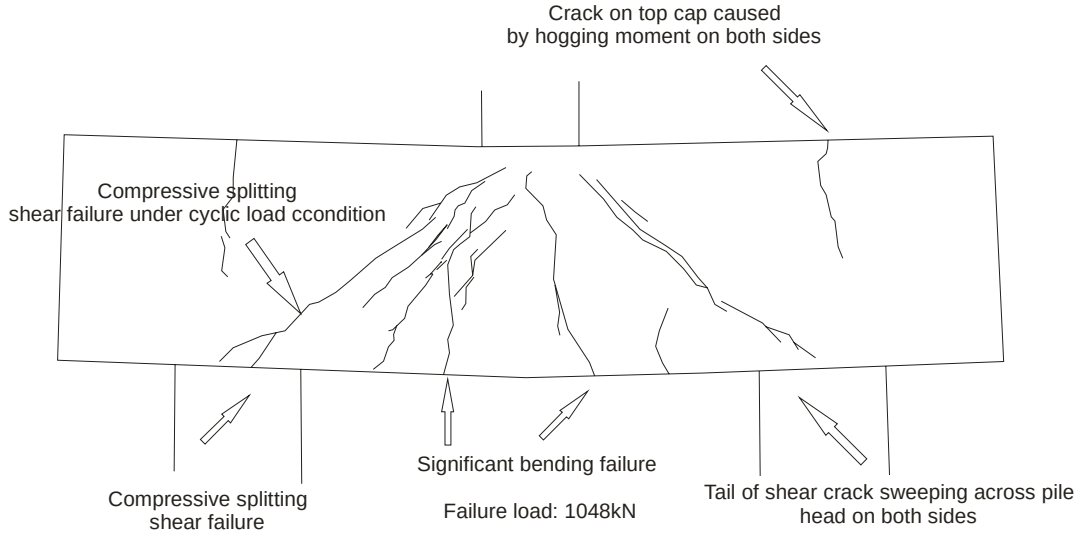

B4B4 Front surface

Figure AIII Crack distribution (continued)

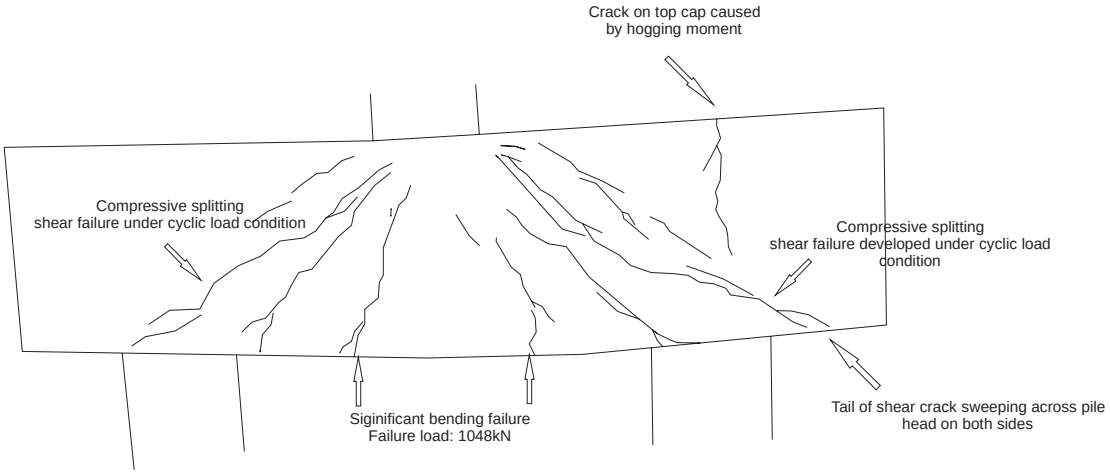

B4B4 Back surface

Back surface

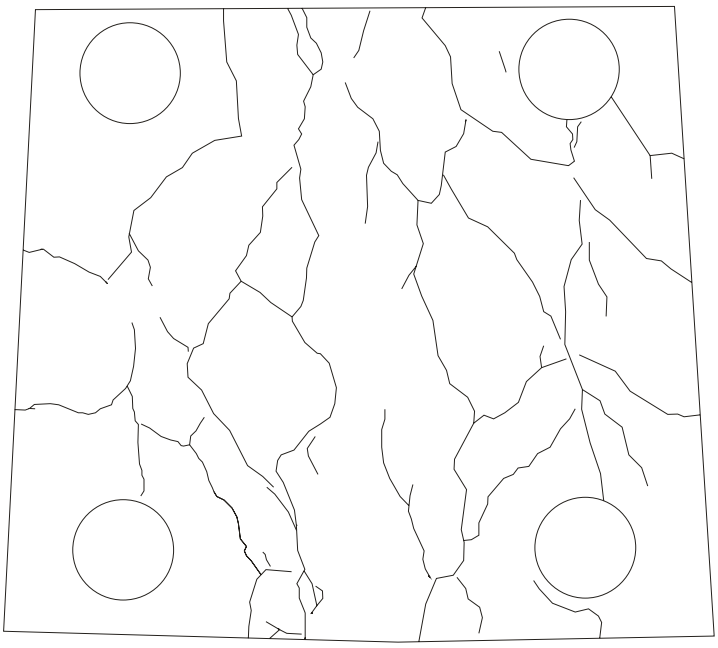

Front surface

B4B4 Cap soffit

Figure AIII Crack distribution

Appendix IV iDIANA batch commands

Batch commands for models of experimental samples (B4A4)

```
! iDIANA Version 9.1 Release 04
 ! Installed for : Univ. of Southampton
 ! History file for model : A4

 FEMGEN A4
 PROPERTY FE-PROG DIANA STRUCT_3D  ; YES
 UTILITY SETUP UNITS LENGTH MILLIMETER
 UTILITY SETUP UNITS MASS KILOGRAM
 UTILITY SETUP UNITS FORCE NEWTON
 UTILITY SETUP UNITS TIME SECOND
 UTILITY SETUP UNITS TEMP CELSIUS
 UTILITY SETUP UNDO ON
 UTILITY SETUP BINSET OFF
 MESHING OPTIONS CHECK STRUCTURED OFF
 UTILITY SETUP OPTIONS ANALYSIS SOLVER-COMMAND diana_w
 GEOMETRY POINT COORD P1 0 0 0
 GEOMETRY POINT COORD P2 350 0 0
 GEOMETRY POINT COORD P3 0 250 0
 GEOMETRY POINT COORD P4 350 250 0

 GEOMETRY LINE STRAIGHT L1 P1 P2 40
 GEOMETRY LINE STRAIGHT L2 P3 P4 40
 GEOMETRY LINE STRAIGHT L3 P1 P3 20
 GEOMETRY LINE STRAIGHT L4 P2 P4 20

 GEOMETRY POINT COORD P5 85  100
 GEOMETRY POINT COORD P6 150 100
 GEOMETRY POINT COORD P7 215 100
 GEOMETRY POINT COORD P8 150 35
 GEOMETRY POINT COORD P9 150 165

 GEOMETRY LINE STRAIGHT L5 P5 P6
 GEOMETRY LINE STRAIGHT L6 P8 P6
 GEOMETRY LINE STRAIGHT L7 P7 P6
 GEOMETRY LINE STRAIGHT L8 P9 P6

 GEOMETRY LINE ARC L9 P5 P8 P6
 GEOMETRY LINE ARC L10 P8 P7 P6
 GEOMETRY LINE ARC L11 P7 P9 P6
 GEOMETRY LINE ARC L12 P9 P5 P6

 CONSTRUCT SET SOFFLOOP APPEND L1 L2 L3 L4
 CONSTRUCT SET PILELOOP APPEND L9 L10 L11 L12
 GEOMETRY SURFACE REGION S1 SOFFLOOP PILELOOP
 GEOMETRY SWEEP L4 L13 8 TRANSLATE TR1 50 0 0
```

```
GEOMETRY SURFACE 3SIDES S3 L5 L9 L6
GEOMETRY SURFACE 3SIDES S4 L6 L10 L7
GEOMETRY SURFACE 3SIDES S5 L7 L11 L8
GEOMETRY SURFACE 3SIDES S6 L8 L12 L5
CONSTRUCT SET PILETOP APPEND S3 S4 S5 S6
CONSTRUCT SET SOFFIT APPEND S1 S2 S3 S4 S5 S6

GEOMETRY SWEEP SOFFIT TOP 20 TRANSLATE TR2 0 0 230

GEOMETRY SWEEP PILETOP PILEBOTT 8 TRANSLATE TR3 0 0 -260

CONSTRUCT SET PILECAP APPEND ALL

GEOMETRY POINT COORD P28 0 0 31
GEOMETRY POINT COORD P29 400 0 31
GEOMETRY POINT COORD P30 400 250 31
GEOMETRY POINT COORD P31 0 250 31
REINFORCE GRID SECTION RE1 P28 P29 P30 P31
REINFORCE GRID STEEL RE1

PROPERTY BOUNDARY CONSTRAINT SIDE S23 X
PROPERTY BOUNDARY CONSTRAINT BACK1 S15 Y
PROPERTY BOUNDARY CONSTRAINT BACK2 S22 Y
PROPERTY LOADS DISPLACE DISPLAC S8 -0.1 Z
PROPERTY BOUNDARY CONSTRAINT PILE PILEBOTT Z

MESHING TYPES ALL HE20 CHX60
MESHING GENERATE


PROPERTY MATERIAL MASTEEL STATNONL REINFORC VMISES NONE 547
PROPERTY MATERIAL MACONCRE ELASTIC ISOTROP 28000 0.2
PROPERTY MATERIAL MACONCRE STATNONL CONCBRIT CRACK CONSTA
TENSIO1 ULTIMATE TAUCRI1 VMISES NONE 2.44 0.000311 0.2 24.4
PROPERTY MATERIAL MASTEEL ELASTIC REINFORC BOND 210000
PROPERTY PHYSICAL PHSTEEL GEOMETRY REINFORC GRID 2.26 2.26 1 0 0
PROPERTY ATTACH PILECAP MACONCRE
PROPERTY ATTACH STEEL MASTEEL PHSTEEL
SAVE
! Confirm save?
YES
! Enter model description =>
A4
* M423: Saved to database file
UTILITY WRITE DIANA
! Confirm write to new file?
YES
DRAWING DISPLAY
FILE CLOSE
```

Batch commands for models in parametric study (E1gg)

```
! iDIANA Version 9.1 Release 04
  ! Installed for : Univ. of Southampton
  ! History file for model : E1gg

  FEMGEN E1gg
  PROPERTY FE-PROG DIANA STRUCT_3D  ; YES
  UTILITY SETUP UNITS LENGTH MILLIMETER
  UTILITY SETUP UNITS MASS KILOGRAM
  UTILITY SETUP UNITS FORCE NEWTON
  UTILITY SETUP UNITS TIME SECOND
  UTILITY SETUP UNITS TEMP CELSIUS
  UTILITY SETUP UNDO ON
  UTILITY SETUP BINSET OFF
  MESHING OPTIONS CHECK STRUCTURED OFF
  UTILITY SETUP OPTIONS ANALYSIS SOLVER-COMMAND diana_w
  GEOMETRY POINT COORD P1 0 0 0
  GEOMETRY POINT COORD P2 350 0 0
  GEOMETRY POINT COORD P3 0 350 0
  GEOMETRY POINT COORD P4 350 350 0

  GEOMETRY LINE STRAIGHT L1 P1 P2 40
  GEOMETRY LINE STRAIGHT L2 P3 P4 40
  GEOMETRY LINE STRAIGHT L3 P1 P3 20
  GEOMETRY LINE STRAIGHT L4 P2 P4 20

  GEOMETRY POINT COORD P5 85  100
  GEOMETRY POINT COORD P6 150 100
  GEOMETRY POINT COORD P7 215 100
  GEOMETRY POINT COORD P8 150 35
  GEOMETRY POINT COORD P9 150 165

  GEOMETRY LINE STRAIGHT L5 P5 P6
  GEOMETRY LINE STRAIGHT L6 P8 P6
  GEOMETRY LINE STRAIGHT L7 P7 P6
  GEOMETRY LINE STRAIGHT L8 P9 P6

  GEOMETRY LINE ARC L9 P5 P8 P6
  GEOMETRY LINE ARC L10 P8 P7 P6
  GEOMETRY LINE ARC L11 P7 P9 P6
  GEOMETRY LINE ARC L12 P9 P5 P6

  CONSTRUCT SET SOFFLOOP APPEND L1 L2 L3 L4
  CONSTRUCT SET PILELOOP APPEND L9 L10 L11 L12
  GEOMETRY SURFACE REGION S1 SOFFLOOP PILELOOP
  GEOMETRY SWEEP L4 L13 8 TRANSLATE TR1 50 0 0

  GEOMETRY SURFACE 3SIDES S3 L5 L9 L6
  GEOMETRY SURFACE 3SIDES S4 L6 L10 L7
  GEOMETRY SURFACE 3SIDES S5 L7 L11 L8
  GEOMETRY SURFACE 3SIDES S6 L8 L12 L5
```

```
CONSTRUCT SET PILETOP APPEND S3 S4 S5 S6
CONSTRUCT SET SOFFIT APPEND S1 S2 S3 S4 S5 S6

GEOMETRY SWEEP SOFFIT TOP 14 TRANSLATE TR2 0 0 230

GEOMETRY SWEEP PILETOP PILEBOTT 8 TRANSLATE TR3 0 0 -260

CONSTRUCT SET CAP APPEND B1 B2 B3 B4 B5 B6

CONSTRUCT SET PILE APPEND B7 B8 B9 B10

CONSTRUCT SET PILECAP APPEND ALL

GEOMETRY POINT COORD P28 0 0 31
GEOMETRY POINT COORD P29 400 0 31
GEOMETRY POINT COORD P30 400 350 31
GEOMETRY POINT COORD P31 0 350 31
REINFORCE GRID SECTION RE1 P28 P29 P30 P31
REINFORCE GRID STEEL RE1

PROPERTY BOUNDARY CONSTRAINT SIDE S23 X
PROPERTY BOUNDARY CONSTRAINT BACK1 S15 Y
PROPERTY BOUNDARY CONSTRAINT BACK2 S22 Y
PROPERTY LOADS DISPLACE DISPLAC S8 -0.1 Z
PROPERTY BOUNDARY CONSTRAINT PILEBOT PILEBOTT Z

MESHING TYPES ALL HE20 CHX60
MESHING GENERATE

PROPERTY MATERIAL MASTEEL STATNONL REINFORC VMISES NONE 547
PROPERTY MATERIAL MACONCR1 ELASTIC ISOTROP 28000 0.2
PROPERTY MATERIAL MACONCR1 STATNONL CONCBRIT CRACK CONSTA
TENSIO1 ULTIMATE TAUCRI1 VMISES NONE 2.5 0.001 0.2 25
PROPERTY MATERIAL MACONCR2 ELASTIC ISOTROP 28000 0.2
PROPERTY MATERIAL MACONCR2 STATNONL CONCBRIT CRACK CONSTA
TENSIO1 ULTIMATE TAUCRI1 VMISES NONE 2.5 0.001 0.2 100
PROPERTY MATERIAL MASTEEL ELASTIC REINFORC BOND 210000
PROPERTY PHYSICAL PHSTEEL GEOMETRY REINFORC GRID 2.26 2.26 1 0 0
PROPERTY ATTACH CAP MACONCR1
PROPERTY ATTACH PILE MACONCR2
PROPERTY ATTACH STEEL MASTEEL PHSTEEL
SAVE
! Confirm save?
YES
! Enter model description =>
E1gg
* M423: Saved to database file
UTILITY WRITE DIANA
! Confirm write to new file?
YES
DRAWING DISPLAY
FILE CLOSE
```

Appendix V Published papers

Cao J, Bloodworth A. G., (2007). “Shear Capacity of Reinforced Concrete Pile Caps.” *Proceedings of the IABSE Symposium, Weimar, Sept 19-21 2007*

Cao J, Bloodworth A.G. and Xu M, (2007). “Observations of truss action in reinforced concrete pile caps.” *Proceedings of the Third International Conference on Structural Engineering, Mechanics and Computation, Cape Town, South Africa 10-12 Sept 2007*